

A Thesis Submitted for the Degree of PhD at the University of Warwick

Permanent WRAP URL:

<http://wrap.warwick.ac.uk/78792>

Copyright and reuse:

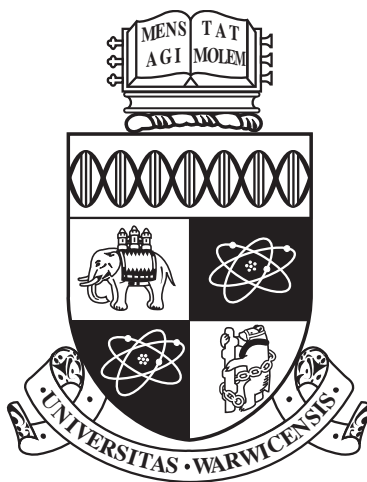
This thesis is made available online and is protected by original copyright.

Please scroll down to view the document itself.

Please refer to the repository record for this item for information to help you to cite it.

Our policy information is available from the repository home page.

For more information, please contact the WRAP Team at: wrap@warwick.ac.uk



**Investigating the Adsorption of Select Polar
Functionalities with the Aqueous
Electrolyte/Amorphous Silica Interface to
Understand the 'Low Salinity' Effect**
by

Jasmine L. Desmond

Thesis

Submitted to the University of Warwick

for the degree of

Doctor of Philosophy

Department of Chemistry

September 2015

THE UNIVERSITY OF
WARWICK

Contents

List of Tables	v
List of Figures	vii
Acknowledgments	xxiii
Declarations	xxiv
Abstract	xxv
Abbreviations	xxvi
Chapter 1 Introduction	1
1.1 Aim: Understanding the 'Low Salinity' (LS) Effect and Enhanced Oil Recovery (EOR)	1
1.1.1 The 'Low Salinity' (LS) Effect	3
1.1.2 'Low-Salinity' Enhanced Oil Recovery Mechanisms Explored in This Thesis	6
1.2 The Aqueous Electrolyte/Mineral Interface	6
1.2.1 Importance of Biomolecule-Silica Interactions	6
1.2.2 A Brief Overview of Silica Literature to Date	7
1.3 Experimental Studies at the Silica/Water Interface	7
1.3.1 The Effect of Ionic Strength	9
1.3.2 The Effect of Ion Type	10
1.4 The Gouy-Chapman-Stern (GCS) Model	11
1.5 Simulation Studies of the Silica/Water Interface	15

1.5.1	The Silica/Pure Water Interface	15
1.5.2	The Amorphous Silica/Pure Water Interface	17
1.5.3	The Aqueous Electrolyte/Quartz Interface	18
1.5.4	The Aqueous Electrolyte/Amorphous Silica Interface	20
1.6	Molecular Adsorption at the Silica/Water Interface	21
1.6.1	Force-Field Inter-operability	22
1.6.2	The Silica/Pure Water Interface	24
1.6.3	The Amorphous Silica/Aqueous Electrolyte Interface	26
1.6.4	Probes of Molecular Adhesion to Amorphous Silica	26
1.7	Aims and Objectives	32
1.7.1	Chapter 4	33
1.7.2	Chapter 5	34
1.7.3	Chapter 6	34
Chapter 2	Methods	35
2.1	Simulation Methods	35
2.1.1	Simulation Background	35
2.1.2	Simulation Setup	49
2.1.3	Simulation Analysis	57
2.2	Experimental Methods	63
2.2.1	Experimental Background	63
2.2.2	Experimental Protocol (Chapter 5)	65
Chapter 3	Testing the Inter-Operability of the CHARMM and SPC/Fw Force-Fields for Conformational Sampling	67
3.1	Simulation Protocol in Brief	68
3.2	Ramachandran Plots	69
3.3	Backbone Atom Cluster Analysis	76
3.4	All-Atom Peptide Cluster Analysis	81
3.5	Radial Distribution Functions	85
3.6	Convergence	88
3.7	Effectiveness of Replica Exchange Molecular Dynamics	89
3.8	Conclusions	91

Chapter 4 Water and Ion Structure at the Aqueous Electrolyte/Amorphous

Silica Interface	93
4.1 Simulation Protocol in Brief	94
4.2 Ion Concentration as a Function of Distance Normal to the Surface . . .	96
4.2.1 A General Overview of the Ion Distributions	96
4.2.2 Deprotonated Silanol Groups: the Key Surface Adsorption Site	99
4.2.3 Distributions of the Angle Between the Surface Normal and the O ⁻ -M Vector	107
4.2.4 Alternative Surface Adsorption Sites	112
4.2.5 Comparisons to Previous Work	115
4.2.6 Interfacial Ion Structure Summary	116
4.3 Interfacial Water Structure	118
4.3.1 Water Density as a Function of Distance Normal to the Surface .	118
4.3.2 Interfacial Water Density Summary	127
4.3.3 Water Orientation as a Function of Distance Normal to the Surface	127
4.3.4 Interfacial Water Orientation Summary	134
4.4 Perpendicular and Parallel Diffusion as a Function of Distance Normal to the Surface	135
4.5 Conclusion	137

Chapter 5 The Role of Ion Type in the Low Salinity Effect: an Experimental and Computational Study

140

5.1 Experiment and Simulation Protocol in Brief	143
5.2 Force-mapping atomic force microscopy data	143
5.3 Ion Structuring at the Aqueous CaCl ₂ /Amorphous Silica Interface . . .	146
5.4 Developing MetaD Protocol	147
5.4.1 Metadynamics Trials: Parameter Optimisation	148
5.4.2 Final System Setups for Metadynamics Simulations	153
5.4.3 Evidence of Convergence of Metadynamics Simulations using the Optimised Protocol and Procedure for the Estimation of Un- certainties in the Vertical Free Energy Profiles	155
5.5 Vertical Free Energy Profiles for Methylammonium Adsorption at the Interface between Amorphous Silica and NaCl, KCl and MgCl ₂ solutions	157

5.6	Lateral Free Energy Profiles for Methylammonium Adsorption at the Interface between Amorphous Silica and NaCl, KCl and MgCl ₂ solutions	158
5.7	Free Energy Profiles for Methylammonium Adsorption at the Interface between Amorphous Silica and CaCl ₂ solution	162
5.8	Force vs Distance Profiles and the Origin of the Low Salinity Effect . .	168
5.8.1	Determination of the Equilibrium Distribution of Site Types . .	169
5.9	Conclusions	170
Chapter 6 Further and Future Investigation of the Low Salinity Effect: A More Sophisticated Model of the Functionalized Atomic Force Microscopy (AFM) Tip		173
6.1	Simulation Protocol in Brief	174
6.2	Tip Force as a Function of Distance from the Surface	176
6.3	Limitations of this Approach	178
6.4	Conclusion and Future Work	178
Chapter 7 Conclusion		180
Appendix A Additional Information: Methods		203
Appendix B Additional Information: Testing the Inter-Operability of the CHARMM and SPC/Fw Force-Fields for Conformational Sampling		213
Appendix C Additional Information: Water and Ion Structure at the Aqueous Electrolyte/Amorphous Silica Interface		218
Appendix D Additional Information: The Role of Ion Type in the Low Salinity Effect: an Experimental and Computational Study		233
Appendix E Additional Information: Further and Future Investigation of the Low Salinity Effect: A More Sophisticated Model of the Functionalized Atomic Force Microscopy (AFM) Tip		238

List of Tables

2.1	Number of waters required to achieve a bulk water pressure of 1 atm for the different electrolyte solutions.	55
2.2	Total simulation time and time taken for equilibration.	55
3.1	RMSD values (nm) for matchings of the representative structures from the top four TIPS3P and SPC/Fw backbone clusters.	80
3.2	Classification of the top 4 TIPS3P clusters to regions of the Ramachandran plot	81
3.3	RMSD values (nm) between all unique pairs among top four peptide clusters obtained with the same water model, for both TIPS3P and SPC/Fw.	83
3.4	RMSD values (nm) for matchings of the representative structures from the top four TIPS3P and SPC/Fw peptide clusters.	85
3.5	Cross terms for the interaction between the oxygen atoms of the terminal carboxylate group and the hydrogen atoms of water.	87
3.6	Exchange probabilities (Ex. P.) and number of exchanges (No Ex.) between adjacent replicas for RGD solvated by TIPS3P and SPC/Fw . . .	90
4.1	Predicted width of the double layer (from simulation) for the different electrolyte solutions.	97
4.2	Summary of cation- O^- RDF first peak separations and corresponding cation σ values.	100
4.3	Time averaged proportion of different site types in $CaCl_2$ solution. . . .	112
4.4	Residence time (r_t) for $M_{(O^-)}$ and $Cl^-_{((M)-O^-)}$	122

A.1	Non-bonded force-field parameters - RGD - ARG.	204
A.2	Non-bonded force-field parameters - RGD - GLY.	205
A.3	Non-bonded force-field parameters - RGD - ASP.	205
A.4	Non-bonded force-field parameters - SPT - SER.	206
A.5	Non-bonded force-field parameters - SPT - PRO.	207
A.6	Non-bonded force-field parameters - SPT - THR.	208
A.7	Non-bonded force-field parameters - Methylammonium.	209
A.8	Non-bonded force-field parameters - Gold and 11-amino-1-undecanethiol. 210	
A.9	Non-bonded force-field parameters - Silica.	211
A.10	Non-bonded force-field parameters - SPC/Fw.	211
A.11	Non-bonded force-field parameters - TIPS3P.	212
A.12	Non-bonded force-field parameters - ions.	212
A.13	Repulsive potential between different ion pairs in metadynamics aq. CaCl ₂ /amorphous silica simulations.	212
C.1	Number of waters required to achieve a bulk water pressure of 1 atm for the different electrolyte solutions.	219
C.2	Summary of distances from the surface of peaks in the ion density profiles.	225

List of Figures

1.1	Schematic of the amorphous silica/water interface adapted from Butenuth <i>et. al.</i> ¹ Red represents oxygen atoms, white hydrogen atoms and orange silicon atoms.	2
1.2	Schematic of the key bridging mechanisms important to the 'low salinity' effect and the functional groups through which they can occur.	5
1.3	Equilibrium reactions showing the two stage mechanism for the detachment of carboxylic acids from the silica surface.	5
1.4	Suggested predominant water interactions at the quartz/water interface at low and high pH according to. ² The geometric criteria for defining a H-bond is generally when the distance between a heavy atom (O or N) and water oxygen is 3.5 Å or less and when the angle between the acceptor and the donor hydrogen is 30° or less.	8
1.5	Schematic of the different silanol types: isolated, vicinal and geminal. .	11
1.6	Schematic of the Gouy-Chapman-Stern layer. The inner Helmholtz plane (IHP), outer Helmholtz plane (OHP) and Stern layer have been labelled.	13
1.7	Schematic of a selection of quartz/water interfaces adapted from Notman <i>et. al.</i> ³ Red represents oxygen atoms, white hydrogen atoms and orange silicon atoms.	16
1.8	Schematic of the quartz(100)- and cristobalite(001) surfaces adapted from Sodupe <i>et. al.</i> ⁴ Red represents oxygen atoms, white hydrogen atoms and orange silicon atoms.	17

1.9	Si-O hydrolysis for hydrated Ca_{2+} , with outer sphere paths shown in red, inner sphere paths shown in red as adapted and the barrier to hydrolysis in the absence of ions in black from Dove <i>et. al.</i> ⁵	19
1.10	Flat physisorbed ODT molecules on Au(111) (left) and chemisorbed ODT molecules on Au(111) (right) as adapted from Ahn <i>et. al.</i> ⁶	29
1.11	Interaction force on approach and retraction of the wall to the gold sphere from Patrick <i>et. al.</i> ⁷	32
2.1	Schematic of the bond between atoms i and j	37
2.2	Schematic of the angle made between the atoms i , j and k	37
2.3	Schematic of a proper dihedral angle.	38
2.4	Schematic of a improper dihedral angle.	38
2.5	Exemplar Lennard-Jones Potential Energy Curve.	39
2.6	Schematic of periodic boundary conditions.	44
2.7	Schematics of a potential energy landscape (PEL): 3D (left) and 2D (right) representations.	45
2.8	Structure of the model amorphous silica surface used in the MD simulations: (a) side on view (b) view of the surface in the xy-plane (c) zoomed in side-on view (d) zoomed in view of the surface in the xy-plane. The different types of silanol are denoted UL, LL and R, as labelled.	53
2.9	Schematic to illustrate the concept of surface roughness and the slices used for binning the data.	59
2.10	Schematic to illustrate how solution volume was estimated considering the occupation of a lateral 12×12 grid. (a) close to the surface, where the volume of water is at its lowest (b) further from the surface, where the volume of water has increased (c) at a distance from the surface, where the entire lateral area of the surface is accesible to water oxygens.	60
2.11	Adhesion force maps from a $5 \mu \times 5 \mu$ area on SiO_2 surfaces, as adapted from Stipp <i>et. al.</i> ⁸	64

2.12	Schematic of the CFM-AFM setup, as adapted from Lieber <i>et. al.</i> ⁹ The sample is positioned on a piezoelectric xyz translator. A laser beam is reflected from the tip onto a photodiode to detect the force experienced by the tip. The movement of the tip up and down reflects the force experienced by the tip.	64
2.13	Schematic of approach and retraction curves Stipp <i>et. al.</i> ⁸	65
3.1	Structures of the tripeptides (a) RGD (b) SPT. Backbone atoms are highlighted in red and Φ and Ψ dihedral angles marked.	70
3.2	2D representation of the bonds involved in a dihedral angle centred on the black bond, with the corresponding Newman projections for a selection of angles.	70
3.3	Ramachandran plots for the four cases (a) RGD with TIPS3P (b) RGD with SPC/Fw (c) SPT with TIPS3P and (d) SPT with SPC/Fw. Note that ϕ and ψ are both periodic, and so some of the regions are split across boundaries	71
3.4	Population distribution over regions of the Ramachandran plots. (a) RGD; regions a-g are defined in Figure 3.3(a). (b) SPT; regions a-b are defined in Figure 3.3(c).	72
3.5	Pictorial diagrams of representative structures from regions (a) g and (b) b . The backbone is shown in yellow and the central bonds of Φ and Ψ angles are labelled. For region g , bond distances between key atoms have been displayed. H-bonds are labelled by the bold, black lines. . . .	73
3.6	Distribution of transitions between regions of the Ramachandran plots for RGD (a) TIPS3P (b) SPC/Fw. The labels of the x -axis indicate the initial state and colour indicates the final state. Region h represented the area of the plot not defined by boundaries.	75
3.7	Number of clusters as a function of simulation timestep (a) RGD, backbone; (b) RGD, peptide; (c) SPT, backbone (d) SPT, peptide	77
3.8	Population distribution of RGD clusters over 50 ns. Inset: as the main graph, but on a semi-log scale. (a) backbone and (b) peptide. Analogous data for SPT are given for (c) backbone and (d) peptide.	78

3.9	Population distribution of RGD for the top four clusters, for (a) backbone and (b) peptide clusters, using TIPS3P cluster IDs. Analogous data for SPT are given for (c) backbone and (d) peptide clusters, using TIPS3P cluster IDs. Standard errors are given to 95% confidence (a) backbone (b) peptide.	79
3.10	Centroid (as defined in section 2.1.3) cluster structures for the top four peptide clusters of RGD obtained using the TIPS3P model.	82
3.11	Exemplar RDFs for RGD: (a) $g_{O-H_W}(r)$ between the oxygen atoms of the terminal carboxylate group and the hydrogen atoms of water and (b) $g_{O-O_W}(r)$ between the oxygen atoms of the terminal carboxylate group and the oxygen atoms of water.	87
3.12	Histograms of different aspects of the hydrogen bonds between the peptide and water for (a) distances (b) angles. Distributions were the same for both the RGD and SPT peptides.	88
3.13	The percentage growth of the different regions of the RGD Ramachandran plot as a function of simulation timestep for the two water models (a) TIPS3P (b) SPC/Fw. Region h again represented all the areas of the plot that were not defined by boundaries.	89
3.14	Replica pathway of the initial 'replica 0' for the RGD system as an example for (a) TIPS3P (b) SPC/Fw.	90
3.15	The effect of the length of time between replica exchange attempts on the growth of clusters in the RGD system as an example for (a) backbone (b) peptide.	91
4.1	Schematic to show the start structure (left), optimised structure (centre) and final frame of MD simulation (right).	95

4.2	Ion concentration as a function of distance from the surface for the ions in the NaCl, KCl, CaCl ₂ and MgCl ₂ solutions (low salinity - LS 0.1 M, high salinity - HS 0.3 M). Cation concentration is represented by black and anion concentration is represented by red. For these two colours, the solid lines represent LS solution and the dashed lines HS. However, in the majority of cases only the dark blue function is visible, as it overlays the light blue. LS and HS refer to the 'bulk' concentrations <i>i.e.</i> the concentrations far from the surface.	98
4.3	Schematic of how the thickness of the EDL was calculated from ion density distributions, using aqueous NaCl as an example.	99
4.4	Rdfs between the deprotonated silanol O ⁻ and all cation types studied (Na ⁺ , K ⁺ , Ca ²⁺ and Mg ²⁺) and rdf between Ca _(O⁻) ²⁺ ions and Cl ⁻	100
4.5	Contribution to the surface density profile arising from cations associated with the first peak of the deprotonated silanol-cation rdfs (Figure 4.4), CSDP(O ⁻ -Mrdfp1) . Analogous data is given for the second rdf peak for MgCl ₂ (CSDP(O ⁻ -Mg ²⁺ rdfp2)) and the first rdf peak of the O ⁻ -associated calcium-chloride rdf CSDP(O ⁻ -Ca ²⁺ -Cl ⁻ rdfp1). The complete surface density profiles are reproduced from Figure 4.2 to aid comparison. As in Figure 4.2, cation concentration is represented by black and anion concentration is represented by red. Green represents the CSDP(O ⁻ -Mrdfp1) and, for MgCl ₂ , pink is the CSDP(O ⁻ -Mg ²⁺ rdfp2). Orange represents the CSDP(O ⁻ -Ca ²⁺ -Cl ⁻ rdfp1). The solid lines represent LS solution and the dashed lines HS. In part c) of this diagram, the CSDP(O ⁻ -Ca ²⁺ rdfp1) overlays the complete Ca ²⁺ density profile and CSDP(O ⁻ -Ca ²⁺ -Cl ⁻ rdfp1) the Cl ⁻ density profile for both LS and HS.	102
4.6	$\rho_{Zmax}(xy)$ (<i>i.e.</i> lateral distribution of cations found within a horizontal layer of thickness 0.1 Å and centred on the peaks in density as shown in Figure 4.2c) for CaCl ₂ solution (LS 0.1 M). The units of the number density are arbitrary and the same in all lateral profiles throughout this section.	103

4.7	$\rho_{Zmax}(xy)$ (<i>i.e.</i> lateral distribution of Cl^- ions found within a horizontal layer of thickness 0.1 \AA and centred on the peaks in density as shown in Figure 4.2c) for $CaCl_2$ solution (LS 0.1 M)). The units of the number density are arbitrary and the same in all lateral profiles throughout this section.	106
4.8	Schematic of the angle made between the surface normal and the $O^- - M^+$ vector.	107
4.9	Distributions of the angle made between the surface normal and: (a) r_{Ca-O} , where $r_{Ca-O} = r_{Ca} - r_O$ (b) r_{Cl-O} , where $r_{Cl-O} = r_{Cl} - r_O$. p refers to the particular peak in the CSDP(rdfp1) and n Cl^- indicates the distributions when n Cl^- ions were associated. $\cos(\theta)$ distributions are presented in Appendix C.	108
4.10	Distributions of the distances to the three different protonated silanols for Ca^{2+} ions in peak 1 and 2 of the z -density distributions (LS, 0.1 M and HS, 0.3 M). UL stands for upper left, LL lower left and R right and are defined in Figure 2.8.	109
4.11	Distributions of the angle made between the surface normal and r_{Cl-O} , where $r_{Cl-O} = r_{Cl} - r_O$ ($CaCl_2$) (LS 0.1 M). p refers to the particular peak in the CSDP(rdfp1)	110
4.12	CSDP arising from Ca^{2+} that have chloride ions from a particular peak ($p = p1, p2, \dots$ where $p1$ is the first peak, <i>etc</i>) in the Cl^- z -density distribution associated with them The complete surface density profiles for Ca^{2+} z -density are reproduced from Figure 4.2 to aid comparison. As in Figure 4.2, cation concentration is represented by black and the solid lines represent LS solution, while the dashed lines represent HS. The CSDP is given in solid lines of different colours in both the LS, 0.1 M subfigure (a) and the HS 0.3 M subfigure (b): Orange for Ca^{2+} with Cl^- from $p1$ of the Cl^- z -density profile, pink for $p2$, light green for $p3$, dark green for $p4$	111

4.13	$\rho_{Zmax}(xy)$: lateral cation density profiles at maxima in the ion concentration <i>vs</i> distance from the surface distributions for KCl solution (LS 0.1 M). The units of the number density are arbitrary and the same in all lateral profiles throughout this section. (Note that the graph for K^+ peak 1 is zoomed-in compared to those of the other peaks, to show the smaller areas of high density in a greater level of detail.)	114
4.14	Schematic of the adsorption of Cl^- to surface adsorbed Ca^{2+} at an angle of $\sim 89^\circ$ with respect to the surface normal.	117
4.15	Water density as a function of distance from the surface for the NaCl, KCl, $CaCl_2$ and $MgCl_2$ solutions (low salinity - LS 0.1 M, high salinity - HS 0.3 M). The solid lines represent LS solution and the dashed lines HS.	118
4.16	$\rho_{Zmax}(xy)$ for water density (within a horizontal layer of thickness 0.1 Å and centred on the peaks in density as shown in Figure 4.15) for 0.1 M NaCl solution and 0.1 M $MgCl_2$. Only $\rho_{Zp3}(xy)$ is shown here for the latter solution, as those for the first two were not significantly different in character to those of the other solutions. The labels SA and SB are used to highlight different structural characters.	120
4.17	Rdfs between O^- and the hydrogen atoms of water for all electrolyte solutions.	121
4.18	Rdfs between O^- and the oxygen atoms of water for all electrolyte solutions.	121
4.19	Surface topology: van der Waals representation of the amorphous silica surface.	121
4.20	$\rho_{Zmax}(xy)$ for water density (within a horizontal layer of thickness 0.1 Å and centred on the peaks in density as shown in Figure 4.15) for $CaCl_2$ solution at ionic strengths of 0.1 M and 0.3 M. The labels are used to highlight different structural characters that correspond to different site-types: O^- (T1), O^-Ca^{2+} (T2), $O^-Ca^{2+}Cl^-$ (T3) and $O^-Ca^{2+}Cl_2^-$ (T4).124	124

4.21	Water Density and ion concentration as a function of distance from the surface for the ions in the NaCl, KCl, CaCl ₂ and MgCl ₂ solutions (low salinity - LS 0.1 M, high salinity - HS 0.3 M). Cation concentration is represented by black and anion concentration is represented by red. For these two colours, the solid lines represent LS solution and the dashed lines HS. Light blue represents H ₂ O from LS solution and dark blue represents H ₂ O from HS solution. However, in the majority of cases only the dark blue function is visible, as it overlays the light blue. LS and HS refer to the 'bulk' concentrations <i>i.e.</i> the concentrations far from the surface. Ion concentration distributions are reproduced from Figure 4.2 and water density distributions are reproduced from Figure 4.15. O ⁻ density is shown as a pink line on the plots. A lateral density profile of the water represented by the second peak in the water density (at ~3 Å from the surface) is shown in Figure 4.20 (CaCl ₂ , 0.1 M and 0.3 M) and Figure 4.16 (NaCl, representative of all other solutions). Lateral water density profiles for the KCl and MgCl ₂ cases are given in Appendix C, Figure C.9.	126
4.22	Net water orientation as a function of distance for a selection of the electrolyte solutions investigated. The uncertainties are standard errors given to 95 % confidence. Lateral water orientation profiles, with the lateral location of SiO ⁻ and SiOH groups superimposed, are shown in Figures 4.25 and 4.26 and show how waters partition between the different functional groups of the surface.	129
4.23	P(cos(θ)) distributions were calculated between distances of 4-4.5 Å (black), 4.5-5 Å (red), 5-5.5 Å (green) and 5.5-6 Å (pink). The solid lines represented 0.3 M CaCl ₂ solution and the dotted lines represented 0.1 M NaCl.	130
4.24	P(cos(θ)) distributions between 6.5-12.5 Å for (a) 0.3 M CaCl ₂ denoted Ca and (b) 0.1 M NaCl, denoted Na.	131

4.25	Exemplar $ori_{Z(4.5-5)}(xy)$ (lateral water orientation) profiles. U1 represents O^- , U2 , O^-Ca^{2+} , U3 , $O^-Ca^{2+}Cl^-$ and U4 , $O^-Ca^{2+}Cl^-_2$. Blue dots represent the superimposed lateral locations of deprotonated silanol oxygens (O^-) and the green dots represent those of protonated silanol oxygens.	133
4.26	Exemplar $ori_{Z(5.5-6)}(xy)$ (lateral water orientation) profiles. U1 represents O^- , U2 , O^-Ca^{2+} , U3 , $O^-Ca^{2+}Cl^-$ and U4 , $O^-Ca^{2+}Cl^-_2$. Blue dots represent the superimposed lateral locations of deprotonated silanol oxygens (O^-) and the green dots represent those of protonated silanol oxygens.	134
4.27	Perpendicular ('perp.') and Parallel ('lat.') Diffusion as a Function of Distance from the Surface for water and cations in 0.1 M NaCl solution.	137
5.1	AFM force mapping data: the average maximum adhesion during an AFM approach-retract cycle (full method details in Section 2.2.2 of (a) NH_3^+ and (b) $COOH/COO^-$ functionalized tips during interaction with the amorphous silica during exposure to the solutions at low salinity (LS) 0.1 M and high salinity (HS) 0.3 M. The labels 1 and 2 in the Experiment ID are used to denote the experiment number as salinity was cycled twice between LS and HS concentrations.	145
5.2	A high resolution image in normal AFM mode of the surface scanned in our study (amorphous silica).	145
5.3	Graphical representations of the different possible states for surface deprotonated oxygens in $CaCl_2$ solution. Ca^{2+} ions are represented by the dark blue atoms and Cl^- ions are represented by the green atoms. (a) unoccupied O^- (b) Ca^{2+} occupied O^- (c) upright $Ca^{2+}Cl^-$ occupied O^- (d) flat $Ca^{2+}Cl^-$ occupied O^- (e) $Ca^{2+}Cl^-_2$ occupied O^-	147
5.4	Initial free energy profiles from metadynamics simulations (a) NaCl - after 180 ns (b) KCl - after 130 ns (c) $CaCl_2$ - after 130 ns (d) $MgCl_2$ - after 130 ns	149

5.5	NaCl LS - several demonstrations that the metadynamics simulations had not converged (a) Evolution of the free energy profile with time. (b) Free energy difference between 2 distinct points of the free energy profile with time. Comparison to high salinity included. (c) Histogram of CV space explored over the final 25 ns. Comparison to high salinity included.	150
5.6	NaCl LS, a smaller volume of CV space - several demonstrations that the metadynamics simulations had not converged (a) Evolution of the free energy profile with time (b) Free energy difference between 2 distinct points, the minimum centered at ~ 0.25 nm and a point in the plateau region, of the free energy profile with time (c) Histogram of CV space explored over the final 20 ns.	152
5.7	Lateral free energy profiles taken over the total volume of available CV space for the entire metadynamics simulations (a) low salinity NaCl, 80 ns (b) low salinity CaCl_2 , 27 ns.	153
5.8	Evidence of convergence (a) Distribution of CV (distance from surface) values (b) Evolution of the free energy profile with time (c) Free energy difference between points marked 'FED1' on Fig 5.8b as a function of time (d) Free energy difference between points marked 'FED2' on Fig5.8b as a function of time	155
5.9	Two examples of the free energy profiles from the final metadynamics simulations, a comparison between the corrected and uncorrected versions for (a) low salinity aqueous NaCl and (b) the $\text{O}^- \text{Ca}^{2+} \text{Cl}^-_2$ adsorption site configuration, low salinity aqueous CaCl_2	157
5.10	Free energy profiles determined from the MD simulations for the adsorption of N to the silica surface in (a) NaCl solution (b) MgCl_2 solution, Mg^{2+} -occupied O^-	158
5.11	Lateral free energy profiles at distances from the surface for the major minima (at 3.2, 3.5 and 3.9 Å from the surface) in the low salinity NaCl solution. The lateral positions of the surface oxygen are superimposed on the free energy profile.	160

5.12	Lateral free energy profiles at distances from the surface for the major minima (at 3.2, 3.6 and 4.0 Å from the surface) in the low salinity MgCl ₂ solution. The lateral positions of the surface oxygen are superimposed on the free energy profile.	161
5.13	Free energy profiles determined from the MD simulations for the adsorption of N to the silica surface at different O ⁻ -based adsorption site configurations in CaCl ₂ solution (a) unoccupied O ⁻ (b) Ca ²⁺ occupied O ⁻ (c) flat Ca ²⁺ Cl ⁻ occupied O ⁻ (d) Ca ²⁺ Cl ⁻ ₂ occupied O ⁻	162
5.14	Lateral free energy profiles at distances from the surface for the major minima (as defined in the main text) in aqueous LS CaCl ₂ at unoccupied O ⁻ . The lateral positions of the surface oxygen are superimposed onto the free energy profile.	164
5.15	Lateral free energy profiles in aqueous low salinity CaCl ₂ for various attachments at O ⁻ at the distance of (a) minimum 1 (2.1-2.45 Å), (b) minimum 2 (3.7 Å). The lateral positions of the surface oxygen are superimposed onto the free energy profile.	165
5.16	Lateral free energy profiles at distances from the surface for minimum 2 (2.1-2.45 Å) in aqueous low salinity CaCl ₂ for various attachments at O ⁻ . The lateral positions of the attached Ca ²⁺ are represented as red crosses superimposed onto the free energy profile and appeared as a single continuous region that is slightly elongated away from the ammonium adsorption site.	167
5.17	(a) Lateral free energy profile for the CaCl ₂ attachment at O ⁻ at the distance of minimum 2 (3.7 Å). The lateral positions of the surface oxygen are superimposed onto the free energy profile. The positions of particular bridging oxygens have been labelled '1', '2' and '3'. (b) Schematic of corresponding physical system with the same bridging oxygens labelled '1', '2' and '3'. Apart from the labelled ions, Ca ²⁺ and Cl ⁻ , oxygen atoms are shown in red, silicon in yellow, hydrogen in white, nitrogen in dark blue and carbon in light blue.	168

5.18	The force curves were generated by taking the gradient of the free energy profiles for methylammonium adsorption in solutions of NaCl and CaCl ₂ specifically where Ca ²⁺ Cl ⁻ ₂ is associated with the deprotonated surface oxygen.	169
5.19	Replica mobility in the MD simulation using the more efficient REST technique ¹⁰ for 72 replicas.	170
6.1	Schematic of the starting configuration of the model tip simulation at a certain distance from the surface. The gold atoms of the tip are shown in pink, with attached organics (bright blue C, dark blue N and white H), Cl ⁻ ions are green and Ca ²⁺ ions dark blue, silicon atoms are yellow, oxygen atoms are red and hydrogen white.	175
6.2	(a) Force experienced by the model tip atoms and (b) average minimum N atom distance to the silica surface when the gold and sulfur atoms of the model tip were restrained at different distances from the surface. For (b), 'min 1' and 'min 2' mark the approximate position of minimum 1 and the exact position of minimum 2 for the different adsorption site configurations in at the aqueous CaCl ₂ /silica interface.	177
B.1	RDFs $g_{O-H_W}(r)$ between RGD's (a) oxygen atoms of the sidechain carboxylate group (b) nitrogen atoms of the guanidinium group (c) ammonium nitrogen atom and the hydrogen atoms of water. RDFs $g_{O-O_W}(r)$ between RGD's (d) oxygen atoms of the sidechain carboxylate group (e) nitrogen atoms of the guanidinium group (f) ammonium nitrogen atom and the oxygen atoms of water	214
B.2	Exemplar RDFs for RGD: (a) $g_{O-H_W}(r)$ between the oxygen atoms of the terminal carboxylate group and the hydrogen atoms of water and (b) $g_{O-O_W}(r)$ between the oxygen atoms of the terminal carboxylate group and the oxygen atoms of water.	215
B.3	Dihedral angle distributions for (a) terminal N-C _α -C _β -C _γ , residue R (b) C _α -C _β -C _γ -C _δ , residue R (c) C _β -C _γ -C _δ -sidechain N, residue R (d) C _γ -C _δ -sidechain N-C _δ -C _ε , residue R (e) N-C _α -C _β -C _γ , residue D (f) C _α -C _β -C _γ -O, residue D	216

B.4	The percentage growth of clusters for the RGD peptide as a function of simulation timestep for (a) TIPS3P, backbone (b) SPC/Fw, backbone (c) TIPS3P, peptide (d) SPC/Fw, peptide.	217
B.5	Replica pathway of the initial 'replica 0' for the SPT system for (a) TIPS3P (b) SPC/Fw.	217
C.1	$\rho_{Zmax}(xy)$: lateral cation density profiles at maxima in the ion concentration vs distance from the surface distributions for NaCl and MgCl ₂ solutions (LS 0.1 M). The units of the number density are arbitrary and the same in all lateral profiles throughout this section.	220
C.2	$\rho_{Zmax}(xy)$: lateral cation density profiles at maxima in the ion concentration vs distance from the surface distributions for NaCl, KCl, CaCl ₂ and MgCl ₂ solutions (HS 0.3 M). The units of the number density are arbitrary and the same in all lateral profiles throughout this section. . . .	221
C.3	$\rho_{Zmax}(xy)$: lateral Cl ⁻ density profiles at maxima in the ion concentration vs distance from the surface distributions for CaCl ₂ solution (LS 0.3 M). The units of the number density are arbitrary and the same in all lateral profiles throughout this section.	222
C.4	Distributions of the angle made between the surface normal and r_{M-O} , where $r_{M-O} = r_M - r_O$. p refers to the peak in the CSDP(O ⁻ -Mrdfp1).	223
C.5	Distributions of the angle made between the surface normal and r_{M-O} , where $r_{M-O} = r_M - r_O$. p refers to the peak in the CSDP(O ⁻ -Mrdfp1).	224
C.6	Distributions of cos(θ) where θ is the angle made between the surface normal and: (a) r_{Ca-O} , where $r_{Ca-O} = r_{Ca} - r_O$ (b) r_{Cl-O} , where $r_{Cl-O} = r_{Cl} - r_O$. p refers to the particular peak in the CSDP(rdfp1) and n Cl ⁻ indicates the distributions when n Cl ⁻ ions were associated	225
C.7	Distributions of cos(θ) where θ is the angle made between the surface normal and r_{M-O} , where $r_{M-O} = r_M - r_O$. p refers to the peak in the CSDP(O ⁻ -Mrdfp1).	226
C.8	Distributions of cos(θ) where θ is the angle made between the surface normal and r_{M-O} , where $r_{M-O} = r_M - r_O$. p refers to the peak in the CSDP(O ⁻ -Mrdfp1).	227

C.9	$\rho_{Zmax}(xy)$: additional lateral water density profiles at maxima in the water density vs distance from the surface distributions for KCl and $MgCl_2$ solution (0.1 M). Blue dots represent deprotonated silanols and green dots represent protonated silanols. The units of the number density are arbitrary and the same in all lateral profiles throughout this section. .	228
C.10	$\rho_{Zmax}(xy)$: lateral water density profiles at maxima in the water density vs distance from the surface distributions for NaCl, $MgCl_2$ and $CaCl_2$ solution (0.3 M). The units of the number density are arbitrary and the same in all lateral profiles throughout this section.	229
C.11	$\rho_{Zmax}(xy)$: Lateral water density profiles at maxima of the secondary layers in the water density vs distance from the surface distributions for 0.3 M $CaCl_2$ solution and at the counterpart distances in 0.1 M solution. The units of the number density are arbitrary and the same in all lateral profiles throughout this section.	230
C.12	Net water orientation as a function of distance for a selection of the electrolyte solutions investigated.	231
C.13	Full distributions of $\cos(\theta)$ between 0-2.5 Å and between 2.5-4 Å for 0.3 M $CaCl_2$ denoted Ca and 0.1 M NaCl, denoted Na.	232
C.14	Full distributions of $\cos(\theta)$ between 4-6 Å for 0.1 M and 0.3 M $CaCl_2$. .	232
D.1	RDFs between (a) O^- to 'bound' Ca^{2+} (b) Ca^{2+} to 'bound' Cl^- (c) O^- to 'bound' Cl^-	234
D.2	rdfs between (a) O^- bound Ca^{2+} and all chloride ions apart from any officially associated Cl^- . (b) O^- and all Ca^{2+} ions.	235
D.3	Cation-deprotonated oxygen and chloride ion-surface bound calcium ion RDFs	235

D.4	The remainder of the free energy profiles from the final metadynamics simulations, a comparison between the corrected and uncorrected versions for (a) HS aq. NaCl (b) LS aq. KCl (c) HS aq. KCl (d) unbound state, LS aq. MgCl ₂ (e) unbound state, HS aq. MgCl ₂ (f) bound state, LS aq. MgCl ₂ (g) O ⁻ , aq. LS CaCl ₂ (h) O ⁻ , aq. HS CaCl ₂ (i) O ⁻ Ca ²⁺ , aq. LS CaCl ₂ (j) O ⁻ Ca ²⁺ , aq. HS CaCl ₂ (k) O ⁻ Ca ²⁺ Cl ⁻ , aq. LS CaCl ₂ (l) O ⁻ Ca ²⁺ Cl ⁻ , aq. HS CaCl ₂ (m) O ⁻ Ca ²⁺ Cl ⁻ ₂ , aq. LS CaCl ₂ (n) O ⁻ Ca ²⁺ Cl ⁻ ₂ , aq. HS CaCl ₂	236
D.5	Free energy profiles for the adsorption of the nitrogen of methylammonium to the silica surface in different salt solutions (a) KCl (b) MgCl ₂ solution, unoccupied O ⁻	237
E.1	Evidence for the equilibration of the infinitely-sized monolayer. SP refers to starting point. (a) water density as a function of distance from the vacuum/gold surface (b) Cl ⁻ density as a function of distance from the vacuum/gold surface (c) N density profiles as a function of distance from the vacuum/gold surface (d) monolayer thickness with time (e) tilt angle with time (f) azimuthal tilt angle with time.	239
E.2	Evidence for the equilibration of the system that featured the model AFM tip and the model tip as a reasonable representation of the infinite monolayer (a) water density as a function of distance from the silica surface (b) Cl ⁻ density as a function of distance from the silica surface (c) Ca ²⁺ density as a function of distance from the silica surface (d) maximum N atom distance from the surface - minimum N atom distance from the surface (e) tilt angle of each of the Au-adsorbed molecules with time (f) mean square displacement of the N atom of the head group of each of the adsorbed molecules with time.	240

Dedicated to my grandad, Raymond William ('Sam') Scott.

Acknowledgments

First and foremost I would like to acknowledge my two supervisors Tiffany Walsh and Mark Rodger, a synergistic team! I have enjoyed working with them and learnt a lot from both: Mark my supervisor here at Warwick and Tiff in my first year here and throughout, a strong presence even from the other side of the world! I will miss this chapter in my life.

I thank Susan Stipp for the opportunity to visit her labs at The University of Copenhagen, as well as Tue Hassenkam and Klaus Juhl for sharing their expertise and training me in force-mapping AFM. The entire NanoGeoScience Group made me feel very welcome and I would like to extend particular thanks for this to Bärbel Lorenz, Akin Budi, Johanna Generosi and Dominique Tobler.

Special thanks to Louise Wright for advice, wisdom and friendship throughout, Aaron Finney for constructive criticism of this thesis and encouragement in general, particularly in the final stages of this PhD and my graphics guru, Annalaura Del Regno.

Thanks to my office mates (current and past) and those based in the CSC: Julia Choe, Alaina Emmanuel, Chimie Gamot, Salvatore Cosseddu, Chinedu Nwaigwe, Yuanwei Xu, Paul Oluwunmi, Yuriy Bushuev, Tony Zhang, Minsouk Kim, Iresha Atthanayake, Toon Vasil Sirilapanan, David O'Neill, Jenny Webb, David Bray, Aaron Brown and Oliver Yang.

Thanks to the wider scientific community at Warwick and beyond: Gil Rutter, Marina Cendic, Stepan Ruzicka, Matt Bano, Bart Vorselaars, Max Saller, Boy Lankhaar, Lewis Baker, Anja Humpert, Rebecca Notman, Scott Habershon, David Quigley, Mike Allen, my advisory board Ale Troisi and Rob Deeth, those of the mIb consortium and many more, including those I haven't mentioned but nonetheless have meant a lot along the journey!

Thanks to the CSC computing and administrative staff: Vida Glanville, Christine Jarvis, Natalie Tyldesley Marshall, Magnus Lewis-Smith, Grok (Jaroslaw Zachwieja), Olav Smorholm, Marius Bakke and Matthew Ismail.

Finally, thanks to those friends not mentioned above who have shared this time with me and especially to my father, Graham Desmond and mother, Christine Desmond.

Declarations

This thesis is my own work. Results based on collaborative efforts have been explicitly stated in the text (Chapter 5). No part of this report has been previously submitted for examination for any other higher degree or for a degree at an establishment other than the University of Warwick. The work of Chapter 3 has been published as the following journal article: J. L. Desmond, P. M. Rodger and T. R. Walsh, *Mol. Sim.*, **2013**, *40*, 912.

Abstract

Low-salinity enhanced oil recovery (EOR) uses low-salinity seawater in the water flooding of sandstone reservoirs to maximise oil yields. Because oil is strongly adsorbed onto mineral surfaces, understanding the interactions involved at the oil/mineral interface, and how to weaken them, is crucial to design more efficient, low-cost EOR.

This thesis focuses on the influence of electrolyte concentration on the interaction of alkylammonium (R-NH_3^+) and alkylcarboxylic acid/carboxylate (R-COOH/COO^-) functionalities, present in crude-oil, with the amorphous silica (mimic for quartz grains in sandstone)/aqueous electrolyte interface. Both computational (molecular dynamics, MD) and experimental (chemical force mapping atomic force microscopy, CFM-AFM) techniques were used.

Firstly (Chapter 3), we tested the inter-operability of the new SPC/Fw water force-field with CHARMM. No significant differences were found between the data generated from SPC/Fw-CHARMM and TIPS3P-CHARMM, therefore the latter, computationally more efficient, was used in Chapters 4-6.

The behaviour of the four electrolyte solutions at two concentrations was tested in Chapters 4-5 (NaCl , KCl , CaCl_2 and MgCl_2 at 0.1 and 0.3 M); interfacial ion and water structuring has been investigated in Chapter 4, while the effect of the electrolytes on the adsorption of R-NH_3^+ and alkylcarboxylic acid/carboxylate (R-COOH/COO^-) was explored in Chapter 5. Interfacial ion concentration was greatest in the CaCl_2 case, with various long-lived surface-site types involving different combinations of ions identified. CFM-AFM showed a substantial concentration-dependent difference in adhesion for R-NH_3^+ in CaCl_2 and R-COOH/COO^- in the divalent ion solutions.

The free energy of adsorption for NH_3^+CH_3 was investigated using metadynamics. Force curves were calculated from the generated free energy profiles. The greatest force is, indeed, observed for one particular surface-site type in CaCl_2 solution, prevalent in more concentrated solutions.

Finally, a more sophisticated computational model for the experimental AFM tip, a small array of $\text{S(CH}_2_{11}\text{NH}_3^+$, is presented in Chapter 6, laying the basis for future work.

Abbreviations

ADF Angular Distribution Function

AFM Atomic Force Microscopy

AIMD *Ab Initio* Molecular Dynamics

ASW Artificial Seawater

CFM-AFM Chemical Force-Mapping Atomic Force Microscopy

COM Centre of Mass

CSDP Contribution to the Surface z -density Profile

CSDP(O^- -MrdfpN Contribution to the Surface z -density Profile for ions in the Nth peak in the silica surface O^- to cation rdf

CV Collective Variable

DFT-MD Density Functional Theory-Based Molecular Dynamics

EDL Electrical Double Layer

EOR Enhanced Oil Recovery

Ex. P. Exchange Probabilities

FED Free Energy Difference

FEP Free Energy Perturbation

FES Free Energy Surface

GCS Gouy-Chapman-Stern

HCP Hexagonal Close Packed

H-REMD Hamiltonian Replica-Exchange Molecular Dynamics

HS High Salinity (0.3 M)

H-S Helmholtz-Smoluchowski

IDP Intrinsically Disordered Protein

IEP Isoelectric Point

LJ Lennard Jones

LLO Lower Left Oxygen

LS Low Salinity (0.1 M)

MD Molecular Dynamics

metaD Metadynamics

MSD Mean Squared Displacement

N the NH_3^+ Group of Methylammonium

NEMD Non-Equilibrium Molecular Dynamics

No. Ex. Number of Exchanges

NPT Isothermal-Isobaric ensemble (constant number, pressure and temperature)

NMR Nuclear Magnetic Resonance

NVT Canonical Ensemble (constant number, volume and temperature)

ODT 1-Octadecanethiol

$ori_{Z(z_1-z_2)}(xy)$ lateral water orientation profiles, where z_1 is the z -distance from the surface where the horizontal slice starts and z_2 is where it ends.

p1 Peak 1

p2 Peak 2

$P(\cos(\theta))$ Full $\cos(\theta)$ distributions

P2VP poly(2-vinylpyridine]

PEL Potential Energy Landscape

PME Particle Mesh Ewald

PMF Potential of Mean Force

PZC Point of Zero Charge

rdf Radial Distribution Function

REMD Replica-Exchange Molecular Dynamics

RMSD Root-Mean Squared Deviation

REST Replica-Exchange with Solute Tempering

RO Right Oxygen

SAM Self-Assembled Monolayer

SFG Sum-Frequency Generation

SHG Second Harmonic Generation

T-REMD Temperature Replica-Exchange Molecular Dynamics

ULO Upper Left Oxygen

vdW van der Waals

WT Well-Tempered

XPS X-ray Photoelectron Spectroscopy

XR X-ray Reflectivity

ZPC Zero Point Charge

$\rho_{Z_{max}}(xy)$ lateral density profile for ions within a small range of z -distances from the surface centered at the N th peak in ion z -density. Z_{max} is equal to Z_{pN} (the N th peak in the ion z -density profile, where $N = 1, 2, \dots$).

Chapter 1

Introduction

1.1 Aim: Understanding the 'Low Salinity' (LS) Effect and Enhanced Oil Recovery (EOR)

The influence of ionic strength on the molecular adsorption of polar compounds is of particular importance to the investigation of enhanced oil recovery, EOR (a collection of techniques used to increase yields of crude oil from oil reservoirs, one of which is low-salinity EOR). Indeed, the main aim of this thesis was to increase understanding of the 'low salinity' effect (as defined in section 1.1.1) and thus low salinity EOR, with a particular focus on low salinity EOR from sandstone reservoirs. Since current oil recovery methods may leave up to 65 % of the original oil in the reservoir, the need for improved understanding of low-salinity EOR is clear.¹¹ Amorphous silica was considered as a model for sandstone, the R-NH_3^+ and R-COOH/COO^- functional groups were selected as mimics for the polar components of oil and the aqueous electrolytes represented the different ionic components present in seawater. The mineral composition of sandstone is dominated by silica, as quartz and it is assumed that oil is exposed to this material in the pores of sandstone reservoirs.⁸ Amorphous silica (Figure 1.1) and natively-oxidised silicon (Figure 2.8) surfaces are often used as models for exploring the behavior of the surfaces of quartz grains in sandstone.⁸ The polar functionalities, R-NH_3^+ and R-COOH/COO^- , were selected for investigation, as the presence of polar functionalities in crude oil is a requirement for the 'low salinity' effect to be observed.⁸ Although the presence of nitrogen-containing compounds in crude oil, particularly

aliphatic amines, is small, the interaction of the functionality with the aqueous electrolyte/amorphous silica interface is thus far underexplored.^{12,13} The use of chemical force mapping atomic force microscopy, CFM-AFM (described in Chapter 2, section 2.2.1) and molecular simulation (described in Chapter 2) is an excellent way to study interfacial phenomena, with the CFM-AFM providing macroscopic adhesion force values and the simulation giving atomistic-level insight. In this thesis, a combined experimental/simulation approach has been taken, using both techniques. In experiment, an AFM tip has been functionalised with long-chain hydrocarbons terminated by the desired functionality (both NH_3^+ and COOH/COO^- have been analysed in this way). In simulation, the focus has been on the interaction of the R-NH_3^+ functionality at the aqueous electrolyte/amorphous silica interface. This was explored initially with a single methylammonium molecule and then, in a more complex model of the experimental AFM tip, as an array of long-chain hydrocarbons terminated with NH_3^+ . The introduction has been structured by first discussing the main motivation for this work and how it will be explored, wider-ranging applications of the silica/aqueous electrolyte interface and then experimental studies at the silica/water interface, the Gouy-Chapman-Stern model (a commonly used theoretical model for charged surface/aqueous electrolyte interfaces), simulation studies at the silica/water interface, a mixed experimental/simulation section concerning molecular adsorption at the silica/water interface, including force-field inter-operability, an important aspect of such simulations and atomic force microscopy (AFM) by simulation, concluding with a detailed aims and objectives section.

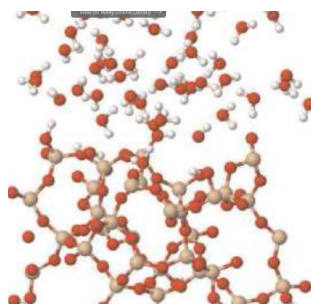


Figure 1.1: Schematic of the amorphous silica/water interface adapted from Butenuth *et. al.*¹ Red represents oxygen atoms, white hydrogen atoms and orange silicon atoms.

1.1.1 The 'Low Salinity' (LS) Effect

In EOR, there is clear evidence that production from sandstone reservoirs increases when the water used to sweep the reservoir and to maintain pressure has salinity below about 5000 ppm, compared to undiluted seawater of salinity 30000 ppm or more.¹⁴ Several hypotheses have been proposed to explain the mechanisms responsible for this 'low salinity' (LS) effect, as described in a recent review by Sheng.¹⁵ A selection have been discussed in detail.

Electric Double Layer (EDL) Expansion and Fines Migration Theory

The EDL is a description of the electric field at a charged interface, such as a charged colloidal particle or a flat surface in contact with water. It has been described in more depth in section 1.4, where it is illustrated schematically in Figure 1.6. The depth of the EDL can be predicted by DLVO theory, as described by Overbeek *et. al.*¹⁶ Further, according to DLVO theory, the width of the EDL will increase as salinity decreases. In the case of a negatively charged surface, negatively charged molecules in the interfacial region will become less strongly attracted to the surface as the width of the EDL increases and the shielding of the surfaces negative charge by interfacial cations decreases. EDL expansion is also key to fines migration theory.¹⁴ The greater the width of the EDL, the more likely the interaction of colloidal EDLs and bulk clay swelling. In this theory, it was proposed that the fine clay particles that result from such a process are released, along with associated oil.

Multicomponent Ionic Exchange

Various mechanisms have been proposed for the binding of oil to the sandstone surface. Four mechanisms, believed to be important to the 'low salinity' effect, are depicted in Figure 1.2, with several examples of the functional groups likely to be involved in each case.¹⁷ Ligand bridging (Figure 1.2a) and cation bridging (Figure 1.2b) both describe mechanisms where a multivalent cation forms bonds with a negatively charged oxygen of the surface and a negatively charged organic molecule. The type of bonding, however, differs. In the ligand bridging mechanism, it is covalent, whereas in the cation bridging mechanism it is ionic. For strongly solvated ions, for example Mg^{2+} , a water bridging mechanism (Figure 1.2c) can occur. In this case, the solvation shell orders and

interacts with the organic molecule through dipole-dipole interactions (where the positive end of a polar molecule interacts with the negative end of another polar molecule). The cation exchange mechanism describes the process whereby interfacial cations are replaced by positively charged organic molecules (Figure 1.2d). It is suggested that monovalent ions readily replace divalent ions in 'low salinity' water leading to the displacement of organic molecules bound through the mechanisms shown in Figure 1.2a-c. It has also been suggested to be an equilibrium effect, with the divalent ions that linked organic molecules to the surface and were originally present in the higher salinity solution moving away from the surface to reach equilibrium with the newly introduced low salinity solution.¹⁸

Interfacial pH Effects

It has been proposed that the interaction of cations with the silica surface leads to the formation of hydroxyl ions. The hydroxyl ions can deprotonate carboxylic acids present in oil. If the carboxylic acid had been hydrogen-bonded (an attractive interaction between a highly electronegative atom, *i.e.* oxygen, nitrogen or fluorine, and a hydrogen that is bonded to another highly electronegative atom) to the surface, this deprotonation event will remove the hydrogen bonding mechanism and the acid may detach from the surface. This is shown by chemical equations in Figure 1.3.

Salt-In Effect

The solubility of organic compounds is affected by electrolyte concentration. Salting-in describes the increase in solubility of organic compounds that occurs when the electrolyte concentration is decreased. It is suggested that this may aid desorption from the sandstone surface.¹⁹

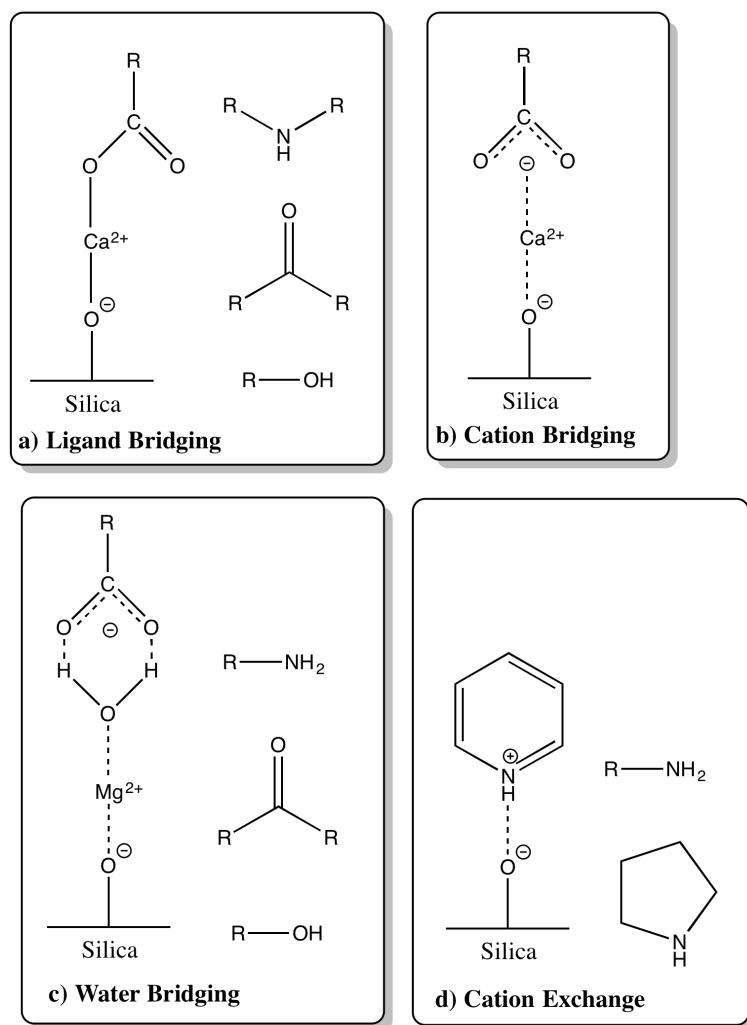


Figure 1.2: Schematic of the key bridging mechanisms important to the 'low salinity' effect and the functional groups through which they can occur.

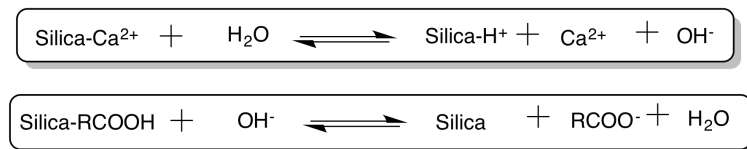


Figure 1.3: Equilibrium reactions showing the two stage mechanism for the detachment of carboxylic acids from the silica surface.

1.1.2 'Low-Salinity' Enhanced Oil Recovery Mechanisms Explored in This Thesis

Changes to the width of the EDL with concentration and electrolyte type and their impact on molecular adsorption, have been explicitly explored in this thesis through the analysis of ion distributions in molecular dynamics (MD) simulations and calculation of free energy of adsorption values using an advanced MD technique, metadynamics (as will be described in Chapter 2, section 2.1.1). Concentration-dependent differences give some insight to the fines migration theory hypothesis. However, since only a single stationary silica surface was probed rather than a collection of mobile colloidal particles, interaction of EDLs cannot be observed and a full testing of the hypothesis is beyond the scope of this thesis. Furthermore, electrolyte-dependent differences in the EDL reflect the various affinities of the ions for the silica surface, allowing testing of the multicomponent ion exchange mechanisms.

1.2 The Aqueous Electrolyte/Mineral Interface

Aqueous electrolyte/mineral interfaces are ubiquitous in nature and technology, and play a role in many commercial applications, such as solar cells, electronics and biodegradable coatings of drug molecules.²⁰ However, despite this and even though the ability of minerals to induce dramatic structural changes to interfacial water has been long-established,²¹ the physical details of such structure remain underexplored. This interfacial solvent structure is important to understanding chemical processes occurring at the surface, such as mineral dissolution and molecular adsorption, processes which often underpin the commercial applications.^{22, 23, 24}

1.2.1 Importance of Biomolecule-Silica Interactions

Silica will be considered as a prototypical example. The mineral is terrestrially predominant, featuring in various natural phenomena and applications, many of which involve molecular adsorption at the interface of silica with physiological solution or seawater.²⁰ The interaction of biomolecules with bioglass, a material primarily composed of silica, is key to the successful integration of prosthetic limbs with bone tissue in the human

body.^{25,26} The adsorption behavior of polar compounds at the silica/aqueous electrolyte interface is relevant to the understanding of enhanced oil recovery (EOR) from sandstone reservoirs.⁸ In nature, intrinsically disordered proteins (IDPs) - proteins which lack a fixed three dimensional structure - and long-chain polyamines are involved in the biomineralization of several silica-based structures, including the cell wall of marine diatoms and skeletal form of Radiolarians.^{27,28}

1.2.2 A Brief Overview of Silica Literature to Date

Silica has been intensely studied as a substrate, and a wealth of experimental data is available, as reviewed recently by Rimola *et. al.*²⁰ The properties and behavior of any surface are controlled by its process history and silica is no exception.^{29,20} For example, if an amorphous silica sample is heated to more than 1000 K, condensation of surface silanol groups irreversibly changes the surface structure, even after cooling and water adsorption.³⁰ The dependence of silica surface charge density on pH, cation type and ionic strength of solutions has been extensively documented using various experimental techniques, ranging from acid-base titration to evanescent cavity wave ring-down spectroscopy.^{31,32,33,34,35} Much of the past research efforts have been devoted to investigating the effect of ionic strength and electrolyte type on silica dissolution.^{36,37,38,39,40} Ion specific adsorption is also an important aspect of the aqueous electrolyte/silica interface interaction and has been widely studied.^{41,42,43,44,45}

1.3 Experimental Studies at the Silica/Water Interface

Rimola *et. al.* have noted two particularly enlightening studies concerning water structure at the interface between silica and water.²⁰ The studies, both conducted in 2004, reported regions of 'ice-like' and 'liquid-like' water. Shen and co-workers performed sum frequency generation (SFG) spectroscopy experiments at the (0001) quartz/water interface.² The spectra featured two peaks, occurring at $\sim 3200\text{ cm}^{-1}$, a position normally associated with the ice phase of bulk water, and $\sim 3400\text{ cm}^{-1}$ a position correlated with the less ordered, liquid water phase. The peak within the 'ice region' became more intense with higher pH. At high pH, it is suggested that the increased order originated from the formation of strong hydrogen bonds between water molecules

and deprotonated silanols. A different bonding mechanism, where silanols act as hydrogen bond donors to water, was proposed responsible at low pH. The two bonding mechanisms have been illustrated in Figure 1.4. The suggestion was supported by SFG phase measurements, which indicated that the dipole moment of the water molecules was orientated oppositely at low and high pH. Engemann *et. al.* studied the amorphous silica/ice interface using high-energy x-ray transmission reflection and found evidence for a 'liquid-like' interfacial ice layer.⁴⁶ Further evidence for a difference in interfacial solvent structure compared to that in bulk solution has been provided by various experimental techniques, including nuclear magnetic resonance (NMR) spectroscopy and neutron reflectivity with quartz crystal microbalance measurements.^{47,48} These studies clearly demonstrate that solvent structure can be significantly modified by the silica surface. No information, however, was given regarding the distribution of the 'ice-like' and 'liquid-like' regions.

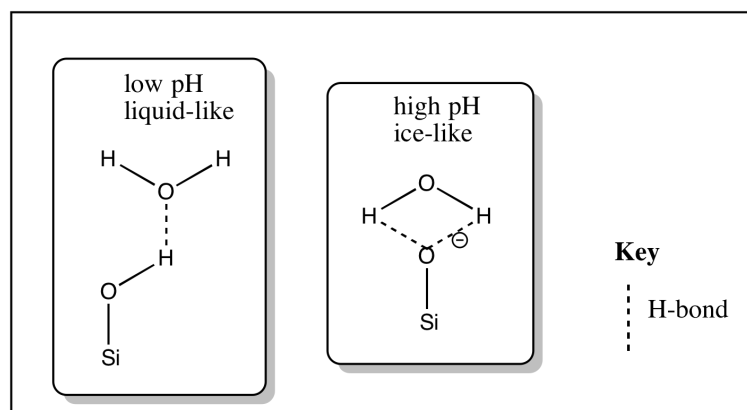


Figure 1.4: Suggested predominant water interactions at the quartz/water interface at low and high pH according to.² The geometric criteria for defining a H-bond is generally when the distance between a heavy atom (O or N) and water oxygen is 3.5 \AA or less and when the angle between the acceptor and the donor hydrogen is 30° or less.

With the aim of determining the distribution of 'ice-like' and 'liquid-like' water at the fused-silica/aqueous electrolyte interface, Hore *et. al.* manipulated the width of the interfacial region, the region responsible for the SFG signal, by varying the concentration of NaCl from 0 to 0.12 M.⁴⁹ This exploited the well-accepted prediction of DVLO theory that the higher the ionic strength, the smaller the width of the interfacial region.¹⁶ Since the SFG peak at $\sim 3200 \text{ cm}^{-1}$, associated with 'ice-like' water,

decreased relative to that at $\sim 3400\text{ cm}^{-1}$ with increasing ionic strength (as the width of the double layer decreased), it was concluded that the ice-like region existed further from the surface. In other words, the data was interpreted to suggest that the character of the water depended on proximity to the surface. This is in contrast to an interpretation of SFG data at the quartz/water interface of Shen and co-workers that silanol groups of different acidities were responsible for the two characteristic regions.^{50,32} It is proposed that in the 'ice-like' regions, water molecules were more likely to bind to SiOH groups *via* their oxygen atoms, compared to through their hydrogen atoms to SiO⁻ groups in 'liquid-like' regions.

1.3.1 The Effect of Ionic Strength

Rather than viewing ionic strength as a tool to change the Debye length (in other words, the thickness of the electric double layer (EDL), a term which will be defined in section 1.4 and shown schematically in Figure 1.6), several experimental studies have explored how ionic strength affects solvent structure at the aqueous electrolyte-silica interface. Surface charge is particularly important, as demonstrated by Borguet *et. al.* in a study concerned with the pH dependence of the addition of 0.1 M NaCl on SFG spectra taken at the fused silica-water interface.⁵¹ The addition of salt only affected interfacial water structure at pH values above the isoelectric point (IEP) of silica, when the surface was negatively charged and ions were attracted into the interfacial region. At such pHs, the addition of electrolyte ions resulted in a decrease in spectral intensity. The magnitude of the influence of the electrolyte depended on pH and was greatest at near-neutral pH. In a constant-pH study, Hore and co-workers varied the ionic strength of NaCl solution over a range from 0.05 mM to 4 M at a charged fused silica surface.^{52,53} The peak corresponding to ice-like water dominated until 1.1 M, when the peak associated with liquid-like water became more predominant, with, it was suggested, ion adsorption displacing surface bound water molecules and disrupting the hydrogen bonding network. It was suggested that in the low ionic strength regime there was a balance between the decrease in intensity of the SFG signal, *i.e.* polar water ordering, as a consequence of the decrease in interfacial depth and the increase in intensity due to the increased surface charge. The latter factor dominated until $\sim 0.7\text{ M}$, when the signal began to decrease, in qualitative agreement with the results of Borguet *et. al.* It was clear that ionic strength

played an important role in influencing interfacial water structure. This could be by changing water orientation through altering surface charge or, at high ionic strength, by adsorption of ions at the surface and disruption of the hydrogen bond network.

1.3.2 The Effect of Ion Type

The effect of ion type on the perturbation of interfacial water structure has also been investigated. Chou and co-workers recorded IR-visible sum frequency vibrational spectra at the interface of fused silica and a range of alkali chloride (LiCl, NaCl and KCl) and sodium halide (NaCl, NaBr and NaI) solutions.⁵⁴ In every case and as in previous studies, 'ice-like' and 'liquid-like' peaks appeared at their characteristic wavenumbers and spectral intensity decreased with increasing ionic strength. Although alteration of the anion had no significant impact on the spectral intensity, the degree of water perturbation occurred in the order $K^+ > Li^+ > Na^+$ for the alkali chloride solutions. The authors proposed two factors to rationalize this behavior: the equilibrium constant of hydrated cation association with SiO^- groups ($K_{K^+} > K_{Na^+} > K_{Li^+}$) and the effective ionic radii of the hydrated cations ($r_{Li^+} > r_{Na^+} > r_{K^+}$). A larger equilibrium constant corresponds to a larger proportion of hydrated cation-associated siloxide groups and thus a greater perturbation of water structure. The larger the hydrated ion, the greater the amount of water that would be displaced on its surface adsorption. Furthermore, the peak associated with 'ice-like' water was more vulnerable to cation perturbation than the 'liquid-like' peak. It was suggested that vicinal silanol groups (a schematic of the different silanol types is shown in Figure 1.5) were responsible for the more ordered ice-like structure and, with their higher local surface charge density compared to other silanol types, were more likely to attract cations. In a vibrational sum frequency spectroscopy study at the negatively charged quartz-water interface, Cremer *et. al.* found a correlation between the charge density of the cation and the extent of interfacial water perturbation⁵⁵ It was argued that the higher the charge density, the more favorable the adsorption of the cation and the greater the disruption to interfacial water. The highly charged Li^+ , however, was an anomaly to the trend. This was ascribed to Li^+ 's strongly bound hydration shell and the concomitant decrease in its effective charge density. In a parallel, anion-focused study at the same interface, Cremer and co-workers found the more weakly hydrated the anion, the greater the penetration into the interfacial region

and perturbation of water.⁵⁶ Since the degree of surface ionization has been shown to influence water perturbation, the effect of the electrolyte type on SiOH and SiO⁻ stabilization is also important. Using second harmonic generation (SHG) spectroscopy at the aqueous fused-silica interface, Gibbs-Davis *et. al.* determined that for a range of alkali chlorides, LiCl, KCl, CsCl and NaCl, only NaCl stabilized the deprotonated state.⁵⁷ Electrolyte identity did impact the degree of perturbation of interfacial water structure and, as noted in one study, particularly disrupted regions of 'ice-like' water. A variety of ion-dependent characteristics were used to explain trends in the degree of interfacial water perturbation.

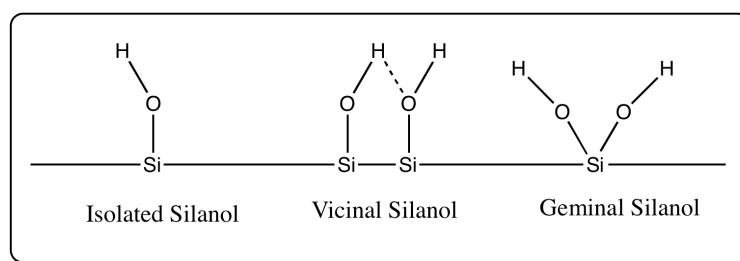


Figure 1.5: Schematic of the different silanol types: isolated, vicinal and geminal.

1.4 The Gouy-Chapman-Stern (GCS) Model

Although techniques such as X-ray photoelectron spectroscopy (XPS) have provided information on ion structure at the aqueous silica interface,^{58,59,60} experimental methods that allow the direct observation of the interfacial ion distribution with subnanometer resolution, as demonstrated in a recent high resolution atomic force microscopy (AFM) study, have not yet been well-established generally.⁶¹ Thus, theoretical models dating back to the early 20th century are still routinely used to describe the interface and interpret experimental data.⁶²

The majority of materials will experience surface charging when placed in contact with an aqueous solution. For the natively oxidised silicon surface, this charging is due to deprotonation/protonation of silanol groups (giving SiO⁻, SiOH and SiOH₂⁺), a pH and salt concentration dependent process. Electrostatic attraction results in a higher concentration of counterions near the surface compared to the concentration in bulk so-

lution, whilst repulsion means co-ions (ions of the same charge as the surface) will be more concentrated in the bulk. The net charge in a solution volume near the surface balances the surface charge. This liquid region and the charged surface is defined as the electrical double layer (EDL). Different affinities between the ions and the surface may also lead to the formation of an EDL.^{63,64,65,66} Indeed, the existence of an EDL at charge-neutral surfaces has been confirmed experimentally.⁶⁷

The EDL can be further characterised and various models have been developed. The Helmholtz⁶⁸ -Gouy⁶⁴ -Chapman⁶⁵ -Stern⁶⁶ -Grahame⁶⁹ model, commonly termed the Gouy-Chapman-Stern (GCS) model, has been frequently employed, even in recent years, and was shown to quantitatively explain most experimental results within the low to moderate surface charge regime.^{70,71} The model is shown schematically in Figure 1.6. In this model, an EDL formed as result of electrostatic interactions between the charged surface and ions in solution, with counterions being more concentrated near the surface compared to bulk and a higher concentration of co-ions in the bulk.⁶² The EDL was classed into two distinct regions: the Stern layer, composed of the inner Helmholtz plane where counterions specifically adsorbed to the surface and the outer Helmholtz plane where hydrated ions were adsorbed; and a diffuse outer layer with a net charge that gradually decayed to zero as bulk solution was approached (the lower the ionic strength of solution, the wider this layer will be). The classical GCS model has been criticized for several reasons and many variants of the classical GCS model have been developed.⁶¹ Dukhin *et. al.* presented experimental evidence that indicated EDL formation could occur at charge-neutral surfaces and suggested that interfacial water structure should be considered as a governing influence.⁶⁷ The importance of solvent structure was also emphasized by Wu and co-workers.⁷¹ Cardenas attributed the success of the model to its ability to describe experimental results from the classical mercury-solution interface and other Nernstian systems, arguing that the model broke down for non-Nernstian systems, such as oxides.⁵⁸ Experimental data at the subnanometer scale is limited and despite its widespread use, the GCS model may not be applicable to oxide systems. Furthermore, interfacial solvent structure could be more important than accounted for in the model.

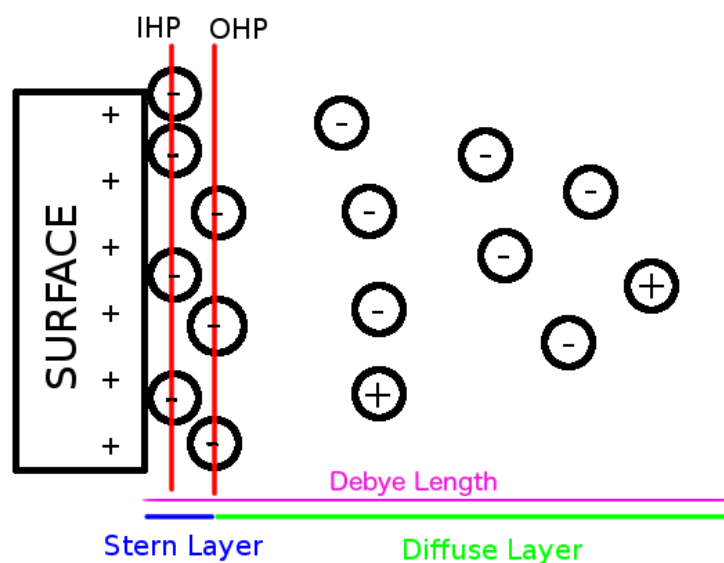


Figure 1.6: Schematic of the Gouy-Chapman-Stern layer. The inner Helmholtz plane (IHP), outer Helmholtz plane (OHP) and Stern layer have been labelled.

There was a dynamic aspect to the GCS model. In standard models, the fluid within the Stern layer was considered immobile and a plane of shear - where the viscosity changed sharply from an infinite value to the bulk solution viscosity - was located at the boundary between this immobile region and the diffuse layer.⁷² This concept has been well-accepted and used in the physics, electrochemistry and colloidal science communities. Indeed, the zeta potential, an experimentally accessible parameter commonly used as a measure of surface charge, was defined as the electrostatic potential at the slipping plane. Crucially, however, surface conduction measurements higher than could be produced solely from ions outside of the Stern layer have been recorded.⁷³ Furthermore, there are many cases where zeta potentials obtained by different experimental techniques varied unless a contribution to surface conductivity from ions in the Stern layer was included; the Helmholtz-Smoluchowski (H-S) equation, often used in the interpretation of electrokinetic data and zeta potential calculation, did not account for it.^{74,75,73,76} A 'dynamic Stern layer', in which ions with near bulk mobility migrate through immobile water, was proposed.^{74,75,73,77} Lyklema proposed that ions were able to move through the regions located at the distances of the solvent density minima.⁷³ Some, however, did not interpret the 'dynamic Stern layer' model in a literal way. Indeed, Saville and Zukoski, who derived such a model, viewed it as 'one that allows

the introduction of certain functional relationships which reproduce the experimental results'.⁷⁴ An alternative model, where water was also mobile within the Stern layer, was suggested.⁷⁸ Although variants of the traditional model have been developed to rationalize higher than expected surface conduction measurements, experimental support at the atomic scale is limited and this area, as with that of interfacial ion structure, has particularly benefited from the insight of atomistic simulations.

Most attempts to locate the slipping plane using atomistic simulation have focussed on determining the 'sharp' boundary between the mobile and immobile layers through calculation of dynamic properties, such as velocities, viscosities and diffusion constants. This method directly probes hypotheses based on a mobile Stern layer. The ultimate aim of some attempts to locate the slipping plane is to calculate the zeta potential.

The validity of the traditional GCS model and 'dynamic Stern layer' at the aqueous electrolyte-amorphous silica interface was specifically addressed in a non-equilibrium molecular dynamics (NEMD) study of Singer *et. al.* in 2011.⁷² Ion and water surface parallel velocities were calculated as a function of distance from the surface and found to be qualitatively the same for the interface with NaCl solution at three different concentrations, 0 M, 0.30 M and 0.55 M. Though water mobility gradually reduced in a region 3 Å from the surface and approached zero, it was not immobile. Furthermore, ion mobility followed the same trend and was not enhanced compared to that of the solvent. Indeed, solvent immobility was only observed when the surface charge was increased to an extremely high value and coincided with a region of immobilized cations. Surface conductivity calculations from the simulation were, however, similar to the corresponding experimental values. The absence of quiescent layers of water at typical surface charge densities was supported by a simulation study of Lorenz *et. al* featuring the calculation of electro-osmotic velocities of 0.4 M NaCl and 0.2 M CaCl₂ solutions in an amorphous silica nanopore of width 7.5 nm.⁷⁹ Classical simulation studies of the charge-neutral quartz/pure water interface also reported a region of reduced solvent mobility close to the surface.^{80,3} Joseph and Aluru calculated surface parallel ion and water diffusion coefficients from an NEMD simulation of a flat, neutral, crystalline α -quartz surface in 1 M KCl solution.⁸¹ Close to the surface, in the first layer of water molecules, water diffusion coefficients had reduced to 38% of the bulk value. Although the observance of a region of immobile water or ions was not commented

on, in a 2014 study of amorphous silica nanoparticles, Heinz *et. al.* did note a correlation between the amount of higher mobility, free cations and experimentally determined values of the zeta potential as a function of pH and particle size.⁸² Computed interfacial ion and solvent dynamics did not support the 'dynamic Stern layer' concept of the traditional and widely-applied GCS model and provided insight that could inform the development of future theoretical models.

1.5 Simulation Studies of the Silica/Water Interface

Molecular dynamics (MD) and *ab initio* molecular dynamics (AIMD) methods - both of which have been used to study the silica/water interface - are discussed in section 2.1.1 and 2.1.1, Chapter 2 ('Methods').

1.5.1 The Silica/Pure Water Interface

Several computational studies concerned solvent structure at the silica/pure water interface, with crystalline forms of silica, such as quartz and cristobalite, being the most widely analysed. Notman and Walsh investigated the interface of water with the (10 $\bar{1}$ 0), (0001) and (01 $\bar{1}$ 1) faces of quartz, as depicted in Figure 1.7³. The water density as a function of distance normal to the surface was similar in all three cases, with peaks occurring in the same positions, but differing in magnitude. There were at least two layers of structured water, with an additional layer at the (10 $\bar{1}$ 0) interface, where gaps between hydroxyl groups of the surface were sufficiently large to allow the water to approach the surface more closely. The lateral arrangement of water within the first major layer was distinct between the three faces, with the regions of the highest density closely following the pattern of surface hydroxyl groups. Although the average water orientation as a function of distance normal to the surface followed the same trend at the (10 $\bar{1}$ 0) and (0001) faces, at the (01 $\bar{1}$ 1) face this trend was reversed in the region corresponding to the first layer of water. Cummings *et. al.* investigated the quartz/water interface using different force-fields and compared the interfacial water structure from classical MD simulations to data from *ab initio* molecular dynamics (AIMD) and, in one study, x-ray reflectivity (XR) experiments.^{83,84} It was evident that certain force-fields were better at capturing certain characteristics than others. For instance, the Lopes *et. al.*

force-field underestimated the extent of hydrogen bonding between hydroxyl groups and water.^{85,84} Electron density distributions determined from XR were, however, in good agreement with those calculated using the Lopes *et. al.* force-field. In practice, force-field differences such as this led to subtle variations in the magnitude and position of peaks in the water density and orientation profiles for the quartz($10\bar{1}1$)/water interface.⁸³ A parallel study at the cristobalite/water interface was carried out by Cole *et. al.*⁸⁶ AIMD simulations at the quartz(0001)/water interface were conducted by Sprik and co-workers.^{87,88} The orientation of water molecules was found to influence hydrogen bond strength, a property proposed to be responsible for the 'ice-like' and 'liquid-like' regions of interfacial water. The strongest H-bonds were formed between the oxygen atom of water and hydrogen of out-of-plane silanols, while the weakest occurred when the hydrogen of adsorbed water acted as a donor to the oxygen of an in-plane silanol. In an AIMD study that encompassed both the quartz(100)- (Figure 1.7) and cristobalite(001)-water interfaces (Figure 1.8), 'ice-like' regions were more pronounced when the silanol surface density was higher.⁴ Molecular simulation has provided atomic-level insight, not yet feasible experimentally, into the structure of interfacial water at the crystalline silica/water interface and has enabled the resolution of silica-type dependent differences in interfacial solvent structure.

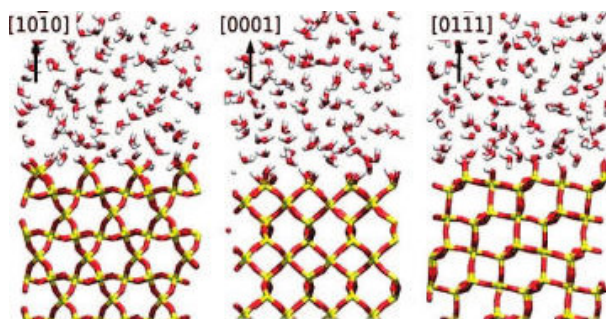


Figure 1.7: Schematic of a selection of quartz/water interfaces adapted from Notman *et. al.*³ Red represents oxygen atoms, white hydrogen atoms and orange silicon atoms.

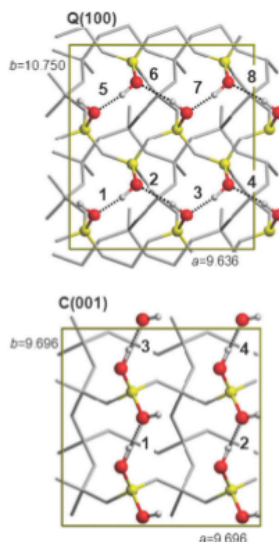


Figure 1.8: Schematic of the quartz(100)- and cristobalite(001) surfaces adapted from Sodupe *et. al.*⁴ Red represents oxygen atoms, white hydrogen atoms and orange silicon atoms.

1.5.2 The Amorphous Silica/Pure Water Interface

The amorphous silica/water interface has not been so thoroughly explored computationally and was sometimes considered synonymous with the aqueous quartz interface. Indeed, in a recent experimental study, Borguet *et. al.* argued that, due to similar points of zero charge (PZCs) and dissolution behaviors, the character of this interface should be qualitatively the same as that of the quartz/water interface.⁵¹ However, quartz and amorphous silica are sufficiently different structurally that different interfacial characters would be expected. Other studies suggest that there are significant differences between these two surfaces, however. In 2014, Costa and co-workers used AIMD to directly investigate the nature of the water structure at the amorphous silica/liquid water interface.⁸⁹ In contrast to that at the quartz(0001) surface, the first water layer was overall very disordered. There was, however, a degree of local organization. Three domains with distinct water orientation behaviors were observed, where water orientation was defined as the angle between the water dipole vector and the vector normal to the silica surface. In Domain 1, the orientation angle varied from 0° - 60° , corresponding to when the dipole on average pointed out from the surface and water oxygens accepted H-bonds

from out-of-plane silanols. Angles varied from 70° - 140° in Domain 2, where dipoles pointed towards the surface and, on average, one water hydrogen atom donated a H-bond to a surface silanol. Both O-H groups of the water molecules pointed towards the surface in Domain 3, with angles in a range from 140° - 180° . Molecules from all three domains were found to H-bond with vicinal silanols, while for geminal and isolated silanols (a schematic of the different silanol types is shown in Figure 1.5), the range of orientation angles was narrower, from $\sim 20^\circ$ - 80° , *i.e.* the water dipoles pointed away from the surface. Pandit *et. al.* also reported the polarization of water molecules close to the amorphous silica surface in a reactive MD study.⁹⁰ Water structure at the amorphous silica/water interface was distinct from that at the aqueous quartz(0001) interface and although overall disordered, displayed a local organization.

1.5.3 The Aqueous Electrolyte/Quartz Interface

Some computational studies have focused on the aqueous electrolyte/quartz interface. Insight into the dissolution mechanism of silica was often cited as a major motivation, and thus an emphasis was placed on ion/water structure at and interaction with silanol or bridging oxygen groups. In 2010, Dove *et. al.* calculated the reaction pathways for Si-O hydrolysis using B3LYP and PBE1PBE functionals (examples of functionals used in Density Functional Theory (DFT) - a modelling technique used to investigate electronic structure - where the functional describes electron density as a function of space and time) for the adsorption of inner- and outer-sphere complexes of $\text{Mg}^{2+}(\text{6H}_2\text{O})$ and $\text{Ca}^{2+}(\text{6H}_2\text{O})$ at a neutral silica cluster ($\text{H}_8\text{Si}_6\text{O}_{16}$) that was extracted from a larger quartz crystal structure.⁵ The data for Ca^{2+} is shown in Figure 1.9 as an example. Although the barrier to hydrolysis in the presence of the outer-sphere complexes was larger than the water-induced reaction, it was reduced in the presence of the inner-sphere complexes. Recently, in 2014, Sofo and co-workers conducted AIMD simulations of a selection of α -quartz (101) systems, featuring HCl, NaCl, MgCl_2 , $\text{Mg}(\text{OH})_2$ and NaOH.⁹¹ The presence of ions significantly changed the distribution of water molecules without altering their minimum distance to the surface. Angular distribution functions (ADF) showed water molecule orientation was dependent on ion type. Hydrolysis involved proton transfer to the bridging oxygens of the silica surface. Peak positions in radial distributions, RDFs (defined in Chapter 2) revealed that the hydrogen bonds between

water, including H_3O^+ , and bridging oxygens were weaker than those between water and a particular type of silanol. Intra-surface proton transfer, rather than direct transfer to bridging oxygens, was thus considered the more likely mechanism for dissolution. This conclusion was supported by an earlier study of Kubicki *et. al.*,⁹² which found statistically significant increases in the proportion of internal $\text{SiOH-O}_{\text{bridging}}\text{Si}$ H-bonds when cations such as Na^+ or Mg^{2+} were added to solution.

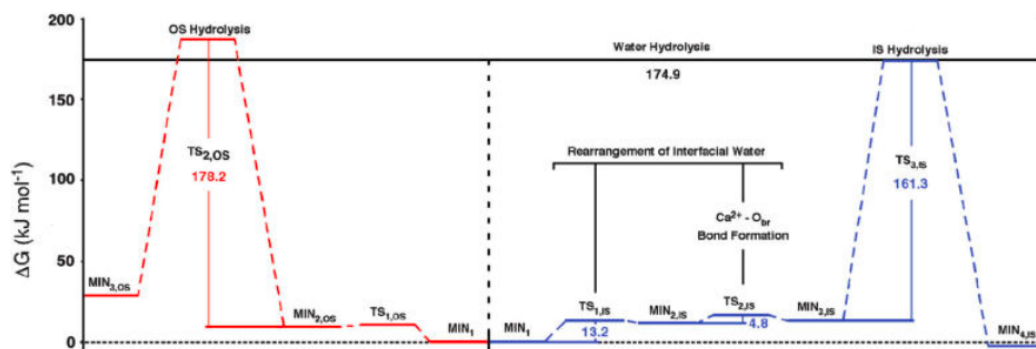


Figure 1.9: Si-O hydrolysis for hydrated Ca^{2+} , with outer sphere paths shown in red, inner sphere paths shown in red as adapted and the barrier to hydrolysis in the absence of ions in black from Dove *et. al.*⁵

Classical MD studies of the quartz/aqueous electrolyte interface have also been conducted. Though it will not be the focus, it should be noted that much experimental and simulation work has been carried out at the aqueous electrolyte/aluminosilicate clay interfaces, minerals highly analogous in structure.¹¹ One such study of the quartz (111)/aqueous sodium sulphate interface suggested that there were several layers of water and ionic species at the interface, including a significant concentration of sulphate ions before the second water layer.⁹³ Water was found to have three adsorption sites at the silica surface and one, where water molecules were orientated parallel to the surface normal, was highlighted. In 2015, Predota *et. al.* used a modified ClayFF force-field⁹⁴ in classical MD simulations to investigate interfacial ion and water structure for a series of aqueous alkali and alkaline earth metal chlorides at the interface with a (101) quartz surface with different surface charge densities (0, -0.03 , -0.06 and -0.12 C m^{-2}).⁹⁵ Water structure was unaffected by electrolyte type and the peaks of the water oxygen density profiles only slightly shifted further from the surface with increasingly negative surface charge. For all ion types, the number of ions close to the surface increased with

surface charge. Inner-sphere and outer-sphere complexes with different types (termed inner and outer) of silanol and siloxide oxygens were suggested to be responsible for the various peaks in the profiles of ion density as a function of vertical distance from the surface. Although the patterns in Na^+ and Rb^+ vertical ion densities were similar, the larger ionic radius of the Rb^+ ion compared to Na^+ shifted the peaks to larger distances from the surface. The more highly charged Sr^{2+} ion had a more tightly bound hydration shell and as a result different bonding preferences to the monovalent ions, with adsorption to the 'outer' silanols comparatively dominant. Lateral ion density profiles in the xy plane revealed preferences for particular adsorption sites. For example, Na^+ ions had a greater affinity for protonated oxygens compared to deprotonated due to the stronger solvation of the latter. Voitchovsky and co-workers investigated lateral ion structure at the interface between mica and several aqueous electrolytes (RbCl , NaCl and KCl) at a range of electrolyte concentrations using MD in combination with AFM.⁹⁶ It was suggested that the interfacial ion structuring was driven by interfacial water structure. Computational studies have provided detailed structural information on the subnanometer scale for the quartz/aqueous electrolyte interface and the influence of ions on the orientational behavior of nearby water molecules was clear.

1.5.4 The Aqueous Electrolyte/Amorphous Silica Interface

In 2015, Miranda *et. al.* investigated the influence of cation identity and concentration on EDL formation at interface of amorphous silica nanoparticles and electrolyte solutions.⁹⁷ NaCl , CaCl_2 and MgCl_2 solutions were used and mole fractions from 0.06×10^{-3} to 3.00×10^{-3} were investigated. As electrolyte concentration was increased, the sign of the effective charge of the first ion layer inverted. The width of the EDL for a certain ionic strength was observed to decrease in the order NaCl to CaCl_2 to MgCl_2 . The results were supported by data from previous experimental investigations (fourier transform infrared spectroscopy, ultraviolet-visible spectroscopy, zeta potential analyses and dynamic light scattering), which quantitatively reproduced the trend⁹⁸.

An MD simulation of the interface of a planar amorphous silica surface, as described by the Cruz-Chu *et. al.* force-field,⁹⁹ with two aqueous electrolytes, 0.35 NaCl M and 0.35 CsCl M, was conducted by Borguet *et. al.* in 2014.¹⁰⁰ Distinct differences in ion adsorption behavior and interfacial water structure were observed. Ion and water

density was calculated as a function of distance normal to the surface. For NaCl, the first major peak in Na^+ density occurred at a distance closer to the surface than the first major peak in the profile for the oxygen atoms of water. In contrast, for CsCl, the major peak in Cs^+ density was observed further from the surface than that of the water oxygens. This indicated that Na^+ ions adsorbed directly to the surface and Cs^+ ions adsorbed in their hydrated form. Profiles for water orientation as a function of distance normal to the surface were presented. For NaCl, the first layer of water molecules was oriented with hydrogens pointing away from the surface and suggested Na^+ effectively screened the negative charge of the surface. The reverse is observed in the CsCl solution, with hydrogens pointing towards the surface in the first layer and indicated that Cs^+ did not screen the surface charge so effectively. Furthermore, the average number of adsorbed Na^+ ions per area of the silica surface was $\sim 10\%$ greater than the corresponding number for Cs^+ ions. Layerwise distributions of the orientations of the water molecules further demonstrated differences in the screening effect of the interfacial cations. The number of water molecules with $\cos(\theta)$ values of 1 (water hydrogens pointing away from the surface) or -1 (hydrogens pointing towards surface) in the first layer was far greater in the CsCl solution than in the NaCl solution. For CsCl, this was followed by a drop in the number of extreme orientations of water molecules in the second layer, the water dipoles of the first layer acting to screen the negative surface charge. The balance between the ion-surface adsorption energy and entropy loss associated with the adsorption of ions was used to rationalize these differences. The larger size of the Cs^+ meant a lower electrostatic interaction energy with the surface and made adsorption less favorable compared to the smaller Na^+ . Another key difference that the authors did not much comment on was the increased interfacial Cl^- ion concentration in the NaCl solution compared to aqueous CsCl. Ion-specific effects clearly influenced the orientation behavior of interfacial water, with the difference in the ability of the two featured cations, Na^+ and Cs^+ , to screen the negative surface charge highlighted as an important factor.

1.6 Molecular Adsorption at the Silica/Water Interface

This section describes molecular adsorption at the silica/water interface, as investigated by both simulation and experiment. As will be discussed in Chapter 2 ('Methods'),

molecular modelling requires force-fields to describe each part of the simulation. Indeed, the molecular modelling of molecular adsorption at mineral/water interfaces requires the use of using various force-fields which might not traditionally be combined. This might be, for example, the use of a force-field for biomolecules or organic compounds with a force-field for a mineral, such as calcite or silica. Thus, the first part of the section is dedicated to describing the importance of force-field interoperability, with one particular combination of force-fields used as an example: CHARMM which is traditionally used to describe biomolecules and SPC/Fw, a force-field to describe water that has previously been used in combination with a force-field for calcite. The successful incorporation of biomolecules to the calcite/water system would require compatibility between the CHARMM and SPC/Fw force-fields. Furthermore, the compatibility of SPC/Fw with CHARMM - the force-field used to model the ions and organic components of the simulations in the research of this thesis - would be essential if the water force-field were to be used in the simulations of the silica/aqueous electrolyte interface. This is followed by sections on molecular adsorption at the silica/water interface and silica/aqueous electrolyte interface, concluding with a simulation-focused section on probes of molecular adsorption, including the modelling of self-assembled monolayers (SAMs), a parallel to the SAM that forms on a functionalised AFM tip and different approaches to the modelling of atomic force microscopy (AFM).

1.6.1 Force-Field Inter-operability

One of the challenges in the area of molecular simulation of biointerfaces is to ensure that the interatomic potentials used to describe such interfaces capture the essential chemistry and physics of the system. The compatibility of the force-fields that describe the inorganic and biomolecular components of the system, components that correspond to very different types of matter, is essential to the successful incorporation of a description of biomolecules and inorganic matter. Although the silica force-field used in this work¹ was *designed* to be compatible with common biomolecular force-fields, such as CHARMM and AMBER, this is not always the case. Gale *et. al.* recently developed a flexible force-field for calcium carbonate and chose the flexible SPC/Fw potential as the corresponding water model.¹⁰¹ In order to reliably model the protein-mediated control of biomineralisation using this force-field, a longer term goal, SPC/Fw must be compat-

ible with established biomolecular force-fields, for example, CHARMM or AMBER, force-fields that are traditionally used with the TIP3P model for water.¹⁰²

The Importance of the Water Model to the Potential Energy Landscape (PEL)

In their biological environment, non-membrane-bound proteins are typically surrounded by water. It has long been acknowledged that the medium of liquid water has a significant impact on the three-dimensional protein structure (secondary and tertiary), with the most energetically favourable arrangements being those in which the hydrophobic residues are sequestered to the protein interior.¹⁰³ Such structures are typically found as the lowest minima of the potential energy landscape (PEL), with exceptions for *e.g.* intrinsically disordered proteins. The influence of water on the protein PEL also has an impact on the frictional and random forces experienced by proteins, affecting protein dynamics.¹⁰⁴ Considering the influence of water on both the PEL and dynamics of proteins, it follows that in the field of molecular simulation, the means by which we describe the liquid water is of crucial importance to the results obtained from a simulation.

Computational Representation of Water

The large number of water molecules typically needed to keep the protein in a biologically relevant state requires that the computational representation of solvent be implemented as economically as possible to ensure that calculations remain feasible. One option is to treat the water as a continuum dielectric, as is done in implicit solvent models.^{105, 106, 107, 108} However, the approximations inherent to this approach may miss important microscopic physical details, particularly where molecular recognition of/by the protein is important. Water could also be represented explicitly using electronic structure methods; however, the significant computational cost heavily restricts the accessible system sizes and simulation timescales. A compromise is atomistic molecular dynamics (MD) used in partnership with molecular mechanics force-fields, an approach that provides an explicit treatment of water molecules within viable timescales. The molecular mechanics approach for describing interatomic potentials in itself covers a range of complexity, including the incorporation of atomic polarisation.¹⁰⁹

The success of MD simulations is strongly dependent on the reliability of the

intermolecular potential functions used to describe the system. It is testimony to the importance and complexity of water that a range of force-fields have been developed to model it. As it is a challenge to adequately represent *all* properties of water on an equal footing, different water models have been devised to possess different strengths, with most better at capturing some properties of water over others. Thus, the water model should be chosen appropriately, considering which properties are relevant to the scientific questions under investigation. The most popular models, such as TIP3P¹⁰² and SPC,¹¹⁰ are rigid body and have three interaction sites.

Compatibility of Biomolecular and Water Force-Fields

When modelling biomolecules in aqueous solution, the force-field to describe water must be used in combination with a biomolecule force-field, such as CHARMM,^{111,112} AMBER,^{113,114} OPLS^{115,116} or GROMOS.^{117,118} The combination of TIP3P¹⁰² (and TIPS3P, a modified version¹¹⁹) with CHARMM and AMBER is successful and widely documented in the literature. Furthermore, several studies have already directly investigated the impact of the choice of the water potential on the biomolecular system by simulating a particular protein/peptide (described by a certain biomolecule force-field) with different water models.^{120,121,122,123,124,125} However, some of the more recently developed force-fields are yet to be extensively employed in conjunction with common biomolecule potentials, as compatibility of these models with the biomolecular component has not yet been established. SPC/Fw, a more recent flexible variant of the rigid SPC water model, is one such water force-field.¹²⁶ The model has been optimised to better reflect the dynamical and dielectric properties of bulk water. We note that Takemura and Kitao¹²⁵ have previously evaluated the effect of water model (including SPC/Fw) in combination with a biomolecule force-field (AMBER), but with an exclusive focus on the dynamical properties of proteins, such as diffusion and time-correlation functions. These authors reported that SPC/Fw reproduced both the translational and rotational motion of their protein relatively well.

1.6.2 The Silica/Pure Water Interface

Although a large number of studies, both experimental and computational have investigated the adsorption of small organic molecules and biomolecules at the aqueous silica

interface, few have explored how this adsorption is influenced by electrolyte concentration.^{20,29,57} The potential of mean force (PMF) approach (defined in section 2.1.1) has been used to predict the adsorption strength of several amino acid analogues to different facets of hydroxylated α -quartz in pure water using molecular dynamics (MD) simulations.^{3,127} Schneider and Colombi Ciacchi employed metadynamics (defined in section 2.1.1) with replica exchange with solute tempering (REST) (defined in section 2.1.1 and steered MD simulations in which you apply an external force to one or more atoms to study the binding behavior of a hexapeptide, RKLPDA, to an oxidised silicon surface.²² Their results showed quantitative agreement with data from atomic force microscopy (AFM) experiments. In a more recent 2015 study, Colombi Ciacchi employed the same approach to study the adsorption of the **GCRL** tetrapeptide at the amorphous silica/pure water interface.¹²⁸ Recently, Meissner *et. al.* used modelling to predict the loss of helicity upon peptide adsorption to silica.¹²⁹ Heinz and co-workers developed a force-field for silica with a focus on improving the accuracy of the computation of interfacial properties.⁸² A major conclusion from these studies is that solvent structuring at the solid interface exerts a strong influence over molecule-surface adsorption. It follows that factors that alter the binding environment, either directly by their presence in the interfacial region, or indirectly through their effect on this interfacial solvent structure, could play a critical role in influencing adsorption behaviour.

Indeed, it has been demonstrated that the binding environment impacts adsorption properties. It is well-known that the presence of surfactant inhibits the adsorption of oil and certain proteins on silica.¹³⁰ Adsorption inhibition is thought to result from the change in character of the silica surface after surfactant adsorption and the formation of surfactant complexes with protein or oil components. Solution pH can also alter the nature of the surface and protein adsorbates through change in the protonation state. In an experimental study, Puddu and Perry observed that adsorption of charged and uncharged peptides to amorphous silica nanoparticles was highly sensitive to pH as hydronium ions mediated peptide and nanoparticle charge state and thus electrostatic, hydrophobic and hydrogen bonding interactions.¹³¹ Surface functionalisation of silica nanoparticles was also a factor that if slightly altered could lead to dramatic changes in biomolecule adsorption at the solution particles interface.¹³²

1.6.3 The Amorphous Silica/Aqueous Electrolyte Interface

Some previous studies have focused on the effect of ionic strength on the adhesion of organic molecules to the silica surface. Dreschler *et. al.* used AFM to measure the adhesion of silica microparticles on a poly(2-vinylpyridine) (P2VP) brush in KCl solutions as a function of ionic strength.^{133,134} Whether the interaction was repulsive or attractive depended on the pH of the solutions over a range of ionic strength. These data were very complex to interpret because the conformation of P2VP is thought to be affected by changes in pH and solution composition. In a simpler study, the adsorption of a range of amino acids (arginine, lysine and ornithine) to a surface of highly dispersed silica, with zero point charge (zpc) at pH 5 in NaCl solutions (concentrations 0.01 M and 0.1 M) was investigated using acid-base titration.¹³⁵ Numerous studies have used molecular simulation and/or experiment to investigate adsorption of amino acids or peptides at the aqueous silica interface.^{135, 136, 137, 138, 139, 140, 141, 142, 143, 144, 145, 146, 147} Furthermore, in 2015, Greenwell *et. al.* investigated the 'low salinity' (LS) effect in a study of the simultaneous adsorption of multiple organic compounds at the interface between aqueous NaCl/CaCl₂ and montmorillonite, a clay mineral.¹¹ However, to our knowledge, there has been no conclusive study of the mechanism by which this adsorption is affected by salt concentration.

AFM experiments have confirmed the 'low salinity' (LS) effect described earlier in the text and applied in EOR.⁸ Adhesion of AFM tips functionalized with -CH₃ and -COOH on sandstone model surfaces in seawater concentrations (ASW, artificial seawater, 36,500 ppm), was higher than in solutions diluted by a factor of about 20 (1500 ppm). For example, the adhesion force between a natively-oxidized silicon surface and a COOH terminated tip decreased from 46 +/- 8 pN in high salinity (HS) solution to 33 +/- 7 pN in low salinity (LS). Note, however, this was still within experimental uncertainty. In Chapter 5, we present further insights into the origins of this 'low salinity' effect, where we have taken a reductionist approach and considered pure saline solutions of NaCl, KCl, CaCl₂ and MgCl₂.

1.6.4 Probes of Molecular Adhesion to Amorphous Silica

The main experimental probes of organic adhesion at solid/liquid interfaces involve self-assembled monolayers (SAMs) on AFM tips (functionalised AFM tips). In this

section, therefore, the simulation studies of SAMs will first be considered, followed by a review of computational modelling of AFM.

Simulation of Self-Assembled Monolayers (SAMs)

It is generally accepted that thiols bind to the Au(111) surface in a $(\sqrt{3} \times \sqrt{3})R30^\circ$ overlayer with a thiolate (Au-S) bonding mechanism and this has been adopted in the most recent simulation studies.^{148,149,150,151,152} There has been much debate surrounding the binding site of the sulfur atom to the gold surface. Electronic structure calculations have suggested several possibilities: above a single Au atom (an atop site); two Au atoms (a bridge site); or above a 3-fold hollow site.^{153,154,155,156,157} In simulation, the latter was the most commonly employed binding site. In 2010, Hase *et. al.* considered binding to this 3-fold hollow site at the vacant face centered cubic (fcc) site of the first layer of the surface and that to the Au atom in the second hexagonal close packed (hcp) layer.¹⁵⁸ The attachment point did not impact the molecular dynamics (MD) simulation results, with data generated from both models being statistically the same. In the majority of investigations, the gold atoms of the substrate were fixed.^{159,160,161,162,163,164,6,165,166,167,168,169,170,171,172,173} There were further cases where the sulfur atoms were also fixed.^{174,175} CHARMM does not provide parameters for Au and has been used with many different models for the gold substrate and Au-S interaction, including a LJ parameterisation specifically designed for interfacial calculations and to be compatible with CHARMM.^{176,173,175}

Since the majority of studies employed periodic boundary conditions in at least two dimensions (xy) so that an infinite monolayer was modelled, comparatively less is known about what happens at the edge of the monolayer and minimum SAM size limitations.^{161,158,166,167,168,169,172,173} Jang *et. al.* have investigated further.^{6,177,169,170} For all of the following studies, it is important to note that a Morse potential was used to describe the Au-S bonding interaction, thus enabling the making and breaking of thiol to gold substrate bonds. Harmonic potentials - which do not allow the making or breaking of bonds - are standardly to describe bonds. In an initial study in 2011, Jang *et. al.* modelled the formation of an 1-octadecanethiol, $\text{SH}-(\text{CH}_2)_{17}\text{CH}_3$ (ODT or C18) monolayer.¹⁷⁷ A decrease in van der Waals (vdW) energy was observed as the SAM grew. Since the ODT-Au interaction energy increased with SAM size, it was

concluded that this decrease in vdW energy was due to favourable ODT-ODT intermolecular interactions. It was only after a certain size-limit, when there were enough favourable ODT-ODT intermolecular interactions, that formation of the SAM island becomes favourable. This system size dependence was analysed systematically in a further study by Jang *et. al.*⁶ In contrast to the starting configuration in the initial study, where the ODT molecules were arranged flat, physisorbed to the Au(111) surface, the thiols were already chemisorbed to the surface and as a monolayer see Figure 1.10. The starting configurations were made by first preparing a circular SAM of 50 ODT molecules, with the S atoms forming a $(\sqrt{3} \times \sqrt{3})R30^\circ$ overlayer on the Au(111) surface. After an equilibration period of 20 ns, molecules at the periphery were removed to give approximately circular SAM islands ranging from five to forty-five molecules in size. MD simulations were then run for 10 ns, with the first 100 ps discarded as equilibration. It was found that at least 20 molecules, corresponding to a SAM diameter of 1.9 nm, were required to form an ordered, upright and immobile SAM. In such SAMs, the tilt angle of the hydrocarbon molecule with reference to the surface normal and packing of the S atoms were almost the same as that in the bulk SAM. However, it should be noted that at the periphery, chains were folded and S atoms departed from the hexagonal close packed structure (hcp) structure. SAMs made up of thiols of different lengths (12, 16 and 24 carbon atoms) were later studied.¹⁶⁹ A similar procedure was used to prepare the approximately circular SAMs as in the previous study.⁶ While for the C24 thiol, 20 molecules was enough to form an ordered, upright SAM, the C16 and C12 thiols required at least 35 and 40 molecules respectively. Although both ordered, distinct differences were observed for SAM islands dependent on the chain length of the constituent thiols. In C12 and C16 islands, chemisorbed thiols were more tilted from the surface normal, had a lower percentage of *trans* conformation and less orientational order compared to the longer chain thiols, C20 and C24. Rectangular ODT monolayers of infinite length and varying width were examined.¹⁶⁵ The minimum line width necessary to form an ordered SAM was found to be 1.7 nm. There were, however, some differences compared to bulk: the alkyl chains were more upright; less compact packing of sulfur atoms; and a more ordered backbone orientation; The bulk reference is not given, so this could be an experimentally determined bulk value, a value determined using the same force-field or using another parameter set. If it was the first or latter of these options, it could be an artefact of the force-field. At the periphery, some

attached sulfurs would occasionally move away (this is cited as the reason for the less compact and one thiol was even observed to lay down on the surface, although it almost immediately returned to the upright position. Chain bending at the periphery was not noted. Rectangular SAMs of finite size (a width of 1.7 nm, but 4 nm, 6 nm, 8 nm and 10 nm in length) were also modelled. The 4 nm long-chain SAM became almost circular in shape within 120 ns, with the shape of the longer-chain SAMs also deforming within 140 ns. This suggests that the threshold stability width of finite SAMs is 4 nm. In cases where it is not possible for the bonds to break (when harmonic potentials are used to describe bonds) the SAMs would not be able to rearrange even though they may not be that stable.

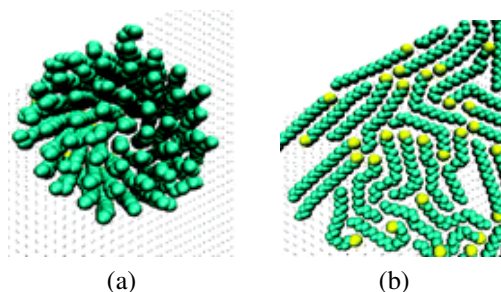


Figure 1.10: Flat physisorbed ODT molecules on Au(111) (left) and chemisorbed ODT molecules on Au(111) (right) as adapted from Ahn *et. al.*⁶

Atomic Force Microscopy (AFM) by Simulation

CustiC (CUDA Atomistic Code) is software that was designed specifically to simulate AFM experiments.¹⁷⁸ In a mimic of experiment, an atomistic tip was gradually displaced vertically with respect to a surface, after each harmonic oscillation. The forces acting on the atoms in the tip are recorded at every step and were used to generate force curves. An experimentally accessible oscillation amplitude of 1 nm was used and was matched in the corresponding experiments. The frequency of 100MHz, however, was 100 times faster than its experimental speed. This was to make the simulation practicable and was not expected to have a big effect on the results, as it was still four orders of magnitude slower than the vibrational frequencies of the system that determine the details of atomic motion. Indeed, test simulations, where the oscillation frequency ranged from 100 GHz to 100 MHz showed there was no significant difference in results ob-

tained below 500 GHz.¹⁷⁸ Another constraint was system size, since the computational cost scales dramatically as it is increased. The authors also note that very little is known about the atomic structure of the tip, with the model of the tip, a mix of MgO and NaCl, being a best guess.

Another approach is to calculate the free energy profile as a function of distance between the AFM tip and surface and to take the derivative to obtain the force curve. Watkins *et al.* used 2 methods, umbrella sampling and free energy perturbation (FEP) (as described in section 2.1.1), on 2 surfaces, calcium fluoride and calcium chloride.¹⁷⁹ Since the dynamics of water and other molecular species in the system were of a much higher frequency than typical cantilever oscillation frequencies, they would have been averaged over and the system can be considered in equilibrium during an oscillation cycle, providing justification for this method. The simulation box contained several layers of surface material and a nanocluster as a model for the apex region of the tip, with the remaining volume filled by water. The lateral translational and rotational degrees of freedom of the tip were constrained to account for the missing part of the tip and cantilever. Different tip constraints were tested. There was a negligible effect on the free energy profile, whether all or just the upper atoms of the tip were constrained. Both umbrella sampling and FEP techniques provided effectively equivalent free energy profiles. The former, however, was more efficient.

Earlier work of Watkins *et al.* involved the use of FEP to study the adsorption of nanoclusters (model tip apexes) to calcium fluoride and magnesium oxide surfaces¹⁸⁰ The influence of tip structure on the free energy profile was investigated by considering a range of tips of varying 'sharpness' and polarity. As is commonly assumed, tip apices were taken to be made up of the same material as the surface they are probing. The authors were particularly concerned with whether AFM can directly measure surface topology or if it rather measures the solvent structure near the surface. As the tip approached close to the surface, the potential energy became largely repulsive and the entropy increased due to the movement of confined water near the tip or surface to the bulk. The balance of the repulsive potential energy and entropic gain is found to differ depending on tip 'sharpness' and polarity. For sharp tips, the direct interaction is significant, while for blunt tips, the overall interaction becomes strongly repulsive before this direct interaction can be reached. Thus, tip 'sharpness' and polarity are seen to have significant effects on force curves. Detailed analysis of the water structure was carried

out in a further publication.¹⁸¹

Chemical force microscopy (CFM) has been studied using atomistic simulation.^{182,183} Patrick *et. al.* modelled the tip apex as a gold sphere with a diameter of 10 nm that was partially coated with dodecanethiolate ($\text{S}(\text{CH}_2)_{11}\text{CH}_3$) and interacted with a planar surface.⁷ 278 thiols were attached to the bottom of the gold sphere, with an outer ring of 52 frozen in order to prevent splaying or migration of attached organic molecules at the edge of the monolayer. The planar wall and gold sphere were kept rigid, with only the SAM allowed to deform. In an initial simulation, the wall was raised about 1.25 nm to bring it into contact with the model tip and then lowered to its initial position at a rate of 2 m s^{-1} . 24 different tip heights were chosen and the system simulated for each for 1-2 ns until all the parameters had reached steady-state values. An additional 1.5-2 ns was then simulated, from which equilibrium properties were calculated. Graphs of interaction force on approach and retraction of the wall to the gold sphere have been presented, as shown in Figure 1.11. In 2010, Vlugt *et. al.* used constraint molecular dynamics to calculate the PMF of a capped nanoparticle as a function of distance from an Au(111) surface.¹⁶² Various parameters were investigated: the length of the alkylthiols (butanethiol to dodecanethiol); the temperature (250-400 K); and nanoparticle size (1.8-2.7 nm). The gold slab and center of mass (c.o.m.) - point that represents the average position of matter in a body - of the nanoparticle were fixed during the simulations, with the rotation of the rigid nanoparticle about its c.o.m. made possible using quaternion rigid body dynamics. Movement of the nanoparticle in the *xy*-plane was unnecessary since the PMF was isotropic in the horizontal direction. The system was in vacuum. In order to generate starting configurations, the capped nanoparticle was pushed towards the gold slab from a distance far above the slab using an artificial spring. The c.o.m. of the nanoparticle was then constrained and the configuration equilibrated for 500 ps.

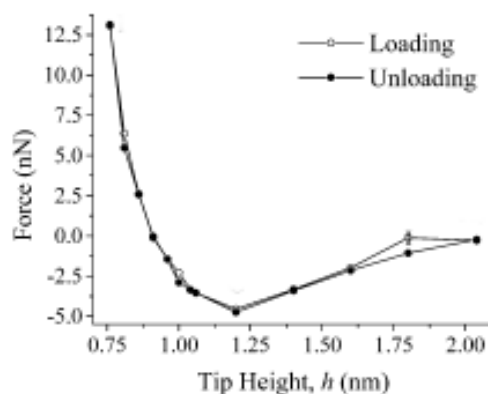


Figure 1.11: Interaction force on approach and retraction of the wall to the gold sphere from Patrick *et. al.*⁷

1.7 Aims and Objectives

The main aim of this thesis was to gain insight into the mechanism of 'low salinity' enhanced oil recovery (EOR) from sandstone reservoirs, using a combined experimental/simulation approach to study the interaction of selected functional groups (R-NH_3^+ and R-COOH/COO^-) with the amorphous silica/aqueous electrolyte interface. Both the influence of concentration and electrolyte type on the interaction of the functional groups at the interface will be explored and a new hypothesis for the 'low salinity' effect may be proposed. The data generated from MD simulations will be analysed to gain information about interfacial ion and water structure and their impact on molecular adsorption considered. Furthermore, previously developed hypotheses, in particular electric double layer (EDL) expansion, fines migration theory and multicomponent ion exchange, will be tested. Another important objective concerns connecting the data generated from simulation to the experimental force curves. In order to do this, the derivative of the free energy profiles generated from metadynamics (an advanced MD technique, that will be explained in the Methods Chapter) will be calculated to produce force curves. Chapter 2 details the methods used for this research, while Chapters 3-6 are results based, finalising with Chapter 7, the conclusion. While Chapters 4-6 directly concern the aqueous electrolyte/amorphous silica interface, in Chapter 3 some validation work was undertaken on peptides to test whether the flexible water force-field,

SPC/Fw, was compatible with CHARMM. The SPC/Fw model will be considered for use in Chapters 4-6, where it would be used in combination with CHARMM (to describe ions and organic molecules) and the force-field chosen to describe silica.¹ Chapters 4-6 will now be discussed with reference to the relevant literature, with the main objective of each Chapter highlighted.

1.7.1 Chapter 4

Few atomistic MD simulation studies have concerned the aqueous electrolyte/silica interface in general, with even fewer focused on amorphous silica. Indeed, even the amorphous silica/pure water interface is underexplored computationally, with some arguing that the character of the interface should be qualitatively the same as the quartz/water interface. Borguet *et. al.*, for example, cited the similar points of zero charge (PZCs) and dissolution behaviours of quartz and amorphous silica as the justification for this hypothesis.⁵¹ However, Costa and co-workers disproved this hypothesis in a recent comparative AIMD study of the quartz(0001)/water and amorphous silica/water interfaces, where distinct structural behaviors of the interfacial water were observed.⁸⁹ Indeed, to the best of our knowledge, there has been only one atomistic MD study of the interface between electrolyte solution and the planar amorphous silica interface.¹⁰⁰ This study, conducted in 2014, explored the interfaces made between amorphous silica and two aqueous electrolytes: NaCl M and CsCl M, both at 0.35 M 'bulk' ion concentration. The surface charge density was -0.208 C m^{-2} and corresponded to pH 10-11, a higher pH than is relevant for EOR from sandstone reservoirs geochemically and physiologically. Net water orientation and ion/water density was recorded as a function of z -distance (vertical distance) from the silica surface. Chapter 4 of this thesis explores ion and water structure at the aqueous electrolyte/amorphous silica interfaces for four aqueous electrolytes (NaCl, KCl, CaCl_2 and MgCl_2) at two 'bulk' ion concentrations (0.1 M and 0.3 M) when the amorphous silica surface had a charge density of -0.136 C m^{-2} (*i.e.* pH 5.5, a geochemically relevant pH), as determined using atomistic MD.

1.7.2 Chapter 5

Some experimental studies have focused on the concentration-dependence of molecular adsorption at the aqueous electrolyte/amorphous silica interface. In 2012, Dreschler *et al.* used AFM to study the adhesion of a P2VP brush to silica microparticles in aqueous KCl at various ionic strengths. The adhesion of the $-CH_3$ and $-COOH$ functionalities at the interface between amorphous silica and artificial seawater (ASW) at two concentrations was investigated using CFM-AFM.⁸ The latter study was designed to probe the underlying mechanism of the 'low salinity' (LS) effect - a phenomenon whereby oil yields from sandstone reservoirs are significantly increased when diluted seawater is used for water flooding. While many computational studies have concerned molecular adsorption at the silica/pure water interface, none have featured aqueous electrolyte, let alone investigated a concentration-dependence on molecular adsorption. The LS effect at the interface between aqueous NaCl/CaCl₂ and the clay mineral montmorillonite has, however, been investigated by atomistic MD simulation.¹¹ Chapter 5 outlines our combined experimental (CFM-AFM) - computational (atomistic MD) study of the adsorption of the NH_3^+ functionality to the amorphous silica/aqueous electrolyte interface (the interaction of the $COOH/COO^-$ functionality was investigated by experiment only), where the interfacial systems are the same as those explored in Chapter 4.

1.7.3 Chapter 6

While a methylammonium molecule is used to investigate the adsorption of the NH_3^+ group to the amorphous silica/aqueous electrolyte interface in the simulation part of Chapter 5, the adsorption of an array of NH_3^+ -terminated hydrocarbons is the remit of Chapter 6. This array of molecules is a more sophisticated model of the functionalised AFM tip compared to the methylammonium molecule. Computational studies of the interaction of any kind chemical surface with model functionalised AFM tips composed of multiple molecules are rare.^{7,162}

Chapter 2

Methods

The main methods used are atomistic simulation and chemical force mapping atomic force microscopy (CFM-AFM). There is great potential to use the two techniques together, with CFM-AFM providing initial insight into which systems it would be interesting to study at a greater level of detail using atomistic simulation. In this section, first the simulation, then CFM-AFM will be covered.

2.1 Simulation Methods

2.1.1 Simulation Background

Introduction

The aim of molecular modelling is to add insight and/or to predict properties of chemical systems. On the macroscopic scale, as in experimental measurements, the system contains extremely large numbers of atoms, with an enormous number of minima in the potential energy surface (defined in section 2.1.1). In computer simulation, a small replication of the full experimental system is considered with computationally-managable numbers of atoms. Representative configurations of the system are generated from simulation (how this is done is discussed in section 2.1.1) and averages of macroscopic properties can be calculated by averaging over a large enough set of configurations (as discussed further in section 2.1.1). Molecular modelling is particularly useful in systems that are hard to probe and characterise experimentally, such as the

mineral/water interface.

In a simulation, the first step is to set-up a starting configuration for a system. This starting configuration is defined by considering a set of atoms. In molecular mechanics force-fields, each have a set of xyz-coordinates, charges (for calculating non-bonded electrostatic terms), epsilon and sigma pairs (for calculating Van der Waals interactions). The relationship between 2, 3 or 4 connected atoms is defined by bonding, angle bending and dihedral terms respectively. The next section, Section 2.1.1, describes this process - the generation of a potential energy surface - in more detail.

Generation of Potential Energy Surfaces: Molecular Mechanics Force-Fields

Molecular mechanics force-fields are functions that are used to generate potential energy surfaces. All of the force-fields used within the work of this thesis, CHARMM,¹¹¹ TIPS3P,¹⁰² SPC/Fw¹²⁶ and that developed by Butenuth *et. al.* to describe the natively oxidised silicon surface,¹ are atomistic. Within such force-fields, the system is made up of atoms, each represented as a point mass with a fixed charge. The interactions between the system's constituent atoms are divided into two broad categories: bonded and non-bonded.

Bonded Terms

A common feature to all the bonded terms is that there is an energy penalty when the bond length, bond angle, etc deviates from a preferred reference value.

1. Bond Stretching

In all the force-fields used, a harmonic potential describes the bond stretching that occurs between pairs of directly connected atoms:

$$V_{bond}(r_{ij}) = \frac{1}{2}k_{ij}^b(r_{ij} - r_{ij}^0)^2 \quad (2.1)$$

where r_{ij} is the distance between the pair of directly bonded atoms **i** and **j**, k_{ij}^b is the bond-stretching force constant and r_{ij}^0 is the reference bond length. This is shown schematically in Figure 2.1.

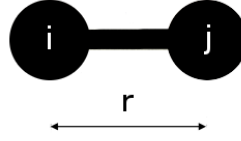


Figure 2.1: Schematic of the bond between atoms **i** and **j**.

2. Angle Bending

In a similar manner to the bond stretching description, the force-fields for silica and water (TIP3P and SPC/Fw) used a simple harmonic potential to describe angle bending:

$$V_{angle}(\theta_{ijk}) = \frac{1}{2}k_{ij}^{\theta}(\theta_{ijk} - \theta_{ijk}^0)^2 \quad (2.2)$$

where θ_{ijk} is the angle between the three connected atoms **i**, **j** and **k**, k_{ijk}^b is the angle bending force constant and θ_{ijk}^0 is the reference angle.

In CHARMM however, angle bending is modelled using the more complex Urey-Bradley potential, encompassing a harmonic bond stretching correction term between atoms **i** and **k** in addition to the harmonic potential for angle bending given in equation 2.2:

$$V_{angle}(\theta_{ijk}) = \frac{1}{2}k_{ij}^{\theta}(\theta_{ijk} - \theta_{ijk}^0)^2 + \frac{1}{2}k_{ik}^b(r_{ik} - r_{ik}^0)^2 \quad (2.3)$$

where r_{ik} is the distance between the atoms **i** and **k**, k_{ik}^b is the 'bond'-stretching force constant, r_{ik}^0 is the reference 'bond' length between atoms **i** and **k**, θ_{ijk} is the angle between the three connected atoms **i**, **j** and **k**, k_{ijk}^b is the angle bending force constant and θ_{ijk}^0 is the reference angle. This is shown schematically in Figure 2.2.

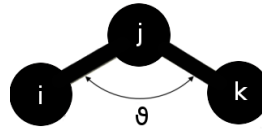


Figure 2.2: Schematic of the angle made between the atoms **i**, **j** and **k**

3. Proper and Improper Dihedral Angles

In CHARMM, proper dihedrals are modelled by a periodic cosine function:

$$V_{properdihedral}(\phi_{ijkl}) = \frac{1}{2}k_{ijkl}^{\phi}(1 + \cos(n\phi_{ijkl} - \phi_{ijkl}^0)) \quad (2.4)$$

where k_{ijkl}^{ϕ} is the dihedral force constant, ϕ_{ijkl}^0 is the reference dihedral angle and n is the multiplicity. Figure 2.3 shows that ϕ_{ijkl} is the angle between the plane defined by atoms **i**, **j** and **k** and the plane defined by atoms **j**, **k** and **l**. This is shown schematically in Figure 2.3.

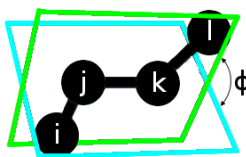


Figure 2.3: Schematic of a proper dihedral angle.

Improper dihedrals are used to preserve the planarity of planar groups such as aromatic rings and, for chiral molecules, to maintain a particular handedness. Such angles are modelled using a harmonic potential:

$$V_{improperdihedral}(\xi_{ijkl}) = \frac{1}{2}k_{ijkl}^{\xi}(\xi_{ijkl} - \xi_{ijkl}^0)^2 \quad (2.5)$$

where k_{ijkl}^{ξ} is the force constant and ξ_{ijkl}^0 the reference angle for the improper dihedral. As with ϕ_{ijkl} , ξ_{ijkl} is The torsional angle ξ_{ijkl} , the angle between planes defined by the two sets of atoms, **i**, **j** and **k** and **j**, **k** and **l**, is shown schematically in Figure 2.4. This is shown schematically in Figure 2.4.

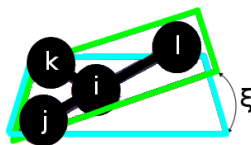


Figure 2.4: Schematic of an improper dihedral angle.

Nonbonded Terms

1. Van der Waals Interactions

The 12-6 Lennard-Jones potential is used to represent van der Waals interactions:

$$V(r_{ij}) = 4\epsilon_{ij} \left[\left(\frac{\sigma_{ij}}{r} \right)^{12} - \left(\frac{\sigma_{ij}}{r} \right)^6 \right] \quad (2.6)$$

where r_{ij} is the distance between atoms **i** and **j**, ϵ_{ij} is a measure of the strength of the attraction between the two atoms **i** and **j** and σ_{ij} is equal to the internuclear distance of the two non-bonding atoms **i** and **j** at 'closest' contact and, as a result, is often referred to as the van der Waals diameter. This is shown schematically in Figure 2.5.

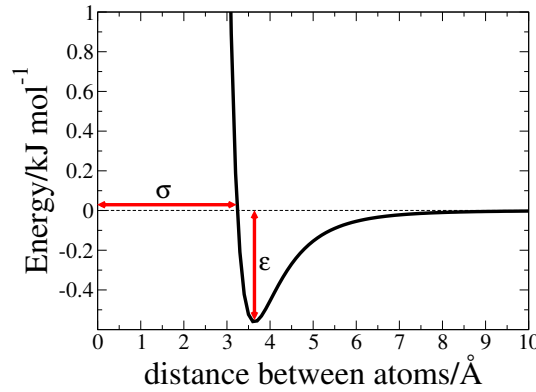


Figure 2.5: Exemplar Lennard-Jones Potential Energy Curve.

For all the force-fields used, each atom is assigned particular σ and ϵ values, which are combined to describe the interaction between pairs of atoms using the Lorentz-Bertholot mixing rules:

$$\sigma_{ij} = \frac{1}{2}(\sigma_i + \sigma_j) \quad (2.7)$$

$$\epsilon_{ij} = (\epsilon_i \epsilon_j)^{\frac{1}{2}} \quad (2.8)$$

Particular care should be taken when mixing potentials that correspond to different types of bonding, such as biomolecules and inorganic materials. Indeed, the Butenuth *et. al.* force-field for silica¹ used in this work was specifically parameterised to be used

in combination with standard biomolecular force-fields including CHARMM. An exemplar Lennard-Jones potential is shown schematically in Figure 2.5. The attractive r^{-6} term dominates after the minimum of the curve, while at shorter distances the repulsive r^{-12} term is prevalent. Furthermore, van der Waals forces are short range and tend towards zero at relatively short atom-atom separations. The extremely small forces between atoms beyond a certain spherical cut-off distance, in our work 10 Å, are normally not calculated, as the inclusion of such interactions would significantly decrease computational efficiency whilst having negligible impact on the overall potential energy surface.

2. Electrostatic Interactions

The electrostatic force between atoms **i** and **j** is represented by the Coulomb potential:

$$U(r_{ij}) = \frac{q_i q_j}{4\pi\epsilon_0 r_{ij}} \quad (2.9)$$

where q_i and q_j are the charges of atoms **i** and **j** and ϵ_0 is the permittivity of free space. In contrast to the van der Waals interactions, electrostatic forces are long-range and the simple truncation of the Coulomb potential by a spherical distance cut-off would result in severe artifacts. Instead, the Particle Mesh Ewald (PME) method (described in detail by Darden *et. al.*¹⁸⁴), a computationally efficient form of Ewald summation,^{185,186} was implemented.

The calculation of both van der Waals and electrostatic interactions involves spherical distance cutoffs. Since the system is dynamic, the atoms within the cutoff for a particular atom, 'neighbouring atoms', will change with time. However, an atoms 'neighbours' are unlikely to change every timestep and so for computational efficiency, the identity of the neighbours is evaluated every 10 timesteps.

Molecular Dynamics (MD)

Preparation: Minimisation of the Initial Configuration

It is very common for atoms to 'overlap', *i.e.* for pairs of atoms **i** and **j** to be closer than the distance σ_{ij} in the initial created system configuration and the forces between

the atoms can be extremely high. The implementation of Molecular Dynamics (MD) at this stage would be likely to fail. Thus, a common first step is to perform a local minimisation procedure. Steepest Descent Minimisation is the most frequently employed optimisation method in the work of this thesis. In this algorithm, the system undergoes an initial displacement, h_0 , in the direction of the most negative gradient of the potential energy surface:

$$\mathbf{r}_{n+1} = \mathbf{r}_n + \frac{\mathbf{F}_n}{\max(|\mathbf{F}_n|)} h_n \quad (2.10)$$

where \mathbf{r}_{n+1} are the new atomic coordinates, \mathbf{r}_n are the old atomic coordinates, \mathbf{F}_n is the force and $|\mathbf{F}_n|$ is the largest of the absolute values of the force components. If ($V_{n+1} < V_n$) (where V is the potential energy) then the new positions are accepted and $h_{n+1} = 1.2 h_n$. Otherwise, the original positions are retained and $h_{n+1} = 0.2 h_n$. The process is iterated for either a predefined number of iterations or until the potential energy is below a certain threshold. A second optimisation algorithm, conjugate gradient,¹⁸⁷ is used in our work to a lesser extent. This uses information about the force calculated in previous steps and is particularly effective when the system is close to a local minimum (see Figure 2.7).

Molecular Dynamics (MD): Solving Newton's Equation of Motion

Molecular dynamics (MD) is a method of exploring the PEL. In MD, a time evolution of the system of interacting atoms is obtained by solving Newton's classical equations of motion:

$$m_i \frac{\delta^2 \mathbf{r}_i}{\delta t^2} = \mathbf{F}_i, i = 1 \dots N. \quad (2.11)$$

where m_i is the mass of atom \mathbf{i} , \mathbf{r}_i is the position of atom \mathbf{i} , t is time, \mathbf{F}_i is the force on atom \mathbf{i} and N is the total number atoms in the system.

The forces are the negative derivative of the potential $V(\mathbf{r}_1, \mathbf{r}_2, \dots, \mathbf{r}_N)$:

$$\mathbf{F}_i = -\frac{\delta V}{\delta \mathbf{r}_i} \quad (2.12)$$

where V is the potential energy.

The basic MD protocol is to:

1. Assign velocities to the atoms of the optimised initial configuration according to the Boltzmann distribution.
2. Calculate the forces acting on all atoms using the model for the potential energy surface.
3. Calculate the new positions of the atoms after a small timestep, for example 1 fs.
4. Output the values of physical properties, such as atom positions and velocities.
5. Repeat steps 2-4.

Leapfrog Integration Algorithm

Integration algorithms assume that the atomic positions can be approximated by a Taylor series expansion:

$$r_i(t + \delta t) = r_i(t) + v_i(t)\delta t + \frac{1}{2}a_i(t)\delta t^2 + \dots \quad (2.13)$$

$$r_i(t - \delta t) = r_i(t) - v_i(t)\delta t + \frac{1}{2}a_i(t)\delta t^2 - \dots \quad (2.14)$$

where v_i is the velocity of atom \mathbf{i} and a_i is the acceleration of atom \mathbf{i} .

By taking the difference between equations 2.13 and 2.14, the velocity at time \mathbf{t} is thus:

$$v_i(t) = \frac{r_i(t + \delta t) - r_i(t - \delta t)}{2\delta t} \quad (2.15)$$

In a similar manner:

$$v_i(t - \frac{\delta t}{2}) = \frac{r_i(t) - r_i(t - \delta t)}{\delta t} \quad (2.16)$$

$$v_i(t + \frac{\delta t}{2}) = \frac{r_i(t + \delta t) - r_i(t)}{\delta t} \quad (2.17)$$

Equation 2.17 can be rearranged to give:

$$r_i(t + \delta t) = r_i(t) + v_i(t + \frac{\delta t}{2})\delta t \quad (2.18)$$

Equation 2.17 - equation 2.18 leads to a way of calculating the half time step velocities:

$$v_i(t + \frac{\delta t}{2}) = v_i(t - \frac{\delta t}{2}) + a\delta t \quad (2.19)$$

In the leapfrog algorithm, velocities are calculated at $(t + \frac{\delta t}{2})$ using equation 2.19. These velocities are then used in equation 2.18 to calculate the atomic positions at time $(t + \delta t)$.

Ensembles

In order to conserve energy over the course of the simulation, ensembles are used. The canonical (*i.e.* *NVT*) and isothermal-isobaric (*i.e.* *NPT*) ensembles are commonly employed in simulations studies and are used in this work. The three specified physical properties in each ensemble remain constant throughout the simulation. *N* is the number of atoms, *T* is the temperature, *P* is the pressure and *V* is the volume. When the volume is kept constant, the pressure changes and *vice versa*. Temperature is controlled using thermostats and pressure is controlled using barostats. For most real-life applications, the *NPT* ensemble is most appropriate, as temperature and pressure are generally known.

Periodic Boundary Conditions

The number of atoms that make up a system is limited by the execution speed of the calculation. Computational feasibility makes it desirable to study small systems. Indeed, a particular challenge faced by computational chemists is to simulate bulk matter (10^{23} atoms) with a much lower number of atoms. However, if the simulated system were a simple box of a small number of molecules, the proportion of molecules at the surface would be significant compared to those in the bulk and surface effects would dominate. For example, if 1000 molecules were arranged in a 10×10 cube, almost 50 % (488) would appear at the faces of the cube. In order to overcome this problem periodic boundary conditions are implemented. The simulation box is surrounded by an infinite array of its periodic images, as shown in Figure 2.6 and thus there are no walls

or surface molecules. The molecules in all of the boxes will undergo exactly the same movement and movement between boxes is possible. So if a molecule moves from the central box in to a neighbouring box, it will be replaced by its image from another box. This periodicity has an impact on the choice of the size of the cutoff for non-bonded interactions. In order to stop a particle and its own image interacting with the same particle, the *minimum image convention*, which states that the cutoffs should not be greater than half of the shortest box vector, is invoked.

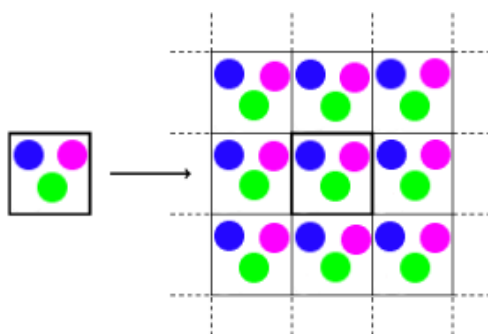


Figure 2.6: Schematic of periodic boundary conditions.

Exploration of the Potential Energy Landscape (PEL)

The relation of microscopic properties, such as atomic positions and velocities, to macroscopic quantities like temperature and pressure is the remit of statistical mechanics. Such atomic positions can be thought of as coordinates on a multidimensional potential energy landscape (PEL), as shown in Figure 2.7. In molecular mechanics methods (used in the work of this thesis) and the vast majority of electronic structure methods, the Born-Oppenheimer approximation, which states that electrons rapidly adjust to any changes in nuclear positions as a result of their small mass relative to that of the nuclei, is invoked. Thus, the atomic positions are more precisely defined as nuclear coordinates. This approximation is sufficient when the investigation does not depend critically on changes in electronic structure and makes feasible the study of larger systems over long time periods compared to *ab initio* electronic structure methods, which are commonly limited to smaller, static systems. One particular extension of molecular mechanics MD is *ab initio* molecular dynamics (AIMD), which represents a pseudo-

relaxation of the Born-Oppenheimer approximation, in that both electronic and nuclear degrees of freedom are treated, albeit under approximate coupling.

The probability of the occurrence of a certain microstate, *i.e.* a particular set of nuclear coordinates, is proportional to the Boltzmann distribution:

$$p \propto e^{\frac{-U}{k_B T}} \quad (2.20)$$

where U is the potential energy, k_B is Boltzmann's constant and T is the temperature. An important feature of this relation is that the lower the energy of a microstate, the more probable it will be. Minima in the PEL correspond to stable states, where the system can become trapped if there is not sufficient energy for the system to surpass a barrier from one minima to another. The goal is to explore the important parts of the PEL with the correct weighting to obtain averages that reproduce experimental observables.

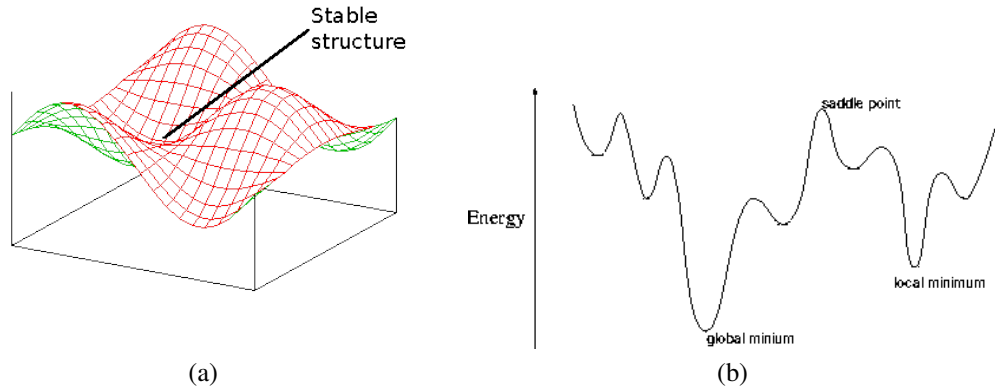


Figure 2.7: Schematics of a potential energy landscape (PEL): 3D (left) and 2D (right) representations.

Advanced Sampling Techniques

The accurate prediction of macroscopic properties from microscopic simulation is reliant on the thorough exploration of the PEL. It is, however, common for a system to become kinetically trapped in the minima of the landscape and advanced sampling techniques, such as replica exchange with solute tempering (REST) and replica exchange with molecular dynamics (REMD), have been developed to overcome this issue and

increase the sampling of the landscape within timescales currently accessible to simulation.

Temperature Replica-Exchange Molecular Dynamics (T-REMD)

In Temperature Replica-Exchange Molecular Dynamics (T-REMD),¹⁸⁸ simulations of a series of non-interacting replicas of the system are run in parallel at different temperatures. The lowest temperature simulation is used to furnish the thermodynamic ensemble data, whilst those at higher temperatures enable barrier crossing. Exchanges are attempted between replicas at regular, defined intervals (*i.e.* after a set number of timesteps from the last exchange attempt). The probability of acceptance of an exchange attempt between replicas **i** and **j** in the *NPT* ensemble is given by:

$$P(i \leftrightarrow j) = \min \left(1, \exp - \left[\left(\frac{1}{k_B T_i} - \frac{1}{k_B T_j} \right) (U_i - U_j) + \left(\frac{P_i}{k_B T_i} - \frac{P_j}{k_B T_j} \right) (V_i - V_j) \right] \right) \quad (2.21)$$

where k_B is Boltzmann's constant, T_i and T_j are the reference temperatures, U_i and U_j are the instantaneous potential energies, P_i and P_j are the reference pressures and V_i and V_j are the instantaneous volumes of replicas **i** and **j**. The spacing between the temperatures is chosen so that there is some overlap of the potential energy distributions of neighbouring replicas. If there were zero overlap, there would be a zero probability of exchange.

Replica Exchange with Solute Tempering (REST)

Replica Exchange with Solute Tempering (REST)¹⁸⁹ is a form of Hamiltonian-(H)-REMD. Although H-REMD uses replicas that correspond to slightly different Hamiltonians or, in other words potential functions, rather than temperature, the underlying principles are the same as T-REMD. In the REST variant of H-REMD, the potential energy scales with temperature in such a way that the part of the system of interest, usually a biological molecule such as a protein, behaves as if it were experiencing an increased temperature, while the water remains at the lowest temperature. In this thesis, surface-adsorbed ions and some of those in solution are the part of the system of

interest. The potential energy of replica **m** was scaled according to:

$$U_m(X) = U_p(X) + \left[\frac{\beta_0}{\beta_m} \right] U_{ww}(X) + \left[\frac{\beta_0 + \beta_m}{2\beta_m} \right] U_{pw}(X) \quad (2.22)$$

where $\beta_m = \frac{1}{k_B T}$, k_B is Boltzmann's constant, T is temperature and the interactions of the system are represented by U_p (those within surface adsorbed ions and a certain number of ions in solution, denoted **p**), U_{ww} (those within water, remainder of ions, silica surface and methylammonium molecule, denoted **w**) and U_{pw} (those between group **p** and group **w**). In the original REST method,¹⁸⁹ the spacing between the different replicas is uniform. However, a more recently developed and more efficient variant uses a non-uniform spacing between replicas¹⁰ and our REST simulations were implemented using the method of Terakawa *et. al.*¹⁹⁰

The impetus for the implementation of REST in our work was to obtain a more reliable estimate of the equilibrium distribution of the various long-lived adsorption site configurations, sites which involved differing numbers and identities of ions.

Free Energy Methods

Metadynamics

Metadynamics (MetaD)¹⁹¹ is an algorithm used to reconstruct the free energy as a function of one or more collective variables (CVs). The CVs describe the state of the system as a function of atomic coordinates, and could be, for example, the vertical distance between the centre of mass of a protein and a surface. An external potential, $V_G(\mathbf{r}^N, t)$ is built up throughout the simulation by the deposition of Gaussians on the PEL, $U(\mathbf{r}^N)$:

$$V_G(\mathbf{r}^N, t) = w \sum_{[t'=\tau_G, 2\tau_G, \dots, (t' < t)]} \prod_{i=1}^d \exp \left(- \frac{s_i((\mathbf{r}^N(t)) - s_i(\mathbf{r}^N(t'))^2)}{2\sigma_i^2} \right) \quad (2.23)$$

where $s_i(\mathbf{r}^N(t))$ is the value of the i th CV at time t , d is the number of CVs, w is the height and σ the width of Gaussians deposited in the simulation and τ_G is the frequency at which Gaussians are deposited. This bias potential forces the system away from areas of the PEL it has already visited and, over time, enables the crossing of potential energy barriers, sometimes insurmountable within feasible timescales in the unbiased

PEL. If the simulation is run for a sufficient amount of time, the sum of the Gaussians can provide a good estimate of the free energy surface (FES):

$$V_G(\mathbf{r}^N), t) \approx -G(\mathbf{r}^N) \quad (2.24)$$

The accuracy of the recovered FES is limited by the Gaussian height, w . Well-tempered (WT) metadynamics¹⁹² was developed as a method of circumventing this issue. In WT-metaD,¹⁹² w is rescaled, gradually decreasing, during the simulation according to:

$$W = W_0 e^{-\frac{V(\mathbf{r}^N, t)}{k_B \Delta T}} \quad (2.25)$$

where W_0 is the initial Gaussian height and ΔT is related to the bias factor, $\frac{(T+\Delta T)}{T}$, and has the dimension of temperature. In this method, the FES converges much more smoothly compared to standard metaD.

Potential of Mean Force

The FES can be calculated using the relation:

$$\Delta G(z) = \int \langle F(z') \rangle dz' \quad (2.26)$$

where z' is the reaction coordinate of interest (*e.g.* the vertical distance from the surface), ΔG is the free energy change for the transition of the system from $z'=0$ to $z'=z$ (*e.g.* the free energy of adsorption of a molecule to a surface) and $\langle F(z') \rangle$ is the average force needed to constrain the system at z' .¹⁹³ In the calculation of the free energy of adsorption, the major focus of the work of this thesis, the adsorbate is typically constrained at a series of distances from the surface. The spacing between distances smaller in the region of minima of the profile compared to large molecule-surface separations where the constraint force is negligible and the profile is not undergoing rapid change.

2.1.2 Simulation Setup

General Simulation Setup

Simulations were carried out using the Gromacs package¹⁹⁴ (version 4.5.5 for Chapter 3 and version 4.5.1 for Chapter 4-6). The PLUMED plugin¹⁹⁵ was used for metaD simulations (Chapter 5). The CHARMM27 force-field¹¹¹ was used to model gold, electrolyte ions and organic molecules, methylammonium, the peptides RGD and SPT and long chain hydrocarbon thiols ((11-amino-1-undecanethiol molecules) terminated by the NH_3^+ functionality. Water was modelled exclusively by TIPS3P¹⁰² apart from one series of REMD simulations where it was modelled using SPC/Fw¹²⁶ (Chapter 3). The natively oxidized silicon surface was described using a force-field reported by Butenuth *et. al*¹ (Chapter 4-6). This force-field was chosen because it had been developed specifically for use with common biomolecule force-fields, such as CHARMM. It should be noted that it is particularly challenging to generate Ca^{2+} /water force-fields that capture all the relevant physical properties. Mamatkulov *et. al.* overviewed the performance of a collection of parameter sets and demonstrated that properties, such as the solvation free energy, for the same ion can differ significantly with force-field.¹⁹⁶ Force-field parameters are often optimized from the single ion properties in solution or the crystalline state and, in practice, fail to reproduce electrolyte thermodynamic properties at finite concentrations. We use a non-polarizable water model in this work. Non-bonded force-field parameters are explicitly stated in Tables A.1-A.13.

The xyz-coordinates of the atoms of silica surface were the same as those used by Butenuth *et. al.*¹ Organic molecules were constructed using TINKER (peptides), Gaussview (long-chain hydrocarbon thiols) and the CHARMM small molecule library (methylammonium).^{197, 198, 111, 199} The Gromacs program, genbox, was used to add ions and an equilibrated box of water to the simulation cell containing silica and organic molecules.¹⁹⁴ A spherical cutoff was used to truncate the Lennard-Jones interactions (cutoff radius = 12 Å (Chapter 3) and 10 Å (Chapter 4-6)).²⁰⁰ The particle mesh Ewald (PME) method was used to treat the Coulombic interactions, with a real-space precision cutoff of 12 Å (Chapter 3) and 10 Å (Chapter 4-6).¹⁸⁴ The Lorentz-Berthelot mixing rules were used to compute inter-force-field Lennard-Jones parameters.²⁰⁰ With the exception of higher temperature replicas in REMD and REST, all simulations were run at 300 K, using a Nosé-Hoover thermostat,^{201, 202} with a coupling constant of 0.2 ps.

When the *NPT* ensemble was used, the pressure was generally coupled isotropically to 1 bar using the Parrinello-Rahman scheme, with a coupling constant of 1 ps.^{203,204} The *NVT* ensemble was always used for the interfacial simulations. In the REMD simulations, however, the Berendsen barostat was used, with a coupling constant of 5 ps.²⁰⁵ A time step of 1 fs was used throughout. Coordinates were saved every 1 ps for later analyses. Cubic periodic boundary conditions were employed in all 3 dimensions.

Simulations were visualised using VMD.²⁰⁶ Calculations were run using 6 compute nodes with 12 cores per node. Cores were Intel Xeon X5650 Westmere 2.66 GHz cores and there were 24 GB per node. A QLogic TrueScale InfiniBand interconnect was used. There was negligible decrease in efficiency compared to when one compute node was used.

Replica Exchange Molecular Dynamics (REMD) (Chapter 3)

Four T-REMD¹⁸⁸ simulations were carried out. In each, one peptide chain (either RGD or SPT) was solvated in a simulation cell containing water: one using the TIPS3P model and the other using SPC/Fw. The initial structure of RGD and SPT was built using the protein module in the TINKER software package,¹⁹⁷ with standard side-chain protonation states corresponding to pH ~ 7 . The N- and C- termini were modelled as uncapped and zwitterionic (*i.e.* as NH_3^+ and COO^- , respectively). All bonds in our simulations were free to vibrate, with the exception of the water OH bond in the case of the TIPS3P water model. The peptide was solvated with 882 explicit water molecules in the TIPS3P case and 895 molecules in the SPC/Fw case. For both water models, the cubic cell size had a dimension of ~ 30 Å.

The interval between exchange attempts between the replicas was 5 ps in both the TIPS3P and SPC/Fw simulations. Simulations were carried out for 50 million time steps (*i.e.* 50 ns) in total. For the TIPS3P system, we simulated 12 replicas at the following temperatures (in K): 298, 304, 311, 318, 325, 331, 338, 346, 353, 360, 368 and 375. For the SPC/Fw system, 12 replicas were simulated at the following temperatures (in K): 298, 304, 310, 317, 324, 330, 336, 343, 350, 357, 364 and 371. Both sets of temperatures were determined using an online temperature generator for REMD simulations.²⁰⁷ The temperature sets are slightly different in order to maintain the same exchange probability of ~ 0.25 in both the TIPS3P and SPC/Fw cases; this is due to the

TIPS3P model being rigid and the SPC/Fw flexible.

To generate the starting configurations for each replica, we carried out a 3 ns MD simulation at 300 K of the geometry optimised peptide in TIPS3P water and conducted clustering analysis²⁰⁸ over the peptide for this trajectory (the clustering method is the same as that described in the 'Cluster analysis' section below), setting the clustering root-mean squared deviation (RMSD) in backbone atom positions cut-off such that six clusters were identified in total. Each of the six representative peptide structures was then duplicated to make a total of 12 structures for our 12 replicas. These 12 structures were then used in the same running order, from lowest to highest temperature replica, for both the TIPS3P and SPC/Fw runs. To generate the starting configurations for each replica in the REMD run, in each case (either SPC/Fw or TIPS3P), each of the 12 structures was geometry optimised and then equilibrated in the *NPT* ensemble for a total of 200 ps at their target temperatures. The lowest temperature trajectories (298 K) were analysed.

In Chapter 5, the attempted REST simulations used the same interval between exchange attempts, 5 ps. Further REST details are given within the Chapter.

Simulation of the Aqueous Electrolyte/Silica Interface (Chapter 4-6)

Eight different electrolyte solutions were modeled: NaCl, KCl, CaCl₂ and MgCl₂, each at two different concentrations (HS, 0.3 M and LS, 0.1 M). For each of the HS and LS systems, the number of cations was consistent. A sufficient number of cations were introduced to balance the $-32e$ surface charge on the amorphous silica surface and then an additional 10 cations and a stoichiometrically equivalent number of anions were added for the LS system and 50 cations (with anions) for the HS system. As will be shown below, there was a substantial surface excess of electrolyte ions at the silica surface, and this 5-fold increase in the number of ions was needed to give a 3-fold increase in the concentration of ions in the bulk (*i.e. middle*) region of the water layer. In Chapters 4 and 5, the natively oxidised silicon substrate was set up with 2016 atoms, with the surface parallel with the $x - y$ plane; by convention, we take this to be the horizontal plane. Both the top and bottom surfaces of the substrate were identical. The slab consisted of a 4×4 super-cell, where each repeat unit featured one deprotonated oxygen (vicinal to a hydroxyl group), three hydroxyl groups and bridging oxygens. The

atomistic structure of our slab model is shown in Figure 2.8 As for all mineral surfaces, amorphous silica is difficult to characterize because in spite of rigorous surface preparation, exposure to air or solutions leads to the adsorption of adventitious carbon.²⁰⁹ This means we cannot yet compare the model results directly with data from experimental surfaces and, although not the case here, adventitious contamination can also lead to problems with the reproducibility of experimental results. All Si and O atoms in the solid slab were immobilized but the H atoms were allowed to move in response to the force-field. The surface charge density of the natively oxidized silicon substrate was -0.136 C m^{-2} , as used by Butenuth *et. al.*, with $-16e$ charge on each of the two surfaces of the slab substrate. This corresponds to the charge state observed at pH 5.5, as used in our experiments. The lateral cell dimensions were $43.4880 \text{ \AA} \times 43.4880 \text{ \AA}$. The dimension perpendicular to the cell plane - the z -dimension - was 159.3424 \AA to provide an ample inter-slab space to be filled with liquid electrolyte solution. The three xyz dimensions were the same for all aqueous electrolytes at both concentrations. Since the simulations were carried out in the NVT ensemble, the dimensions did not change. It should be noted that these systems are not appropriate for isotropic pressure response in the NPT ensemble, as the majority of the atoms of the silica slab (all bar the hydrogen atoms of silanols) are rigid, a slab which is infinite in the xy -plane. The changes in volume that would occur in the NPT ensemble would thus not be appropriate in the xy -plane. In Chapter 6, the $x - y$ dimensions of the silica substrate was $1.5\times$ the size, with 4536 atoms and lateral cell dimensions of $65.2320 \text{ \AA} \times 65.2320 \text{ \AA}$. The slab was first increased by extending the system in the x dimension by half of the initial super-cell, followed by the subsequent extension in the y dimension by half of the resultant super-cell. The equilibrated electrolyte solution that filled the interslab space was also replicated in this manner to produced the system of increased size.

Development and Validation of the Silica Force-Field

The natively-oxidized silicon force-field was developed by Butenuth *et. al.*, with that of Cole and co-workers used as the basis for the force-field.^{1,210} The adsorption of oxygen and water molecules to a Si(001) surface was investigated by DFT (defined in section 1.5.3) and a natively-oxidised silicon surface generated.²¹⁰ Seven oxygen and two water molecules adsorped and the resulting hydroxyl group concentration, 1.2 OH/nm^2 , was consistent with experimentally determined values at the amorphous silica surface,

which ranged between 2.6 and 4.6 OH/nm².^{211,212} Atomic charges were parameterised by Bader charge analysis (as described by Tang *et. al.*²¹³) followed by fitting to the electrostatic potential - the potential energy that a unit of point charge would have at a particular point in space - formed by the *ab initio* (defined in section 2.1.1) electron density. The Lennard-Jones parameters for the Coulomb interaction between water and the silica surface were augmented to match as closely as possible interaction energy vs distance curves determined by DFT over a number of different surface sites, such as deprotonated silanols. Finite size effects were not probed. The computed heat of immersion compared well to experimentally determined values.

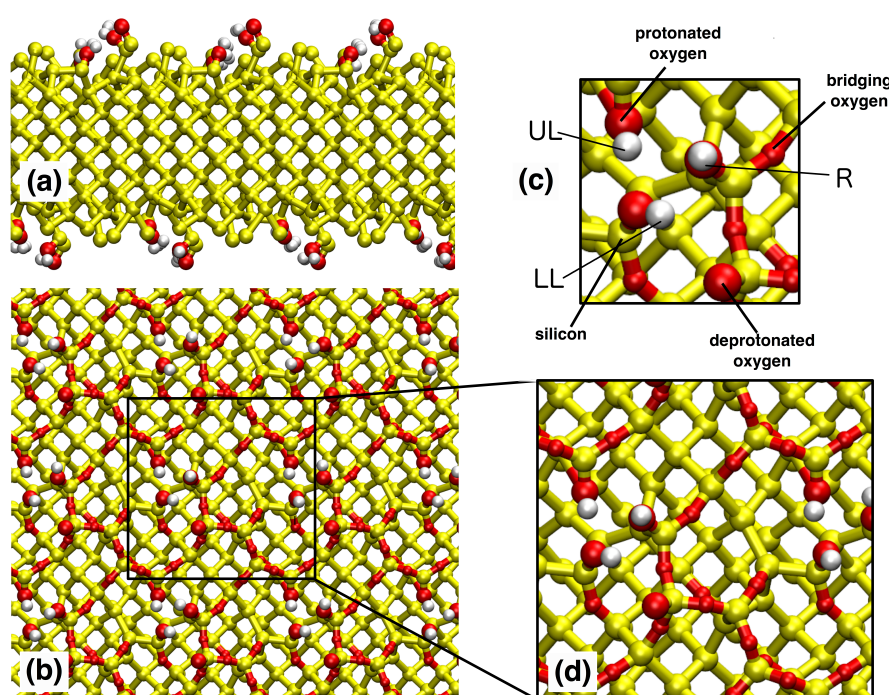


Figure 2.8: Structure of the model amorphous silica surface used in the MD simulations: (a) side on view (b) view of the surface in the *xy*-plane (c) zoomed in side-on view (d) zoomed in view of the surface in the *xy*-plane. The different types of silanol are denoted UL, LL and R, as labelled.

It should be noted that the amorphous silica slab is not far removed from a clay mineral and the charge is somewhere between illite and montmorillonite. The clay literature, thus, would present a large amount of comparable data, albeit attained on a perfectly flat basal surface. Although amorphous silica and quartz, a crystalline form

of silica, are both composed of SiO_4 tetragonal coordination and SiO_2 bridging, there are differences between the two forms of silica. The key distinguishing feature relates to order; while there may be some short range order in the amorphous form, there is definitely not the long-range order that exists in the crystalline form, with a predictable and repeating arrangement of atoms.

Equilibration Simulations

The electrolyte ions were initially positioned randomly in the solution in the inter-slab space. The water density was then corrected by changing the number of water molecules and repeating the minimization and equilibration stages until the bulk water density in the centre of the inter-slab space was the same as the water density obtained from a *NPT* simulation of a bulk liquid system (without the surface present) made up of the same composition of ions and water molecules. The number of water molecules in each system differed depending on the electrolyte type and concentration, but was ~ 9000 in each case (the exact numbers are listed in Table C.1). MD simulations were run until ion density profiles had equilibrated (between 80-140 ns; the equilibration time for each case is provided in Table 2.2). After equilibration, simulations were run for a further production phase (40-60 ns, see Table 2.2 for details) for analysis. For the work of Chapter 5, the methylammonium molecule was inserted into the final configuration of each of the equilibrated systems. No further water density correction was necessary. We then minimized the potential energy of the full system and carried out further equilibration in the *NVT* ensemble for 200 ps. The final system configuration formed the input file for the metadynamics production runs.

Preparation of Model CFM-AFM tip

For the work of Chapter 6, a model tip that encompassed a gold substrate and 20 adsorbed $-\text{S}(\text{CH}_2)_{11}\text{NH}_3^+$ molecules was inserted to the equilibrated 0.3 M CaCl_2 system. The model tip was taken from an equilibrated simulation of an infinitely sized monolayer of the functionalized long chain hydrocarbon thiols at the interface with 0.3 M CaCl_2 solution. Water molecules and ions within the immediate vicinity of the part of the monolayer that formed the model tip were also inserted. Water molecules and ions that were within a certain cutoff of the atoms of the model tip or the additional

inserted water molecules and ions were removed. Further ions were added to charge balance the system. The system was minimised and equilibrated in the *NVT* ensemble for 200 ps. In order to generate the set of configurations at different distances from the surface start, the model tip was moved from its original configuration towards the surface at a rate of 0.01 \AA ps^{-1} . A subset of the generated configurations at a range of tip sulfur atom-surface distances were then minimised and equilibrated in the *NVT* ensemble for 200 ps.

Table 2.1: Number of waters required to achieve a bulk water pressure of 1 atm for the different electrolyte solutions.

Electrolyte Solution	Number of waters
LS NaCl	9028
HS NaCl	9009
LS KCl	8997
HS KCl	8959
LS CaCl ₂	9039
HS CaCl ₂	9017
LS MgCl ₂	9044
HS MgCl ₂	9035

Table 2.2: Total simulation time and time taken for equilibration.

Electrolyte Solution	Simulation Time/ns	Equilibration Time/ns
LS NaCl	170	50
HS NaCl	180	60
LS KCl	150	50
HS KCl	120	40
LS CaCl ₂	180	60
HS CaCl ₂	180	40
LS MgCl ₂	180	60
HS MgCl ₂	120	40

Metadynamics Simulations

Well-tempered metadynamics was used to explore the reaction coordinate (CV) defined as the perpendicular distance between the surface and the nitrogen atom of the methylammonium molecule. We ran eight well-tempered metadynamics simulations (one for each salt solution and each concentration), each with a duration of 150 ns. Gaussian hills with, initially, a height of 2.9 kJ mol^{-1} and a width of 0.1 \AA were deposited every 0.5 ps. The well-tempered ensemble was applied with a bias factor of 10. Given the translational symmetry of the surface, we constrained the simulation to sample just one surface repeat unit of the super-cell by adding constraining walls to the bias potential. The functional form of the wall was:

$$V_{wall}(s) = \kappa(s - s_{lim})^4 \quad (2.27)$$

where κ represents an energy constant, s represents the value of the CV (collective variable) and s_{lim} is a constant denoting the maximum or minimum value the CV can assume.

Lateral $x - y$ dimensions were constrained to one repeat unit of the slab super-cell, centered on the deprotonated oxygen and at a distance $\sim 7 \text{ \AA}$ from the baseline of the surface (*vide infra*) in the z dimension. This also allowed lateral free energy profiles to be calculated as a function of distance from the surface. For this analysis, the simulation cell was divided in the z -dimension into slices of thickness 0.05 \AA and lateral free energy profiles were determined for each of these slices. Lateral free energy profiles at distances where important features of the vertical free energy were located, such as minima, were examined in greater detail.

Potential of Mean Force (PMF) calculation - Model AFM Tip

For the subset of initial configurations generated for the model AFM tip, MD simulations were run for $\sim 10 \text{ ns}$ and the force required to keep the gold and sulfur atoms of the tip constrained to their initial distances from the surface recorded.

2.1.3 Simulation Analysis

Ramachandran Plots

We analysed the distribution of the backbone (Φ, Ψ) angles using Ramachandran plots. (Φ, Ψ) angle pairs were extracted from the trajectories every picosecond using the Gromacs program `g_rama`.¹⁹⁴ A program developed in-house was used to generate colour-coded Ramachandran plots based on intensity. To aid in comparison of results, regions corresponding to locally stable states were delineated in (Φ, Ψ) space (see Figure 3.3, Chapter 3). Programs were written to calculate the frequency distribution for the population of these states and the frequency of transitions between the different regions of the Ramachandran plots. The final 45 ns of each trajectory was divided into three 15 ns sections to estimate statistical uncertainties. Means presented in the population distribution graph were based on the averages of the three time sections. Standard errors are given to 95 % confidence.

Clustering Analysis

The algorithm developed by Daura *et. al.*²⁰⁸ was used to identify related conformations of the peptide and was implemented using the Gromacs program `g_cluster`.¹⁹⁴ In this method, the RMSD of all the peptide atom positions between all pairs of structures was determined. For each structure, the number of neighbours for which the RMSD was within a specified cut-off was counted. The structure with the largest number of neighbours - the 'representative structure' or 'centroid' structure - and its neighbours were considered to define a single cluster and were designated as the 'representative structure' in future analysis. These clusters were then removed from the pool of structures, and the procedure was iterated until all structures had been identified with a cluster. A neighbour cut-off of 0.1 nm was used to define peptide clusters and 0.05 nm to define backbone clusters. Clustering analysis was conducted on the 50,000 recorded structures for all systems.

The four most popular clusters identified from each cluster assignment were further analysed to see how similar the regions of conformational phase space represented by them were. To accomplish this, we took each of the representative structures from the top four backbone clusters for the TIPS3P system (Clusters **T1**, **T2**, **T3** and **T4**)

and calculated the backbone RMSD with each of the representative structures of the top four clusters for the SPC/Fw system (Clusters **S1**, **S2**, **S3** and **S4**). In this way, we calculated the backbone RMSD between pairs **T1** and **S1**, **T1** and **S2**, ... **T4** and **S4**. The Gromacs program `g_confrms`¹⁹⁴ was used to perform the RMSD calculations. The peptide clustering analysis used the top four all-atom peptide clusters for the TIPS3P system and the all-atom RMSD. RMSDs between the clusters obtained using the same water model were also calculated using `g_confrms`. To make a like-for-like comparison of the cluster populations for the two systems, we also needed to establish a common set of representative cluster structures. To do this, we used the representative structures of the top four clusters identified from the TIPS3P trajectory, **T1** to **T4** (see above), to define an alternative clustering of the SPC/Fw trajectory. Apart from predefining the cluster representatives, this used the same procedure and parameters as described above. For the RGD peptide clustering analysis, we present two sets of growth data: one for the growth of all clusters during the simulation (denoted herein as 'all') and the other for the growth of significant clusters during each simulation (denoted as 'cut'). We have defined a 'significant' cluster as one that has more than 10 members (determined over the entire 50 ns trajectory).

Dihedral Angle Distributions

Dihedral angle distributions of the peptide side chains were calculated using the Gromacs program `g_angle`.¹⁹⁴

Radial Distribution Functions (RDFs)

The Gromacs program `g_rdf`¹⁹⁴ was used to produce the radial distribution function (RDF) plots. The RDF is the density of a particular type of atom as a function of distance from a certain reference atom (or set of reference atoms). All RDFs are normalised to the bulk number density of the atom type in question.

Hydrogen Bonding Analysis

The number of hydrogen bonds between the peptides **RGD** and **SPT** were calculated using two simultaneous geometric criteria, namely when the distance between the peptide heavy atom (N or O) and the water oxygen was 3.5 Å or less and the angle between

the acceptor and the donor hydrogen was 30° or less. We calculated the average number of peptide-water hydrogen bonds over the entire 50 ns trajectory in each case.

Definition of the Simulated Surface

The analysis presented particular challenges due to the surface roughness of our amorphous substrate. The baseline of the surface (*i.e.* $z = 0 \text{ \AA}$) was defined as the closest approach of the oxygen atoms of water molecules from solution. The simulation cell was divided into slices of thickness 0.1 \AA as a function of distance from the surface, starting with the slice spanning $z = 0 \text{ \AA}$ to $z = 0.1 \text{ \AA}$. This concept is shown schematically in Figure 2.9. Surface roughness meant that the initial slices were occupied by smaller volumes of water than those at more distant locations from the surface. To account for this, the surface was further divided into a lateral grid, with each of the 144 squares of the grid being of dimension $3.624 \text{ \AA} \times 3.624 \text{ \AA}$, as illustrated schematically in Figure 2.10. The number of grid squares occupied by water oxygen atoms was calculated for each of the slices to estimate the solution volume present in each slice. This surface definition did not depend on the concentration or type of ions in the solution. This procedure was carried out using water oxygen position data from the equilibrium MD simulations of the saline solutions.

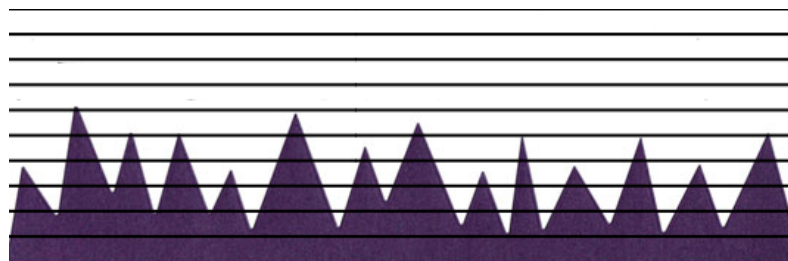


Figure 2.9: Schematic to illustrate the concept of surface roughness and the slices used for binning the data.

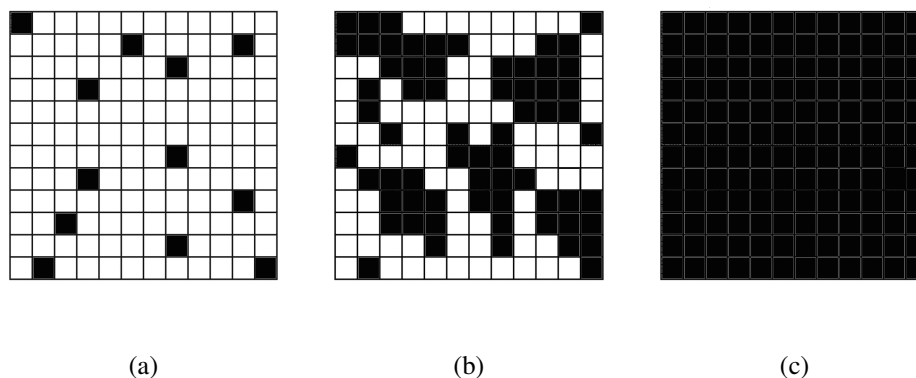


Figure 2.10: Schematic to illustrate how solution volume was estimated considering the occupation of a lateral 12×12 grid. (a) close to the surface, where the volume of water is at its lowest (b) further from the surface, where the volume of water has increased (c) at a distance from the surface, where the entire lateral area of the surface is accessible to water oxygens.

Residence Times for Cations Associated with Silica Surface Deprotonated Oxygen Sites

The silica surface featured deprotonated oxygen sites. Residence times for the cations in the solvation shell of the surface oxygens were calculated by averaging the time the ions were closely-associated to these deprotonated oxygen sites throughout the simulation. An ion was defined as closely-associated if the distance between its centre of mass and that of the deprotonated oxygen site was less than the separation corresponding to the first peak in the deprotonated oxygen-cation rdf. In the case of CaCl_2 solutions, chloride ions associated to calcium ions associated with the deprotonated oxygens. In this case, residence times were calculated by averaging the time the chloride ions were closely-associated with surface bound cations. An ion was then defined as closely-associated if the distance between its centre of mass and that of the surface-bound Ca^{2+} was less than the separation corresponding to the first peak in the surface-bound calcium ion-chloride ion rdf. Standard error, *i.e.* the standard deviation of the mean, was calculated and reported as one σ . An extension of this program was used to calculate the proportion of the different adsorption site configurations at the aqueous CaCl_2 /silica interface at both 0.1 M and 0.3 M concentrations.

Perpendicular and Parallel Diffusion as a Function of Vertical Distance from the Surface

A program was written to calculate the mean squared displacement (MSD) as a function of time at different distances from the surface:

$$MSD(t) = \frac{1}{N} \sum_i^N [\mathbf{r}_i(t) - \mathbf{r}_i(0)]^2 \quad (2.28)$$

The MSD was calculated every picosecond from 0 to 20 ps for all relevant particles (*e.g.* for Na⁺ diffusion, all Na⁺ ions) and for all possible time origins. The system was divided into bins of size 0.1 Å in the *z* dimension. Particles were classified according to their initial position, with the short duration (20 ps) being used to ensure that the dynamics remained confined to the vicinity of that initial position. For parallel diffusion the *x* and *y* components of distance were used in the calculation, while for perpendicular diffusion only the *z* component of distance was used. The diffusion constant was then calculated using data from the last 10 nanoseconds according to:

$$D = \frac{1}{2d} \frac{\delta MSD}{\delta t} \quad (2.29)$$

where *t* is the time and *d* is the number of dimensions. For parallel diffusion *d* = 2 and for perpendicular diffusion *d* = 1.

Water Orientation as a Function of Distance from the Surface

A program was written to calculate the average cos(θ) value of the water molecules, where θ is the angle made between the permanent dipole moment of the water molecule and the surface normal, as a function of vertical distance from the surface. Water molecules where the oxygen atom was closer to the surface than the hydrogen atoms have a value of 1, while water molecules where the hydrogen atoms were closer to the surface than the oxygen atom have a value of -1 . The distance of the water molecule from the surface was classified to a particular bin according to the position of its oxygen atom. Bins were 0.5 Å in thickness. Lateral water orientation profiles were also calculated for slices of the simulation box that corresponded to each point of the vertical water orientation distribution.

MetaD Free Energy Profiles

The program sumhills, part of the PLUMED distribution,¹⁹⁵ was used to transform the Gaussians deposited throughout the metaD simulations to free energy profiles.

Further Analysis

Further programs were written to calculate:

1. Ion concentration and water density as a function of distance from the surface.
2. Histograms of the corresponding distances from the surface of ions represented by the first peak in rdfs.
3. CV histograms.
4. The angle formed between the vector that connects the associated ion and the deprotonated oxygen and the surface normal.
5. Free energy difference profiles.

In the discussion of Chapter 4, we find a number of features that involve the concept of cations bound to deprotonated surface silanol groups, as well as anions (Cl^-) bound to the cations bound to these deprotonated silanols. We will refer to these as bound cations and secondary bound anions, respectively, and denote them as $\text{M}_{(\text{O}^-)}$ and $\text{Cl}^-_{((\text{M})-\text{O}^-)}$ or $\text{Cl}^-_{(\text{Cl}^--(\text{M})-\text{O}^-)}$, where M is the (metal) cation. Furthermore, new terminologies, are defined and explained thoroughly in the text of the Chapter. In brief, $\text{CSDP}(\text{O}^- - \text{MrdfpN})$ for example, refers to the contribution to the surface z -density profile for ions from the Nth peak in the RDF of the silica surface O^- to the relevant cation (see Section 2.1.3) for a definition of the RDF in general. In the majority of cases, N is equal to 1, the first peak. $\rho_{Z_{\text{max}}}(\text{xy})$, where Z_{max} is equal to Z_{pN} (the Nth peak in the ion z -density profile, where $N = 1, 2, \dots$), represents the lateral density profile for ions within a small range of z -distances from the surface centered at the Nth peak in ion z -density and z is the vertical distance from the silica surface to some point in the solution. Lateral water orientation profiles are denoted $\text{ori}_{Z(z_1-z_2)}(\text{xy})$, where z_1 is the z -distance from the surface where the lateral slice starts and z_2 is where it ends.

2.2 Experimental Methods

2.2.1 Experimental Background

Chemical Force Mapping Atomic Force Microscopy (CFM-AFM)

Chemical Force mapping is a commonly-used mode of atomic force microscopy (AFM), an experimental technique which enables the measurement of the adhesion force between functionalized AFM tips and surfaces.^{214,215} In this variant, force curves over many lateral sample positions are recorded. An example of two maps of the adhesion forces across a lateral area of a sample and the corresponding histograms is shown in Figure 2.11. Liquid solutions can be included to allow measurement at liquid/solid interfaces. The tip has a gold coating, a material to which sulfur is strongly attracted and is functionalized by bonding long-chain hydrocarbon thiols terminated by the functionality of interest. The hydrocarbon chains align to minimise unfavourable interactions with the surrounding water molecules. A schematic of the full system is shown in Figure 2.12. There are two types of force curve: approach and retraction (see Figure 2.13 for a schematic of this). For the approach curve, an oscillating AFM tip is moved towards a sample surface over a relatively large distance range, while continuously recording the cantilever deflection. This data is then converted to the force experienced by the tip as a function of distance from the sample.²¹⁶ As the functionalised tip is moved closer to the surface, the repulsive force increases until a certain trigger force is reached. The tip is then removed from the surface to generate the retraction curve. Sloped parts of the curves correspond to heights where the tip is in contact with the surface and flat parts to where it is not. The adhesion force can be calculated from the difference between the cantilever deflection just before (*i.e.* the lowest point of the force curve) and just after pulling away from the sample. Adhesion force data from the set of force curves taken across an area of the sample is often presented as a 2D map. Further details regarding CFM-AFM can be found in a review by Lieber *et. al.*⁹

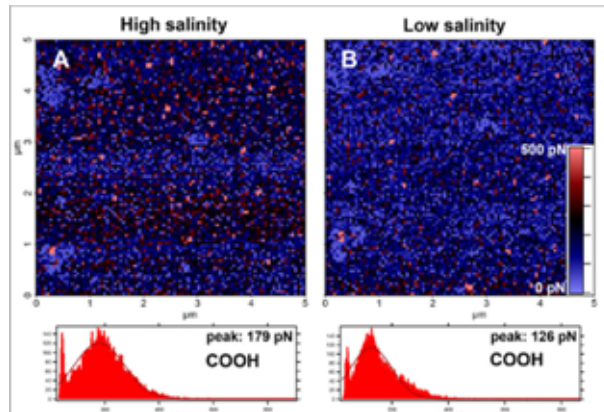


Figure 2.11: Adhesion force maps from a $5\mu \times 5\mu$ area on SiO_2 surfaces, as adapted from Stipp *et. al.*⁸

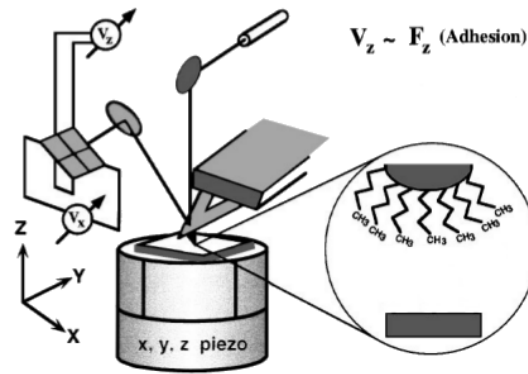


Figure 2.12: Schematic of the CFM-AFM setup, as adapted from Lieber *et. al.*⁹ The sample is positioned on a piezoelectric xyz translator. A laser beam is reflected from the tip onto a photodiode to detect the force experienced by the tip. The movement of the tip up and down reflects the force experienced by the tip.

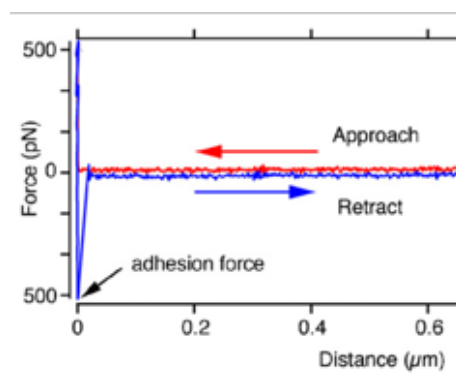


Figure 2.13: Schematic of approach and retraction curves Stipp *et. al.*⁸

2.2.2 Experimental Protocol (Chapter 5)

Experiments were conducted using the protocol developed the NanoGeoScience Group, University of Copenhagen and with the guidance of Klaus Juhl (NanoGeoScience Group, University of Copenhagen). The methods described here are relevant to the Chapter 5. Silica samples were cleaved from a {001} silicon wafer (Montco Silicon inc.) that had developed a thermally oxidized layer of amorphous silica that was ~ 500 nm thick. To map adhesion, we used force mapping, developed and implemented by Asylum Research, with their MFP-3D Atomic Force Microscope (AFM). Details of force mapping are presented elsewhere.²¹⁷ We used functionalized tips to provide information about the physical behavior of the sample surface. This experimental setup allowed us to probe the forces between the organic molecules of the tip and the amorphous silica surface as a function of solution composition and concentration. All the experiments were performed in 0.1 and 0.3 M solutions of either NaCl, KCl, CaCl₂ or MgCl₂. All compounds were reagent grade or better and were purchased from Sigma-Aldrich and used as received (NaCl: ACS reagent, $\geq 99.0\%$, KCl: AG, $\geq 99.5\%$, CaCl₂: ACS Reagent, $\geq 99.0\%$, MgCl₂: ACS Reagent, $\geq 99.0\%$). All the solutions were made with freshly deionized water from a Milli-Q column (ultrapure, deionized and resin exchanged to resistivity ≥ 18.2 M Ω cm). The solutions were adjusted to pH 5.5 with HCl and NaHCO₃. The mass of acid or base added was negligible with respect to the ionic strength of the solutions.

AFM Tip Preparation

The force maps were acquired with Olympus biolever AFM probes that have cantilevers with two different spring constants: 30 and 6 pN/nm. For this study, the tip functionalization only allowed us to use the shorter of the two, which had a nominal spring constant of 30 pN/nm. For each experiment the deflection sensitivity was tested and the individual spring constants were determined more precisely by fitting a Lorentzian function to the thermal spectrum of the cantilever. The spring constant was determined to be 30 +/- 10 pN/nm in all experiments. To make the ammonium terminated tips, the gold-coated biolevers were cleaned in a UV-ozone cleaner (Bioforce Nanosciences, Inc., USA) for 20 minutes and then submerged in an ethanol solution of 4.1 mM 11-amino-1-undecanethiol hydrochloride, $\text{HS}(\text{CH}_2)_{11}\text{NH}_2$, for at least 24 hours to ensure a complete monolayer coverage.

Force Mapping Procedure

The AFM experiments were performed on amorphous silica surfaces that had been UV-ozone cleaned for 20 minutes just before being mounting in the AFM fluid cell. The force maps consisted of 30×30 pixels collected over a $5 \mu\text{m} \times 5 \mu\text{m}$ area to provide enough data for determining reasonable mean values. To start the experiments, both tip and sample were immersed in 3 ml of low salinity solution and adhesion was determined as an average from several sequential force maps. The average adhesion in high salinity solution was determined from several force maps that were taken from the same area on the sample with the same tip so the data could be compared directly. We simply exchanged the low salinity solution with the high salinity solution and repeated the cycle for another two sets of data. For exchanging from low to high salinity or from high to low, about 75% of the solution was removed and replaced with the new solution. We sequentially removed and replaced solution four to six times to avoid the surface and tip from drying and to preserve the precise location of the tip on the surface. Previous experiments demonstrated that five exchanges produces a solution that is within 1% of the target concentration.

Chapter 3

Testing the Inter-Operability of the CHARMM and SPC/Fw Force-Fields for Conformational Sampling

The work of this Chapter has been published as the following peer-reviewed journal article:

'Testing the Inter-Operability of the CHARMM and SPC/Fw Force-Fields for Conformational Sampling' J. L. Desmond, P. Mark Rodger and T. R. Walsh, *Molecular Simulation*, **2013**, *40*, 912.

JLD conducted the simulations and analysis under the guidance and direction of PMR and TRW.

As discussed in section 1.6.1, a key challenge in biointerfacial simulation is to ensure that the interatomic potentials used to describe such interfaces accurately reflect the critical chemistry and physics of the system. The underlying motivation of the work of this Chapter stems from recent studies in the field of biomineralisation, in which a new calcium carbonate force-field that uses a different water model from the standard biomolecule force-fields and thus requires a test of inter-operability.¹⁰¹ In this Chapter, the conformational testing of the inter-operability of the CHARMM and SPC/Fw force fields, the compatibility of which is essential for the successful incorporation of a description of biomolecules into current biomineralisation force-fields, is reported. Furthermore, the validation work described in this chapter will test whether the

flexible water model, SPC/Fw, could be used in combination with the silica force-field employed in Chapters 4-6. The effect of the new water model, SPC/Fw, on the conformational equilibrium of two contrasting exemplar tripeptide sequences, RGD and SPT, as described by the CHARMM force field has been probed by the analysis of results generated from replica-exchange molecular dynamics (REMD) simulations. RGD is an appropriate test case because the charge distribution is reminiscent of the typical sequence stretches found in peptides that are active in biomineralisation. The charge distribution and flexibility of the side chains provide a varied test case for our comparison. On the other hand, the SPT motif is found in biomineralisation proteins associated with iron oxide.²¹⁸ Use of SPT probes the opposite end of the spectrum from RGD; the sequence contains no charged groups and is instead polar. SPT is expected to be more conformationally restricted than RGD due to the presence of proline. Taken together, these two peptides span a range of physicochemical properties, making them ideal test cases for our comparison of water models. Furthermore, the peptides chosen are of relevance to silica biomineralisation.²¹⁹ We have focused on testing tripeptides because these systems should be amenable to comprehensive conformational sampling *via* the use of replica exchange approaches.¹⁸⁸ Thus, we should be able to exclude any artefacts that can arise from sub-optimal exploration of conformational space, giving insight into the genuine differences that may arise from using two different water models. We compare the ensemble of conformational states generated from the CHARMM-SPC/Fw force fields with those obtained from the more typical CHARMM-TIPS3P combination. The appended material (Appendix B) contains further radial distribution functions (rdfs) between key peptide atoms and water oxygen and hydrogen atoms, dihedral angle distributions for various peptide dihedrals, percentage cluster growth data and replica mobility data.

3.1 Simulation Protocol in Brief

Peptides RGD and SPT are described using the CHARMM force-field and have been solvated using two different water models, TIPS3P and SPC/Fw. REMD¹⁸⁸ simulations, an advanced variant of MD that enables a more efficient and thorough sampling of phase space than traditional MD, were carried out for the four systems. Various analyses, including cluster analysis and Ramachandran plots, were conducted to quantify

the similarity between the regions of conformational phase space visited by each peptide when solvated by SPC/Fw compared to TIPS3P. The general simulation protocol is given in section 2.1.2, with REMD-specific details described in section 2.1.2.

3.2 Ramachandran Plots

The 3D structure of polypeptides are determined by the three dihedral angles of the backbone, traditionally denoted Ω , Φ and Ψ . Such angles describe the relative positions of substituents attached to the bonds that make up the backbone. As shown in Figure 3.1 the angle Φ concerns the N-C α bond and Ψ the C α -C bond. Ω describes the bond between the carbonyl and amide group (the peptide bond). The relationship between the value of the dihedral angle and the relative position of the substituents has been illustrated using Newman projections in Figure 3.2. However, as the peptide bond has a partial double bond character due to the delocalisation of the lone pair of electrons of the amide nitrogen into the carbonyl group, the Ω angle generally has a value of 180° and it is the Φ and Ψ angles that are used to characterise peptide structure. The angle pairs are traditionally plotted against one another in a Ramachandran plot, with particular combinations of Φ and Ψ representative of different types of protein secondary structure, such as α -helices (the angles of a geometrically pure α helix are $(-57.8, -47.0)^{220}$) and β -sheets (the approximate angles of a β -sheet are $(-120, 120)^{220}$). (Φ, Ψ) angle pairs are not usually defined for terminal amino acids, so tripeptides, such as RGD and SPT, have just one pair, as depicted in Figure 3.1. Figures 3.3 (a) and (b) show Ramachandran plots compiled over the entire 50 ns TIPS3P and SPC/Fw trajectories for both RGD and SPT. For both RGD and SPT, there was no significant difference between the plots for the TIPS3P and SPC/Fw systems. The same regions were visited and patterns in the relative densities were replicated for both water models. Regions **a** and **b** were populated in both peptide cases and represented right-handed α -helices and β -sheets respectively. For SPT, additional regions were observed. While region **g** corresponded to left-handed α -helices, the other four regions did not represent well-known and characterised structure types. The aliphatic ring that featured in the SPT peptide limited its flexibility and the smaller number of regions visited in the SPT case compared to RGD was a reflection of the decreased backbone flexibility. At a qualitative level, the water model did not impact the peptide structure for either RGD or SPT.

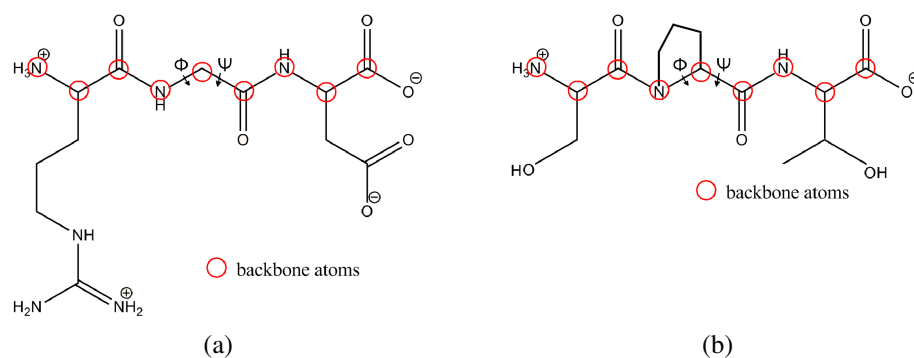


Figure 3.1: Structures of the tripeptides (a) RGD (b) SPT. Backbone atoms are highlighted in red and Φ and Ψ dihedral angles marked.

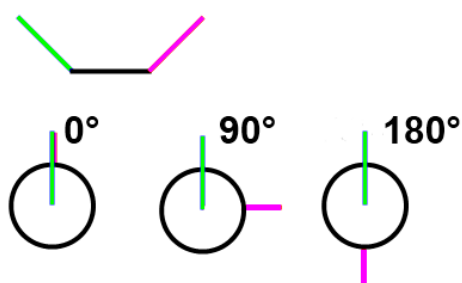


Figure 3.2: 2D representation of the bonds involved in a dihedral angle centred on the black bond, with the corresponding Newman projections for a selection of angles.

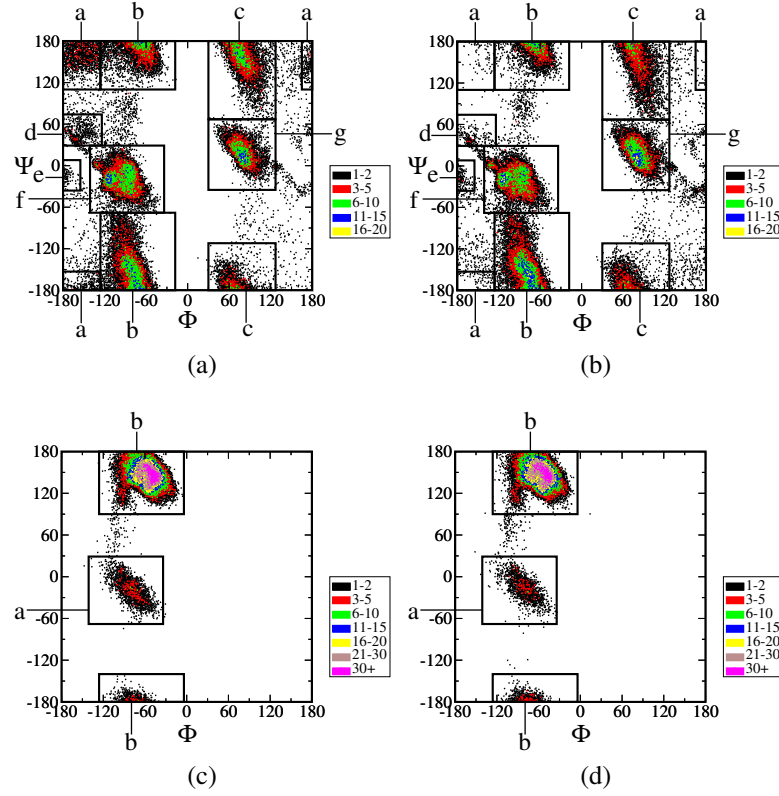


Figure 3.3: Ramachandran plots for the four cases (a) RGD with TIPS3P (b) RGD with SPC/Fw (c) SPT with TIPS3P and (d) SPT with SPC/Fw. Note that ϕ and ψ are both periodic, and so some of the regions are split across boundaries

In order to conduct a more quantitative analysis, boundaries, chosen to be the same in TIPS3P and SPC/Fw plots, were drawn to delineate the different regions used to define locally stable conformers. Figure 3.4(a),(b) shows the net percentage populations of the various conformers defined by these regions for the TIPS3P and SPC/Fw systems for both RGD and SPT, respectively. For RGD, the population distributions followed the same general trend and all major regions (defined as those with population greater than 10%), bar region **g** (where the error bars, which represented the standard error given to 95 % confidence, did not overlap, but were very close), were within error between the two approaches. While the more populated regions (**b**, **c**, **f** and **g**) exhibited a very intensely populated central area that gradually decreased to an edge of very low population, Figure 3.3 shows region **a** did not follow the same trend. In the TIPS3P case, points of slightly higher population were dispersed over an underlying area of low population, whereas in the SPC/Fw case, region **a** featured a sparse distribution of points of the lowest possible population. For SPT, the populations of the two regions of the Ramachandran plots were within error for both water models, a contrast that originated from the relative rigidity of the molecule compared to RGD. Overall, the sampling of conformational phase space in the two water models compared favourably for both peptides.

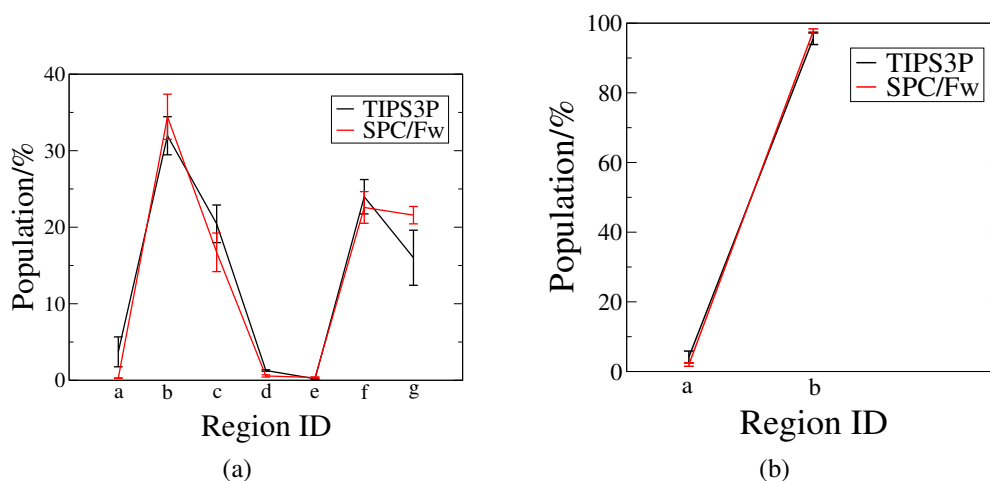


Figure 3.4: Population distribution over regions of the Ramachandran plots. (a) RGD; regions **a-g** are defined in Figure 3.3(a). (b) SPT; regions **a-b** are defined in Figure 3.3(c).

The underlying physical basis for the discrepancy in the populations of region **g** for RGD will now be considered. A representative structure for regions **g** is shown diagrammatically in Figure 3.5. In the area of the (Φ, Ψ) angle pair, the representative structure for region **g** featured bond distances between electronegative and hydrogen atoms that were within the range of typical hydrogen bond distances, as labelled in the diagram. The dielectric constant for SPC/Fw is 80% of the size of that for TIPS3P (100 +/- 2.20 compared to 79.63 +/- 1.62¹²⁶). If SPC/Fw were used in combination with the silica force-field for the work of subsequent chapters, the strength of ion-surface interactions would thus be overestimated due to decreased shielding and this would impact the form of any calculated ion density vs distance distributions. The larger dielectric constant of TIPS3P results in an increased shielding of such hydrogen bonding interactions, an effect which may explain the origin of the decreased population of region **g** in the TIPS3P case compared to SPC/Fw. Differences in the populations of regions **g** between the two water models could be rationalised by considering changes to the dielectric constant.

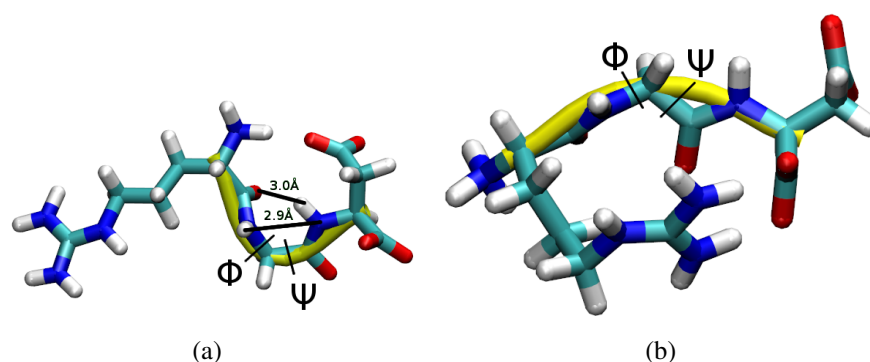
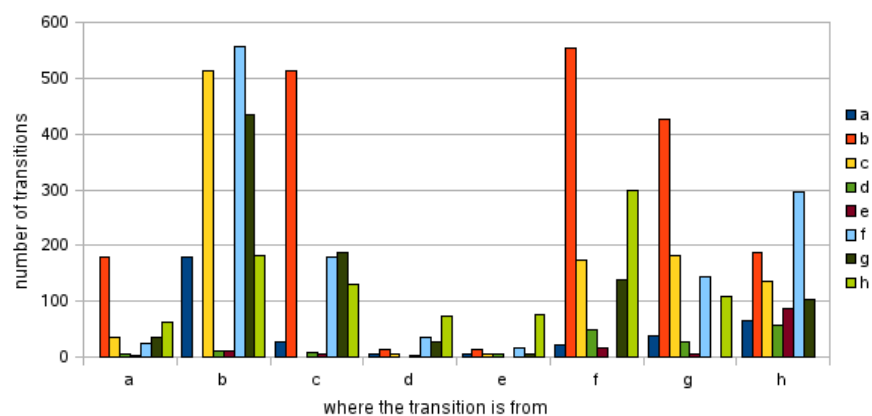


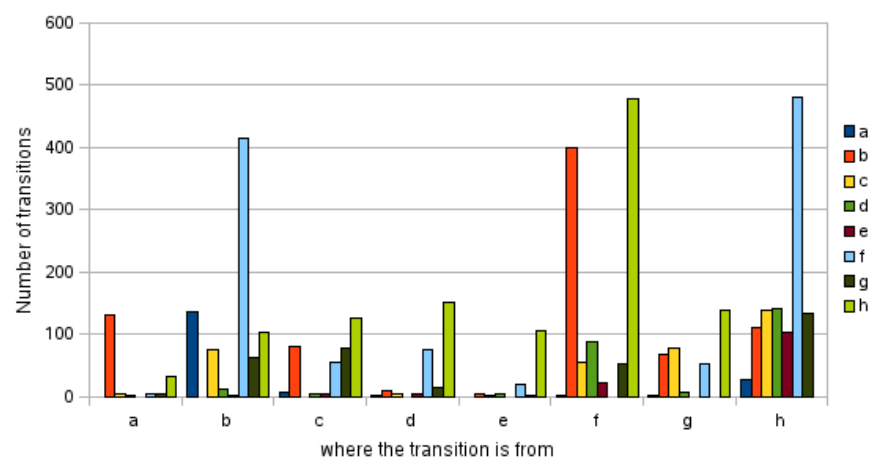
Figure 3.5: Pictorial diagrams of representative structures from regions (a) **g** and (b) **b**. The backbone is shown in yellow and the central bonds of Φ and Ψ angles are labelled. For region **g**, bond distances between key atoms have been displayed. H-bonds are labelled by the bold, black lines.

We needed to ensure that peptide dynamics is also conserved between the water models, and so we have calculated the kinetics of conformational change. At certain points in the MD trajectories, the peptide transitioned from a conformation represented by one region in the Ramachandran plot to another. For each region in the Ramachan-

dran plot, the relative populations of peptide conformations that transitioned from all of the other regions over the 50 ns trajectory have been calculated, as recorded for both water models in Figure 3.6. Generally, there were more transitions between regions of the Ramachandran plot for the TIPS3P case compared to SPC/Fw. For region **g**, the most common region to transition from in the TIPS3P case, region **b**, was less than a fifth of the size in the SPC/Fw case, where the transition from regions **c** and **h** was more likely, the latter was representative of all areas not defined by boundaries. This indicated that the conformations of region **b** were more energetically favourable than those of region **f** in the SPC/Fw case. In support of the suggested impact of the dielectric constant, the representative structure for region **b**, shown in Figure 3.5, did not display a predominance of such hydrogen bonding interactions in the area of the (Φ , Ψ) angle pair.



(a)



(b)

Figure 3.6: Distribution of transitions between regions of the Ramachandran plots for RGD (a) TIPS3P (b) SPC/Fw. The labels of the x -axis indicate the initial state and colour indicates the final state. Region **h** represented the area of the plot not defined by boundaries.

3.3 Backbone Atom Cluster Analysis

Clustering analysis, implemented using the algorithm developed by Daura *et. al.*,²⁰⁸ was used to identify related conformations of the peptide based on the RMSD of atomic positions. In brief, if the RMSD between a pair of peptide conformations was below a certain threshold value, the structures would be classified as belonging to the same cluster. Backbone clustering analysis considered only the backbone atoms of the peptide, whereas all-atom peptide clustering analysis considered all atoms. Full details of the method are provided in section 2.1.3. Peptide structures that belonged to the same backbone cluster sampled similar regions of conformational phase space *ie* had similar relative positions of backbone atoms. The number of RGD backbone clusters has been plotted as a function of simulation time steps in Figure 3.7(a). The number of backbone clusters increased at roughly the same rate for both solvent models and reached a plateau at a value of around 30 clusters. In the analogous data for SPT, shown in Figure 3.7(c), the plateau in the number of clusters was the same for both water models. The greater number of clusters calculated for RGD (approximately 30) compared to SPT (9) was a direct reflection of the comparatively more rigid character of the SPT backbone. The percentage populations of the RGD and SPT clusters defined from the backbone clustering analyses carried out independently for both the TIPS3P and SPC/Fw trajectories are presented in Figure 3.8, running in order of descending population in each system. As opposed to our like-for-like cluster comparison (see Figure 3.9), in Figure 3.8 (a), clusters labelled with the same cluster ID did not share the same cluster representative and so should not automatically be considered as being the same cluster. The population distributions both followed an approximately exponential decrease.

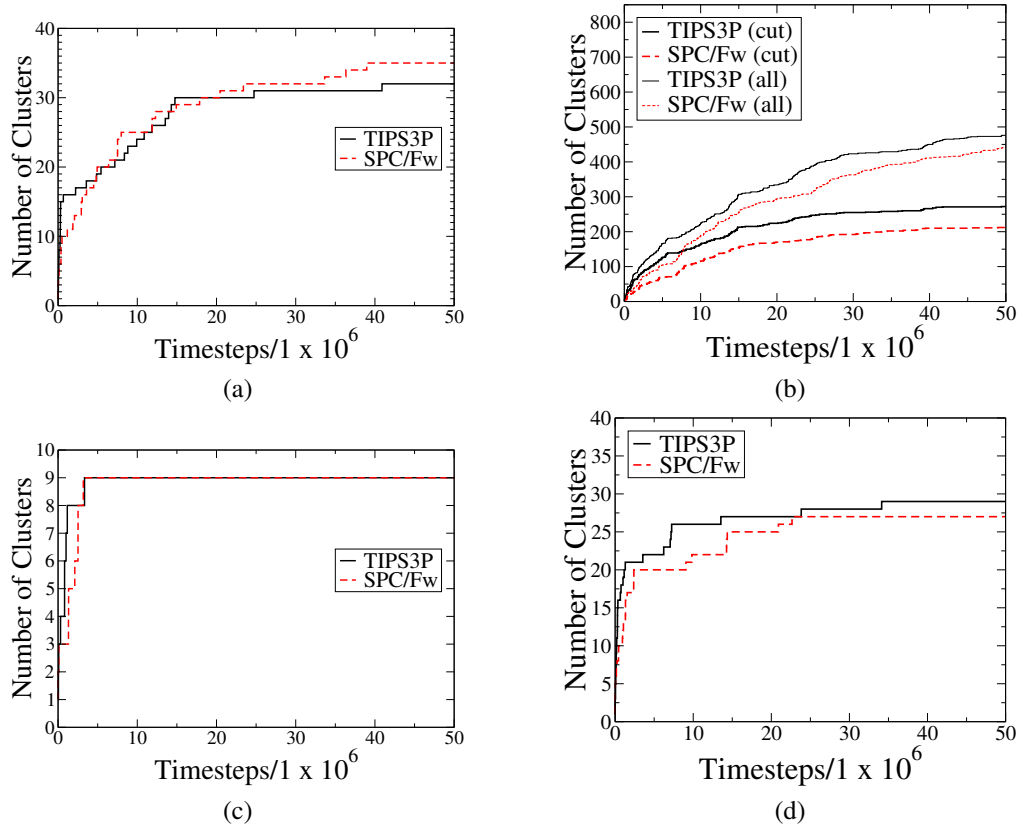


Figure 3.7: Number of clusters as a function of simulation timestep (a) RGD, backbone; (b) RGD, peptide; (c) SPT, backbone (d) SPT, peptide

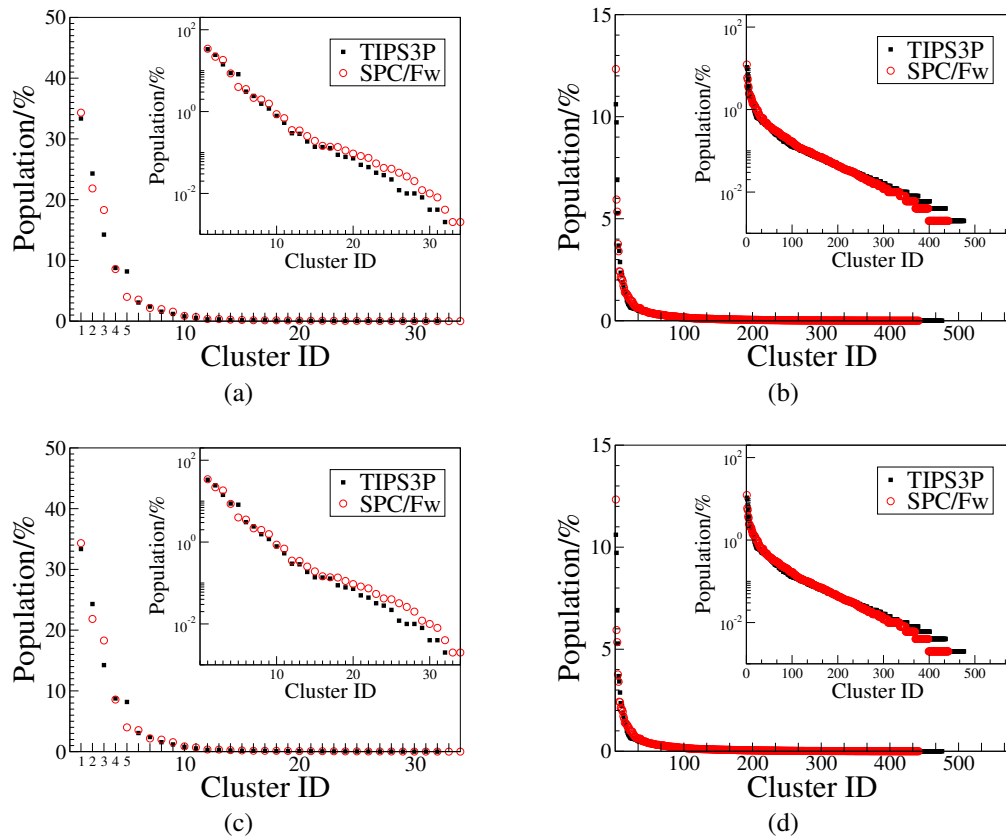


Figure 3.8: Population distribution of RGD clusters over 50 ns. Inset: as the main graph, but on a semi-log scale. (a) backbone and (b) peptide. Analogous data for SPT are given for (c) backbone and (d) peptide.

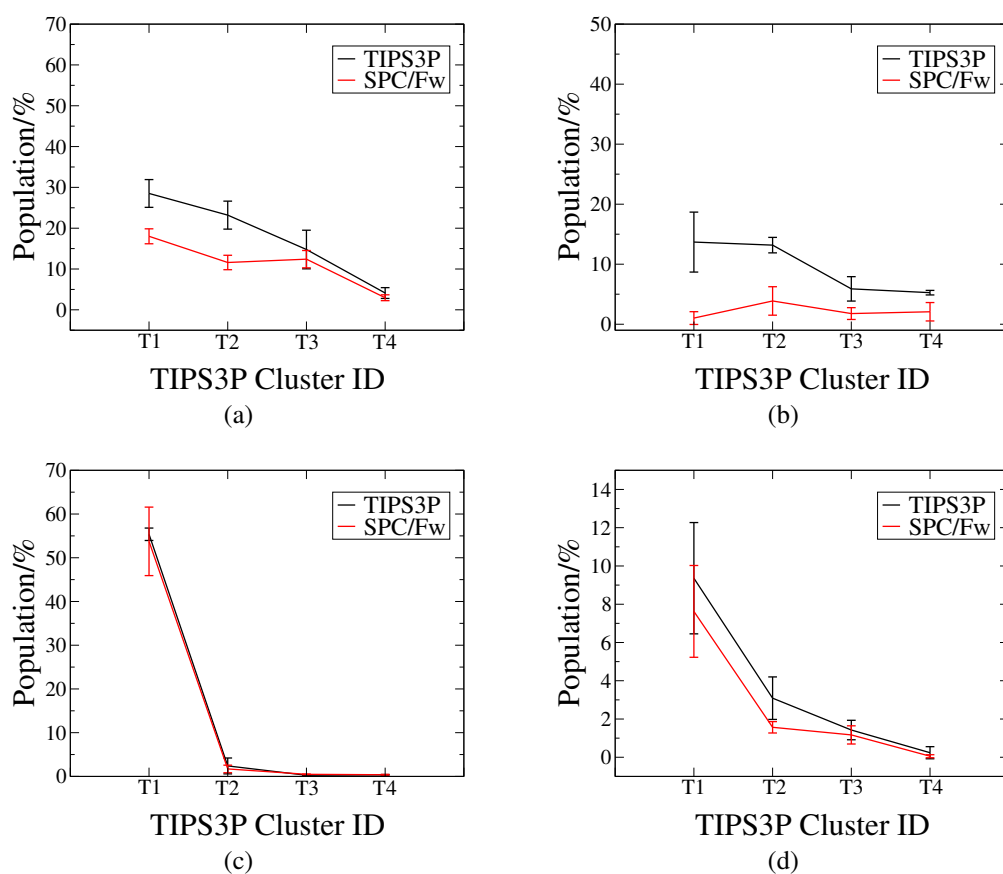


Figure 3.9: Population distribution of RGD for the top four clusters, for (a) backbone and (b) peptide clusters, using TIPS3P cluster IDs. Analogous data for SPT are given for (c) backbone and (d) peptide clusters, using TIPS3P cluster IDs. Standard errors are given to 95% confidence (a) backbone (b) peptide.

The four most populated clusters from each system were further analysed to see how similar the regions of conformational phase space represented by them were. For both RGD and SPT, all of the top four clusters could be matched up within the 0.05 nm cutoff (see Table 3.1) This showed that the most popular regions of phase space sampled by the backbone were similar in both water models for both systems. However, the best way to do a like-for-like comparison based on clustering for the two systems was to use a common set of reference cluster structures. For RGD and SPT, respectively, Figure 3.9(a),(c) shows a direct comparison of the most popular regions of conformational phase space as defined by the representative structures from the top four TIPS3P backbone clusters (**T1-T4**). While for SPT (Figure 3.9(c)), the population distribution between the water models was the same within statistical uncertainty, the same cannot be said for RGD (Figure 3.9(a)). However, in this case, even though the absolute populations do not agree for every cluster, the trend in the cluster population between the two water models was captured. It should also be emphasised that with a small cut-off of 0.05 nm, this conformational analysis was highly resolved, such that very small conformational differences become magnified, thus diminishing the significance of the differences seen in the populations.

Table 3.1: RMSD values (nm) for matchings of the representative structures from the top four TIPS3P and SPC/Fw backbone clusters.

TIPS3P Cluster ID	SPC/Fw Cluster ID	RMSD
<i>RGD</i>		
1	4	0.01
2	2	0.01
3	3	0.01
4	1	0.05
<i>SPT</i>		
1	1	0.01
2	2	0.01
3	4	0.01
4	3	0.01

Furthermore, since this clustering analysis concerned the backbone, it was closely connected to the Ramachandran plot data. For RGD, the peptide with the greatest conformational flexibility, representatives of the top four TIPS3P clusters have been clas-

sified according to their (Φ, Ψ) dihedral angle pairs, as recorded in Table 3.2. While it was likely that differences in the backbone atom positions, particularly those of the bonds of the (Φ, Ψ) pair, were small enough between different members of the cluster, it was not impossible that some corresponded to different regions of the Ramachandran plot and thus results should be interpreted cautiously. Cluster **1**, the most populated cluster, corresponded to the Ramachandran region with the greatest population, region **b**. This supported the idea that the (Φ, Ψ) angle pair of the representative structure was a good approximation of that of the other members of the cluster. The representatives of Clusters **3** and **4** were both classified as region **f**, the Ramachandran region with the second largest population. Backbone clusters were matched to regions of the Ramachandran plot according to the (Φ, Ψ) angle pair of the cluster representative and the most populated cluster corresponded to the Ramachandran region with the greatest population.

Table 3.2: Classification of the top 4 TIPS3P clusters to regions of the Ramachandran plot

TIPS3P Cluster ID	Ramachandran Region
1	b
2	c
3	f
4	f

3.4 All-Atom Peptide Cluster Analysis

As exemplars, in Figure 3.10 we show the centroid structure for each of the top four peptide clusters for RGD, obtained using the TIPS3P water model. To give an idea of the typical RMSD between the peptide clusters obtained using the same water model, in Table 3.3 we summarise these data for RGD and SPT, obtained using both water models for the top four clusters. Since RMSD values were all greater than the 0.1 nm cutoff, this was confirmation that none of the representatives would have been assigned to the same cluster. However, RMSD values were small and ranged from 0.12 to 0.26 nm. This demonstrated that the conformational similarity between clusters and indicated

that a significant number of members of the most popular clusters would have small enough RMSD values to be considered part of the clusters of lesser population had they not already been assigned.

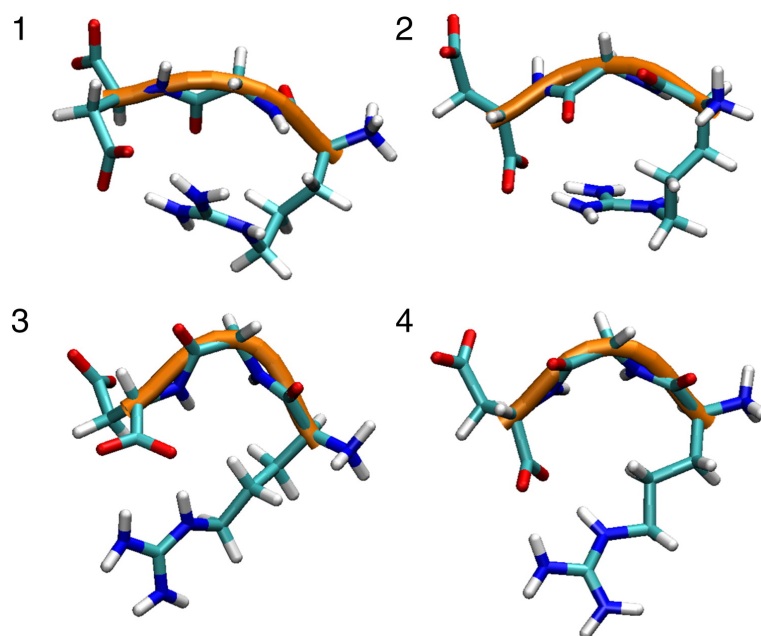


Figure 3.10: Centroid (as defined in section 2.1.3) cluster structures for the top four peptide clusters of RGD obtained using the TIPS3P model.

Table 3.3: RMSD values (nm) between all unique pairs among top four peptide clusters obtained with the same water model, for both TIPS3P and SPC/Fw.

Cluster ID #1	Cluster ID #2	TIPS3P RMSD	SPC/Fw RMSD
<i>RGD</i>			
1	2	0.24	0.19
1	3	0.25	0.17
1	4	0.23	0.24
2	3	0.16	0.14
2	4	0.18	0.21
3	4	0.13	0.23
<i>SPT</i>			
1	2	0.20	0.21
1	3	0.12	0.12
1	4	0.26	0.26
2	3	0.23	0.23
2	4	0.24	0.26
3	4	0.20	0.24

Figure 3.7(b),(d) shows the growth of the number of peptide clusters with simulation time steps for the TIPS3P and SPC/Fw systems, for both RGD and SPT, respectively. We note that, in the case of RGD, unlike in the case of the corresponding backbone clustering analysis, neither the TIPS3P or SPC/Fw plots had a plateau, although the 'cut' data did approach plateau behaviour. The 'cut' data represented significant clusters, which were defined as clusters that had more than 10 members over the 50 ns trajectory. In this instance, both the 'cut' and 'all' data-sets had a greater growth rate in the TIPS3P system. This was in contrast to the backbone clustering analysis, where the number of clusters increased at approximately the same rate for both the TIPS3P and SPC/Fw systems. This suggested that the behaviour of the side chains was affected by the water model. To test this, we calculated the distribution of dihedral angles for each of the side chains in both RGD and SPT for both the water models (see Figure B.3, Appendix A). We found for each dihedral that the angle distribution for TIPS3P and SPC/Fw showed only small differences. Indeed, the distributions had the same general shape and peak positions were the same for both water models. The only differences concerned the magnitude of some of the peaks, particularly for side chains of the R residue, as shown in Figure B.3(b)-(d). The peak that occurred between 50 and

100° was greater in magnitude in the TIPS3P case compared to SPC/Fw for two of the three highlighted cases, while the reverse was true for the corresponding negative part of the distribution. We propose that the cut-off used in our clustering analysis over the whole peptide may have been sufficiently small such that these small differences in dihedral angles translated into different clusters. This effect appeared more profound for RGD where there was considerably more conformational flexibility, compared with SPT. However, the difference in peptide cluster growth between the two water models may also have been due to the different viscosities of the water models. At 300.2 K and constant volume, SPC/Fw had a viscosity of 0.75 cp, while TIPS3P had a viscosity of 0.31 cp (at 293 K).¹²⁶ As the majority of experiments have demonstrated an inverse relationship between folding rate and viscosity,²²¹ it followed that the peptide solvated by the more viscous SPC/Fw might have taken longer to explore conformational phase space. The observation that there were a greater number of transitions between regions of the Ramachandran plot for the RGD peptide solvated by TIPS3P compared to SPC/Fw, as discussed in a previous subsection, added further support to this hypothesis. Conformational rearrangements that enabled the transition from one region of the Ramachandran plot to another were less likely in the SPC/Fw case. Figure 3.8 (b) shows, in order of descending population for the two systems, the percentage populations of the clusters defined from the independent clustering analyses over the entire peptide for the TIPS3P and SPC/Fw systems. As opposed to our like-for-like cluster comparison (see Figure 3.9 (b)), in Figure 3.8 (b), clusters labelled with the same ID did not necessarily have the same cluster representative and so should not be automatically considered as being the same cluster. The general trend in population distribution was the same between the two systems.

For both RGD and SPT, the four most populated peptide clusters for each water model were further analysed to see how similar the regions of conformational phase space represented by them were. All of the top four clusters could be matched up within the 0.1 nm cutoff (see Table 3.4). This showed that the most popular regions of phase space sampled by the peptide were similar for both water models for both peptides. As with the backbone cluster analysis, all-atom peptide cluster analysis for the two systems has also been conducted using a common set of reference cluster structures. Figure 3.9(b),(d) shows a direct comparison of the most popular regions of conformational phase space as defined by the representative structures from the top four TIPS3P peptide

clusters (**T1-T4**). As seen for the backbone cluster populations, the distributions were within statistical uncertainty for the SPT peptide. Again, as found with the backbone clustering analysis, there was relatively less agreement for the RGD peptide between the water models, although for both water models, the absolute populations were low and the population distributions were quite flat. Overall, the *trends* between the two models were not too dissimilar. It should be emphasised that as with the backbone cluster analysis, the small cut-off (0.1 nm) again meant that this conformational analysis is highly resolved. Although the top four cluster populations were not within error, there were only slight differences in the side-chain dihedral angle distributions between the TIPS3P and SPC/Fw cases. Again, this suggested that the differences in population are perhaps not as significant as the percentage values suggest.

Table 3.4: RMSD values (nm) for matchings of the representative structures from the top four TIPS3P and SPC/Fw peptide clusters.

TIPS3P Cluster ID	SPC/Fw Cluster ID	RMSD
<i>RGD</i>		
1	2	0.05
2	4	0.02
3	3	0.06
4	1	0.05
<i>SPT</i>		
1	1	0.04
2	2	0.04
3	3	0.11
4	4	0.05

3.5 Radial Distribution Functions

For both peptides and both water models, RDFs have been calculated between water and the oxygen atoms of the carboxylate groups and the nitrogen atoms of the guanidinium group. For the latter system the RDF showed no significant dependence on whether TIPS3P or SPC/Fw was used (Appendix A, Figure B.1(b)). We show exemplar data for RGD in Figure 3.11(a),(b) for the RDFs between the C-term carboxylate oxygen

and (a) the hydrogen of the water and (b) the oxygen of the water. Similar results were found for the SPT peptide (Figure B.2, Appendix A). For the RGD RDFs between water hydrogen and the carboxylate groups, the position of the first peak of the RDF was shifted to smaller values for the SPC/Fw case than for the TIPS3P case. However, the position of the first peak in the carboxylate oxygen-water oxygen RDF (see Figure 3.11(b)) showed a much smaller shift of the SPC/Fw system, compared with the TIPS3P system. As there were small differences in the equilibrium O|H bond length for the two water models (see Table 3.5), with the SPC/Fw bond length being greater, this suggested that the average centre-of-mass position of the water molecules in the vicinity of the carboxylate is not substantially different between the two water models. These data, taken together, suggested that the overall water structuring around the carboxylate group is very similar for the two water models.

We note, however, that the height of the first peak was slightly higher in the SPC/Fw system than in the TIPS3P system (see Figure 3.11(a)). The peak height in the TIPS3P case was 85 % the magnitude of the peak height in the SPC/Fw case. Furthermore, it was shifted to a smaller distance. This increase in peak height was more pronounced in the RDFs between the carboxylate groups and the water hydrogen atoms than was seen for the water oxygen atoms (see Figure 3.11(b)). The increase in peak height in the SPC/Fw system could be a consequence of the shift in peak position to a smaller distance, since rdfs are normalised by $\frac{1}{r^2}$. However, the over-structuring of TIPS3P water adjacent to carboxylate groups described by the CHARMM force field has been reported previously several times.^{222,223,224,225} The hydration number was always higher for the SPC/Fw case than for the TIPS3P case. Further, since the cross interaction terms in the intermolecular potential (terms that describe the interactions between the water and peptide) did differ between the TIPS3P and SPC/Fw systems, differences between the RDFs were expected. See Table 3.5 for an example of how the cross terms differed. These findings from our RGD data were further reinforced by the calculated average number of peptide-water hydrogen bonds. For RGD, this amounted to 22.6 and 22.1 hydrogen bonds for TIPS3P and SPC/Fw, respectively. Similarly, we found very close agreement in the number of SPT-water hydrogen bonds, with 16.1 and 15.6 found for TIPS3P and SPC/Fw, respectively. Histograms of the angles and distances of the hydrogen bonds between the peptide and water did not differ between the RGD and SPT peptides and are shown in Figure 3.12. For TIPS3P, the peak in the

distribution of hydrogen bond distances was sharper and approximately 10 % greater in magnitude than the corresponding distribution for SPC/Fw. Although there were a greater number of hydrogen bonds in the TIPS3P case, the increased magnitude of its peak was in part as a result of the narrower distribution of distances. The flexibility of the SPC/Fw water molecules may have been the origin of the broader distribution for this model. The angular distributions were unimodal for both water models, with the peak shifted to slightly lower values in the SPC/Fw case compared to TIPS3P.

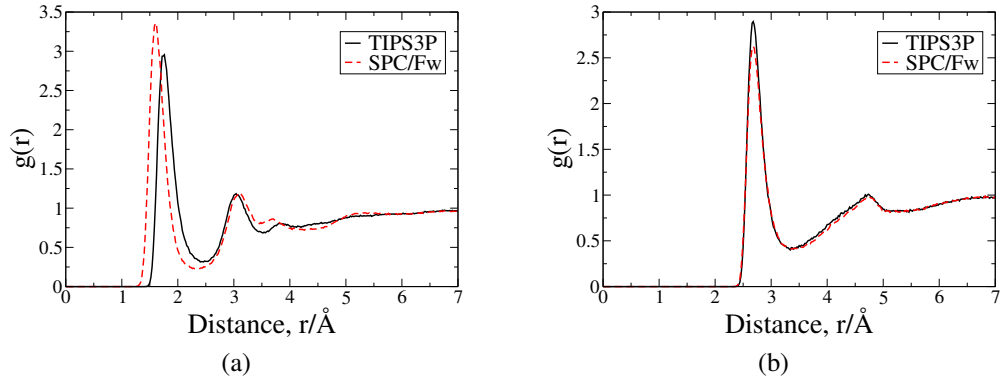


Figure 3.11: Exemplar RDFs for RGD: (a) $g_{O-H_w}(r)$ between the oxygen atoms of the terminal carboxylate group and the hydrogen atoms of water and (b) $g_{O-O_w}(r)$ between the oxygen atoms of the terminal carboxylate group and the oxygen atoms of water.

Table 3.5: Cross terms for the interaction between the oxygen atoms of the terminal carboxylate group and the hydrogen atoms of water.

Cross term	TIPS3P	SPC/Fw
σ/nm	0.171	0
$\epsilon/\text{kJ mol}^{-1}$	0.311	0

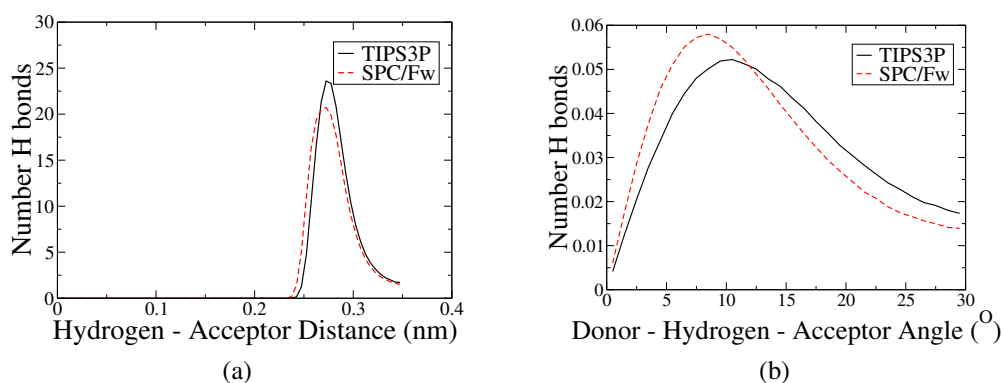


Figure 3.12: Histograms of different aspects of the hydrogen bonds between the peptide and water for (a) distances (b) angles. Distributions were the same for both the RGD and SPT peptides.

3.6 Convergence

In order to provide evidence that the simulations had equilibrated, the growth of the different regions of the Ramachandran plot were monitored as a function of simulation timestep, as shown for RGD in Figure 3.13. Population data was recorded in terms of the proportion of the total number of structures observed thus far in the simulation at each timestep. The backbone and peptide clusters were analysed in a similar manner (Appendix A, Figure B.4). After approximately 30 ns the relative proportions of the Ramachandran regions and backbone clusters remained constant for the peptide in both water models. For peptide clusters it took the slightly longer time period of 35 ns for this plateau region to be reached. The relative populations of peptide and backbone clusters and Ramachandran regions did not change after an initial time period of ~ 30 ns and was an indication that conformational phase space had been well explored and that the systems had equilibrated.

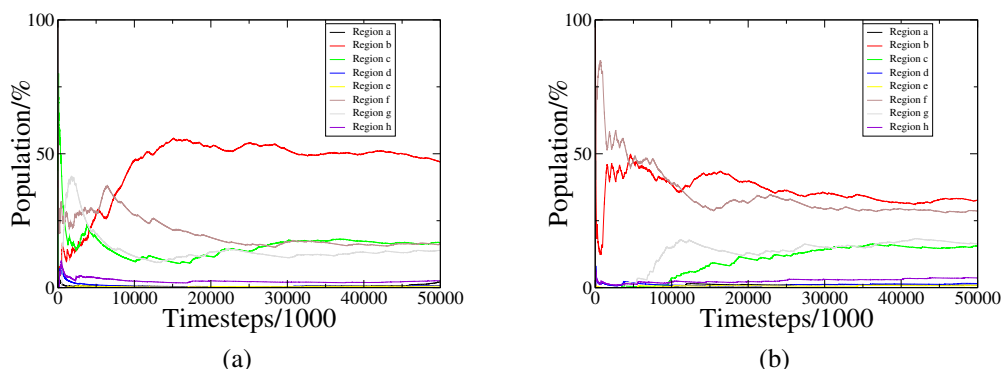


Figure 3.13: The percentage growth of the different regions of the RGD Ramachandran plot as a function of simulation timestep for the two water models (a) TIPS3P (b) SPC/Fw. Region **h** again represented all the areas of the plot that were not defined by boundaries.

3.7 Effectiveness of Replica Exchange Molecular Dynamics

The exploration of conformational phase space was aided by REMD for all systems. In order to be effective the replica that began in position 0, *i.e.* temperature 300 K in this case, would have to transverse the full set of temperatures (replicas) and return to its initial position at 0. The pathway taken by the replicas is shown in Figure 3.14 for RGD and in Figure B.5 (Appendix A) for SPT. The number of times that the replica which began at 0 transversed the full set of temperatures and back was 9 for all systems, except for SPT solvated by TIPS3P water where it was 10. Details of the exchange probabilities and number of exchanges over the final 5 ns of the 50ns trajectories are summarised in Table 3.6 for RGD as an example. The exchange probabilities were all roughly equal, in a range from 0.22 to 0.25 for the TIPS3P system and 0.24 to 0.28 for the SPC/Fw system. It was essential that the probabilities displayed this behaviour so that the ability of the replica to transverse the full temperature set was maximised. The slightly higher probabilities observed for the SPC/Fw system was reflected by the greater number of exchanges on average, which varied in a range from 119-156 compared to the TIPS3P case, where the number varied from 106-123. The initial replica 0 transversed the full range of temperatures a number of times which indicated that the enhancement of

conformational sampling by REMD was effective.

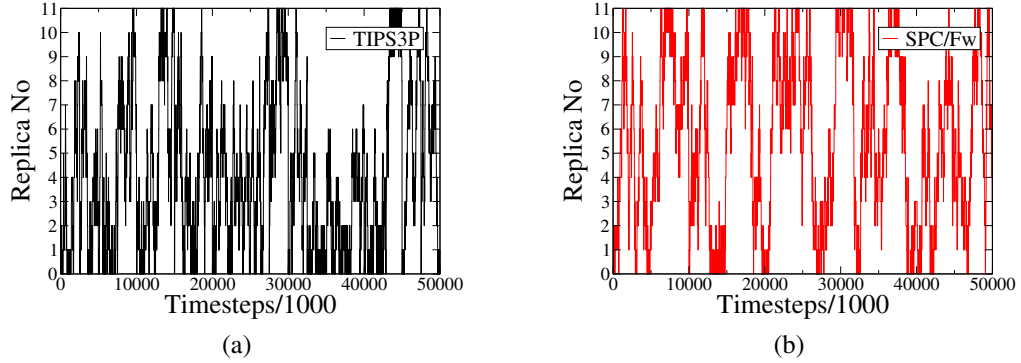


Figure 3.14: Replica pathway of the initial 'replica 0' for the RGD system as an example for (a) TIPS3P (b) SPC/Fw.

Table 3.6: Exchange probabilities (Ex. P.) and number of exchanges (No Ex.) between adjacent replicas for RGD solvated by TIPS3P and SPC/Fw

Replica Nos	TIPS3P Ex. P.	SPC/Fw Ex. P.	TIPS3P No. Ex.	SPC/Fw No. Ex.
0-1	0.22	0.26	114	124
1-2	0.24	0.25	121	125
2-3	0.23	0.28	108	138
3-4	0.25	0.24	123	119
4-5	0.22	0.28	106	140
5-6	0.25	0.26	118	120
6-7	0.23	0.27	109	125
7-8	0.23	0.28	121	146
8-9	0.24	0.25	113	120
9-10	0.24	0.28	113	156
10-11	0.22	0.28	112	129

The impact of the length of time between exchange attempts on the exploration of conformational phase space was investigated. Figure 3.15 shows the growth of the number of backbone and peptide clusters with simulation timesteps for different exchange intervals. For the backbone clustering, the plateau region occurred at a value of ~ 30 for exchange attempt intervals of both 1 and 5 ps. There was, however, an ~ 3 -fold increase in the rate at which the plateau region was reached when the smaller 1 ps interval was used. A greater number of peptide clusters was observed for the system with

the 1 ps interval compared to 5 ps, which indicated that conformational phase space was even better explored when the smaller interval was used. In parallel to the data of Figure 3.7(b), the populations of a large number of the clusters were likely to have been very small and thus the most important regions of conformational phase space have been sampled. Although the decrease in the length of the interval between exchange attempts from 5 ps to 1 ps led to an increase in the total number of peptide clusters, it had no impact on the number of backbone clusters and indicated that all major regions of conformational phase space had been explored when the 5 ps interval was used.

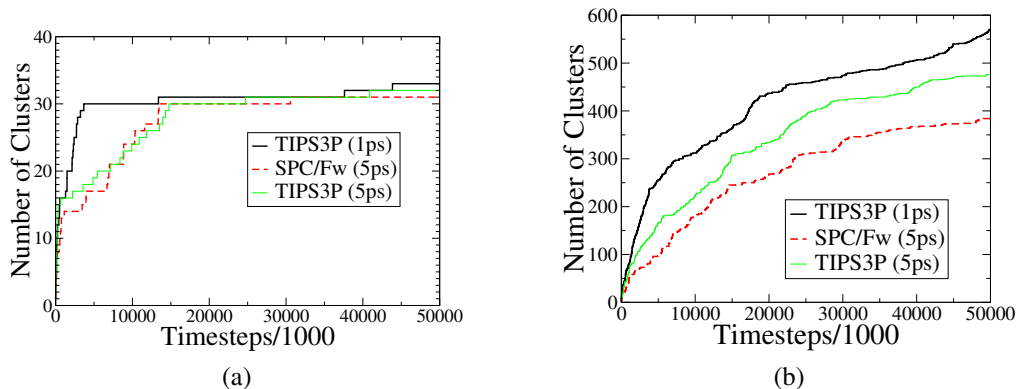


Figure 3.15: The effect of the length of time between replica exchange attempts on the growth of clusters in the RGD system as an example for (a) backbone (b) peptide.

3.8 Conclusions

The ensemble of conformations generated by REMD simulations of the solvated RGD and SPT tripeptides described with the CHARMM force-field with both the TIPS3P and SPC/Fw water potentials has been compared. The effect of the water model on the conformational equilibrium of these peptides has been analysed using Ramachandran plots, clustering analyses, RDF profiles, hydrogen-bonding analysis and side-chain dihedral angle analysis. The equilibrium distribution of population over the Ramachandran plots compares favourably between the two water models for both the peptides. The populations of all regions of the Ramachandran plots were within error, apart from one in the RGD case, region **g** and even then it followed the same general trend with respect to the populations of the other regions. This difference may be due to the dielectric

constant which, for SPC/Fw, was 80 % the size of the value for TIPS3P. For both the backbone and all-atom peptide clustering analyses, sampling of conformational phase space is seen to be very similar. Populations of clusters are within error for the SPT case and follow the same general trend for the RGD case. RDFs between key atoms of the peptide and the oxygen and hydrogen water atoms showed that differences in water structuring around several groups in the tripeptide were also found to be negligible. There was a slight difference in the rate of conformational sampling. Furthermore, there were generally more transitions between the regions of the Ramachandran plot in the TIPS3P case compared to the SPC/Fw case. This was, however, entirely consistent with the 50 % lower viscosity of the TIPS3P model compared to SPC/Fw. Overall, we found that the equilibrium conformations sampled for each force field combination to be sufficiently similar which suggest that CHARMM and SPC/Fw can be combined with a reasonable level of reliability, at least for our two exemplar tripeptides. As with all force fields, regardless of their maturity, further testing will be required to establish a greater measure confidence.

In spite of the suggested compatability of the two force-fields, CHARMM and SPC/Fw, in the validation study of this chapter, it has not been used in the work of subsequent chapters. TIPS3P is computationally more efficient and has been used reliably with the CHARMM force-field in many previous studies. Furthermore, the difference in dielectric constant between SPC/Fw and TIPS3P could have a significant impact on ion-surface interactions and lead to inaccurate results concerning analysis, such as ion density distributions, which - given the importance of electric double layer (EDL) effects, particularly the change in Debye length with concentration, to many hypotheses of the 'low-salinity' effect - is particularly important. Furthermore, the silica force-field used in Chapters 4-6 was parameterised to be used with common biomolecule force-fields, including CHARMM and AMBER.

Chapter 4

Water and Ion Structure at the Aqueous Electrolyte/Amorphous Silica Interface

Silica is one of the most abundant minerals on Earth and the interface it makes with aqueous electrolyte, for example seawater or physiological solution, is ubiquitous in nature and technology. Atomistic-level insight into the structure of ions and water at the interface is of great importance to a range of commercial applications. For instance, the impact of changes to the bulk concentration of the solution would provide valuable insight into the mechanism of enhanced oil recovery (EOR) from sandstone reservoirs⁸; amorphous silica is often used as a model for the quartz grains in the sandstone pores. In EOR, as discussed in section 1.1.1, the use of low-salinity seawater in the water flooding of oil reservoirs increases oil yields compared to when normally concentrated seawater is used. Interfacial solvent structuring has previously been described as 'governing' the adsorption of organic molecules at mineral/water interfaces, an example of which is oil at the silica/water interface.²² Furthermore, many previously developed hypotheses used to explain the 'low salinity' effect and EOR, such as fines migration theory, are centered around changes to the electric double layer (EDL), a description of the distribution of ions in the region close to the surface (more details of the hypotheses and a definition of the EDL are given in section 1.1.1) The concentration dependence of interfacial ion and water structure, if there is such a dependence, is therefore of great

interest. In this Chapter, we have taken a reductionist approach, using MD simulation to investigate the interface between amorphous silica and pure saline solutions of some of the electrolyte types present in seawater: NaCl, KCl, CaCl₂ and MgCl₂, at both high and low salinity. This is in contrast to previous experimental studies designed to elucidate the mechanism of enhanced oil recovery, where the full mixture of ions present in seawater was used. Adsorption of the NH₃⁺ functionality, one of the basic functional groups in crude oil, at the interfaces of the same eight solutions with amorphous silica is considered in Chapter 5. While the proportion of nitrogen-containing compounds in crude oil, particularly aliphatic amines, is small, a significant change in the adhesion force of the R-NH₃⁺-functionalised AFM tip to the aqueous electrolyte/amorphous silica interface on changing electrolyte concentration is observed experimentally in this work (see Chapter 5) and the presence of polar functionalities is a known requirement for the 'low-salinity' effect.^{12,13,8} Furthermore, the interaction of the functionality with the aqueous electrolyte/amorphous silica interface is thus far underexplored.

The model amorphous silica surface used features both protonated and deprotonated silanols, as depicted in Figure 2.8. In this Chapter, a number of new terminologies are introduced, the definitions of which can be found in section 2.1.3.

Appendix C contains: details of the number of water molecules used in each simulation, further lateral ion and water density profiles, further angular distributions of the angle made by the O⁻-M⁺ vector and the surface normal, a summary of distances from the surface of peaks in the ion density profiles, net water orientation as a function of distance from the surface and full cos(θ) distributions.

4.1 Simulation Protocol in Brief

Classical MD simulations of the aqueous electrolyte/amorphous silica interface were conducted. The amorphous silica surface was modelled using the force-field developed by Butenuth *et. al.*,¹ while the ions were modelled using CHARMM¹¹¹ and the water by TIPS3P.¹¹⁹ After the validation work of Chapter 3, the TIPS3P water model was chosen, as it is computationally more efficient than SPC/Fw. Eight different electrolyte solutions were modelled: NaCl, KCl, CaCl₂ and MgCl₂, each at two different bulk concentrations (high salinity, 0.3 M and low salinity, 0.1 M). Full details of the general simulation protocol is given in section 2.1.2, with details specific to the amorphous

silica/aqueous electrolyte interfacial simulations described in section 2.1.2, including details of how the aqueous electrolyte/silica interface systems were constructed and modelled. These details are summarised here, with reference to a schematic in Figure 4.1. The starting configuration of the silica slab was the same as that of Butenuth *et al.*¹ An equilibrated box of water was added using the Gromacs program, genbox, followed by another Gromacs program, genion, to add ions.¹⁹⁴ The electrolyte ions were initially positioned randomly in the solution in the inter-slab space, as shown in Figure 4.1. The water density was then corrected by changing the number of water molecules and repeating the minimization and equilibration stages until the bulk water density in the centre of the inter-slab space was the same as the water density obtained from a *NPT* simulation of a bulk liquid system (without the surface present) made up of the same composition of ions and water molecules. MD simulations were run until ion density profiles had equilibrated (between 80-140 ns; the equilibration time for each case is provided in Table 2.2). After equilibration, simulations were run for a further production phase (40-60 ns, see Table 2.2 for details) for analysis. .

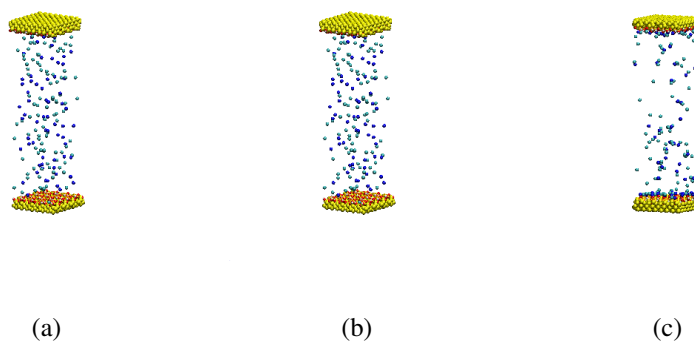


Figure 4.1: Schematic to show the start structure (left), optimised structure (centre) and final frame of MD simulation (right).

Physical details of the eight aqueous electrolyte/amorphous silica systems under investigation are provided in Section 2.1.2. All were of the same *xyz*-system dimensions. The number of water molecules needed to achieve the correct bulk water density far from the surface for each of the systems was ~ 9000 , with precise numbers given in Table C.1. For the LS systems, the 'bulk ion concentration' (*i.e.* the concentration far from the surface) was ~ 0.1 M and that for HS systems was ~ 0.3 M. The baseline of the

surface (*i.e.* $z = 0 \text{ \AA}$) was defined as the closest approach of the oxygen atoms of water molecules from solution. Full details of the surface definition, namely how the solution volume close to the surface baseline was calculated, are provided in Section 2.1.3.

4.2 Ion Concentration as a Function of Distance Normal to the Surface

4.2.1 A General Overview of the Ion Distributions

Electrolyte Type

Vertical profiles of ion concentration as a function of distance normal to the surface for the eight electrolyte solutions, aqueous NaCl, KCl, CaCl₂ and MgCl₂ at 0.1 and 0.3 M, are shown in Figure 4.2. Cation identity had a significant impact on the distributions and each had a distinct, electrolyte-dependent character. Ion structuring varied most significantly between aqueous CaCl₂ and the rest of the electrolyte solutions (NaCl, KCl and MgCl₂). For CaCl₂ solution, the interfacial cation concentration was over double that of the other aqueous electrolytes, and there was a significant presence of anions in the interfacial region that was not observed for any of the other solutions. Unlike the cations present in the other solutions (Na⁺, K⁺ and Mg²⁺), the Ca²⁺ ion density did not follow the exponential decay to bulk concentration described by Gouy-Chapman theory,^{64,65} instead changing sharply to near-bulk concentration after the two major peaks in ion density.

Electrolyte Concentration

The effects of changes in electrolyte concentration were more subtle. The main differences were intensity based. On increasing concentration, peak-surface separations, summarised in Table C.2 (Appendix C), did not alter. The width of the double layer was defined as the distance from the surface where the cation and anion concentrations were within 0.01 M of each other (as shown schematically in Figure 4.3) and was generally of a lesser width ($\sim 25 \text{ \AA}$) for the more concentrated 0.3 M solution compared to

0.1 M solution (~ 40 Å). This was as expected from the prediction of DLVO theory.¹⁶ The exception was MgCl_2 , where no decrease in the width of the double layer between 0.1 M and 0.3 M solutions was observed (both were ~ 16.5 Å in size). The Mg^{2+} ion is strongly hydrated and it has previously been reported that DLVO theory breaks down due to effects such as hydration.²²⁶ In the case of CaCl_2 , the distribution of the Cl^- counterions was non-standard; unlike the Cl^- distributions for the other electrolyte pairs, a high interfacial ion concentration was observed within 1 nm of the surface. This suggests that DLVO theory is not an effective model at describing electrolyte distributions in this case and may contribute to why the expected difference in Debye length compared to that of monovalent ions is not observed. Moreover, an increase in the intensity of the overall distributions with concentration was observed. Apart from the Ca^{2+} distributions, such increases occurred uniformly across the entire ion distribution and the general shape was maintained, the relative proportions of the peaks unchanged. For Ca^{2+} , the magnitude of peak 1 was $\sim 3\times$ bigger for 0.3 M solution compared to 0.1 M while the magnitude of peak 2 did not alter. Distinct from the other ions, a non-uniform increase in intensity was observed for the Ca^{2+} distribution on changing from 0.1 M to 0.3 M solution, with one peak in particular of increased magnitude.

Table 4.1: Predicted width of the double layer (from simulation) for the different electrolyte solutions.

Electrolyte Type	Width/Å
LS NaCl	42.7
HS NaCl	24.9
LS KCl	39.8
HS KCl	24.2
LS CaCl_2	41.5
HS CaCl_2	25.4
LS MgCl_2	16.6
HS MgCl_2	16.4

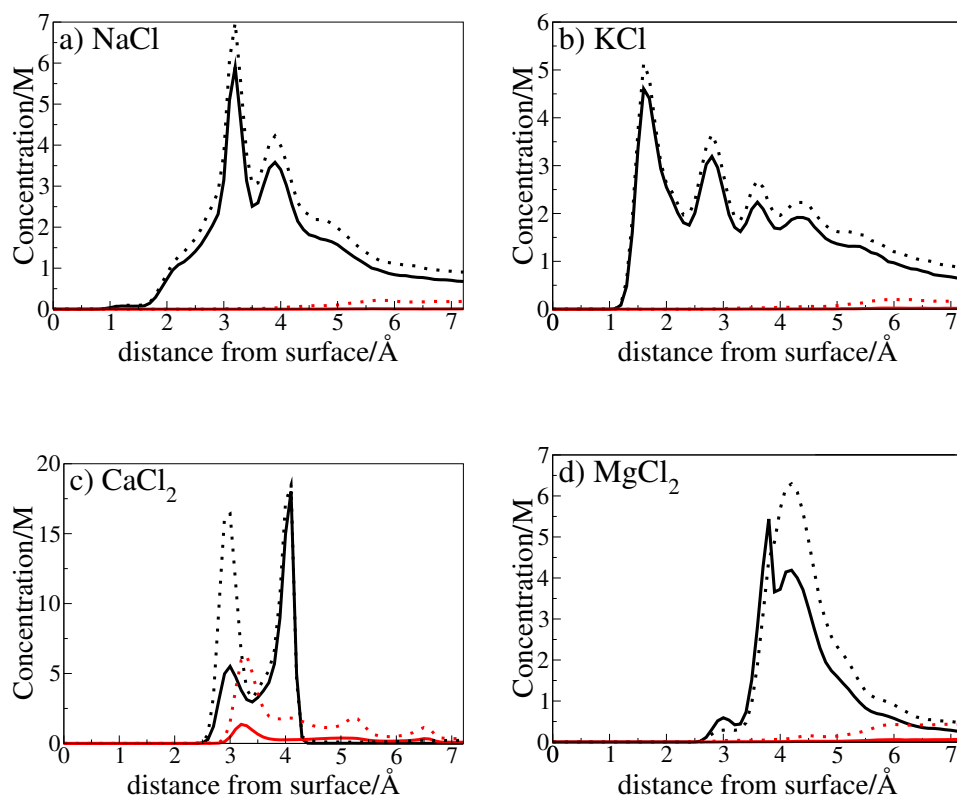


Figure 4.2: Ion concentration as a function of distance from the surface for the ions in the NaCl, KCl, CaCl₂ and MgCl₂ solutions (low salinity - LS 0.1 M, high salinity - HS 0.3 M). Cation concentration is represented by black and anion concentration is represented by red. For these two colours, the solid lines represent LS solution and the dashed lines HS. However, in the majority of cases only the dark blue function is visible, as it overlays the light blue. LS and HS refer to the 'bulk' concentrations *i.e.* the concentrations far from the surface.

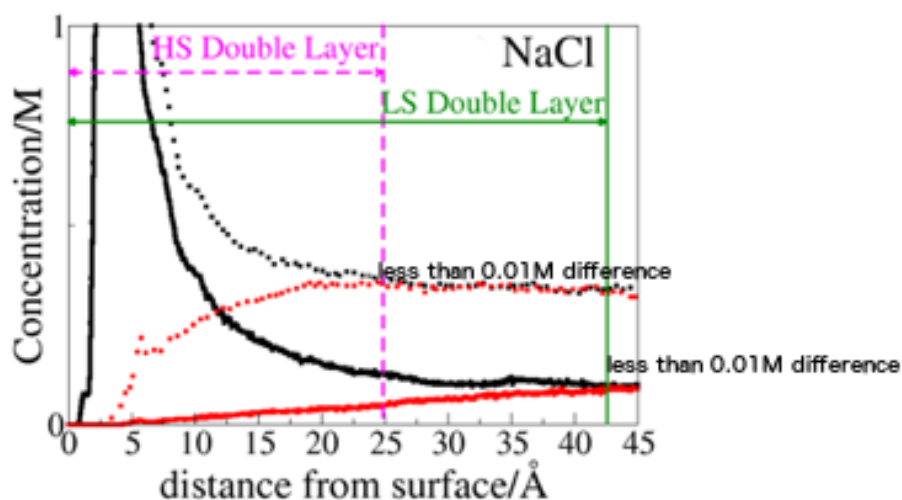


Figure 4.3: Schematic of how the thickness of the EDL was calculated from ion density distributions, using aqueous NaCl as an example.

4.2.2 Deprotonated Silanol Groups: the Key Surface Adsorption Site

Another probe of interfacial structure in the electrolyte is to examine the distribution of ions about specific features of the silica surface. We have therefore calculated radial distribution functions (rdfs) for each of the cations about the deprotonated surface silanol groups. Figure 4.4 shows rdfs between the negatively charged, deprotonated silanol groups on the silica surface and each of the types of cation studied (Na^+ , K^+ , Ca^{2+} and Mg^{2+}). All featured a dominant peak centered at $\sim 2\text{\AA}$ that represented direct cation- O^- adsorption, which suggested that such adsorption could dominate the interfacial distributions of cations. The precise peak positions and the corresponding cation Lennard Jones σ values are given in Table 4.2. The smaller the σ value, the closer the ion was able to approach the O^- adsorption site. For the comparably-sized Na^+ and Ca^{2+} ions, the more highly charged Ca^{2+} approached more closely due to increased electrostatic attraction. Of all of the cations, Ca^{2+} had by far the greatest affinity for the O^- adsorption site, with the peak in the Ca^{2+} - O^- rdf $4\times$ greater than that in the Mg^{2+} - O^- rdf (the rdf with the next greatest peak height) and $26\times$ the smallest, the major peak in the K^+ - O^- rdf.

Table 4.2: Summary of cation- O^- RDF first peak separations and corresponding cation σ values.

Solution	Concentration/M	Ion	distance from $O^-/\text{\AA}$	$\sigma/\text{\AA}$
MgCl ₂	0.1 & 0.3	Mg ²⁺	1.78	2.11
CaCl ₂	0.1 & 0.3	Ca ²⁺	2.08	2.44
NaCl	0.1 & 0.3	Na ⁺	2.16	2.43
KCl	0.1 & 0.3	K ⁺	2.56	3.14

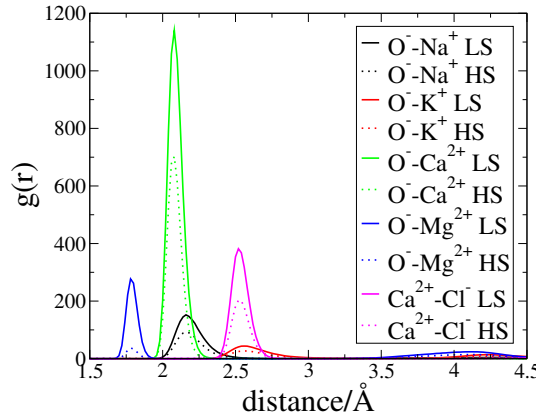


Figure 4.4: Rdfs between the deprotonated silanol O^- and all cation types studied (Na^+ , K^+ , Ca^{2+} and Mg^{2+}) and rdf between $Ca^{2+}_{(O^-)}$ ions and Cl^- .

In order to test this hypothesis - that the interfacial distribution of cations was dominated by adsorption to the surface O^- groups - further, we have used the O^- -cation rdfs to decompose the surface density profiles into contributions from ions that are strongly associated with the surface O^- , and those that are not. In most it was sufficient to use the first peak in $g(r_{(O-M)})$ to define 'strongly associated', though for Mg^{2+} we found it useful to consider both the first and second peaks. The resulting distributions are provided in Figure 4.5 and termed contribution to the surface z -density profile (CSDP) herein. The full notation, CSDP(O^- -MrdfpN), is used to indicate which peak of the O^- -M rdf was being considered, where N = 1 or 2, represents the first or second peak of the rdf, respectively. The coincidence of the majority of peaks clearly demonstrated that cations specifically-adsorbed to O^- were major contributors to peaks in the overall distributions. Adsorption to the O^- site particularly dominated surface- Ca^{2+} interactions and the z -density distributions were almost exactly reproduced. In contrast,

the literature commonly describes the different peaks present in the concentration vs distance profiles as being due to inner-sphere and outer-sphere complexes.¹⁰⁰

Lateral cation density profiles at the distances of the maxima of the z -density profile, referred to as $\rho_{Zmax}(xy)$ herein (where max identifies the particular maximum being considered, *e.g.* p1 or p2), for 0.1 M CaCl₂ solution, a case where both peaks were coincident, are shown in Figure 4.6. The xy -coordinates of the O[−] atom and the oxygen atoms of the protonated silanols, which occurred at different z -distances from the surface to those of the considered xy -planes, were superimposed on the profiles. Rings of high density surrounded the location of the surface O[−] atoms and provided further confirmation of O[−] as the primary adsorption site for cations. Further examples of such profiles are given in Figure C.1 and C.2 for 0.1 M and 0.3 M solution respectively (Appendix C). The specific adsorption of cations to the deprotonated silanols largely accounted for interfacial ion structuring, particularly that of Ca²⁺.

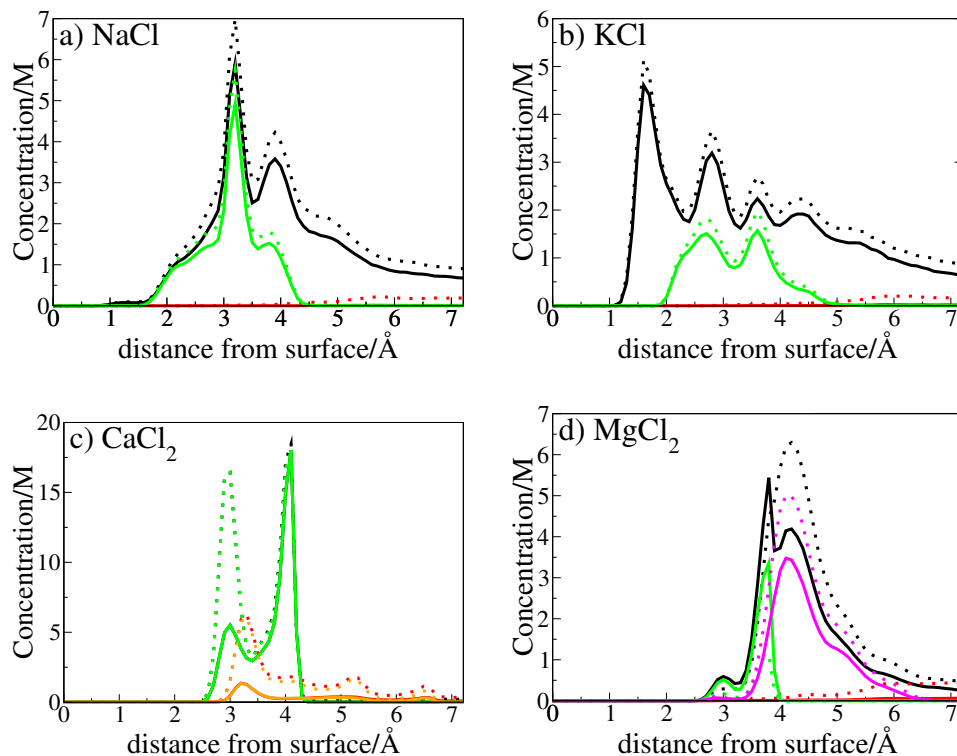


Figure 4.5: Contribution to the surface density profile arising from cations associated with the first peak of the deprotonated silanol-cation rdfs (Figure 4.4), CSDP(O^- -Mrdfp1) . Analogous data is given for the second rdf peak for MgCl_2 (CSDP(O^- - Mg^{2+} rdfp2)) and the first rdf peak of the O^- -associated calcium-chloride rdf CSDP(O^- - Ca^{2+} - Cl^- rdfp1). The complete surface density profiles are reproduced from Figure 4.2 to aid comparison. As in Figure 4.2, cation concentration is represented by black and anion concentration is represented by red. Green represents the CSDP(O^- -Mrdfp1) and, for MgCl_2 , pink is the CSDP(O^- - Mg^{2+} rdfp2). Orange represents the CSDP(O^- - Ca^{2+} - Cl^- rdfp1). The solid lines represent LS solution and the dashed lines HS. In part c) of this diagram, the CSDP(O^- - Ca^{2+} rdfp1) overlays the complete Ca^{2+} density profile and CSDP(O^- - Ca^{2+} - Cl^- rdfp1) the Cl^- density profile for both LS and HS.

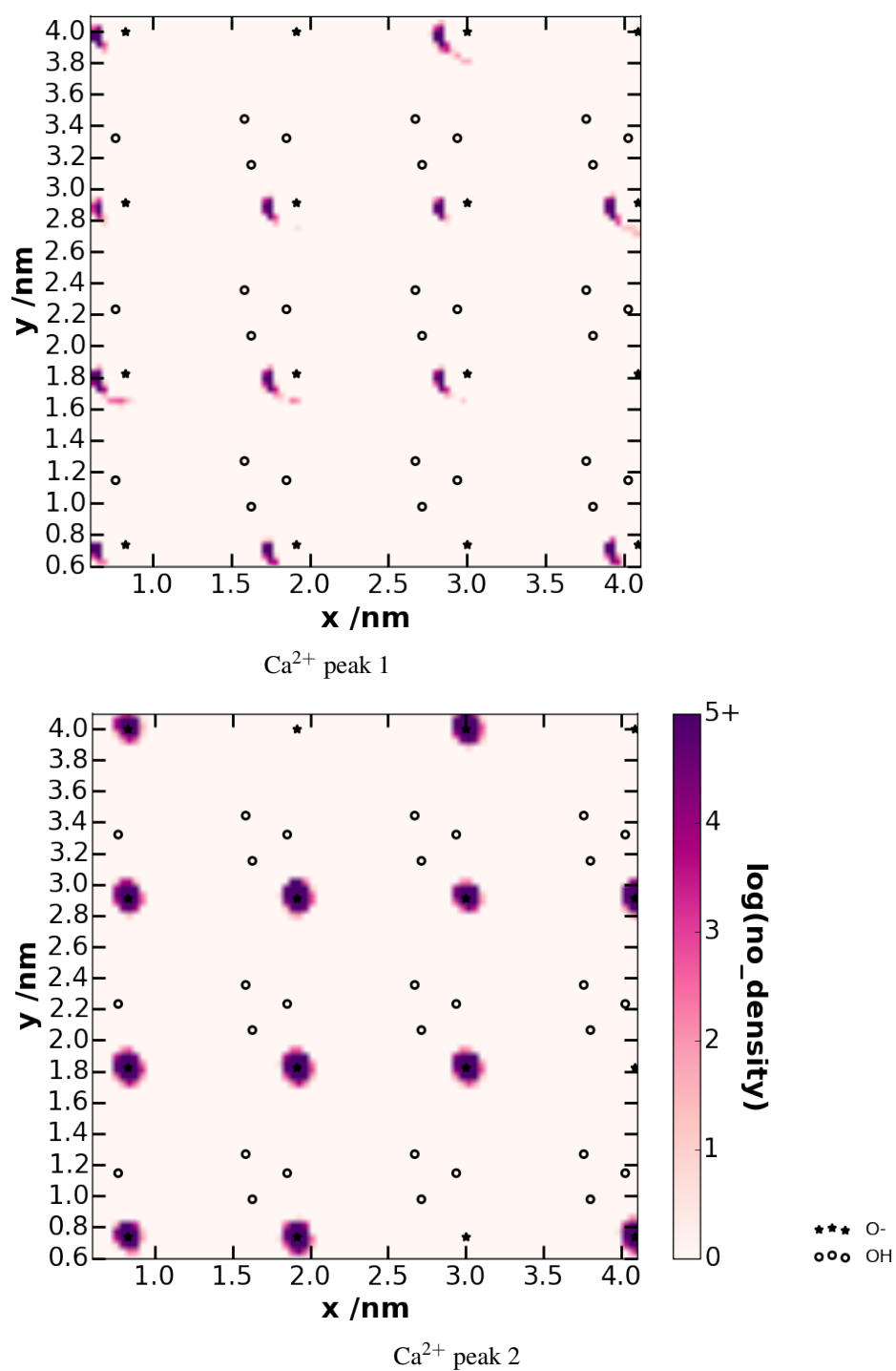


Figure 4.6: $\rho_{Z_{max}}(xy)$ (*i.e.* lateral distribution of cations found within a horizontal layer of thickness 0.1 Å and centred on the peaks in density as shown in Figure 4.2c) for CaCl₂ solution (LS 0.1 M). The units of the number density are arbitrary and the same in all lateral profiles throughout this section.

A broad second peak, centered at 4.08 Å, featured in the O^- - Mg^{2+} rdf, Figure 4.4. This represented solvent separated Mg^{2+} - O^- pairs. CSDP(O^- - Mg^{2+} rdfp2), shown in Figure 4.5d, indicated that solvent separated Mg^{2+}/O^- pairs were the prime contributor to the broad peak centered at 4.2 Å from the surface in the Mg^{2+} ion density profile. The two peaks in the rdf translated to two overlapping peaks when CSDP(O^- - Mg^{2+} rdfp1) and CSDP(O^- - Mg^{2+} rdfp2) were combined. It was the relative magnitudes of the two peaks in the O^- - Mg^{2+} rdfs that determined the number of peaks in the full Mg^{2+} density distributions, Figure 4.2d. The magnitudes were such that the two overlapping peaks effectively merged to one in the 0.3 M case. Cations from solvent separated Mg^{2+}/O^- pairs made a significant contribution to the interfacial structure of the cation. The rdf, $g(r_{(Ca^{2+}-Cl^-)})$ (Figure 4.4), shows a single peak at 2.52 Å, while the CSDP (Figure 4.5c) indicates that $Cl^-_{((M)-O^-)}$ and $Cl^-_{(Cl^--(M)-O^-)}$ were the only Cl^- in the interfacial region (2.8-6.9 Å).

The discussion above noted that the surface O^- affected the interfacial cation distribution, which in turn affected the anion distribution. One outworking of this hierarchy of interactions is that it becomes useful to identify several different types of site: O^- ; Ca^{2+} -associated O^- ; $Ca^{2+}Cl^-$ -associated O^- ; and $Ca^{2+}Cl^-_2$ -associated O^- . Figure 4.7 shows the $\rho_{Zmax}(xy)$ profiles for the Cl^- distributions presented in Figure 4.2c for 0.1 M solution (Figure C.3, Appendix C, shows those for 0.3 M solution). Clear structuring around the O^- sites and thus O^- associated Ca^{2+} ions was observed. The specific adsorption of Cl^- ions to Ca^{2+} ions associated with deprotonated silanols accounted for the interfacial anion structure in the $CaCl_2$ case.

For all cation types, the single peak in the O^- -cation rdf translated to several peaks in the corresponding CSDP. This suggested that cation adsorption was more favourable at certain parts of (*i.e.* orientations from) the deprotonated silanols than others *i.e.* different parts of the surface area of the O^- atom corresponded to different chemical environments. The O^- ions protuded further from the surface than any other component of the silica, being 2.1 Å above the surface and, thus, were very exposed. It was possible for the cation to adsorb to the top area of the O^- atom or to regions closer to the surface, where further chemical environments resulted from the surrounding non-uniform structural arrangement of atoms and chemical groups, as shown schematically in Figure 2.8. The balance of attractive and repulsive forces that O^- -adsorbed ions would experience in the different chemical environments was a key factor in determin-

ing the resultant distribution. The atoms and chemical groups surrounding O^- , as well as how exposed or distant from the surface the particular part of the O^- surface area the cation was interacting with was, had an impact on the association of ions, which resulted in adsorption to certain parts of the O^- atom being more favourable than others.

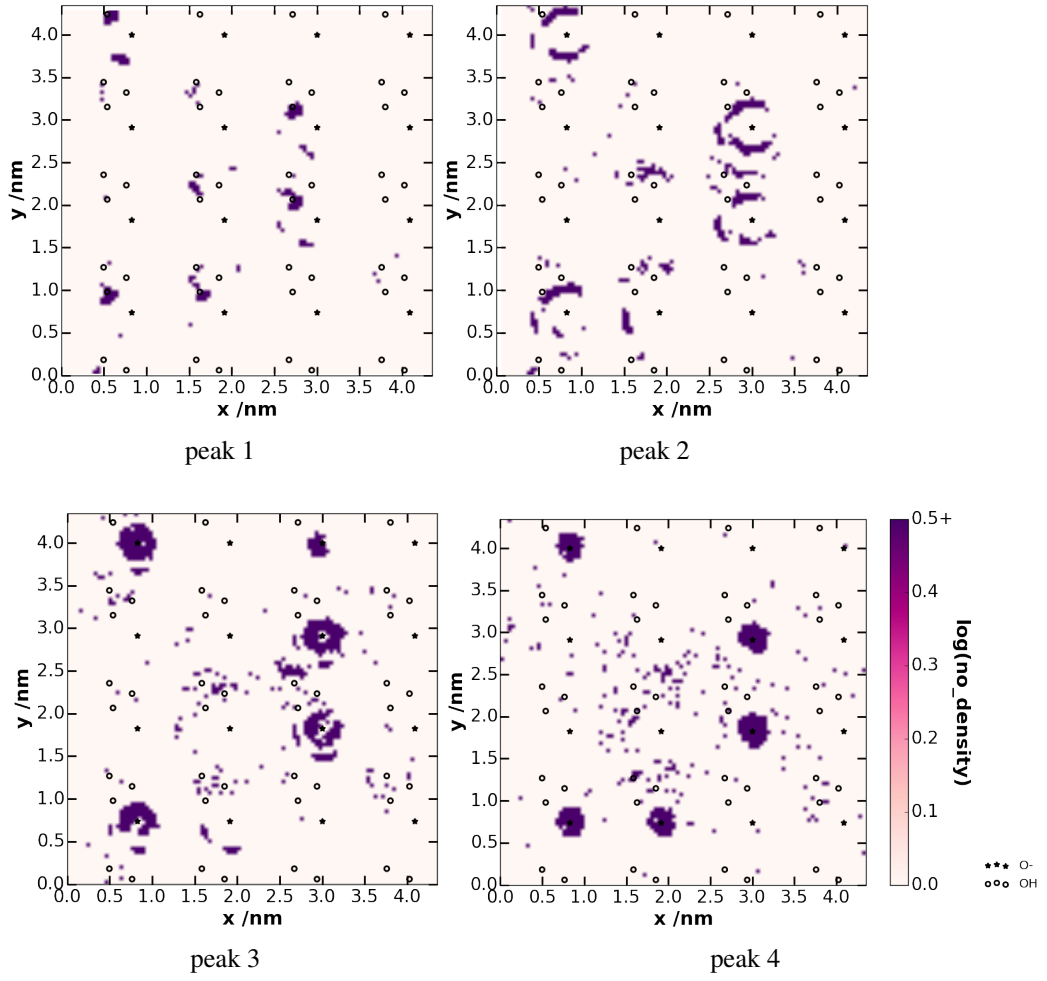


Figure 4.7: $\rho_{Zmax}(xy)$ (*i.e.* lateral distribution of Cl^- ions found within a horizontal layer of thickness 0.1 \AA and centred on the peaks in density as shown in Figure 4.2c) for CaCl_2 solution (LS 0.1 M). The units of the number density are arbitrary and the same in all lateral profiles throughout this section.

4.2.3 Distributions of the Angle Between the Surface Normal and the O^- -M Vector

Angular Distributions - a Brief Methods Section

In addition to the lateral $\rho_{Zmax}(xy)$ profiles, further information regarding the chemical environment associated with each peak was provided by distributions of the angle made between the surface normal and the vector that connected O^- to the associated ion as shown in Figure 4.8. An angle of 0° represented ions that adsorbed directly atop the O^- atom. The angle was assigned as negative if $M(x) - O(x) < 0$ and positive if $M(x) - O(x) > 0(x)$. Angular distributions were recorded for particular z -ranges that were chosen to correspond to peaks in the z -density. For Ca^{2+} , the impact of associated Cl^- ions on the angular distribution was also probed. The lateral ion density profiles provided a detailed description of the preferred positions of the adsorbed ions in the xy -plane at specified distances from the surface. Angular distributions and lateral ion density profiles, recorded for all cations and, for aqueous $CaCl_2$, Cl^- ions, provided insight into the different chemical environments responsible for the peaks in the ion z -density profiles (Figure 4.2).

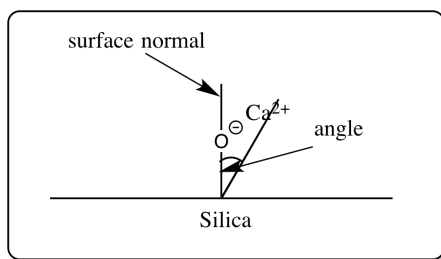


Figure 4.8: Schematic of the angle made between the surface normal and the O^- - M^+ vector.

Angular Distributions: aqueous $CaCl_2$

The $O^-Ca^{2+}Cl^-_2$ case will be considered first. The overall angular distributions for Ca^{2+} , Figures 4.9 and C.5 (Appendix C) for 0.1 M and 0.3 M solutions respectively, featured a sharp peak at -76° , associated with ions in the first peak of the ion z -density

profile (Figure 4.2c), and a broad, bimodal distribution centered at 0° with peaks at -27° and 16° , corresponding to ions in the second peak of the cation z -density distribution. $\rho_{Zp1}(xy)$ (Figure 4.6), showed a patch of high density from the centre-to-lower left of the O^- atom centre, where stronger interactions with surface bridging oxygens and some of the silanol oxygens were possible due to the decreased distance to the associated Ca^{2+} ion. The decreased distance for such ions was further confirmed by distributions of the distances of Ca^{2+} ions in peak 1 and peak 2 of the z -density distribution to the different silanols are given in Figure 4.10. $\rho_{Zp2}(xy)$ (Figure 4.6) confirmed that adsorption at this distance occurred directly above the centre of the O^- atom.

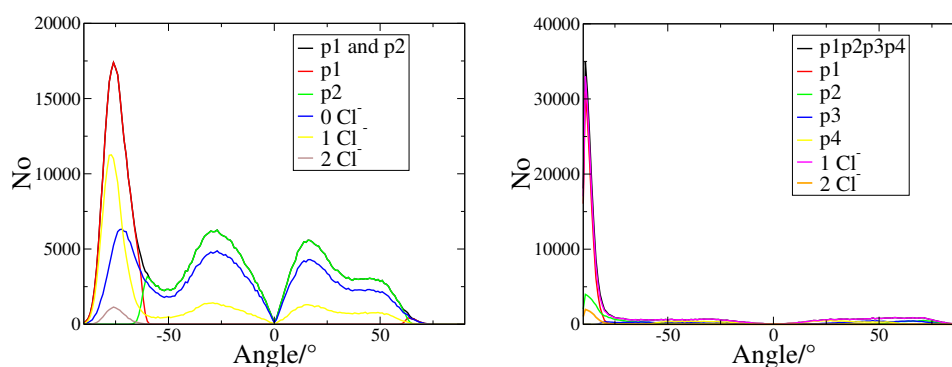


Figure 4.9: Distributions of the angle made between the surface normal and: (a) r_{Ca-O} , where $r_{Ca-O} = r_{Ca} - r_O$ (b) r_{Cl-O} , where $r_{Cl-O} = r_{Cl} - r_O$. p refers to the particular peak in the CSDP(rdfp1) and n Cl⁻ indicates the distributions when n Cl⁻ ions were associated. Cos(θ) distributions are presented in Appendix C.

The relative proportions and exact values of the peaks in the angular distributions were dependent on how many chloride ions associated with the Ca^{2+} - O^- ion pair. When zero Cl⁻ ions were associated, the angular distribution sampled all three peaks with approximately the same magnitude. Upon increasing to one associated Cl⁻ ion, a 6-8 \times increase in the single peak at -76° was observed relative to the peaks of the bimodal distribution. Only the single peak was observed when 2 Cl⁻ ions were attached. Furthermore, the single peak moved from -72° when zero Cl⁻ ions were associated to -76 to -77° when there were 1-2 associated Cl⁻ ions. This suggested that repulsion between the highly electronegative O^- site and any associated Cl⁻ ions was minimised when Ca^{2+} could adsorb to this region of the atom surface area (*i.e.* at this orientation). Adsorption of Ca^{2+} to O^- occurred in two distinct environments: directly above

the O^- atom centre, peak 2 of the Ca^{2+} z -density profile; and closer to the surface at $x < \text{O}^-(x)$ and $y < \text{O}^-(y)$, a position which likely facilitated maximum shielding between the highly electronegative O^- and any associated Cl^- ion(s), peak 1 of the Ca^{2+} z -density profile.

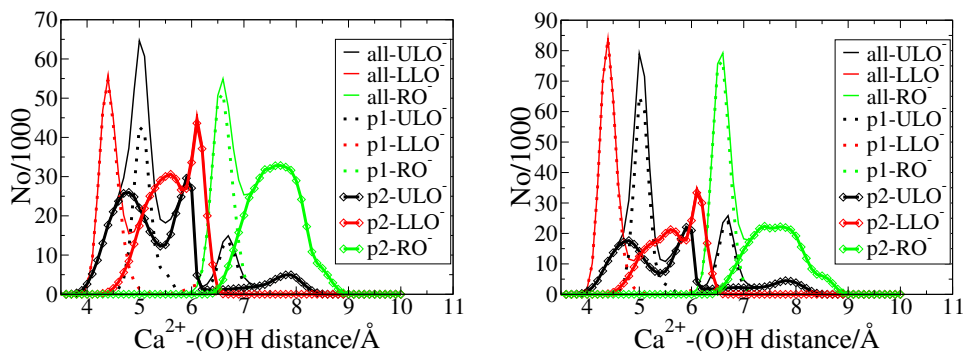


Figure 4.10: Distributions of the distances to the three different protonated silanols for Ca^{2+} ions in peak 1 and 2 of the z -density distributions (LS, 0.1 M and HS, 0.3 M). UL stands for upper left, LL lower left and R right and are defined in Figure 2.8.

Ca^{2+} -associated Cl^- ions also adsorbed at characteristic angles with respect to the surface normal, as shown in Figure 4.11. The predominant angle, -89° , was even more negative than that of the single peak in the Ca^{2+} angular distribution and corresponded to ions in the first and second peak of the Cl^- z -density distribution (Figure 4.2c). Figure 4.12 shows that Cl^- ions that adsorbed at this extreme angle were largely associated with cations in the first peak of the Ca^{2+} z -density distribution. Cl^- ions at an angle of -89° were approximately in the same xy -plane as the silica O^- ion, which, given the surface topology in the region and the corresponding orientations of associated Ca^{2+} , indicated that the ion was within a hollow of the surface and supported the idea of increased shielding for ions associated with such Ca^{2+} ions. $\rho_{Zp1}(xy)$, Figures 4.7 and C.3 (Appendix C), showed a high density of Cl^- to the upper left of the O^- centre. A partial ring of high density surrounded the O^- centre $\rho_{Zp2}(xy)$, with the very highest density concentrated above and below the atom in the xy -plane. The non-uniform preferences reflected the location of surface hollows that enabled maximum O^- - Cl^- shielding. The angular distributions formed by Cl^- ions in the third and fourth peaks of the Cl^- z -density profile were symmetric and spread sparsely over a wide range of angles from -84 - 84° and -64 - 64° respectively. The symmetry indicated that

the distribution was not biased by surface topology differences either side of the O^- site at these further distances from the surface. $\rho_{Zp3}(xy)$ and ρ_{Zp4} , Figures 4.7 and C.3 (Appendix C), showed that there was a high density circular region of Cl^- ions directly above the O^- centre, and thus associated Ca^{2+} ions from peak 2 of the Ca^{2+} z -density distribution. The ability of the Cl^- ion to adsorb at the extreme angle of -89° , *i.e.* within a hollow close to the surface where the O^- - Cl^- repulsive force was at a minimum, was facilitated by the adsorption of Ca^{2+} ions at distances within the first peak of the z -density profile.

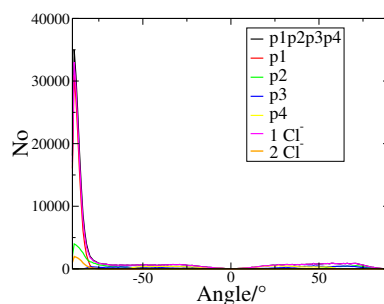


Figure 4.11: Distributions of the angle made between the surface normal and r_{Cl-O} , where $r_{Cl-O} = r_{Cl} - r_O$ ($CaCl_2$) (LS 0.1 M). p refers to the particular peak in the CSDP(rdfp1)

The increased magnitude of the first peak in the Ca^{2+} z -density profile (Figure 4.2c) on changing from 0.1 M to 0.3 M solution could be linked directly to changes in the Ca^{2+} angular distributions, where it mainly translated to ions represented by the single peak centered at $\sim -76^\circ$. In such angular distributions, the magnitude of the single peak relative to that of the bimodal distribution doubled on increasing concentration from 0.1 M, where it was $3\times$ bigger, to 0.3 M, where it was $6\times$ the size. This, together with that fact that the single peak in the angular distribution was predominantly due to Ca^{2+} with associated Cl^- ions, suggested the proportion of $O^-Ca^{2+}Cl^-$ and $O^-Ca^{2+}Cl^-_2$ sites had altered with concentration. Table 4.3 lists the calculated proportions of the different site types. $O^-Ca^{2+}Cl^-$ and $O^-Ca^{2+}Cl^-_2$ were, indeed, more predominant at the interface with the more highly concentrated 0.3 M solution compared to 0.1 M. The significant increase in the intensity of the first peak in the Ca^{2+} z -density profile for 0.3 M solution compared to 0.1 M was a result of the formation of a greater proportion of O^- sites with associated Cl^- ions.

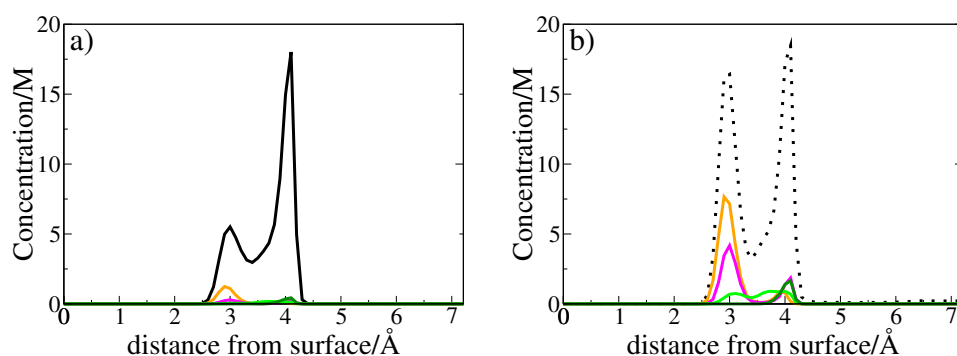


Figure 4.12: CSDP arising from Ca^{2+} that have chloride ions from a particular peak ($p = p1, p2, \dots$ where $p1$ is the first peak, *etc*) in the Cl^- z -density distribution associated with them. The complete surface density profiles for Ca^{2+} z -density are reproduced from Figure 4.2 to aid comparison. As in Figure 4.2, cation concentration is represented by black and the solid lines represent LS solution, while the dashed lines represent HS. The CSDP is given in solid lines of different colours in both the LS, 0.1 M subfigure (a) and the HS 0.3 M subfigure (b): Orange for Ca^{2+} with Cl^- from $p1$ of the Cl^- z -density profile, pink for $p2$, light green for $p3$, dark green for $p4$.

Table 4.3: Time averaged proportion of different site types in CaCl_2 solution.

Site Type	Concentration/M	Proportion/%
O^-	0.1	28.6
	0.3	4.7
$\text{O}^- \text{Ca}^{2+}$	0.1	46.0
	0.3	28.1
$\text{O}^- \text{Ca}^{2+} \text{Cl}^-$	0.1	24.1
	0.3	51.9
$\text{O}^- \text{Ca}^{2+} \text{Cl}^-_2$	0.1	1.3
	0.3	19.9

Angular Distributions: The Other Aqueous Electrolytes

Angular distributions for the other cations (Na^+ , K^+ and Mg^{2+}) shared some common features with that of Ca^{2+} (Figures C.4 and C.5, Appendix C). The first peak in the CSDP(O^- -Mrdfp1) of the O^- -cation rdf, Figure 4.5, always translated to a distribution with either one peak at an extreme (*i.e.* greater than 70° in magnitude) negative angle (Mg^{2+}) or two at both extreme negative and positive angles. The second peak, however, always corresponded to a bimodal distribution centered at 0° . The angular distribution for Mg^{2+} was thus most similar to Ca^{2+} , though, in contrast, the bimodal distribution dominated relative to the peak at an extreme negative angle and was not symmetric in terms of magnitude, with a bias to negative values. Both divalent, the ions were the most highly charged and had the highest charge densities of the range studied, which indicated that electrostatic factors were an important influence. For Na^+ and K^+ , the bimodal distributions were both biased to positive values. While of approximately equal magnitude in the K^+ case, the extreme angle peak in the negative part of the distribution was $\sim 2\text{-}3\times$ the size of that in the positive part. Although all angular distributions featured a bimodal distribution centred at 0° and one extreme negative angle peak or two extreme negative and positive angle peaks, their relative magnitudes differed.

4.2.4 Alternative Surface Adsorption Sites

The extent to which the CSDP(O^- -Mrdfp1)s reproduced the ion z -density distributions was dependent on the electrolyte. For aqueous CaCl_2 , the ion z -density profiles were

reproduced almost exactly, Figure 4.5c, while, at the other extreme, the K^+ -distributions were not reproduced either in terms of the full shape or peak magnitude, Figure 4.5b. In cases where the ion z -density distributions were not fully reproduced, there were significant alternative adsorption sites.

For K^+ , such alternative adsorption sites were particularly important. $\rho_{Zp1}(xy)$ (Figures 4.13 and C.2, Appendix C) showed an area of very high density to the right of the silanol groups that represented adsorption in a surface hollow where K^+ interacted with several bridging oxygens simultaneously. This interaction was solely responsible for peak 1 in the K^+ z -density distribution, the peak with the greatest magnitude. The large size of K^+ compared to the other cations may have particularly favoured the interaction. Less intense high density regions associated with further bridging oxygens and the oxygens of silanol groups were observed in the lateral profiles at the distances of the other peaks. Such chemical groups also acted as significant subsidiary adsorption sites for Na^+ and Mg^{2+} . A previous investigation of Li-, Na-, and K-Wyoming montmorillonites using Monte Carlo simulations found that K^+ behaved differently to the other monovalent ions.²²⁷ Upon hydration, Li^+ and Na^+ detached from the surface, whereas K^+ was reluctant to hydrate and remained bound to the clay surface. The negative charge of K^+ -saturated clays is thus more effectively shielding and the interaction of clay particles less likely, inhibiting clay swelling and oil recovery through this mechanism. Cygan *et. al.* investigated the influence of the hydration enthalpies of divalent ions (Mg^{2+} and Ca^{2+}) on clay swelling (montmorillonite and beidellite clay minerals) using Monte Carlo simulations.²²⁸ It was found that even at very low water content (2-4 $H_2O.u.c^{-1}$ for montmorillonite and 4-6 $H_2O.u.c^{-1}$ for beidellite) the divalent ions hydrate. This was correlated with interlayer expansion. Bridging oxygens and silanols were important alternative adsorption sites for cations, particularly for K^+ where a simultaneous interaction with a closely spaced set of bridging oxygens in a surface hollow was responsible for the largest peak in the ion z -density profile.

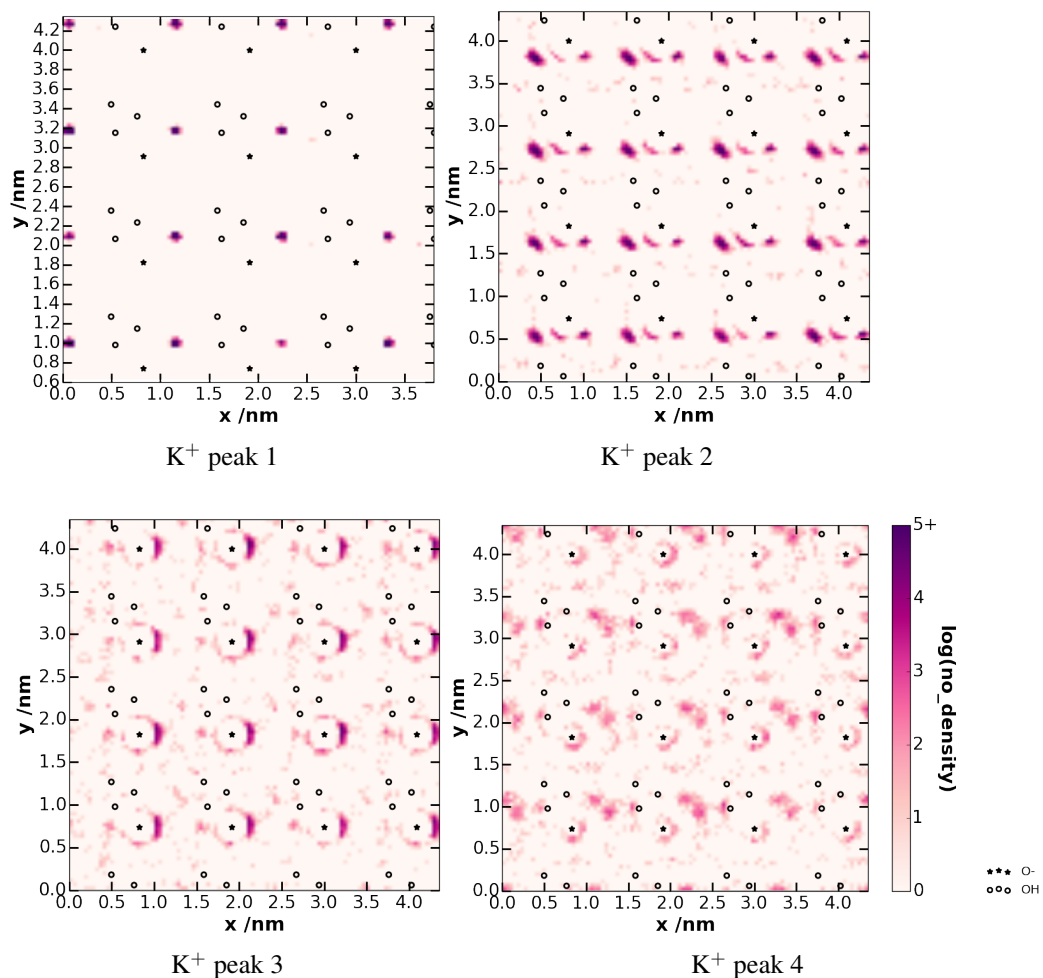


Figure 4.13: $\rho_{Zmax}(xy)$: lateral cation density profiles at maxima in the ion concentration vs distance from the surface distributions for KCl solution (LS 0.1 M). The units of the number density are arbitrary and the same in all lateral profiles throughout this section. (Note that the graph for K^+ peak 1 is zoomed-in compared to those of the other peaks, to show the smaller areas of high density in a greater level of detail.)

4.2.5 Comparisons to Previous Work

The interface between alkali chloride (NaCl and CsCl) solutions in the presence of two types of idealized charged surface (one with charge density localised at discrete sites and the other with a homogeneously distributed charge) and a realistic model of the amorphous silica surface was investigated in the 2014 MD simulation study of Borguet *et. al.*¹⁰⁰ The depth of the interfacial region - defined as the distance over which water shows a net polar ordering - was correlated with the extent of adsorption of cations on the surface. Indeed a diffuse layer did not exist for the surface with discrete charge sites, with all ions adsorbing directly to the surface. This interfacial region had two distinct regions: a compact layer close to the surface which exhibited oscillations in water orientation and a diffuse layer. The diffuse layer depth was dependent on ionic strength (as expected from DLVO theory) and the type of charge distribution. For the more realistic model of amorphous silica, Na⁺ ions were found to directly bind to the silica surface, while Cs⁺ did not. While the direction of the orientation of water molecules and the width of the compact layer were dependent on cation type, the depth of the diffuse region was independent of cation type and persisted for ~ 1 nm, *i.e.* 3-4 monolayers from the negatively charged surface.

The work of Borguet *et. al.* - in particular that concerning the aqueous NaCl/silica interface - will now be compared to our study.¹⁰⁰ It was not possible to discern whether the major peak in the Na⁺ density profile occurred at the same distance from the surface as the first peak in our study, as a definition of the zero distance of from the surface, in our study given as the closest the O atoms of water molecules approached the surface, was not provided in this study. Since concentration was given in arbitrary units in the density profile of the Borguet *et. al.* study, comparison of absolute values of the major peaks between the two studies was also not possible. Furthermore, the surface charge density considered by Borguet *et. al.* was more negative than in our study, -0.208 C m² (*i.e.* pH 10-11) compared to -0.136 C m² (*i.e.* pH 5.5), and the electrolyte concentration, 0.35 M, was greater than our most concentrated solution, 0.3 M. While the force-fields used to model the water and ions, CHARMM27¹¹¹ and TIP3P,¹⁰² were common to both investigations, the potentials and the structural model used to describe the silica surface differed.^{1,99} The major peak in the Na⁺ concentration profile was $\sim 15\times$ the size of the largest peak in the Cl⁻ density, compared to in our study where

the magnitude of the first peak was $\sim 15000\times$ the interfacial Cl^- concentration. While Borguet *et. al.* observed 3 clear peaks in the Cl^- density, in our study, the concentration gradually increased to the bulk value of 0.3 M. Given the greater negative surface charge density and greater electrolyte concentration in the Borguet *et. el.* study compared to our work, this was the opposite of the expected trend. However, the width of this region of increased Na^+ density, $\sim 5 \text{ \AA}$, was common to both studies. Although the interfacial Na^+ density profile was of a similar shape between the two studies, interfacial Cl^- ion structuring was much increased in the investigation of Borguet *et. al.*.

Underwood *et. al.* investigated interfacial ion structure at the aqueous NaCl and CaCl_2 at the interface with a similar clay mineral, montmorillonite.¹¹ The electric field strength as a function of distance from the surface (up to 2 nm) was recorded for the two electrolytes, at a range of concentrations, including 'fresh water', 'low salinity', 'high salinity' and 'seawater'. Not only were identical trends observed for both Na^+ and Ca^{2+} , the concentration had no impact on the width of the double layer. Hypotheses which feature EDL expansion or ion-type dependent differences in the debye length are thus not supported. Similarly, in our study, the width of the EDL was not observed to change between Na^+ and Ca^{2+} ion types. However, for three of the four electrolytes studied (NaCl, KCl and CaCl_2), the width of the EDL did change when electrolyte concentration was varied between 0.1 and 0.3 M.

4.2.6 Interfacial Ion Structure Summary

Ion structuring at the aqueous CaCl_2 /silica interface displayed a distinct behaviour compared to that of the other electrolyte solutions investigated (NaCl, KCl and MgCl_2). The most significant behavioural differences were the presence of Cl^- ions in the interfacial region and the change in the relative magnitude of the peaks in the Ca^{2+} z -density with increased concentration. Deprotonated silanol groups, which acted as major adsorption sites for all cation types, were particularly important for Ca^{2+} and the Ca^{2+} z -density profile was almost exactly reproduced by the CSDP(O^- - Ca^{2+} rdfp1) (Figure 4.5c). Alternative adsorption sites, namely bridging oxygens and silanols, were of greater significance for the other cation types. Indeed, the first and largest peak in the K^+ z -density profile was solely due to the interaction of the ion with several bridging oxygens simultaneously (K^+ peak 1, Figure C.1). Interfacial Cl^- structuring, unique to

the CaCl_2 case, was a result of the association of $\text{Cl}^-_{((\text{Ca}^{2+})-\text{O}^-)}$ or $\text{Cl}^-_{(\text{Cl}^--(\text{Ca}^{2+})-\text{O}^-)}$, as demonstrated by CSDP(O^- - Cl^- -rdfp1) (Figure 4.5c). Ca^{2+} ions with associated Cl^- ions were primarily represented by the first peak in the Ca^{2+} z -density profile, as supported by select distributions of the angle made between the vector that connected associated cations to O^- and the surface normal (Figure C.4c). Such Ca^{2+} ions facilitated the adsorption of Cl^- ions at an extreme angle of $\sim -89^\circ$ with respect to the surface normal, which, with the O^- and Cl^- ions almost exactly alligned in an xy -plane, physically translated to a position within a surface hollow where repulsion between the highly electronegative O^- and Cl^- was minimised. This has been shown schematically in Figure 4.14. The change in magnitude of the first peak in Ca^{2+} z -density relative to the second on increasing concentration was a response to the greater proportion of O^- sites with associated Cl^- ions in 0.3 M solution compared to 0.1 M (Table 4.3). While the association of cations to deprotonated silanols was common to all aqueous electrolytes and particularly dominated interfacial interactions in CaCl_2 solution, Cl^- ions only associated with O^- adsorbed Ca^{2+} and were responsible for the change in the relative magnitudes of the two peaks in the Ca^{2+} z -density profile, a change largely driven by O^- - Cl^- repulsion.

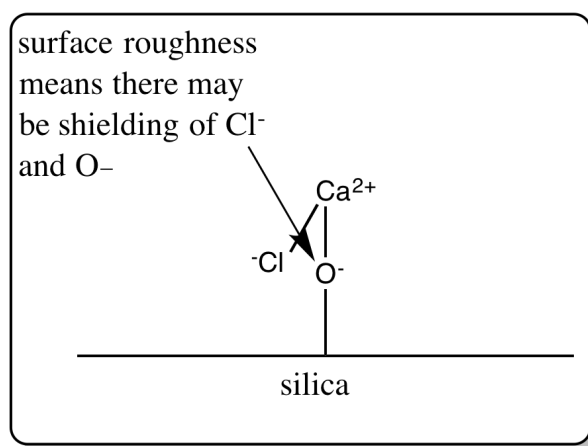


Figure 4.14: Schematic of the adsorption of Cl^- to surface adsorbed Ca^{2+} at an angle of $\sim 89^\circ$ with respect to the surface normal.

4.3 Interfacial Water Structure

4.3.1 Water Density as a Function of Distance Normal to the Surface

The density profile for water oxygen atoms for each of the electrolyte solutions are presented in Figure 4.15. CaCl_2 solution was the only solution for which the water oxygen atom distribution differed with electrolyte concentration. Water density distributions did, however, follow the same general trend for all of the electrolyte solutions, featuring at least three main broad peaks, centered at distances from the surface of 1 Å, 2.9 Å and, for the last peak, 6.2 Å for CaCl_2 solution and 5.9 Å for the other aqueous electrolytes. The first water peak was located before the centres of the uppermost atoms (deprotonated oxygens) of the silica surface at 2.1 Å from the surface. The third primary peak was smooth and rounded for all solutions except aqueous CaCl_2 , where it was sharper and more asymmetric. For 0.3 M CaCl_2 solution, the second major peak was reduced in magnitude compared to that in 0.1 M solution. Furthermore, two smaller, secondary peaks that occurred between the primary peaks at distances from the surface of 1.7 Å and 4.9 Å were observed in the more concentrated case. For MgCl_2 , the second major peak has two shoulders at 2.3 Å and 4.0 Å.

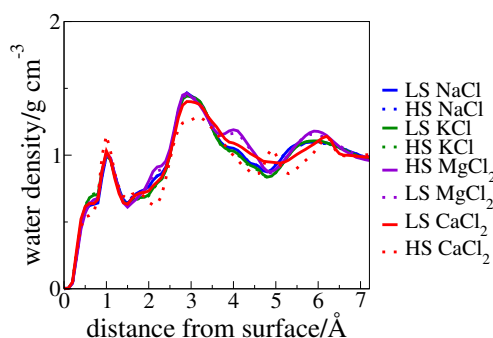


Figure 4.15: Water density as a function of distance from the surface for the NaCl, KCl, CaCl_2 and MgCl_2 solutions (low salinity - LS 0.1 M, high salinity - HS 0.3 M). The solid lines represent LS solution and the dashed lines HS.

Lateral water density profiles provide detailed information on water structure at the interface. $\rho_{Z_{\max}}(xy)$ for the 0.1 M NaCl solution and $\rho_{Z_{p1}}(xy)$ for 0.1 M MgCl_2 are shown in Figure 4.16, with further examples given in the Appendix C, Figure C.9 and

C.10. At the distances of the first and second peaks in water z -density, the three electrolyte solutions, aqueous NaCl, KCl and MgCl₂, displayed the same patterns in lateral water density. The first water peak corresponded to water that penetrated into the voids of the surface, where interaction of water hydrogens with particularly enclosed surface oxygens was possible. The $\rho_{Zp1}(xy)$ profiles indicated which areas of the surface were low enough to accommodate water at this distance from the surface. The $\rho_{Zp2}(xy)$ profile showed that a ring of particularly high density surrounded the O⁻ atom, an indication that water molecules were interacting with the site *via* their hydrogen atoms. Indeed the sharp peak centered at 1.7 Å observed in the O⁻-water hydrogen rdfs for all of the aqueous electrolytes, shown in Figure 4.17, was consistent with the occurrence of hydrogen bonding at the O⁻ site. The peak was of reduced magnitude for aqueous CaCl₂ at both ionic strengths, with the greatest reduction observed for 0.3 M solution. This was due to the presence of the Ca²⁺_(O⁻), Cl⁻_{((Ca²⁺)-O⁻)} and Cl⁻_{(Cl⁻-(Ca²⁺)-O⁻)} ions of the long-lived states. Differences in water structure for aqueous CaCl₂ compared to the other electrolyte solutions are reflected in the O⁻-water oxygen rdfs, shown in Figure 4.18, where the first peak is shifted to higher distances for both aqueous CaCl₂ solutions, with that for 0.3 M CaCl₂ located at the greatest O⁻-water O separation. However, much of the surface was accessible to water and its topology was reflected by the pattern in lateral water density. Another region of high density in $\rho_{Zp2}(xy)$ coincided with the location of a surface hollow at this distance from the surface. The pattern in lateral water structure at the peaks of the first two layers was common to aqueous NaCl, KCl and MgCl₂ and reflected surface topology, as depicted in Figure 4.19, with the interaction with O⁻ being particularly favourable.

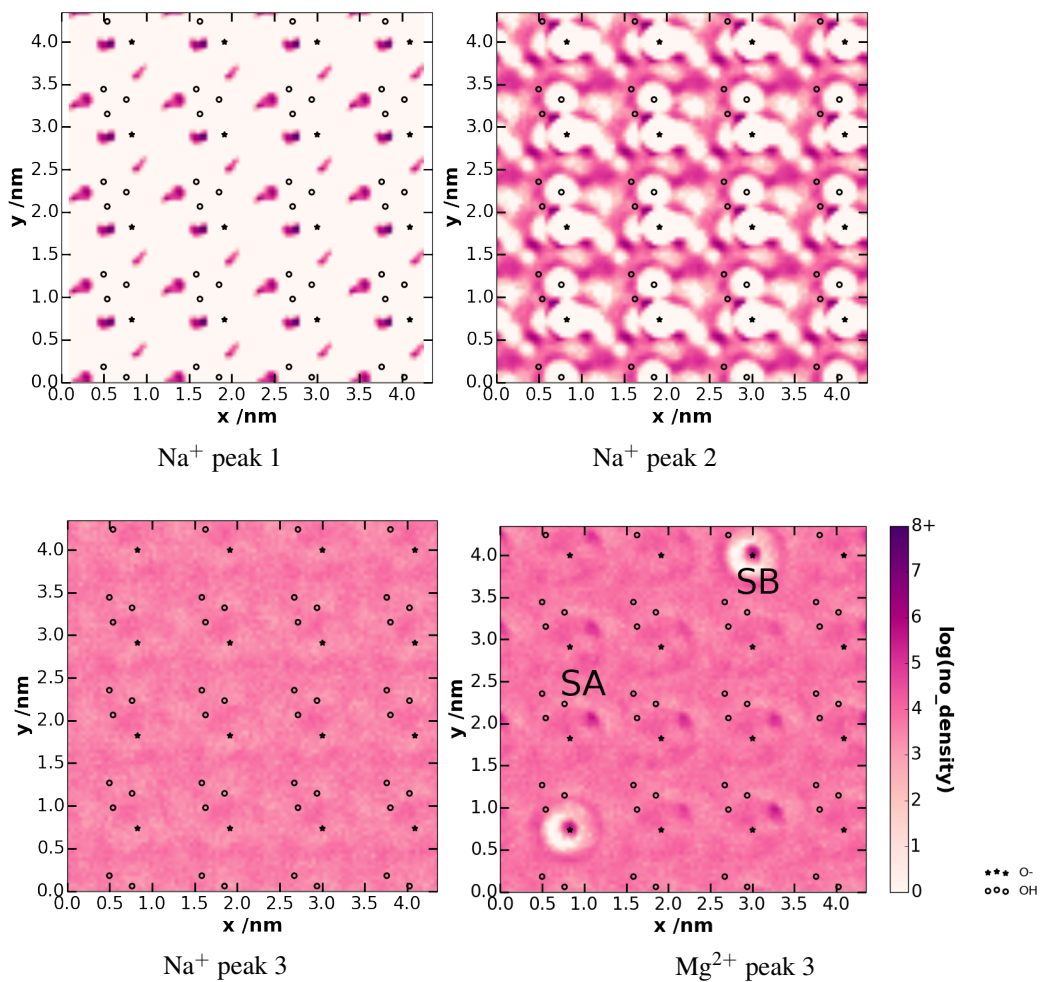


Figure 4.16: $\rho_{Zmax}(xy)$ for water density (within a horizontal layer of thickness 0.1 \AA and centred on the peaks in density as shown in Figure 4.15) for 0.1 M NaCl solution and 0.1 M MgCl_2 . Only $\rho_{Zp3}(xy)$ is shown here for the latter solution, as those for the first two were not significantly different in character to those of the other solutions. The labels **SA** and **SB** are used to highlight different structural characters.

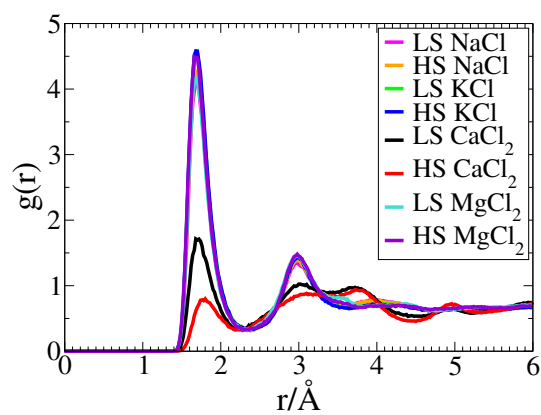


Figure 4.17: Rdfs between O^- and the hydrogen atoms of water for all electrolyte solutions.

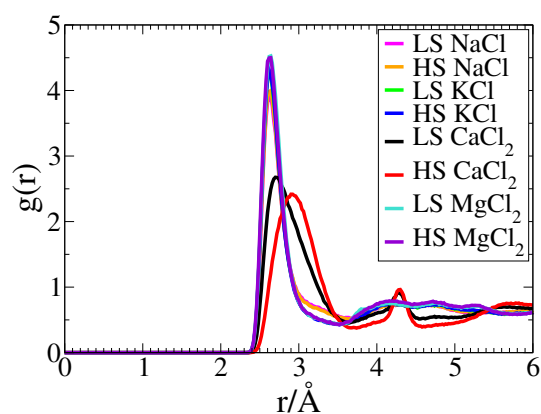


Figure 4.18: Rdfs between O^- and the oxygen atoms of water for all electrolyte solutions.

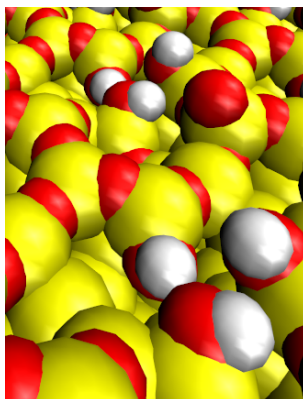


Figure 4.19: Surface topology: van der Waals representation of the amorphous silica surface.

Differences between the $\rho_{Zp3}(xy)$ for aqueous MgCl_2 and those for the monovalent ion solutions were apparent (Figure 4.16). While the same pattern of water structure was repeated for all 16 units of the surface for the NaCl and KCl solutions, for aqueous MgCl_2 there were two distinct structural characters, labelled as **SA** and **SB** in $\rho_{Zp3}(xy)$ for 0.1 M MgCl_2 , that were dependent on whether Mg^{2+} or solvent-separated Mg^{2+} associated with the O^- site. For directly associated Mg^{2+} , which corresponds to character **SA**, a small circle of high density was observed directly above the centre of the deprotonated oxygen. In contrast to the monovalent ions where residence times were of the order of tens to hundreds of picoseconds, this cation remained adsorbed for the duration of the entire simulation, which was tens of nanoseconds for both 0.1 M and 0.3 M solutions (Table 4.4). The pattern in water density that surrounded O^- sites with solvent-separated Mg^{2+} was similar to that observed in the other solutions, with the most significant difference a region of high density labelled as character **SB**.

Table 4.4: Residence time (r_t) for $\text{M}_{(\text{O}^-)}$ and $\text{Cl}^-_{((\text{M})-\text{O}^-)}$.

Solution	Concentration/M	Ion	Cutoff/nm	r_t/ns
NaCl	0.1	Na^+	0.3	0.346 +/- 0.002
	0.3	Na^+	0.3	0.339 +/- 0.002
KCl	0.1	K^+	0.35	0.038 +/- 0.0001
	0.3	K^+	0.35	0.037 +/- 0.0001
CaCl_2	0.1	Ca^{2+}	0.27	57.2 +/- 2.7
	0.3	Ca^{2+*}	0.27	> 40.0
	0.1	Cl^-	0.284	5.1 +/- 3.5
MgCl_2	0.3	Cl^-	0.284	2.9 +/- 3.4
	0.1	Mg^{2+*}	0.25	> 60.0
	0.3	Mg^{2+*}	0.25	> 40.0
	0.1	Mg^{2+}	0.5	0.044 +/- 0.01
	0.3	Mg^{2+}	0.5	0.037 +/- 0.005

*Ions that remained bound for the entire simulation. Standard errors are shown in parentheses Cl^- ions in simulations for NaCl, KCl and MgCl_2 solutions rarely associated so residence times were not determined.

Water density $\rho_{Zmax}(xy)$ for 0.1 M and 0.3 M CaCl_2 solution are shown in Figure 4.20, with those of the two secondary peaks present in the 0.3 M solution and their 0.1 M solution counterparts given in Figure C.11, Appendix C. While water organisa-

tion in the first peak did not significantly alter between aqueous CaCl_2 and the other electrolyte solutions, subtle differences were observed between the $\rho_{Zp2}(\text{xy})$ profiles. The residence time of Ca^{2+} , like Mg^{2+} , was tens of nanoseconds in magnitude, approximately the same length as the simulation, with that of Cl^- also comparatively large (Table 4.4). As a result the local water structure for particular sites could be correlated with a specific site-type. Examples have been labelled (**T1** corresponds to O^- , **T2** to $\text{O}^- \text{Ca}^{2+}$, **T3** to $\text{O}^- \text{Ca}^{2+} \text{Cl}^-$ and **T4** to $\text{O}^- \text{Ca}^{2+} \text{Cl}^-_2$ in the $\rho_{Zp3}(\text{xy})$ profiles for 0.1 and 0.3 M solution. The relative positions of the site types, shown for peak 3, are the same in $\rho_{Zmax}(\text{xy})$ for peaks 1 and 2. The greatest dependence of local water structure on site-type was observed for peak 3, though $\rho_{Zp2}(\text{xy})$ profiles featured subtle local structural differences, with the most significant observed for the $\text{Ca}^{2+} \text{Cl}^-_2$ -associated O^- site. Water density was lower in regions which correlated to such sites and suggested that the two associated Cl^- ions had a significant impact on the accessibility of the surface to water molecules. The long-lived residence times for ions that associated with O^- had such an impact on the arrangement of the local water structure that the shape of the third water density peak altered and, as a result of a change in the proportion of the different site types, two secondary peaks featured in the profile of the more concentrated 0.3 M solution.

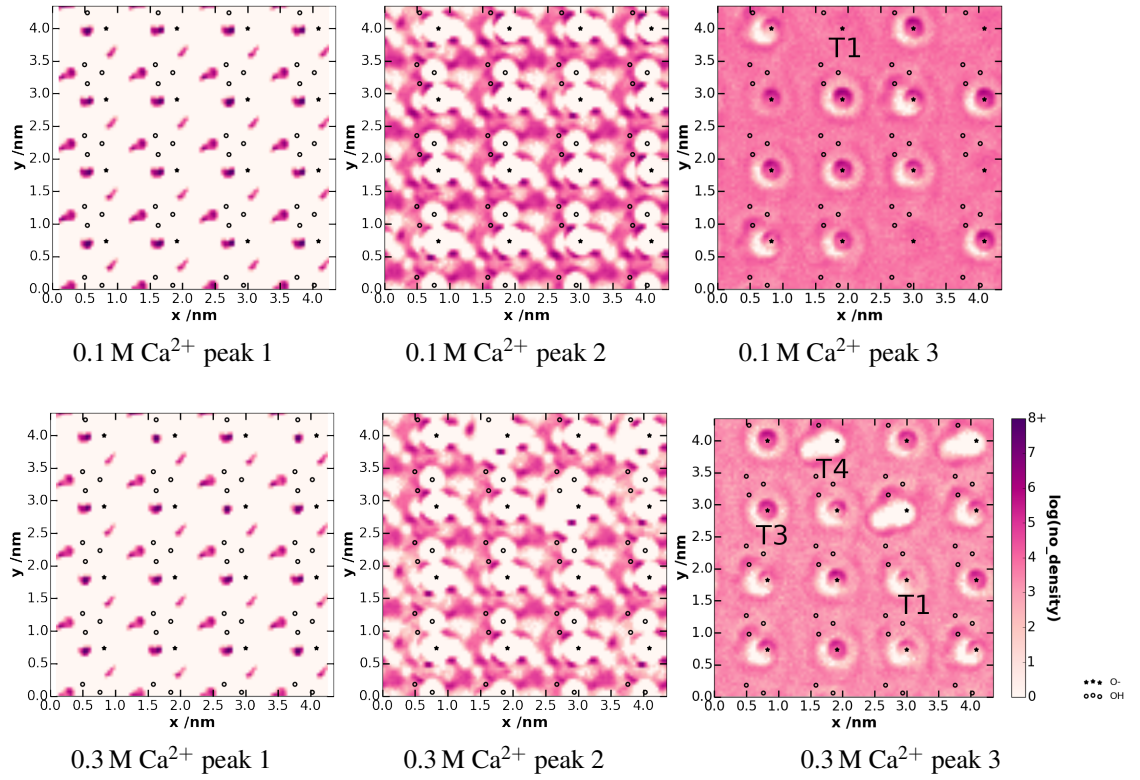


Figure 4.20: $\rho_{Z_{\max}}(xy)$ for water density (within a horizontal layer of thickness 0.1 \AA and centred on the peaks in density as shown in Figure 4.15) for CaCl_2 solution at ionic strengths of 0.1 M and 0.3 M. The labels are used to highlight different structural characters that correspond to different site-types: O^- (T1), $\text{O}^- \text{Ca}^{2+}$ (T2), $\text{O}^- \text{Ca}^{2+} \text{Cl}^-$ (T3) and $\text{O}^- \text{Ca}^{2+} \text{Cl}^-_2$ (T4).

In including both the ion concentration and water density distributions in Figure 4.21, the positions of the peaks in ion concentration relative to those of the water peaks was clear. All except one of the peaks in the ion z -density distributions for the electrolyte solutions were located at the same distance or greater as the position of the second water peak. This exception was the first and largest peak in the K^+ z -density profile that featured at 1.6 Å from the surface, the closest that any of the peaks approached to the surface, a peak due to the adsorption of cations in a void of the surface. For $CaCl_2$, the decrease in magnitude and change in shape of the second water peak when the electrolyte concentration was increased correlated with the dramatic increase in size of the first peak of the Ca^{2+} z -density distribution. The Ca^{2+} ions represented by this peak displaced O^- -adsorbed water molecules. In the $MgCl_2$ case, the shoulder in the second water layer occurred at approximately the same distance as the peak in Mg^{2+} density that represented solvent separated O^-/Mg^{2+} pairs. In contrast to our study, in the results of the Borguet *et. al.*,¹⁰⁰ the major peak in the Na^+ z -density distribution occurred at a distance closer to the surface than the uppermost point of the first water peak, which were measured with respect to the water oxygen atoms. This may be due to differences in the force-field or the structural arrangement of the silica slab atoms. However, two water layers with qualitatively the same shape as the second and third water peaks in our study were reported by Borguet *et. al.*. Sposito *et. al.* analysed water structure at the interface made between mixed electrolyte solution ($NaCl$ and $CaCl_2$) and a clay mineral, smectite.²²⁹ As in our study of the aqueous electrolyte/silica surface, three water layers were observed and within ~ 8 Å of the surface (if defined as the closest approach of water molecules to the surface, as in our case), pronounced water density had dissipated. Furthermore, the water density as a function of z -distance from the surface did not change with electrolyte concentration (0.34 M, 0.67 M, 1.25 M and 1.83 M). The distance between the second and third layers (~ 3 Å) and the second peak of the first layer and the second layer (~ 2 Å) were similar to those observed in our study between the second and third layers, and first and second layers, respectively. Comparison of the position of peaks in ion density relative to the water peaks aided in the explanation of some characteristics of the ion z -density distributions, in particular the changes observed in the second water peak for the $CaCl_2$ case.

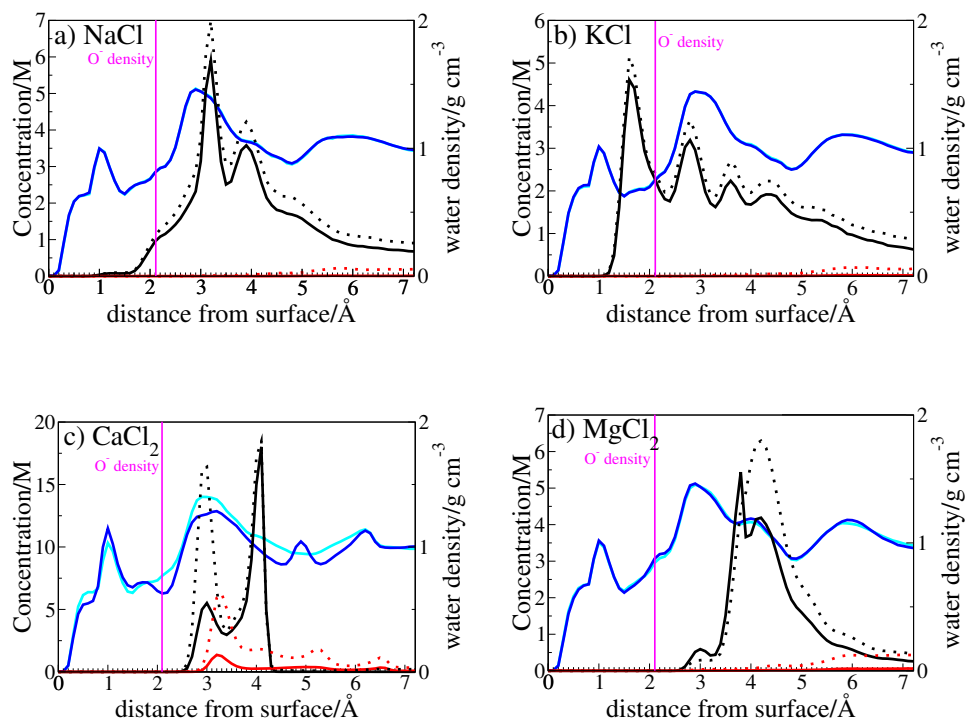


Figure 4.21: Water Density and ion concentration as a function of distance from the surface for the ions in the NaCl, KCl, CaCl₂ and MgCl₂ solutions (low salinity - LS 0.1 M, high salinity - HS 0.3 M). Cation concentration is represented by black and anion concentration is represented by red. For these two colours, the solid lines represent LS solution and the dashed lines HS. Light blue represents H₂O from LS solution and dark blue represents H₂O from HS solution. However, in the majority of cases only the dark blue function is visible, as it overlays the light blue. LS and HS refer to the 'bulk' concentrations *i.e.* the concentrations far from the surface. Ion concentration distributions are reproduced from Figure 4.2 and water density distributions are reproduced from Figure 4.15. O⁻ density is shown as a pink line on the plots. A lateral density profile of the water represented by the second peak in the water density (at ~ 3 Å from the surface) is shown in Figure 4.20 (CaCl₂, 0.1 M and 0.3 M) and Figure 4.16 (NaCl, representative of all other solutions). Lateral water density profiles for the KCl and MgCl₂ cases are given in Appendix C, Figure C.9.

4.3.2 Interfacial Water Density Summary

The water density distributions were near-identical for aqueous NaCl, KCl and MgCl₂ and while that for CaCl₂ deviated from these and even changed with concentration, it followed the same general trend. The most significant differences in the CaCl₂ case were the shape and position of the third water peak and for 0.3 M solution, the reduced magnitude and change in shape of the second primary water peak, as well as the presence of two secondary water peaks. Changes to the second primary water peak connected directly to the increased magnitude of the first peak of the Ca²⁺ z -density distribution and the displacement of O⁻ adsorbed water molecules by the ions it represented. The appearance of the two secondary peaks could be connected to the change in proportion of the different O⁻-based site types (Table 4.3). Water $\rho_{Zmax}(xy)$ profiles provided detailed insight into the organisation of water molecules at the interface. Particularly high density regions were observed around the O⁻ atom, which suggested that it was an important adsorption site for water molecules, as it had been for cations. A correlation between the ions that associated with O⁻ for long periods of time (*i.e.* the O⁻-based site types) and local water organisation was observed. The structural organisation of water varied most dramatically between aqueous CaCl₂ and the rest of the electrolyte solutions, a result of the high concentration of interfacial ions and presence of several long-lived O⁻ based site types.

4.3.3 Water Orientation as a Function of Distance Normal to the Surface

Figure 4.22 shows the net water orientation as a function of distance from the surface for a selection of electrolyte solutions for which the distributions were the most different. Distributions for the remainder of the electrolyte solutions are given in Figure C.12 (Appendix C) and were approximately the same as that for aqueous 0.1 M NaCl. θ is the angle made between the permanent dipole moment of the water molecule and the surface normal. As illustrated in Figure 4.22, a $\cos(\theta)$ value of 1 represented a water molecule for which the oxygen atom was closer to the surface than the hydrogen atoms, while those that were orientated in the opposite direction, with the hydrogen atoms closer to the surface than the oxygen atom were described by a $\cos(\theta)$ value of -1 . A

value of 0 occurs when a molecule is aligned parallel to the surface. The *average* $\cos(\theta)$ value (*i.e.* net orientation, the quantity plotted in Figure 4.22), however, was subject to interpretation. A net value of 0, for example, could mean that all of the molecules were aligned parallel to the surface, or that half of the population had a $\cos(\theta)$ value of 1 and the other half -1 or that the molecules were all oriented in random directions and many further interpretations besides. In this case, net values have been recorded as a function of distance from the surface, so here net refers to the average water molecule orientation within each bin of 0.5 \AA thickness.

The distributions varied the most in the region that spanned $3.5\text{-}6 \text{ \AA}$ from the surface, a region that encompassed the peaks in the ion distributions. The CaCl_2 distributions had a concave-down character and were concentration dependent, with a more positive uppermost point for the 0.3 M solution compared to 0.1 M . In contrast, the distributions of the other solutions were of a concave-up nature. After 6 \AA , the bulk limit was reached, with a value of 0 for CaCl_2 (0.1 and 0.3 M) and 0.3 M MgCl_2 solutions, ~ -0.1 for 0.1 M MgCl_2 and ~ -0.15 for the monovalent ion solutions. The general shape of the net orientation distribution for aqueous NaCl did not match that of Borguet *et. al.*¹⁰⁰ In contrast to our study, they reported net $\cos(\theta)$ values that were near 0 at distances close to the surface and then increased to positive values up until $\sim 3 \text{ \AA}$ from the surface when the curve decreased to the bulk value of 0. This correlated with differences in interfacial ion structuring between the two studies. The net water orientation profiles, Figure 4.22, varied most distinctly between aqueous CaCl_2 and the monovalent ion solutions, while those for aqueous MgCl_2 shared characteristics with both extremes.

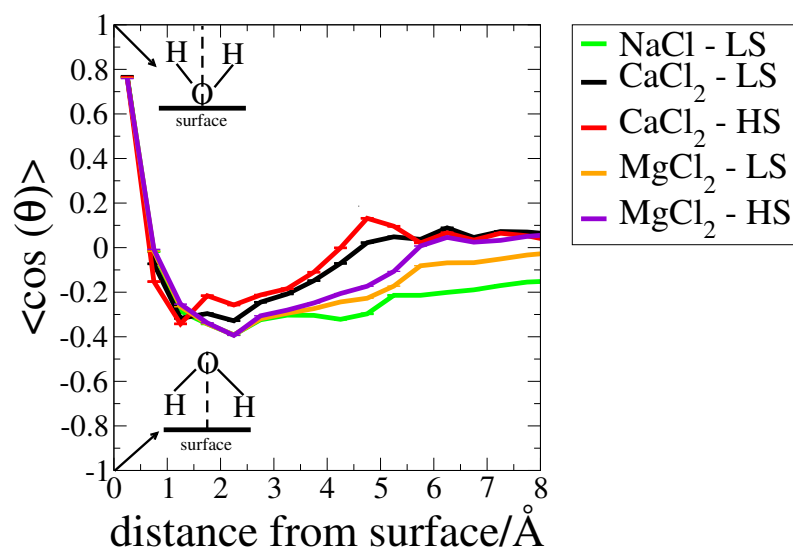


Figure 4.22: Net water orientation as a function of distance for a selection of the electrolyte solutions investigated. The uncertainties are standard errors given to 95 % confidence. Lateral water orientation profiles, with the lateral location of SiO^- and SiOH groups superimposed, are shown in Figures 4.25 and 4.26 and show how waters partition between the different functional groups of the surface.

Full $\cos(\theta)$ distributions, $P(\cos(\theta))$, will now be considered. $P(\cos(\theta))$ have been presented for key values of net orientation in Figures 4.23, 4.24 and C.13, provide information on the relative populations of all of the possible alignments and aided in the correct interpretation of the average $\cos(\theta)$ value. Figure C.13 (Appendix C) features distributions that corresponded to net orientation values that did not significantly vary between solutions (*i.e.* points before 4 Å from the surface). Net orientation varied more dramatically in the regions represented by Figures 4.23 and 4.24 and are discussed in more depth.

As reflected by the values of net water orientation, $P(\cos(\theta))$ distributions varied most for aqueous CaCl_2 compared to the other solutions at distances between 4-6 Å from the surface, as shown in Figure 4.23. For 0.1 M NaCl solution, $P(\cos(\theta))$ distributions formed a slope of approximately constant gradient, with the highest value at $\cos(\theta) = -1$ through to the lowest at $\cos(\theta) = 1$. As the distance from the surface increased, the slopes of the distributions became increasingly reduced in gradient and the number of water molecules with a $\cos(\theta)$ value of -1 , the most populated value in all cases, decreased. In contrast, $P(\cos(\theta))$ distributions for the CaCl_2 solutions featured a broad

peak that centered at increasingly more positive values with increased distance from the surface. The exception to this was the distribution for water molecules between 5-5.5 Å from the surface, which was approximately flat within a range from a $\cos(\theta)$ value of -1 to 0 , followed by a gradual increase in the magnitude as the $\cos(\theta)$ value increased to 1 . The positive values of the peaks meant that there was a bias for water molecules that orientated with hydrogens that pointed away from the surface, correlated with the excess interfacial positive charge observed in Figure 4.2.

The least positive value represented water molecules between 4-4.5 Å from the surface, a region that spanned the latter part of the second peak in Ca^{2+} density (Figure 4.2). Thus, the shift to the more positive $\cos(\theta)$ value of 0.25 occurred as the excess positive charge in the interfacial region increased. Interfacial water orientation followed two distinct behaviours, which, for CaCl_2 , appeared influenced by an excess positive charge, a consequence of the extremely high interfacial cation concentration and for the rest of the aqueous electrolytes resulted from the negative charge of the surface.

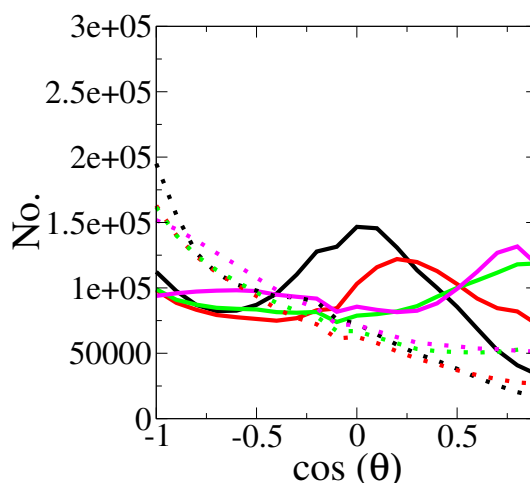


Figure 4.23: $P(\cos(\theta))$ distributions were calculated between distances of 4-4.5 Å (black), 4.5-5 Å (red), 5-5.5 Å (green) and 5.5-6 Å (pink). The solid lines represented 0.3 M CaCl_2 solution and the dotted lines represented 0.1 M NaCl .

$P(\cos(\theta))$ distributions for points in the plateau region of the net water orientation profiles are shown in Figure 4.24. For plateau regions with an approximate value of zero, the distributions (Figure 4.24) were flat with no bias to any particular value of $\cos(\theta)$. For CaCl_2 solutions, the interfacial concentration of Ca^{2+} effectively shielded the negative charge of the surface and was so high that there was an excess interfa-

cial positive charge in spite of the significant presence of interfacial Cl^- (supported by Figure 4.23), an excess that was also counteracted by appropriately aligned water dipoles by the distance from the surface. In comparison, the interfacial concentration of Mg^{2+} was lower and, while high enough to counteract the effects of the surface negative charge by this distance for 0.3 M solution, this was not the case for the less concentrated 0.1 M solution, which still had a negative $\cos(\theta)$ value of -0.2 at 8 \AA from the surface (Figure 4.22). Water represented by such regions was still influenced by the negative charge of the surface and the corresponding $\cos(\theta)$ distributions, Figure 4.24b, were biased towards negative $\cos(\theta)$ values *i.e.* water with both hydrogens pointing to the surface. The distributions had the same shape as those at distances closer to the surface, as exemplified by the full $\cos(\theta)$ distributions for 0.1 M NaCl in Figure 4.23 and the trend of decreased gradient and reduced population of water molecules with a $\cos(\theta)$ value of -1 with increased distance from the surface continued. The $\cos(\theta)$ distributions observed in the study of the more negatively charged (pH 10-11, compared to pH 5.5 in our study) 0.35 M NaCl/silica interface of Borguet *et. al.*¹⁰⁰ were similar in shape - albeit in reverse, with the lowest point when $\cos(\theta)$ was -1 - and followed the same decreased gradient with increased distance from the surface trend. When interfacial positive charge was high enough, *i.e.* for aqueous CaCl_2 and 0.3 M MgCl_2 , the influence of the negative surface charge, and indeed for CaCl_2 excess positive charge, was counteracted by both counterions and appropriately aligned water molecules.

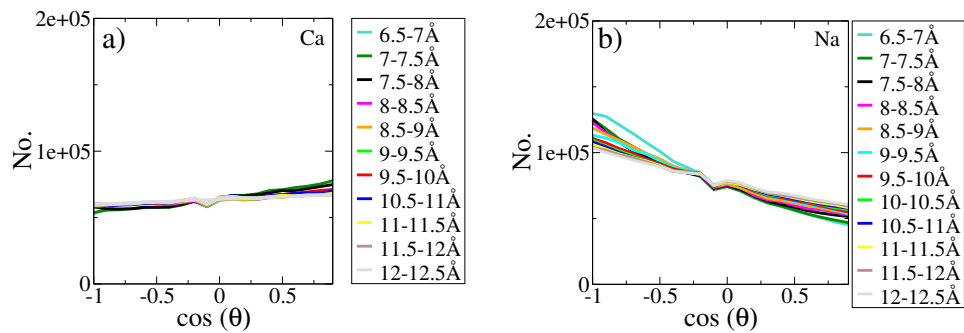


Figure 4.24: $P(\cos(\theta))$ distributions between 6.5-12.5 Å for (a) 0.3 M CaCl_2 denoted Ca and (b) 0.1 M NaCl, denoted Na.

In the net water orientation distributions, Figure 4.22, there was a difference in the absolute magnitude of values in the range 4-6 Å from the surface for 0.1 and 0.3 M CaCl_2 solutions, with the most significant change observed for the point that represented water 4.5-5 Å from the surface. Figure C.14 (Appendix C) shows that $P(\cos(\theta))$ distributions for all such points followed the same general trend at both concentrations. The 4.5-5 Å 0.1 M distribution did, however, deviate slightly with a plateau region after the highest point of the curve rather than a decrease in intensity seen in the corresponding 0.3 M distribution. Lateral water orientation profiles taken in horizontal slices of thickness 0.5 Å were recorded and are denoted $ori_{Z(z_1-z_2)}(xy)$, where z_1 is the z -distance from the surface where the horizontal slice starts and z_2 is where it ends with distances given in Å. $ori_{Z(4.5-5)}(xy)$ and $ori_{Z(5-5.5)}(xy)$ are presented in Figures 4.25 and 4.26 for 0.1 M NaCl and CaCl_2 solutions at both 0.1 and 0.3 M. A clear structuring of water occurred around the O^- atoms in all cases and ions associated with the site for long time periods, Ca^{2+} and Cl^- , had a significant impact on local water orientation. At 4.5-5 Å, as presented in Figure 4.25, the general bias of water orientation for aqueous NaCl was the reverse of that for the CaCl_2 solutions, as supported by the net orientation values of opposite signs. The lateral profile for NaCl solutions featured a periodically repeating pattern of less negative $\cos(\theta)$ values, that included a ring around O^- atoms and a small region associated with protonated silanols. For aqueous CaCl_2 , a similar pattern in water structure occurred when no ions were associated with O^- , labelled as **U1** in Figure 4.25. Circles of less negative-neutral $\cos(\theta)$ values with a positive value close to 1 at the centre and lower left part of the circle featured at Ca^{2+} - and $\text{Ca}^{2+}\text{Cl}^-$ -associated O^- sites (e.g. **U2** and **U3**, respectively, Figure 4.25). The lateral orientation pattern at $\text{Ca}^{2+}(\text{Cl}^-)_2$ -associated O^- sites was similar except with an even larger central region of $\cos(\theta)$ values close to 1 (e.g. **U4**, Figure 4.25). At 5.5-6 Å, as shown in Figure 4.26, 4 distinctive local patterns in water orientation emerged for CaCl_2 . As for the distance range closer to the surface, water structure at unoccupied O^- sites was most similar to that at sites in NaCl solution (e.g. **U1**), Figure 4.26, and had the same general orientational biases as for water in the 4.5-5 Å range. Circles of $\cos(\theta)$ values close to 1 featured at the other site types. For those with associated Cl^- , regions of highly negative $\cos(\theta)$ values were observed, an orientational bias that particularly dominated when there were 2 associated Cl^- ions (e.g. **U4**). Local water orientation was dependent on which ions were associated with O^- and the different proportions of

long-lived O^- -based site types was the origin of the concentration-dependent difference in net orientation for CaCl_2 solution.

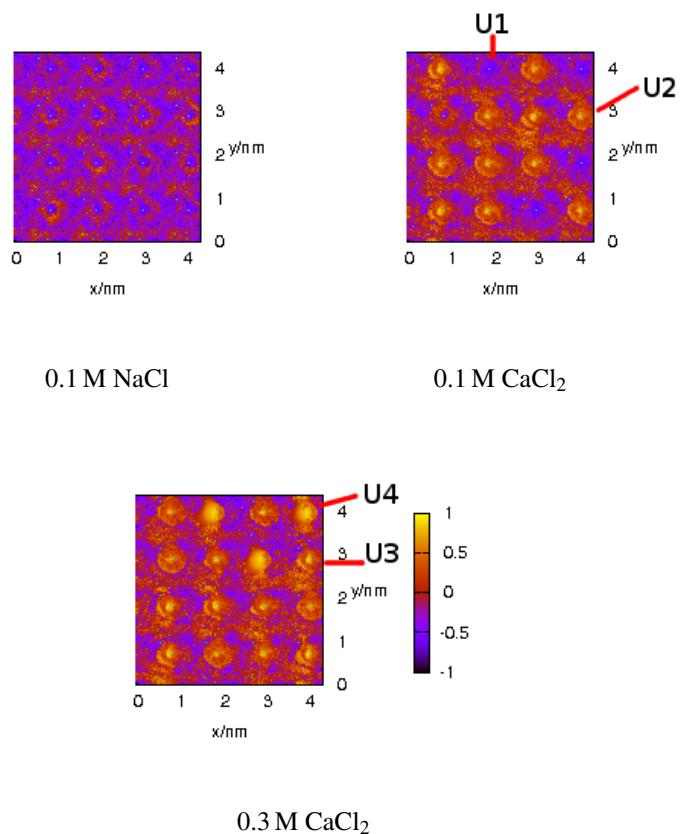


Figure 4.25: Exemplar $\text{ori}_{Z(4.5-5)}(xy)$ (lateral water orientation) profiles. **U1** represents O^- , **U2**, $\text{O}^- \text{Ca}^{2+}$, **U3**, $\text{O}^- \text{Ca}^{2+} \text{Cl}^-$ and **U4**, $\text{O}^- \text{Ca}^{2+} \text{Cl}^-_2$. Blue dots represent the superimposed lateral locations of deprotonated silanol oxygens (O^-) and the green dots represent those of protonated silanol oxygens.

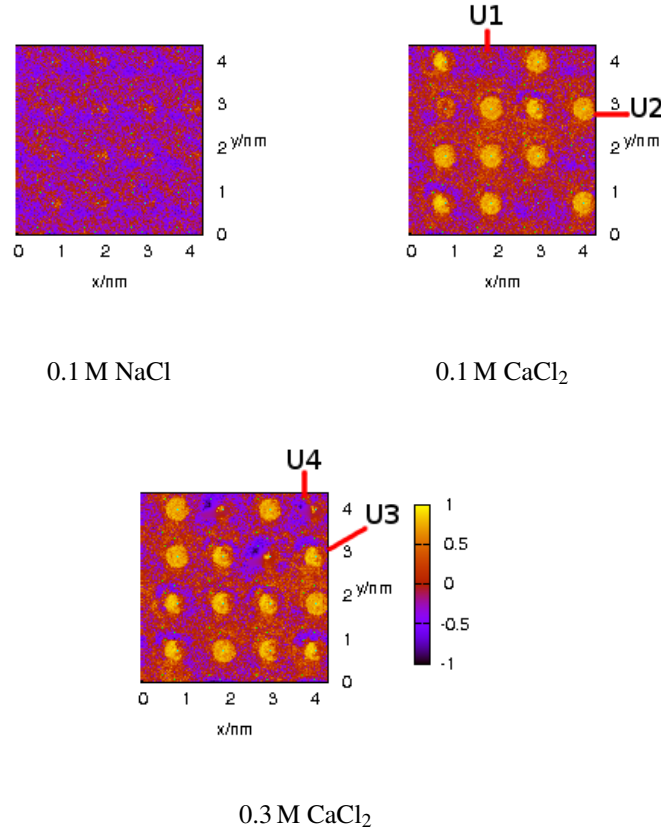


Figure 4.26: Exemplar $ori_{Z(5.5-6)}(xy)$ (lateral water orientation) profiles. **U1** represents O^- , **U2**, O^-Ca^{2+} , **U3**, $O^-Ca^{2+}Cl^-$ and **U4**, $O^-Ca^{2+}Cl^-_2$. Blue dots represent the superimposed lateral locations of deprotonated silanol oxygens (O^-) and the green dots represent those of protonated silanol oxygens.

4.3.4 Interfacial Water Orientation Summary

The net water orientation distributions all followed the same general trend, with the biggest differences observed between 3.5-6 Å from the surface, a region in which the peaks in cation density also featured. In this region, the distributions for $CaCl_2$ solutions were concave-down in character, while those for the other aqueous electrolytes had a concave-up nature. $ori_{Z(4.5-5)}(xy)$ from the surface showed that this was a result of differences in local water structure at O^- sites with Ca^{2+} and Cl^- ions that associated for long-time periods compared to that in the other solutions where the association

of cations was comparatively short-lived and non-existent for anions. Each site type, whether it had only a Ca^{2+} ion, or an additional 1 or 2 Cl^- ions, had its own characteristic water structure. Thus, this indicated that the difference in the proportion of the different site types between 0.1 and 0.3 M CaCl_2 solutions was the origin of the difference in magnitude of the net orientation value that represented water in the 4.5-5 Å region. It was suggested that the difference in the value of the flatter region observed from ~ 6 Å from the surface related to how effectively counterions and aligned water dipoles screened the negative surface charge and any excess charge that resulted from the presence of interfacial ions, with charge effectively screened in cases where the plateau region occurred at 0, namely aqueous CaCl_2 at both concentrations and 0.3 M MgCl_2 . Electrolyte type had a significant impact on interfacial water orientation and water structure varied most distinctly between aqueous CaCl_2 and the rest of the electrolyte solutions.

4.4 Perpendicular and Parallel Diffusion as a Function of Distance Normal to the Surface

The interaction of the NH_3^+ functionality with the aqueous electrolyte/silica interface for the range of solutions considered here has been explored in a subsequent chapter using a combined computational and experimental approach. Thus, it was important that system conditions that were accessible by *both* atomistic MD simulation and force-mapping AFM experiments were chosen. The ζ -potential was a property that could be measured by experiment and, at least in principle, calculated from simulation. One experimental method of determining the ζ potential uses an electrokinetic analyser and is based on measurements of streaming current and streaming potential.⁷⁶ It would provide verification that the simulation provided a reasonable representation of the experiment and *vice versa*. In order to calculate the ζ -potential, the slipping plane, a feature of traditional EDL models, must be located. Since the slipping plane marked the distance from the surface at which water and ion mobilities changed sharply, calculation of diffusion as a function of distance normal to the surface would provide this crucial knowledge.

Figure 4.27 shows the perpendicular (z -direction) and parallel (xy -direction) dif-

fusion constants for water molecules and Na^+ ions in 0.1 M NaCl solution as a function of distance from the surface. Details of how the diffusion constant was calculated are given in Section 2.1.3. This is shown as an example of the typical behaviour of all of the aqueous electrolytes investigated. Although a flat region of reduced mobility was present at 0.8-3.5 Å from the surface for the lateral and perpendicular diffusion of Na^+ ions, no sharp change in mobility was observed. Rather, mobility increased smoothly from 3.5-14 Å from the surface, after which it assumed a constant value as bulk solution was approached. Lateral Na^+ mobility was of a slightly higher magnitude compared to perpendicular mobility within this region 3.5-14 Å from the surface. Since the O^- atom centres were located within the range of distances of the flat region (2.1 Å from the surface), it was probable that this region was due to Na^+ ions that associated with the sites for extended periods of time (Table 4.4). In contrast, the mobility of water molecules increased smoothly from the minimum value at 0.8 Å from the surface and no flat region of reduced mobility was observed. Not only was lateral water mobility in the region 5-15.5 Å from the surface of increased magnitude compared to perpendicular mobility, it also increased with a different nature. For lateral mobility this section of the profile was curved compared to perpendicular mobility where it was of constant gradient. The small peak that occurred before 0.8 Å from the surface for both types of diffusion and chemical species was a result of poor sampling due to the very small numbers of water molecules and Na^+ ions in the region, which corresponded to the those that penetrated into the interstitial gaps of the surface. The absence of a slipping plane at the amorphous silica/aqueous NaCl interface was previously reported by Singer *et al.*⁷² In conclusion, although a flat region of reduced mobility was observed for Na^+ ions, no sharp change in mobility for either water or ions was evident, and thus the slipping plane, as described by traditional EDL models could not be located and thus a reliable value of the ζ -potential could not be calculated.

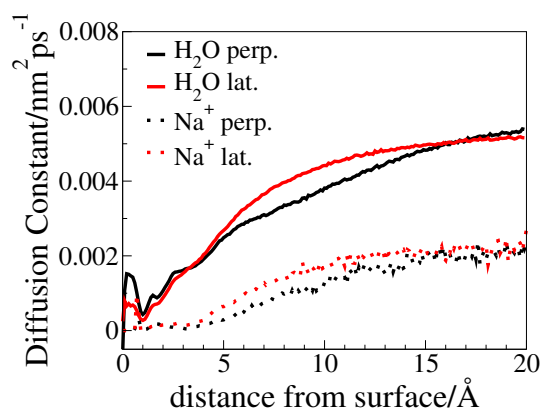


Figure 4.27: Perpendicular ('perp.') and Parallel ('lat.') Diffusion as a Function of Distance from the Surface for water and cations in 0.1 M NaCl solution.

4.5 Conclusion

The behaviour of ions at the aqueous electrolyte/silica interface varied most significantly between aqueous CaCl_2 and the rest of the electrolyte solutions. Interfacial Ca^{2+} concentration was over double that of any of the other cations and there was a significant presence of interfacial Cl^- ions. There were two clear peaks in the Ca^{2+} z -density distribution (at 3 Å and 4.1 Å), with a large Cl^- peak in between (at 3.3 Å). The inner peak was minimal at 0.1 M, but equalled the outer peak at 0.3 M. The lateral distribution of Ca^{2+} within these peaks showed regions of high density in the vicinity of the deprotonated silanol atoms. Once Ca^{2+} adsorbed to an O^- site, it was then found that Cl^- ions could adsorb to the O^-Ca^{2+} ion pair, with long-lived association of up to two Cl^- ions being observed. This led to the formation of four distinct adsorption geometries that persisted for at least tens of nanoseconds: O^- ; O^-Ca^{2+} ; $\text{O}^-\text{Ca}^{2+}\text{Cl}^-$ and $\text{O}^-\text{Ca}^{2+}\text{Cl}^-_2$. The inner peak in Ca^{2+} z -density was observed to be primarily due to ions with two associated Cl^- . The greater proportion of $\text{O}^-\text{Ca}^{2+}\text{Cl}^-_2$ site-types in 0.3 M solution compared to 0.1 M tallied with the increase in the relative magnitude of the inner peak compared to the outer with concentration. It is suggested that in this environment favorable interactions overcome the repulsive forces between O^- and Cl^- . Alternative adsorption sites were more important for the cations of the other aqueous electrolytes, particularly K^+ . Although general cation- O^- residence times ranged from

a few picoseconds to tens of nanoseconds and a region of reduced cation mobility was observed, no evidence was found for the sharp change in mobility, described by traditional electrical double layer (EDL) models. Differences in water structure between the electrolyte solutions were more subtle. z -density distributions all had the same approximate shape, featuring three main peaks. The third peak was of a sharper and more asymmetric nature for aqueous CaCl_2 compared to the other electrolytes. Furthermore, net water orientation profiles were concave-down in character for aqueous CaCl_2 in the region 3.5-6 Å from the surface, compared to the other aqueous electrolytes for which the profiles were concave-up. For aqueous CaCl_2 , distinct patterns in the local lateral water density and orientation were correlated with the different long-lived site types (O^- , O^-Ca^{2+} , $\text{O}^-\text{Ca}^{2+}\text{Cl}^-$ and $\text{O}^-\text{Ca}^{2+}\text{Cl}^-_2$).

The connection and implications of the results of this chapter to commonly used EOR theories, as detailed in section 1.1.1, will now be considered. Concentration and electrolyte dependent differences to the width of the EDL are important to the fines migration theory and multicomponent ion exchange hypotheses respectively. For NaCl, KCl and CaCl_2 , a clear difference in the width of the EDL is observed. For 0.1 M solutions the width of the EDL was ~ 40 Å whereas for 0.3 M solutions, it was ~ 25 Å. This trend is as expected from DLVO theory and provides support for fines migration theory.^{16,14} In this theory, the increased width of the EDL in low salinity solution, makes interaction between the EDLs of colloidal clay particles more likely, which leads to bulk clay swelling. Fine clay particles are then formed and released with associated oil. The divalent ions and monovalent ions have different charges and as such the same concentration is a different ionic strength. However, discarding the MgCl_2 data for which the EDL width did not change with electrolyte concentration, the width of the EDL does not vary significantly with electrolyte type. For 0.1 M solution, it ranges from 39.8 Å (KCl) to 42.7 Å (NaCl) and for 0.3 M solution, it ranges from 24.2 Å (KCl) to 25.4 Å (CaCl_2). This does not add support for the multicomponent ion exchange mechanism. For this to be supported, the width of the EDL for monovalent electrolytes, such as NaCl, should be smaller than for divalents, such as CaCl_2 .

There are other notable changes to interfacial ion and water structure that are likely to have an impact on molecular adsorption, and hence oil adsorption, at the interface. One is the different proportions of long-lived site types in aqueous CaCl_2 (O^- , O^-Ca^{2+} , $\text{O}^-\text{Ca}^{2+}\text{Cl}^-$ and $\text{O}^-\text{Ca}^{2+}\text{Cl}^-_2$). The proportion of $\text{O}^-\text{Ca}^{2+}\text{Cl}^-$ and

$\text{O}^-\text{Ca}^{2+}\text{Cl}^-_2$ is greater in 0.3 M solution compared to 0.1 M solution. For the other two site types, O^- and O^-Ca^{2+} , the proportion is greater in 0.1 M solution compared to 0.3 M solution. The presence of different proportions of groups may impact molecular adsorption. Furthermore, the different groups have been found to be associated with characteristic water structuring patterns. Water structure has previously been described as a governing factor in molecular adsorption.²²

Chapter 5

The Role of Ion Type in the Low Salinity Effect: an Experimental and Computational Study

The interface between mineral surfaces and organic matter in the presence of electrolyte solutions is central to a wide range of naturally-occurring and industrial processes. One example, highlighted in Chapter 4 and discussed in Section 1.1.1 is in the oil industry, where the use of low-salinity water has been shown to enhance oil recovery from sandstone reservoirs. Several hypotheses have been advanced to explain this low-salinity effect, with evidence suggesting that ion bridging, between Ca^{2+} ions and polar compounds, plays a key role. Further hypotheses have been described in Section 1.1.1.

To gain a deeper understanding of the low-salinity effect, we report here a combined experimental and molecular simulation study. Experiments were conducted using the protocol developed by the NanoGeoScience Group, University of Copenhagen and with the guidance of Klaus Juhl (NanoGeoScience Group, University of Copenhagen). Within this study, the NH_3^+ functionality common to many basic functional groups in crude oil was investigated, and natively oxidised silicon (amorphous silica) as a model for sandstone. Methylammonium was used to represent the NH_3^+ functionality in simulation, while long-chain hydrocarbons terminated by NH_3^+ were used to functionalize the experimental AFM tip. Adsorption was investigated using force-mapping AFM and metadynamics, and carried out with four different electrolytes (NaCl, KCl, MgCl_2 and

CaCl₂) and two concentrations (0.1 M and 0.3 M). Another common group found in crude oil, COOH/COO⁻, was investigated using force-mapping AFM. The eight interfaces were the same as those investigated in Chapter 4.

The meaning of 'high' and 'low' salinity, as used within the experiments and simulations of this Chapter, should be clarified. The concentrations used were chosen to be accessible by both experiment and atomistic MD simulation. However, the 'low' salinity concentrations used here were not the same as those used in previous experiments where artificial seawater (ASW) was diluted to the level traditionally used for the real world water flooding of sandstone reservoirs.^{8,230} Indeed, the majority of concentrations - in both ASW and diluted ASW - were too low to be modelled using atomistic MD. The exception was HS NaCl, where the 0.3 M used in our work was comparable to the 0.43 M of ASW. The concentrations of the other aqueous electrolytes used in our study - both LS and HS - were several orders of magnitude larger than their ASW counterparts. For example, Mg²⁺, the next most concentrated ion in ASW, had a concentration of 0.053 M in the undiluted variant. Further, unlike seawater where the concentrations of the constituent electrolytes differed, we used the same LS and HS concentration for all electrolytes. In the LS simulation, the number of cations that are required to balance the surface excess charge is greater than the remainder of the ions required to achieve 0.1 M 'bulk' concentration. In HS simulation, the proportions are comparable. In experiment, however, the size of the bulk region far outweighs that of the interfacial.

Previous studies have used chemical force mapping AFM (CFM-AFM) to investigate enhanced oil recovery (EOR). Skovbjerg *et. al.* investigated the adhesion of a COO⁻ functionalised AFM tip - a model for an oil droplet - to the chalk surface.²³¹ Chalk samples were taken from the Danish sector of the North Sea Basin. The polar groups of the AFM tip had a higher affinity for the clay of the chalk surface, than for the calcite component, a mineral which has traditionally been thought key to the low salinity effect. Matthiesen *et. al.* used CFM-AFM to measure the adhesion force of a CH₂10CH₃ functionalised tip to single quartz grains that had been plucked from core plugs.²³² Samples were either stored in kerosene or solvent cleaned. X-ray photoelectron spectroscopy (XPS) showed that solvent cleaned samples still had a significant quantity of organic material, though it was less compared to the samples that had been stored in kerosene. The average adhesion force, including both samples in artificial

seawater (ASW; 35,600 ppm) and diluted ASW (~ 1500 ppm) was 263 pN for those preserved in kerosene, and 114 pN for those that had been solvent cleaned. Furthermore, the low salinity effect was observed and was stronger on the kerosene preserved samples compared to the solvent cleaned; the average difference in adhesion between low and high salinity solutions was 14 ± 10 pN for solvent cleaned samples and 33 ± 9 pN for the kerosene preserved samples. This work suggested that the character of the pore was determined more by the tightly adsorbed organic material than the underlying mineral. The nearest comparison to the work of this Chapter is a 2012 CFM-AFM study by Stipp *et. al.* which looked at the adhesion of a COOH/COO^- functionalized tip at the interface between artificial seawater and various sandstone model surfaces, including amorphous silica at the same pH, pH 5.5.⁸ This will be discussed in more depth within the CFM-AFM results section of this chapter, Section 5.2.

However, some previous research has looked at the effect of brine composition on EOR.^{233,234} Collins *et. al.* investigated the impact of ion type and ion concentration on the wettability of mica and silica, models for sandstone, by analysing the contact angles of water in decane.²³⁴ The pH was varied from 3 to 10 and concentrations of NaCl, KCl and CaCl_2 from 1 mM to 1 M. For aqueous drops of monovalent ions, the contact angle was small at 2° . In contrast, finite contact angles ($\sim 10^\circ$) were observed for drops with concentrations of divalent ions above 50 mM. When small amounts of polar hydrocarbon (stearic acid) were added, the contact angle increased yet further to 70° . Clarke and co-workers used small-angle neutron scattering to determine the thickness of the water layer that surrounded calcium carbonate particles dispersed in cyclohexane.²³³ The thickness was dependent on both electrolyte concentration and type. A range of electrolytes were explored, including LiCl, NaCl, KCl, MgCl_2 , CaCl_2 , AlCl_3 , Na_2SO_4 and MgSO_4 at concentrations 0.1 M, 0.01 M and 0.001 M. It was found that the lower the concentration, the greater the thickness of the water layer. The greatest water layer widths were observed for divalent ion solutions, CaCl_2 and MgCl_2 .

In this Chapter, the results of the AFM force-mapping experiments are first presented. This is followed by a brief overview of interfacial ion structure at the aqueous electrolyte/silica interface, a topic covered in more depth in Chapter 4. The development of the metaD simulation protocol is then detailed. Free energy profiles, lateral (xy) and as a function of z -distance from the silica surface, are presented. Finally, force curves derived from the metaD-generated free energy profiles are given. This latest

analysis is the most comparable to the experimental measurements.

Appendix D contains: rdfs between atoms associated at the surface and those in the corresponding harmonic restraints, cation-deprotonated oxygen and chloride ion-surface bound calcium ion rdfs, further free energy profiles from the metadynamics simulations for other aqueous electrolytes.

5.1 Experiment and Simulation Protocol in Brief

MetaD simulations of the free energy of adsorption of methylammonium at the aqueous electrolyte/amorphous silica interface were conducted. The force-fields, along with the general (Section 2.1.2) and specific simulation protocol for amorphous silica/aqueous electrolyte interfaces (Section 2.1.2) are the same as those used in Chapter 4. The methylammonium molecule was modelled using CHARMM.¹¹¹ Further, the same eight electrolyte solutions were modelled (NaCl, KCl, CaCl₂ and MgCl₂, each at 0.1 and 0.3 M concentration). Details of the metaD parameters and procedure are given in Section 2.1.2.

Adhesion measurements of NH₃⁺ functionalised tips and COOH/COO⁻ functionalised tips at the same 8 interfaces were carried out using force-mapping AFM. A full description of the specific experimental details used is given in Section 2.2.2.

5.2 Force-mapping atomic force microscopy data

The adhesion forces determined from the AFM experiments are shown in Figure 5.1. A lot of effects are apparent in this Figure, so it will be considered in detail. A clear dependence on concentration was observed for the adhesion of the NH₃⁺-functionalised tip in CaCl₂ solution. For the monovalent ions, in contrast, there was little dependence on concentration and so the adhesion force in these solutions can be used as a standard to compare the strength of the adhesion in other solutions. The adhesion force was 50-100 % higher than in the monovalent solutions when salinity was low and ≥ 300 % higher in the high salinity solutions. Thus, it is evident that the adhesion of the NH₃⁺ functionality in CaCl₂ solution was particularly strong. While no dependence on concentration was observed for the NH₃⁺-functionalised tip in MgCl₂ solution, a

dependence was observed for the COOH/COO⁻ tip. For MgCl₂, the adhesion force was even greater, at ~900 % higher in low salinity solution to ~1200 % greater in high salinity. Compared to the adhesion in monovalent solutions, the adhesion force was 100-200 % higher in low salinity CaCl₂ and 700-800 % higher in high salinity CaCl₂. For the monovalent ion solutions, adhesion was still low and showed no dependence with concentration. The low salinity effect was observed for the NH₃⁺ functionalized tip in CaCl₂ solution and for the COOH/COO₋ functionalized tip in the divalent ion solutions, CaCl₂ and MgCl₂.

There is no similar data for pure electrolytes. The nearest comparison is with artificial brine, and noting the effect of NaCl in our studies, the preponderance of Na⁺ in brine can be expected to lead to an understated effect. Nonetheless, comparison is useful. The previous force mapping AFM measurements concerned the adhesion of the COOH/COO⁻ functionalized tip at the interface between artificial seawater and amorphous silica at the same pH, pH 5.5.⁸ As expected, given our results and the predominance of Na⁺ ions in ASW, the adhesion force was low and comparable to that observed for the monovalent ion solutions in our study. However, a small low salinity effect was observed, with adhesion measured at 46 +/- 8 pN for high salinity and 33 +/- 7 pN for low salinity. It should be noted that in the data presented in Figure 5.1, the effects are a lot stronger than that observed in the previous study by Stipp *et. al.*⁸ One difference between the studies was the amount of time the tips were ozone plasma cleaned for before functionalisation; in our study it was for 20 minutes, whereas in the 2012 study by Stipp *et. al* it was for 30 seconds. Stipp *et. al.* used 100 × 100 data points over a 5 μm × 5 μm area and fitted the resultant adhesion histograms to a Gaussian curve, the peak of which was used as the value for the adhesion force. In our study, we collected 30 × 30 data points over a 5 μm × 5 μm area and repeated the measurement at least 3 times and were used to get a mean value and standard error. A high resolution image in normal AFM mode of the surface scanned in our study (amorphous silica) has been shown in Figure 5.2. While the concentration of Ca²⁺ in the artificial seawater was very low at 4 × 10⁻⁴ M for low salinity and 0.01 M for high salinity, the concentration of Na⁺ was several orders of magnitude greater at 0.02 M for low salinity and 0.41 M for high salinity. The adhesion force of NH₃⁺ functionalized tips at the aqueous electrolyte/silica interfaces are underexplored compared to COOH/COO⁻ and thus the NH₃⁺ moiety was chosen for further investigation with

the advanced MD simulation technique, metadynamics. Adhesion force measurements of the COOH/COO^- functionalized tip at the interface between aqueous CaCl_2 and MgCl_2 solutions and amorphous silica were between 100-1200 % greater in magnitude than previous measurements at the artificial seawater/amorphous silica.

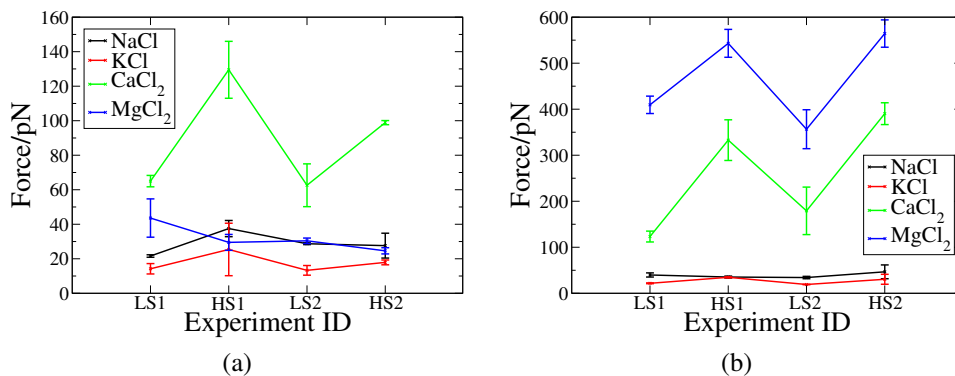


Figure 5.1: AFM force mapping data: the average maximum adhesion during an AFM approach-retract cycle (full method details in Section 2.2.2 of (a) NH_3^+ and (b) COOH/COO^- functionalized tips during interaction with the amorphous silica during exposure to the solutions at low salinity (LS) 0.1 M and high salinity (HS) 0.3 M. The labels 1 and 2 in the Experiment ID are used to denote the experiment number as salinity was cycled twice between LS and HS concentrations.

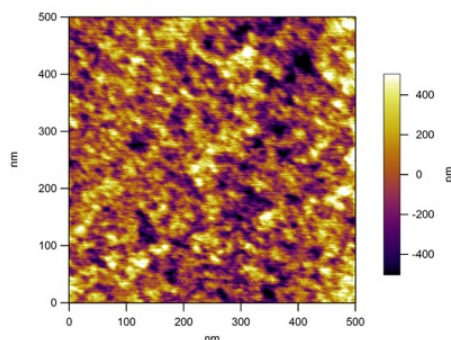


Figure 5.2: A high resolution image in normal AFM mode of the surface scanned in our study (amorphous silica).

5.3 Ion Structuring at the Aqueous CaCl_2 /Amorphous Silica Interface

Ion structuring at the various aqueous electrolyte/amorphous silica interfaces has been discussed in depth in Chapter 4; key points of particular importance to this Chapter are summarised here for convenience. Since the adhesion force of the NH_3^+ -functionalized tip displayed a distinct behaviour in CaCl_2 solution compared to the other aqueous electrolytes, the differences observed between the aqueous CaCl_2 /amorphous silica interface and those of the other aqueous electrolytes will be the primary focus in this section. Ion z -density distributions for aqueous CaCl_2 featured two sharp cation peaks, with an anion peak in the middle, while all others had a broad cation distribution with below average anion concentration in the interfacial region. Ca^{2+} displayed surface residence times that were long compared with the simulations (>40 ns). The properties of the interface for CaCl_2 were best understood in terms of 5 adsorption geometries, as depicted in Figure 5.3. The behaviour of ions at the aqueous CaCl_2 /amorphous silica interface was distinct from that of the other aqueous electrolytes and several long-lived adsorption site configurations were observed.

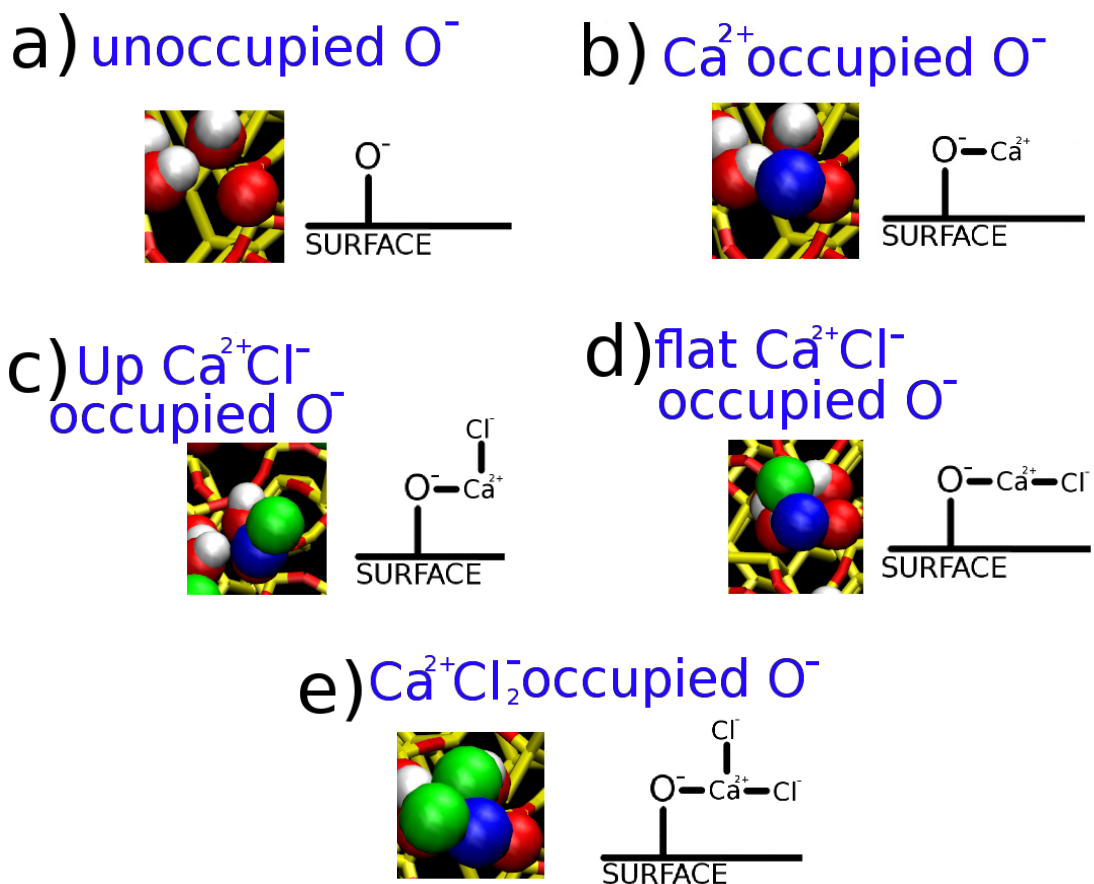


Figure 5.3: Graphical representations of the different possible states for surface deprotonated oxygens in CaCl_2 solution. Ca^{2+} ions are represented by the dark blue atoms and Cl^- ions are represented by the green atoms. (a) unoccupied O^- (b) Ca^{2+} occupied O^- (c) upright $\text{Ca}^{2+}\text{Cl}^-$ occupied O^- (d) flat $\text{Ca}^{2+}\text{Cl}^-$ occupied O^- (e) $\text{Ca}^{2+}\text{Cl}_2^-$ occupied O^- .

5.4 Developing MetaD Protocol

Free energy as a function of z -distance from the surface could be calculated directly using metadynamics. However, it is the derivative of this profile - the associated force curve - that is most comparable to the adhesion force measured in the AFM experiments. The final metadynamics setup focussed on just one unit of the silica surface. In most of

the simulations, rapid exchange of ions was observed between the electrolyte solutions and the immediate environment of the key adsorption site (the deprotonated oxygen), giving rise to a single homogeneous adsorption site. However, for CaCl_2 - as discussed in Section 5.3 - there are 5 different, long-lived O^- -based adsorption site configuration types, as depicted in Figure 5.3. Since we hypothesise that the different proportions of the various sites present at different ionic strengths could underly the 'low salinity' effect, each site-type was considered in a separate metadynamics simulation. Surface- Mg^{2+} residence times were also large, and as a result metadynamics calculations were conducted for both O^- and O^-Mg^{2+} configurations.

5.4.1 Metadynamics Trials: Parameter Optimisation

Metadynamics was performed using the z (vertical) component of the methylammonium N atom as the order parameter. Free energy profiles calculated from these simulations are depicted in Figure 5.4. In order to avoid excessive sampling of the bulk region, a soft Gaussian wall was introduced into the bias potential at $z = 21 \text{ \AA}$. The metadynamics simulations were tested for convergence by: comparing profiles over time; monitoring the free energy difference between two characteristic points of the profile and analysing the distribution of collective variable (CV) space explored towards the end of the metaD simulation. The results for NaCl are shown as an example in Figure 5.5 and show that even over 180 ns the convergence is not complete. Figure 5.5a shows the evolution of the free energy profile with time. The relative depths of the two minima (located at 0.24 and 0.34 nm from the surface) were still changing over the final 20 ns of the 180 ns simulation, which indicated that the simulation had not converged. Changes to the profiles with time have been quantified by taking the free energy difference between the two characteristic points of the profile (the positions of the two minima, 0.24 and 0.34 nm from the surface), as shown in Figure 5.5b. The two characteristic points were the lowest point of the second minimum and a reference point (15 \AA) chosen within the bulk liquid region of the simulated system. Figure 5.5c shows the distribution of the collective variable (CV), distance from the surface of the nitrogen of the methylammonium molecule, over the last 25 ns of the metadynamics simulation. If the metadynamics simulations had converged, these distribution would be flat, as the free energy landscape would have been filled and the nitrogen of the methylammonium

molecule would be equally as likely to occupy any position in CV space. Convergence beyond 4-5 Å from the surface was reasonable, but peaks in the LS system below 4 Å indicate that this free energy minimum has been significantly overestimated. As for all of the other systems, these data indicated that convergence had not been achieved within the timescales given in Figure 5.4.

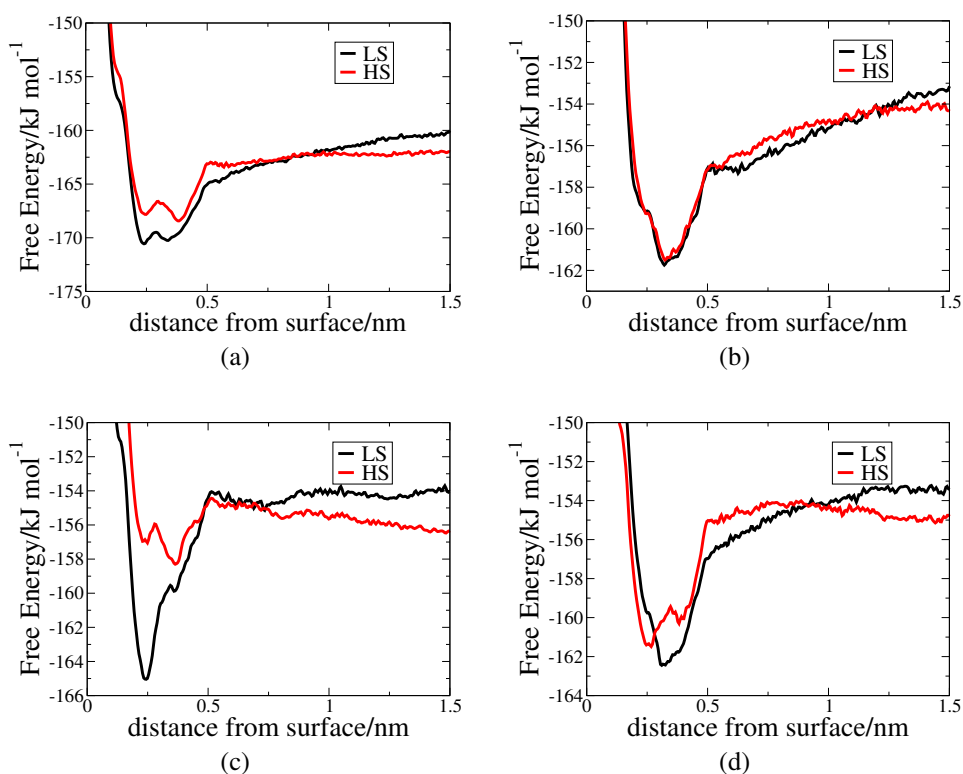


Figure 5.4: Initial free energy profiles from metadynamics simulations (a) NaCl - after 180 ns (b) KCl - after 130 ns (c) CaCl₂ - after 130 ns (d) MgCl₂ - after 130 ns

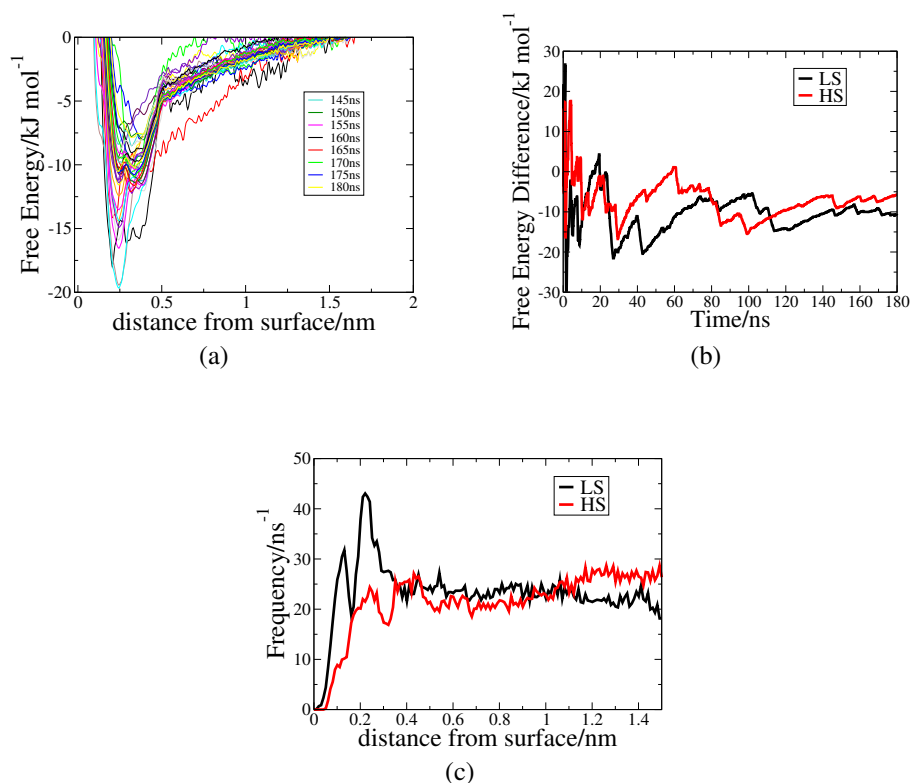


Figure 5.5: NaCl LS - several demonstrations that the metadynamics simulations had not converged (a) Evolution of the free energy profile with time. (b) Free energy difference between 2 distinct points of the free energy profile with time. Comparison to high salinity included. (c) Histogram of CV space explored over the final 25 ns. Comparison to high salinity included.

The underlying reason for the lack of convergence and justification for the next step in this investigation will now be considered. The diffusion coefficient of the methylammonium molecule was calculated by taking the gradient of the mean squared displacement vs time profile calculated over 15 ps over a range of time origins for the molecule in the interfacial region. The simulations from which it was calculated were not biased with respect to the N atom of the methylammonium molecule. It was calculated to be $1.5 \times 10^{-5} \text{ nm}^2 \text{ ps}^{-1}$ in both lateral and perpendicular directions to the surface. Thus, it would be expected to take $\sim 30 \text{ ns}$ for the molecule to diffuse freely across 1 nm, the size of the revised metadynamics space. However, in this case, the successful convergence of free energy profiles determined using the metadynamics technique was reliant on the efficient diffusion of the methylammonium molecule in CV space. One

way of increasing the likelihood of convergence was to decrease the volume of CV space that the methylammonium must explore. This would promote faster convergence and eliminate some repetitive, unnecessary sampling.

In the next set of metadynamics simulations, the bias potential wall was positioned at a distance closer to the surface at 10.91 Å from the start and further bias potential walls were used to confine the molecule to an area of just over one repeat unit of the slab in $x - y$ space. There were 3 CVs: the z -distance from the surface of the N atom of methylammonium, as before; the x -coordinate of N and the y -coordinate of N. Metadynamics simulations were run for 27 ns for all but one of the aqueous electrolytes, 0.1 M NaCl, for which the simulation was carried out for 81 ns. As in the previous simulations, analysis indicated that none had converged. Analysis of the 0.1 M simulation has been shown as an example in Figure 5.6. Figure 5.6a shows that between 60-75 ns the free energy profile does not significantly change. In the final 5 ns, however, the shape changed significantly and the minimum centered at 0.25 nm from the surface decreased to a more negative free energy compared to the others. This is shown quantitatively in the free energy difference graph, Figure 5.6b. The CV histogram, Figure 5.6c, was flatter compared to those of the previous series of metadynamics simulations and suggested that this set were closer to convergence. Lateral free energy profiles for low salinity NaCl and CaCl₂ solutions, taken over the total volume of available CV space for the entire metadynamics simulations, are shown in Figure 5.7. The pattern in free energy that encircled the O⁻ sites was similar for all sites in the NaCl case. For CaCl₂, however, the pattern varied between the four sites. This related to the presence of different long-lived, O⁻-based adsorption configurations, as shown in Figure 5.3, rather than a lack of convergence. These data indicated that a good level of convergence had been achieved and that parameters would be suitable for production runs.

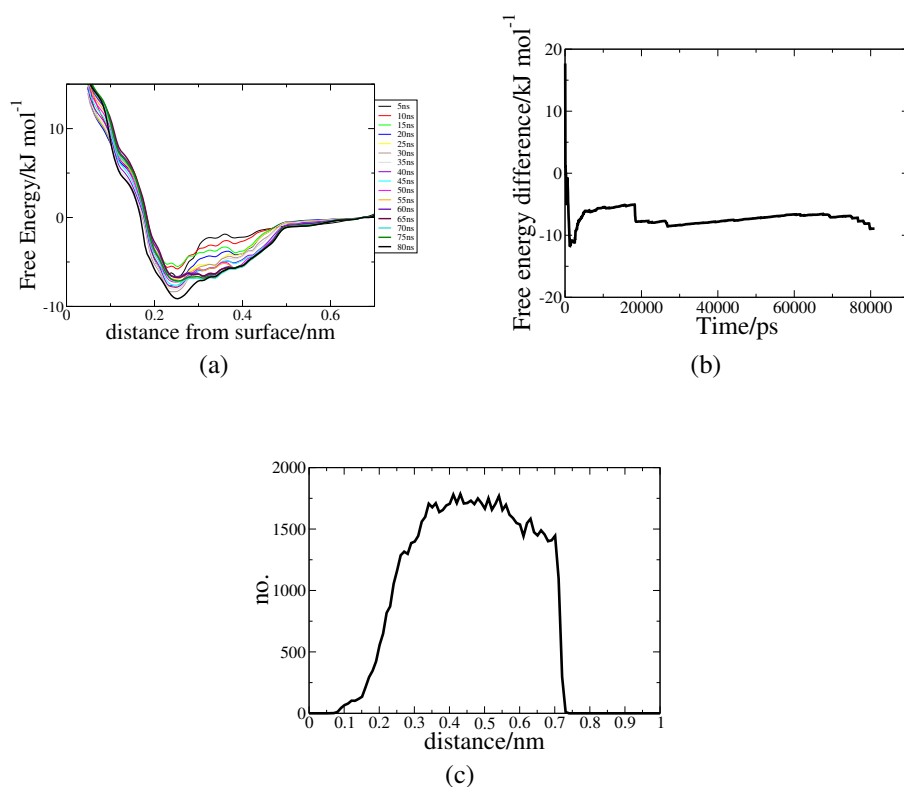


Figure 5.6: NaCl LS, a smaller volume of CV space - several demonstrations that the metadynamics simulations had not converged (a) Evolution of the free energy profile with time (b) Free energy difference between 2 distinct points, the minimum centered at ~ 0.25 nm and a point in the plateau region, of the free energy profile with time (c) Histogram of CV space explored over the final 20 ns.

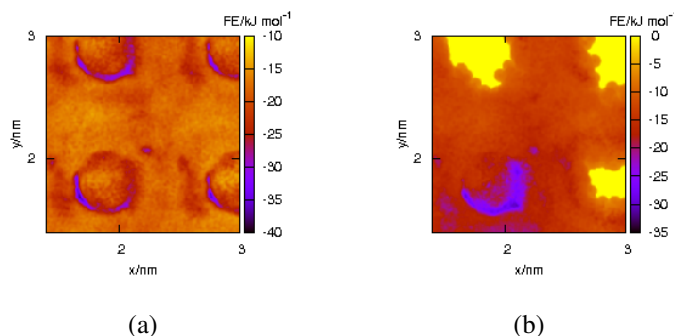


Figure 5.7: Lateral free energy profiles taken over the total volume of available CV space for the entire metadynamics simulations (a) low salinity NaCl, 80 ns (b) low salinity CaCl_2 , 27 ns.

5.4.2 Final System Setups for Metadynamics Simulations

For the production simulations, the system setup developed in Section 5.4.1, for which an acceptable level of convergence had been achieved, was refined by decreasing the volume of available CV space. Bias potential walls were thus positioned to constrain the nitrogen of methylammonium to one repeat unit of the silica slab and to within 6.91 \AA from the surface, the smallest volume of CV space used thus far. It was expected that this change would lead to even greater levels of convergence. The metadynamics again concerned the 3 CVs: the N atoms x and y -coordinate and z -distance from the surface. In reducing the volume of available $x - y$ CV space to encompass one unit of the silica slab and thus, just one O^- -based adsorption configuration, the different site-types, shown in Figure 5.3, could be investigated independently. Although the different site-types, shown in Figure 5.3, were very long-lived and of the same order as the simulation size, harmonic potentials were used to ensure the states remained in tact for the entirety of the metadynamics simulations. As well as being the simplest way of investigating the different configurations, it was hypothesised that the associated ions could significantly impact the adsorption free energy of methylammonium to the surface and thus may underly the low salinity effect. The states shown in Figure 5.3c (upright $\text{Ca}^{2+}\text{Cl}^-$) and d (flat $\text{Ca}^{2+}\text{Cl}^-$) were considered independently since the interchange between them was infrequent, occurring over tens of nanoseconds. Since there was no interchange between the upright and flat states in the test simulation, no angular

constraints were included. However, in the production run the upright state was not sufficiently stable and did not remain in this configuration for long enough to calculate a reliable free energy profile using metadynamics. Figure D.1 (Appendix D) shows how well the harmonically restrained system reproduced the naturally associated system for the $\text{Ca}^{2+}\text{Cl}^-$ -associated cases as an example. While the O^- -associated Ca^{2+} and Ca^{2+} -associated Cl^- rdfs did not differ between the harmonically restrained and naturally associated cases, the rdf between the O^- and associated Cl^- had only one peak in the artificial case compared to the natural, a confirmation that there had been no interchange of the upright and flat states within this test period. Distributions were narrower and of a less asymmetric character in the harmonically restrained case compared to the naturally bound. A smaller force constant for the $\text{Ca}^{2+}\text{-Cl}^-$ bond was tested to see if this would broaden the distribution of bond lengths, but the same behaviour was observed. Another measure taken to preserve the states of Figure 5.3 was the inclusion of repulsive potentials between the O^- atom and free Ca^{2+} ions, as well as between Ca^{2+} and free Cl^- ions. Figure D.2 confirmed that the repulsive potentials did not significantly alter the distribution of the $\text{Ca}^{2+}\text{-Cl}^-$ and $\text{O}^- \text{-Ca}^{2+}$ rdfs beyond the first peak in the rdf that corresponded to specific adsorption of the cation to O^- . In the production runs, the CV space was the smallest used yet and the different adsorption site configurations observed at the aqueous CaCl_2 /silica interface were considered separately.

Several analyses have been conducted to show how well converged the metadynamics simulations that used this optimised system setup were. The data for low salinity NaCl is shown as an example in Figure 5.8. The relatively flat CV frequency profile in Figure 5.8a, which was taken over the final few nanoseconds of the metadynamics simulation period, indicated convergence had been achieved to a reasonable extent. The slight slope between 3 and 4 Å may have been due to there simply being less CV space to occupy in this region (the deprotonated oxygens of the surface are centred at 2.1 Å and hydrogens of some silanol groups can move into positions centred at around 2.1 Å). Figure 5.8b shows changes to the free energy profile were minimal over the last 20 ns. The biggest difference was at around 1.2 Å but the free energy in this region was extremely high. Figure 5.8c and d show fluctuations in the free energy difference between specific points of the free energy profile, as labelled in Figure 5.8b, were small after ~80 ns. In summary, the various analyses suggested that by 105 ns, the metadynamics simulation for the low salinity NaCl case was fairly well converged and

thus this setup was used for the metadynamics simulations of all of the other solutions and adsorption site configuration types.

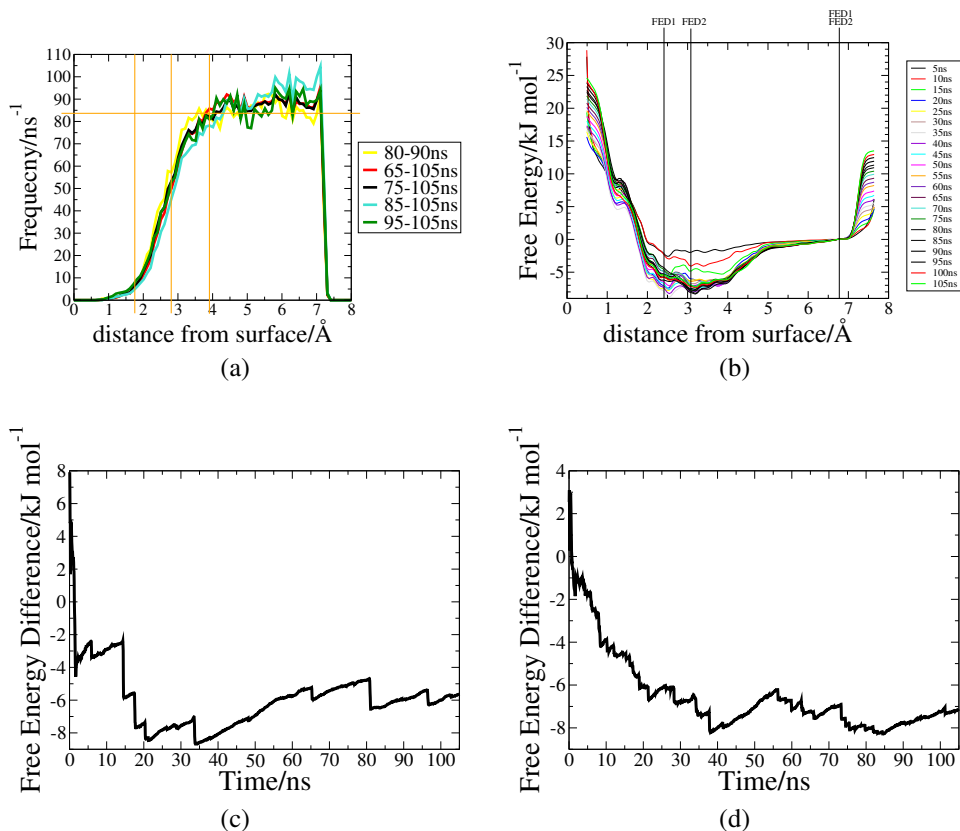


Figure 5.8: Evidence of convergence (a) Distribution of CV (distance from surface) values (b) Evolution of the free energy profile with time (c) Free energy difference between points marked 'FED1' on Fig 5.8b as a function of time (d) Free energy difference between points marked 'FED2' on Fig 5.8b as a function of time

5.4.3 Evidence of Convergence of Metadynamics Simulations using the Optimised Protocol and Procedure for the Estimation of Uncertainties in the Vertical Free Energy Profiles

MD simulations generated after reading in the static bias built up using metadynamics can be utilised to capture the fine detail of the vertical free energy profiles. In this case, a probability distribution of methylammonium's N atom in the MD simulation was

constructed and transformed to a free energy correcting distribution using the equation, $-k_b T \ln[p(x)]$, where k_b is Boltzmann's constant, T is the temperature and $p(x)$ is the probability distribution. The distribution that results from the addition of the free energy correcting distribution to the free energy profile generated from metadynamics has been termed the 'corrected free energy profile'. Figure 5.9 shows the corrected vs uncorrected free energy profiles for aqueous NaCl and the $O^-Ca^{2+}Cl^-_2$ adsorption site configuration in $CaCl_2$ solution. The remainder are shown in Figure D.4, SI. For both examples, as with all cases, after distances ~ 3 Å from the surface, the free energy profile was reproduced when the correcting part was added. At distances closer to the surface, the corrected version of the free energy profile clearly deviated from the uncorrected. For the $CaCl_2$ site, it was particularly clear that while the minimum at ~ 3.5 Å from the surface was well-reproduced, that at ~ 2 Å from the surface was not visited. The free energy profile was well-reproduced after ~ 3.2 Å from the surface for the NaCl case. This indicated that it was difficult to transition from one minimum to the other and that an extended set of collective variables would be more appropriate to fully explore the adsorption behaviour of the nitrogen atom. The adsorption configuration of each of the major minima has been explored in more depth in sections 5.5-5.7 and provides insight into why the transition between the two configurations was not favourable. The uncertainties in the free energy, which appear on the free energy profiles herein, were quantified by calculating the standard error of four estimates of the corrected free energy for minima in regions of the profile that were reproduced. Such estimates were calculated over time periods of ~ 25 ns, with the exception of that for the low salinity NaCl case which was calculated over a time period of ~ 90 ns. Some regions of the free energy profile were well-converged and uncertainties could be estimated for minima in such regions.

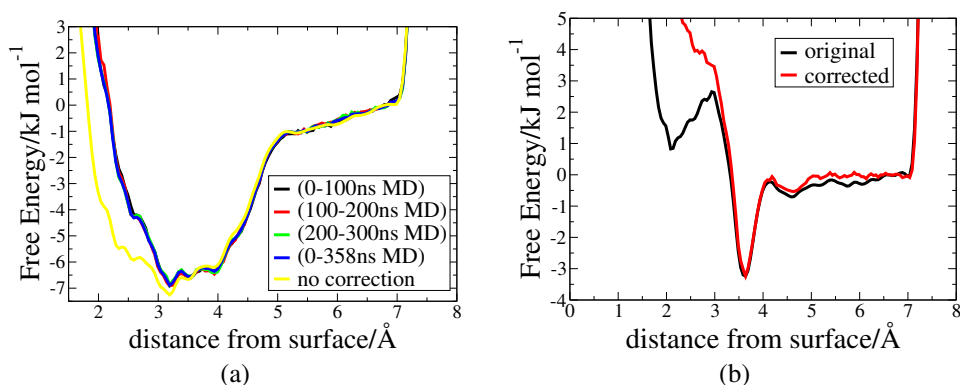


Figure 5.9: Two examples of the free energy profiles from the final metadynamics simulations, a comparison between the corrected and uncorrected versions for (a) low salinity aqueous NaCl and (b) the $\text{O}^- \text{Ca}^{2+} \text{Cl}^-_2$ adsorption site configuration, low salinity aqueous CaCl_2 .

5.5 Vertical Free Energy Profiles for Methylammonium Adsorption at the Interface between Amorphous Silica and NaCl, KCl and MgCl_2 solutions

For the interfaces with the NaCl, KCl and MgCl_2 solutions, the majority of deprotonated oxygens were unoccupied for most of the simulation and thus very accessible to the NH_3^+ group on the methylammonium (denoted herein as N), as discussed in section 5.3. In brief, this was because cation-surface residence times were relatively short in aqueous NaCl and KCl and the majority of sites were vacant throughout the simulation in MgCl_2 solution (on average 91% and 97% for LS and HS conditions, respectively). Free energy profiles for the adsorption of N to the surface are shown in Figure 5.10a for NaCl. Data for KCl and MgCl_2 , which are quite similar, are presented in Figure D.5, Appendix C. The vertical free energy profiles for the adsorption of N to the unoccupied O^- site had approximately the same shape, with one main minimum with a depth of $\sim -7 \text{ kJ mol}^{-1}$. Within the basin of the main minimum, there are a series of minima at distances from the surface of 3.2, 3.5 and 3.9 Å in NaCl, 2.6, 3.3 and 3.6 Å in KCl and 3.3, 3.7 and 4.0 Å in MgCl_2 , at the unoccupied O^- binding site. Herein we denoted these three sites as Minima 1, 2 and 3.

When Mg^{2+} cations were tightly bound, N adsorption to the deprotonated oxy-

gen was completely blocked, as demonstrated by a free energy of adsorption of $\sim 1 \text{ kJ mol}^{-1}$ (Figure 5.10b). In summary, for all cases in NaCl, KCl and MgCl_2 solutions where the deprotonated oxygens of this surface were accessible, the adsorption free energy was always $\sim -7 \text{ kJ mol}^{-1}$ and the free energy profiles had the same general shape and steepness, with the major minima occurring at similar distances from the surface.

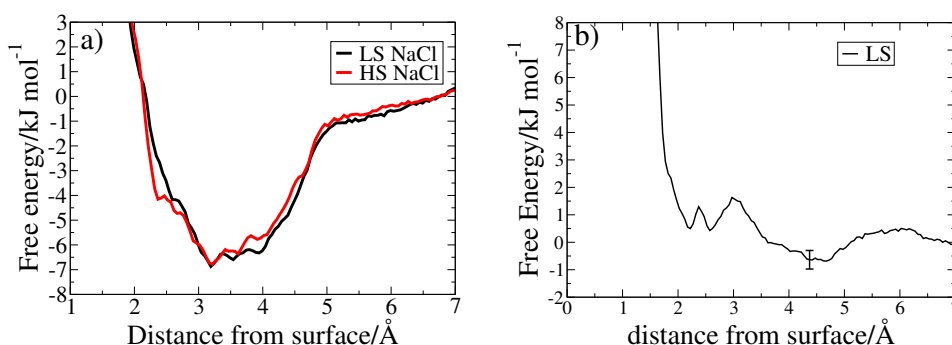


Figure 5.10: Free energy profiles determined from the MD simulations for the adsorption of N to the silica surface in (a) NaCl solution (b) MgCl_2 solution, Mg^{2+} -occupied O^- .

5.6 Lateral Free Energy Profiles for Methylammonium Adsorption at the Interface between Amorphous Silica and NaCl, KCl and MgCl_2 solutions

To understand the nature of the minima in the energy basin of the vertical free energy profiles (Figure 5.10a, representative of the vertical free energy profiles of the aqueous KCl and MgCl_2 in Figure D.5, Appendix C), lateral free energy profiles at the distances of the minima were calculated (a z -range of 0.05 Å around each minimum was used). Example results are presented in Figure 5.11, which shows the lateral free energy profiles in the $x-y$ plane for methylammonium in the low salinity NaCl solution. At these vertical molecule-surface separations, the areas of the lowest adsorption free energy occurred adjacent to O^- , suggesting N was directly associated with the binding site. Such lateral profiles were also characteristic of the major minima in the equivalent free

energy profiles for the other electrolyte solutions. However, for both the low salinity and high salinity aqueous MgCl_2 solution, cylindrically symmetrical profiles were not observed at the major minima. In contrast to Minima 2 and 3 in Figure 5.11, the lateral free energy profiles in the Mg solution were anisotropic, as shown in Figure 5.12. This was correlated with the presence of solvent separated O^- - Mg^{2+} which may have hindered adsorption at the more exposed part of the O^- atom, located at $x = 2.1$ nm and $y = 1.9$ nm. The larger area of free energy of 0 kJ mol^{-1} , as marked by yellow in for minimum 3 in Figure 5.12, supports the idea that the area has been rendered inaccessible by the N atom. . These lateral free energy profiles further confirmed the deprotonated oxygen as the major binding site for N.

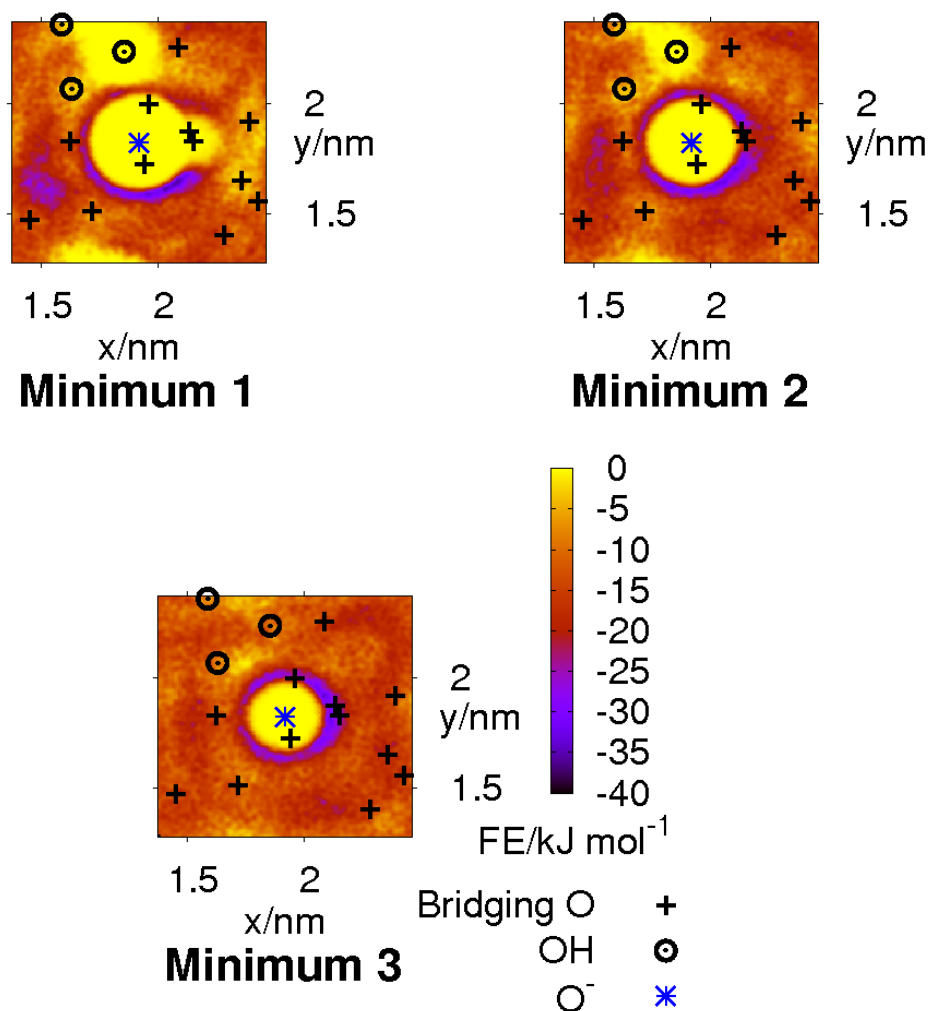


Figure 5.11: Lateral free energy profiles at distances from the surface for the major minima (at 3.2, 3.5 and 3.9 Å from the surface) in the low salinity NaCl solution. The lateral positions of the surface oxygen are superimposed on the free energy profile.

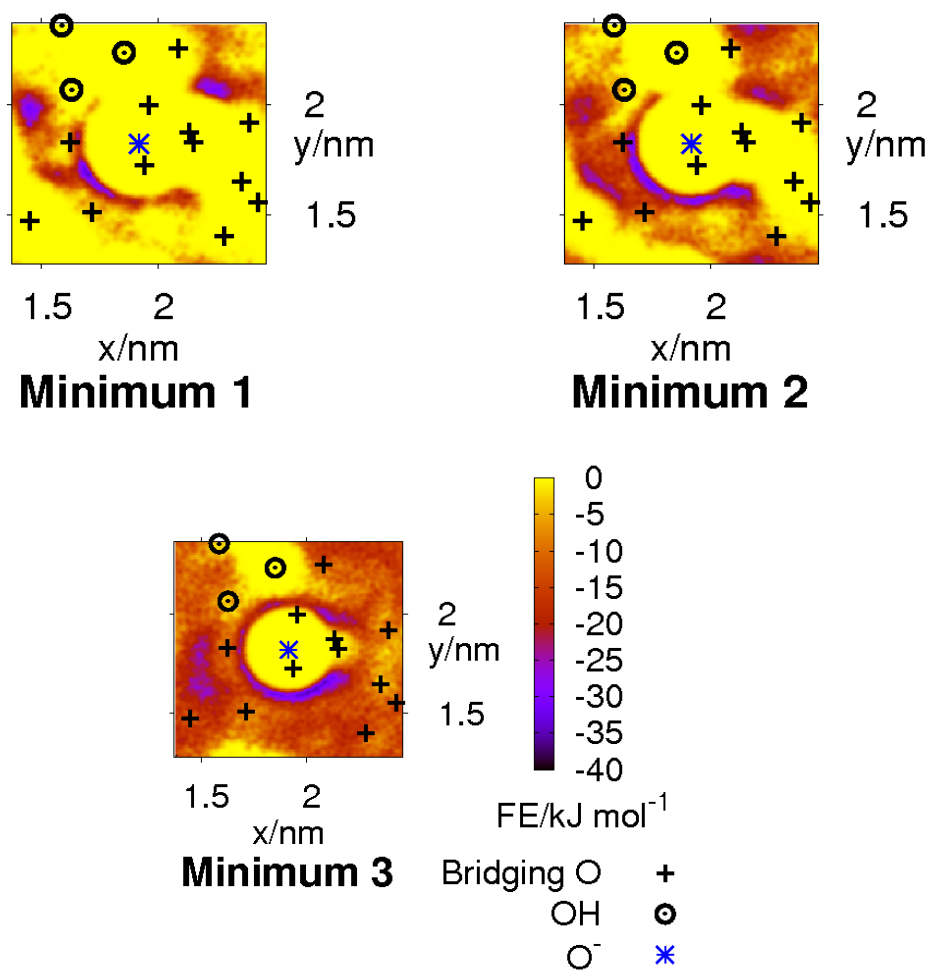


Figure 5.12: Lateral free energy profiles at distances from the surface for the major minima (at 3.2, 3.6 and 4.0 Å from the surface) in the low salinity MgCl_2 solution. The lateral positions of the surface oxygen are superimposed on the free energy profile.

5.7 Free Energy Profiles for Methylammonium Adsorption at the Interface between Amorphous Silica and CaCl_2 solution

As discussed in section 5.3, the character of the CaCl_2 /silica interface was distinct from that of the other solutions and as a result, while the deprotonated oxygen remained the main adsorption site for methylammonium, the possible binding scenarios were more complex, as represented schematically in Figure 5.3. The profiles for the free energy of adsorption of N to the surface have been calculated for all of the states, except the metastable upright $\text{Ca}^{2+}\text{Cl}^-$ state (Figure 5.13a-d).

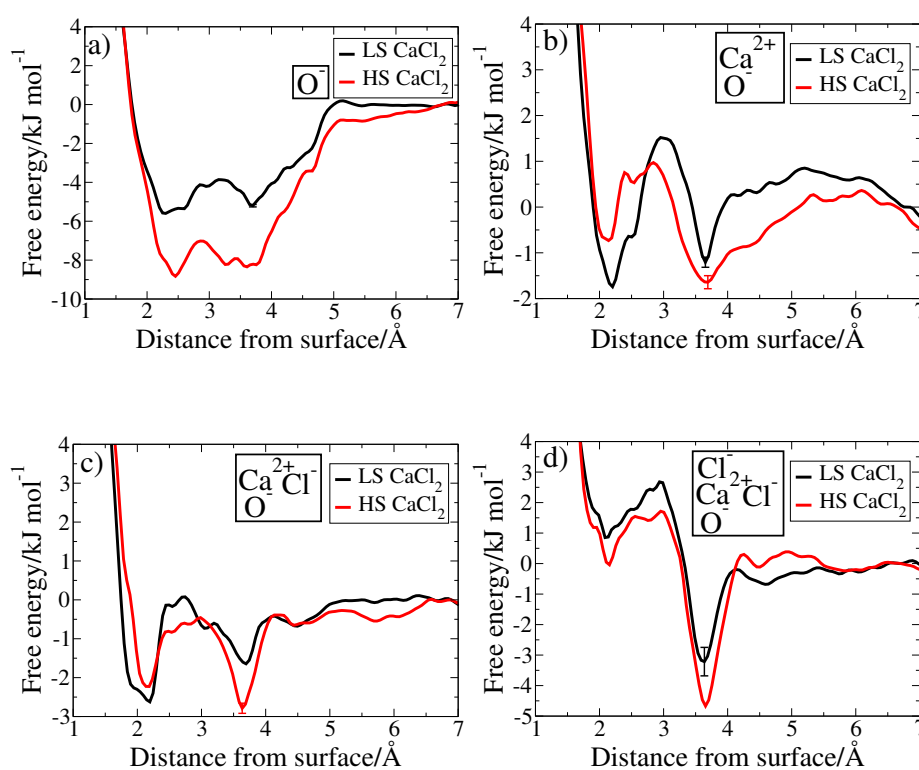


Figure 5.13: Free energy profiles determined from the MD simulations for the adsorption of N to the silica surface at different O^- -based adsorption site configurations in CaCl_2 solution (a) unoccupied O^- (b) Ca^{2+} occupied O^- (c) flat $\text{Ca}^{2+}\text{Cl}^-$ occupied O^- (d) $\text{Ca}^{2+}\text{Cl}_2$ occupied O^-

Unlike any of the other electrolyte solutions, a concentration dependence was observed for the adsorption of N to the unoccupied O^- site in $CaCl_2$. The difference between the free energy profiles for low and high salinity solutions was non-negligible (*i.e.* greater than 1.2 kJ mol^{-1}), as shown in Figure 5.13. However, this was the only configuration type for which adsorption was observed to be concentration-dependent. The general shape of the low salinity and high salinity profiles was the same, but the high salinity version featured a basin 3 kJ mol^{-1} deeper than for low salinity. The profiles featured two minima at distances of 2.2 \AA (Minimum 1) and 3.7 \AA (Minimum 2) from the surface. Lateral free energy profiles taken in the $x - y$ (horizontal) plane at distances from the surface corresponding with Minima 1 and 2, showed that the adsorption sites were the same in the high salinity and low salinity cases, and it was only the magnitude of the free energy that differed (Figure 5.14). The more negative free energy observed in the high salinity case was likely to have been the result of an increased attraction between the NH_3^+ group of methylammonium and the increased number of background interfacial Cl^- ions. For all of the configurations shown in Figure 5.3, Minimum 1 was defined as that located at a distance of $2.1\text{-}2.45 \text{ \AA}$ from the surface and Minimum 2, at 3.7 \AA . Lateral free energy profiles for Minima 1 and 2 (Figure 5.15a and b respectively) show that the N interacted with the same surface oxygens, regardless of what was attached to the deprotonated oxygen. For Minimum 1 (Figure 5.15a), regions of low free energy were located: at $x < O^-(x)$ in a partial ring around the O^- atom centre; in the vicinity of the silanol group with the lowest x and y coordinates and in between 2 bridging oxygens at $x > O^-(x)$ and $y > O^-(y)$. For Minimum 2 (Figure 5.15b), regions of low free energy were located primarily in a ring or partial ring around the O^- centre. The strength of this interaction, however, was not the same across the various site configurations.

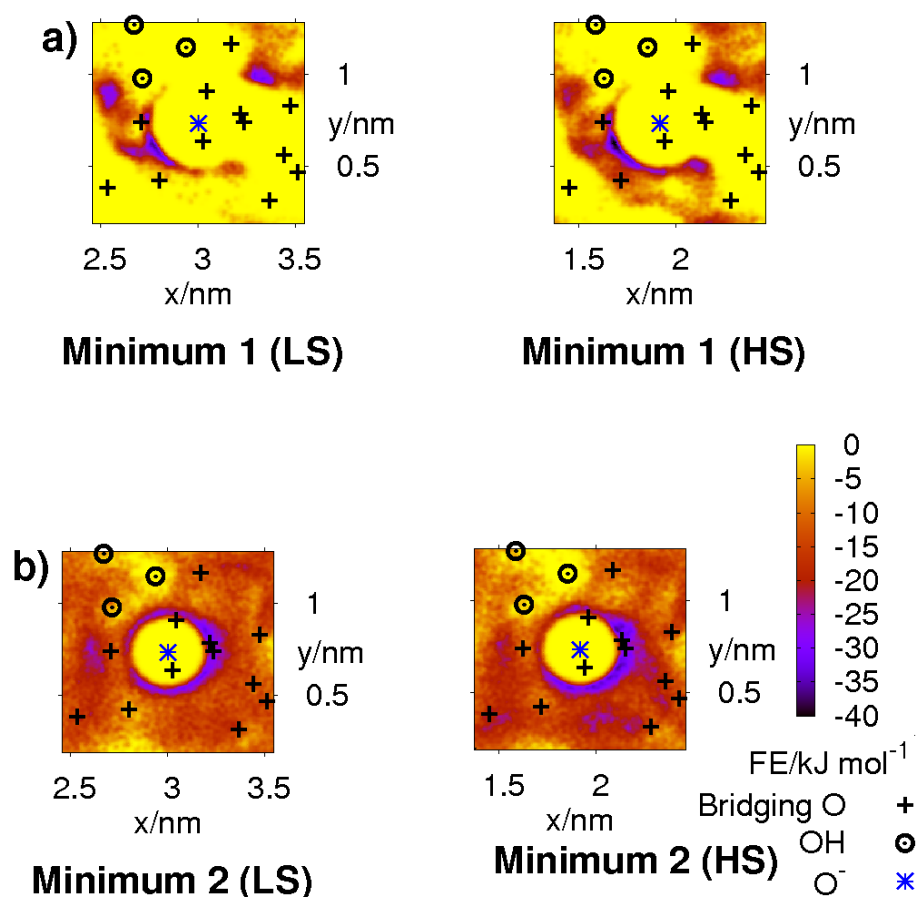


Figure 5.14: Lateral free energy profiles at distances from the surface for the major minima (as defined in the main text) in aqueous LS CaCl_2 at unoccupied O^- . The lateral positions of the surface oxygen are superimposed onto the free energy profile.

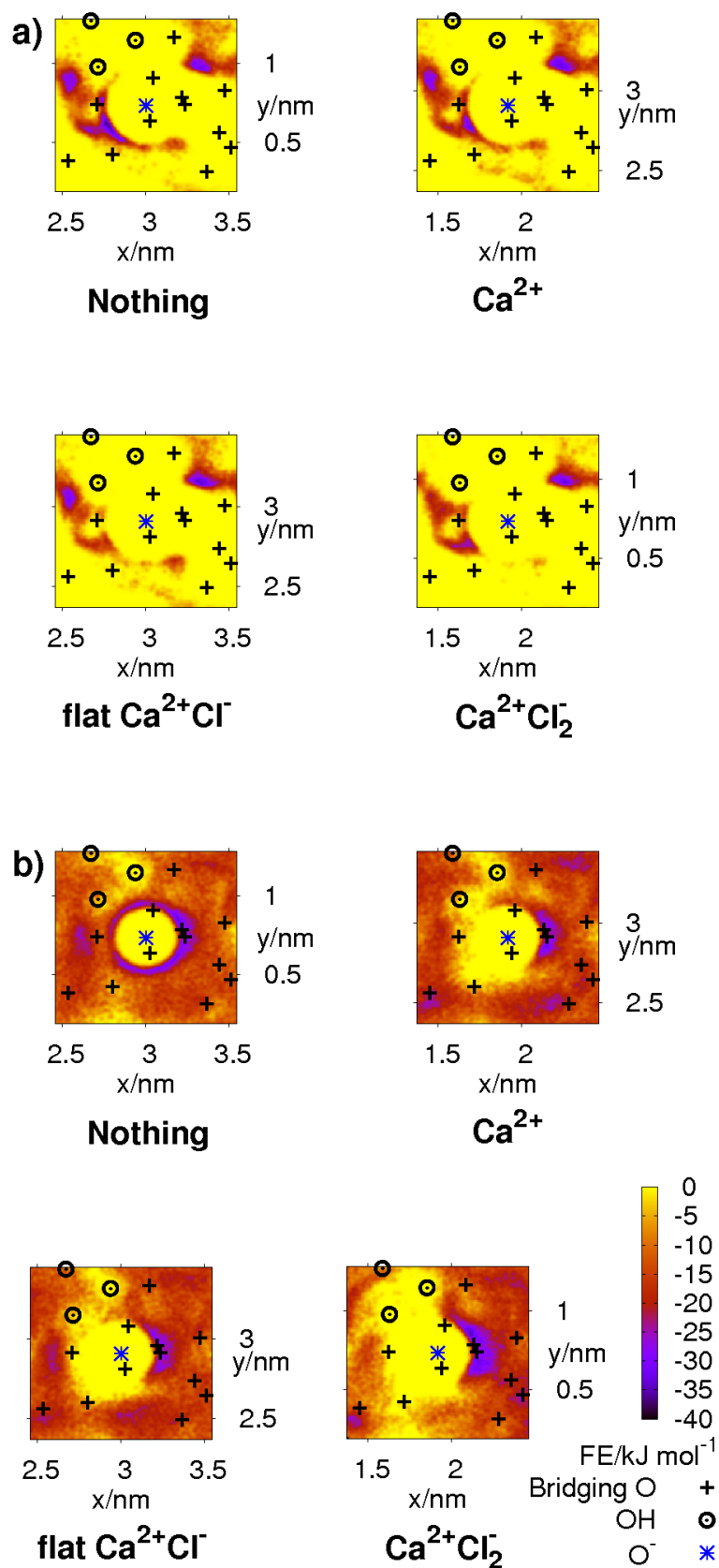


Figure 5.15: Lateral free energy profiles in aqueous low salinity CaCl_2 for various attachments at O^- at the distance of (a) minimum 1 (2.1-2.45 Å), (b) minimum 2 (3.7 Å). The lateral positions of the surface oxygen are superimposed onto the free energy profile.

In Figure 5.15a, 'nothing' and ' Ca^{2+} adsorbed' both show three strong adsorption sites (located at $\sim(2.75, 0.6)$, $\sim(2.5, 0.9)$ and $\sim(3.3, 1)$ in 'nothing' and the same relative positions in ' Ca^{2+} adsorbed'). The last two of these are also found in 'flat $\text{Ca}^{2+}\text{Cl}^-$ ', while ' $\text{Ca}^{2+}\text{Cl}^-_2$ ' shows only the last as a substantial site, albeit with a weak remnant of the first two sites. The first site corresponded to direct adsorption of N to O^- and was at its most favorable in the configuration where no ions were associated. Minimum 2 arose mainly from interaction with O^- as shown by the ring or partial ring of low free energy (purple) that encircled the O^- centre for all cases and dominated the profiles in Figure 5.15. Furthermore, Figure 5.15b shows that the deprotonated oxygen was associated with the biggest volume of attractive energy when the site was unoccupied. Adsorption was most favorable for the $\text{Ca}^{2+}\text{Cl}^-_2$ -occupied site. This was followed by adsorption at the flat $\text{Ca}^{2+}\text{Cl}^-$ -occupied site and then at the Ca^{2+} -occupied site. The increased repulsion between the two attached chlorides and the deprotonated oxygen, compared with the case where one or even no chlorides were attached, made the O^- more accessible. This is also seen in Figure 5.16, which shows a correlation between the available area of the deprotonated oxygen (the central, circular yellow patch, covered by a very dense collection of red crosses that mark the position of adsorbed Ca^{2+}) and low adsorption free energy. The lateral free energy profile for the $\text{Ca}^{2+}\text{Cl}^-_2$ -occupied site is shown again in Figure 5.17(a) with key bridging oxygen sites labelled '1', '2' and '3', alongside a schematic of the corresponding physical system with the same key bridging oxygens labelled. It indicates that simultaneous interaction with bridging oxygen '3' may be important, as well as hydrogen bonding between the Hs of methlammonium's CH_3 and bridging oxygens '1' and '2'.

In summary, our calculated adsorption free energies for methylammonium in CaCl_2 solution showed a clear difference between low salinity and high salinity conditions for the unoccupied O^- surface site (Figure 5.3a). This was also the case where the free energy of adsorption was at its greatest. For the other sites, the adsorption free energy became more negative as the number of attached chloride ions increased.

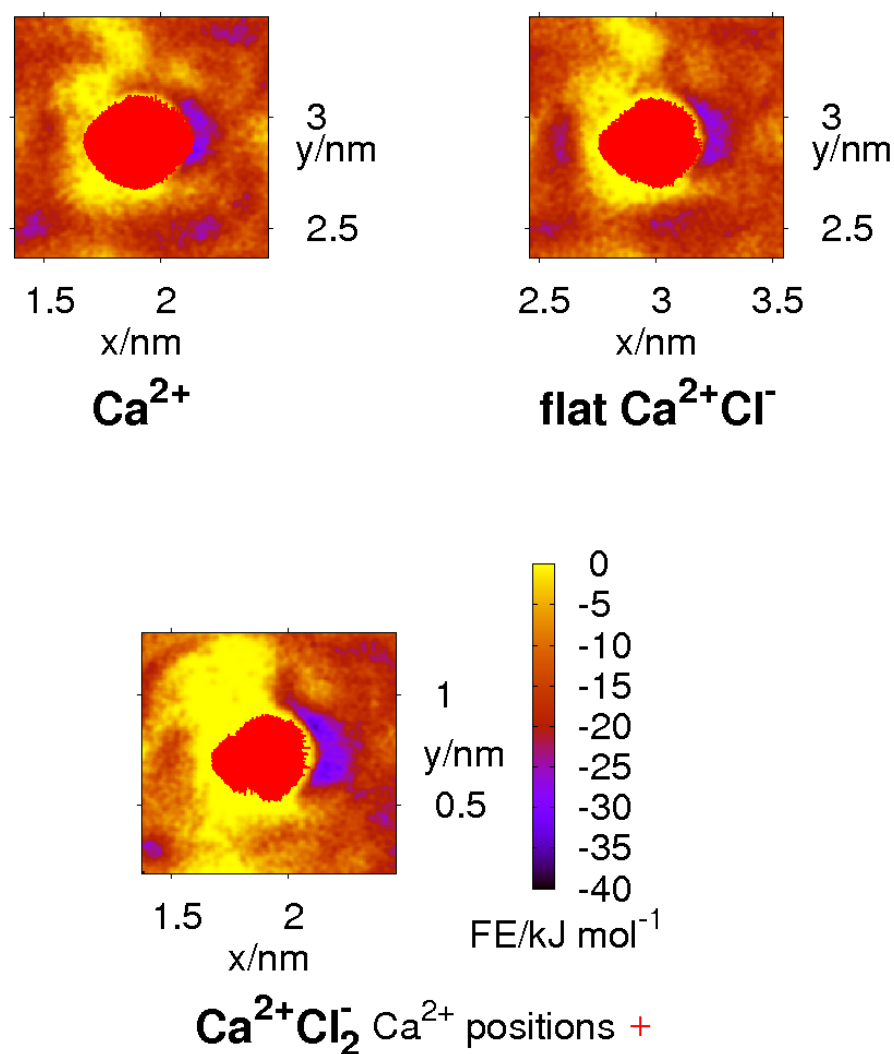


Figure 5.16: Lateral free energy profiles at distances from the surface for minimum 2 (2.1-2.45 Å) in aqueous low salinity $CaCl_2$ for various attachments at O^- . The lateral positions of the attached Ca^{2+} are represented as red crosses superimposed onto the free energy profile and appeared as a single continuous region that is slightly elongated away from the ammonium adsorption site.

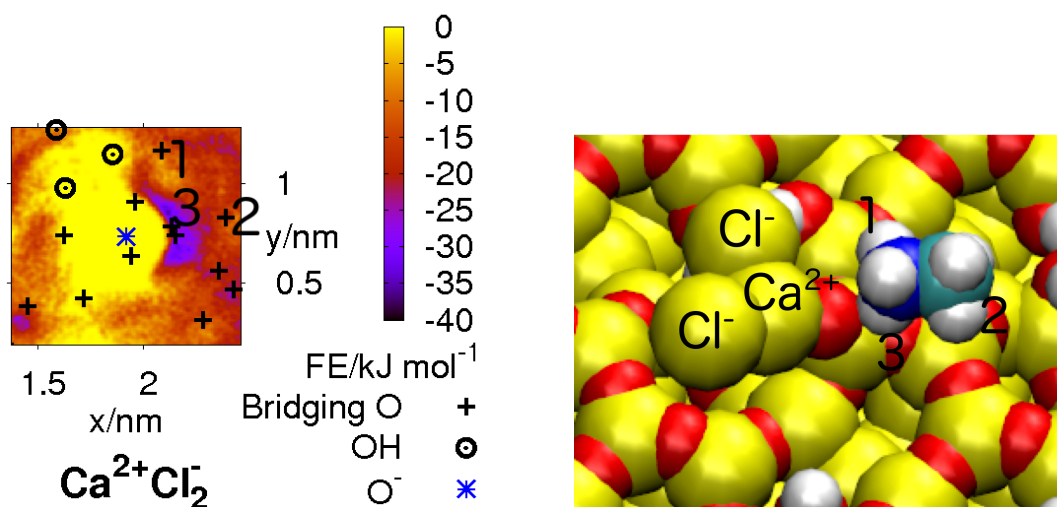


Figure 5.17: (a) Lateral free energy profile for the CaCl_2 attachment at O^- at the distance of minimum 2 (3.7 \AA). The lateral positions of the surface oxygen are superimposed onto the free energy profile. The positions of particular bridging oxygens have been labelled '1', '2' and '3'. (b) Schematic of corresponding physical system with the same bridging oxygens labelled '1', '2' and '3'. Apart from the labelled ions, Ca^{2+} and Cl^- , oxygen atoms are shown in red, silicon in yellow, hydrogen in white, nitrogen in dark blue and carbon in light blue.

5.8 Force vs Distance Profiles and the Origin of the Low Salinity Effect

In order to make closer contact with the experimental adhesion force measurements, we calculated the derivative of our free energy profiles and used it to construct force vs distance profiles (Figure 5.18). These show a clear difference between the force curves for one particular type of coordinated deprotonated oxygen site and all of the others. This indicates that this site - the $\text{Ca}^{2+}\text{Cl}^-_2$ -occupied O^- configuration (Figure 5.3e) - is of crucial importance in the low salinity effect. Only the data for this type of site and for NaCl have been included. The NaCl solution force data is representative for both the MgCl_2 and KCl data as well as for all of the other site types in the CaCl_2 solution. For NaCl, in both low salinity and high salinity conditions, comparatively small fluctuations in force were observed between $2.5\text{--}5 \text{ \AA}$ from the surface. The large change in force that occurred around $3\text{--}4 \text{ \AA}$ for the $\text{Ca}^{2+}\text{Cl}^-_2$ -occupied O^- site was greater than any

other change in force in this 2.5–5 Å window. Because a larger proportion of the site type shown in Figure 5.3e existed in the high salinity simulations, it follows that the overall adhesion force experienced by the NH_3^+ functionalized tip on the silica surface should be higher under high salinity conditions, compared with low salinity.

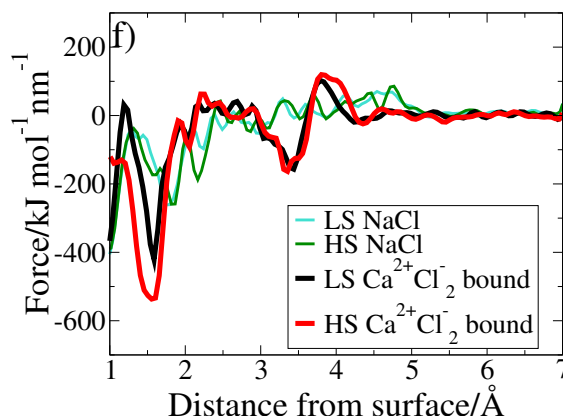


Figure 5.18: The force curves were generated by taking the gradient of the free energy profiles for methylammonium adsorption in solutions of NaCl and CaCl_2 specifically where $\text{Ca}^{2+}\text{Cl}_2^-$ is associated with the deprotonated surface oxygen.

We hypothesize that the large force associated with the $\text{Ca}^{2+}\text{Cl}_2^-$ -occupied O^- site is at the root of the low salinity effect for the ammonium functional group. In the high salinity solution, the interfacial ion concentration was higher than when salinity was lower; consequently, $\text{Ca}^{2+}\text{Cl}_2^-$ -occupied O^- sites were more prevalent. For the low salinity case, this type of site configuration existed at only one O^- site out of a total of 32 possibilities and even then, this configuration was observed only over the last 12.5 ns of the 60 ns MD trajectory. For the high salinity solution, this site configuration was observed at 5 of the 32 O^- sites; in three of those it was present for the entire simulation, while in two it formed during the simulation (32 and 37.5 ns) and persisted until the end (60 ns). three sites of this type prevailed for the entire 40 ns MD trajectory and a further two developed from the last 8 and 2.5 ns.

5.8.1 Determination of the Equilibrium Distribution of Site Types

Replica Exchange with Solute Tempering (REST) simulations^{189,10} were conducted in an attempt to determine the equilibrium distribution of the O^- -based configuration

types with greater accuracy. Various setups were used which ranged from 12 equally spaced replicas using the standard REST method¹⁸⁹ through to the other extreme of 72 replicas which ranged from 300 K to 800 K and used the more efficient variant of REST.¹⁰ However, even in this latter case, replica 0 remained at its original temperature for the entire 10 ns simulation and thus there was no enhancement of ion exchange between solution and surface, as shown in Figure 5.19. If this had been successful, a range of different possibilities for the distribution of the different site types would have been generated and an equilibrium distribution determined.

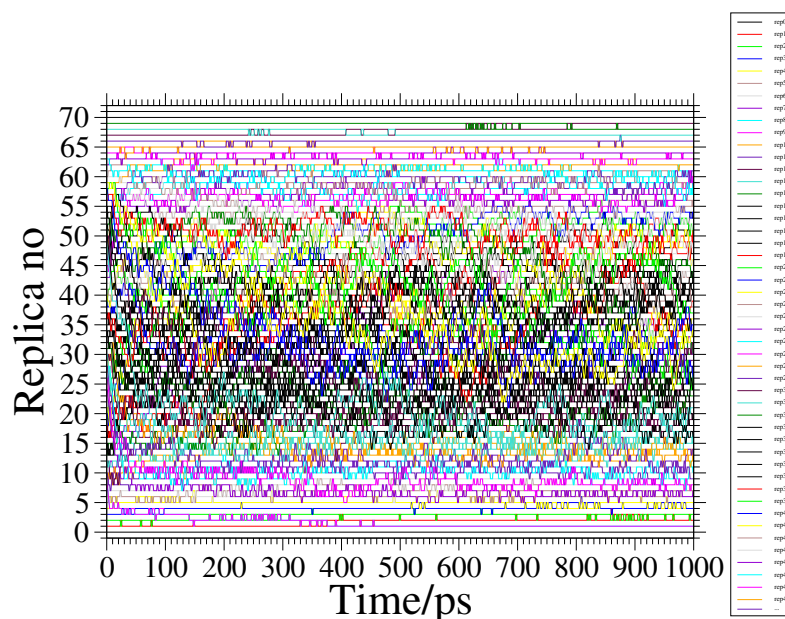


Figure 5.19: Replica mobility in the MD simulation using the more efficient REST technique¹⁰ for 72 replicas.

5.9 Conclusions

In our AFM experiments, substantial differences in the adhesion force of the functionalized tip to the amorphous silica surface were observed for COOH/COO^- functionality in divalent ion solutions and the NH_3^+ functionality in CaCl_2 solution. These differences were not observed in NaCl , KCl and MgCl_2 solutions for the NH_3^+ functionality or in the monovalent ion solutions for the COOH/COO^- moiety. Adsorption of the

NH_3^+ functionality at the aqueous electrolyte/amorphous silica interface is underexplored in the Literature and was a functionality chosen to be investigated further using metadynamics. Simulation showed that for the monovalent ion solutions the environments of the adsorption sites were labile and for aqueous MgCl_2 the majority of deprotonated oxygens were vacant throughout the simulation, which led to similar adsorption behavior. With CaCl_2 however, the Cl^- ion distribution evolved very slowly and five qualitatively-different types of adsorption-site configuration were identified, all featuring the deprotonated silica oxygen, but differing in the local arrangement of chloride ions. Vertical free energy profiles for the adsorption of the nitrogen from methylammonium to the silica surface were determined from metadynamics simulations and force-distance curves were constructed from these data. For the CaCl_2 solution, the greatest difference in the force-distance curves was observed for the $\text{Ca}^{2+}\text{Cl}^-_2$ -substituted O^- surface-site configuration - a site that was predicted to be more abundant under high salinity conditions. This was not a difference between the curves for the low and high salinity cases, but the difference in the force within a particular zone of the graph. This difference was comparable between low and high salinity for this site-type. This type of surface-site configuration was not predicted for any of the other saline solutions. We propose that the prevalence of this type of site in high salinity CaCl_2 solution explains the greater adhesion force. Since more of this site type will exist in high salinity solution, there will be more high force interactions between N and the surface compared to low salinity solution where the presence of the site-type is lower. Thus, overall it follows that the adhesion force of a functionalised tip which featured many NH_3^+ moieties will be higher in the high salinity solution where more of the $\text{Ca}^{2+}\text{Cl}^-_2$ -substituted O^- site type exist. The observed changes in adhesion provided further insight into the mechanism underlying enhanced oil recovery from sandstone reservoirs and indicated that Ca^{2+} and Cl^- ions, *via* the $\text{Ca}^{2+}\text{Cl}^-_2$ substituted O^- surface-site configuration, could control processes involving the adsorption of the NH_3^+ moiety. Our findings also indicated that biomolecule-silica interfaces could in general be amenable to manipulation *via* exploitation of this effect.

In common with our work, previous studies with a focus on EOR have observed in the interfacial behaviour of the aqueous divalent ion solutions in contact with minerals such as silica and mica (mimics for sandstone) or calcium carbonate. Clarke *et al.* found that the water layer which surrounded calcium carbonate particles was greatest

when in aqueous CaCl_2 or MgCl_2 compared to monovalent cation solutions (NaCl , KCl , LiCl , Na_2SO_4) or divalent sulphate (MgSO_4) solutions.²³³ Collins and co-workers observed that the contact angles of aqueous solutions in decane on mica were significantly greater for aqueous CaCl_2 than the monovalent chloride solutions, NaCl and KCl and that this contact angle increased yet further in the presence of the polar hydrocarbon, stearic acid.²³⁴

The results of this Chapter as well as the hypothesis developed within it can be linked to previously suggested hypotheses (Section 1.1.1). The only instance where there was a non-negligible (*i.e.* greater than 1.2 kJ mol^{-1}) difference between the free energy of adsorption of N to the silica surface was at the vacant O^- site in CaCl_2 solution, where it was of a lesser magnitude in 'low salinity' solution (0.1 M) than in 'high salinity' solution (0.3 M). The EDL expansion hypothesis suggests that the attraction in high salinity should be lower for the positively charged adsorbate as the negatively charged silica surface is more shielded by the increased concentration of interfacial cations. In line with this, the Debye length has been observed to be greater in 0.1 M CaCl_2 solution compared to 0.3 M (Chapter 4). However, a significant presence of interfacial chloride ions was observed at the aqueous CaCl_2 /silica interface, which was of greater concentration in the 0.3 M case compared to the 0.1 M case. This is not predicted by DLVO theory.¹⁶ Another interpretation is that there is increased attraction between the positively charged N and the increased concentration of background interfacial Cl^- ions. Within the multicomponent ion exchange mechanism, it has been suggested that ion bridging between Ca^{2+} ions and polar compounds plays a key role in the low salinity effect.¹⁸ It was proposed to be an equilibrium effect with a proportion of the divalent ions that linked organic molecules to the surface in the higher salinity solution migrating to bulk solution and releasing associated organic molecules. Divalent cation bridging of the methylammonium molecule to the silica surface has not been observed in the work of this Chapter, perhaps because the adsorbate, methylammonium, is positively charged. However, the force associated with the adsorption of N at one particular site-type was calculated to be greater for one particular site type, $\text{O}^- \text{Ca}^{2+} \text{Cl}^-_2$, that was more prevalent under high salinity conditions (0.3 M) than low (0.1 M). In the adsorption mechanism, the NH_3^+ group interacts with the O^- atom of the site-type. Negatively-charged adsorbates would need to be used to investigate potential bridging mechanisms between surface-associated Ca^{2+} ions.

Chapter 6

Further and Future Investigation of the Low Salinity Effect: A More Sophisticated Model of the Functionalized Atomic Force Microscopy (AFM) Tip

This Chapter is exploratory, detailing preliminary results and suggestions for future research directions. It builds on the work of Chapter 5, exploring adsorption of the NH_3^+ functionality at one particular interface - the aqueous 0.3 M CaCl_2 /amorphous silica interface - further. While in Chapter 5 the adsorption of the NH_3^+ moiety at the aqueous electrolyte/amorphous silica interface was investigated using methylammonium, in this Chapter a more sophisticated representation of the functionalised AFM tip will be considered. This model is composed of a gold substrate with 20 adsorbed 11-amino-1-undecanethiol ($-\text{S}(\text{CH}_2)_{11}\text{NH}_3^+$) molecules. The use of such a model enables the exploration of the potential cooperative effects of many NH_3^+ functionalities, as well as the impact of interactions between the long chain hydrocarbons not accounted for in the small molecule methylammonium, on adsorption at the aqueous 0.3 M CaCl_2 /amorphous silica interface.

There have been previous simulation studies of chemical force mapping atomic

force microscopy (CFM-AFM). Patrick *et. al.* modelled the interaction between a dodecanethiolate ($\text{S}(\text{CH}_2)_{11}\text{CH}_3$) coated gold sphere (with diameter 10 nm) interacting with a planar surface.⁷ Vlucht and co-workers analysed the interaction of a range of model functionalised AFM tips (using alkylthiols of different lengths from butanethiol to dodecanethiol and various nanoparticle sizes, 1.8-2.7 nm) with a Au(111) surface.¹⁶² Both of these studies have been further described in Section 1.6.4. The impact of monolayer structure on surface curvature was investigated using MD simulation by Ewers *et. al.*¹⁸³

Recently, Voitchovsky *et. al.* studied the aqueous electrolyte/mica interface using a combined MD simulation and 'interfacial dissipation microscopy' (IDM) AFM approach.⁹⁶ In IDM-AFM, the amplitude-modulation mode is used and quantitative information about the local free solvation energy at the solid/liquid interface obtained. In this process, the tip dissipates most of its energy within the interfacial liquid, with minimal interaction between the tip and the solid surface. Since ions perturb local solvent structure, the lateral location of ions with respect to the surface can be located using this approach. The 1 mM KCl/mica and 0.5 mM NaCl/mica interfaces were investigated. The hydrated ions formed ordered structures at the interface that were laterally stabilised by interfacial water molecules. Results from MD simulations indicate a dependence on the hydration structure of the solid and that of the adsorbing ions.

Appendix E contains: details of the initial configurations used in the MD simulations, evidence for the equilibration of the infinitely-sized monolayer and evidence for the equilibration of the model AFM tip system.

6.1 Simulation Protocol in Brief

The adsorption of a model functionalised AFM tip (a gold substrate with 20 adsorbed 11-amino-1-undecanethiol molecules) at the interface between amorphous silica was 0.3 M CaCl_2 solution was investigated. The preparation of the model AFM tip has been described in Section 2.1.2. An exemplar starting configuration of the model AFM tip simulation at a certain distance from the surface has been shown in Figure 6.1. The force required to constrain the S atoms of the tip model at a range of z -distance (vertical) separations from the surface was recorded. The force-fields, along with the general (Section 2.1.2) and specific simulation protocol for amorphous silica/aqueous electrolyte interfaces (Section 2.1.2) are the same as those used in Chapters 4 and 5. The substrate

atoms (Au and S) and thiols of the model tip were modelled using CHARMM.¹¹¹

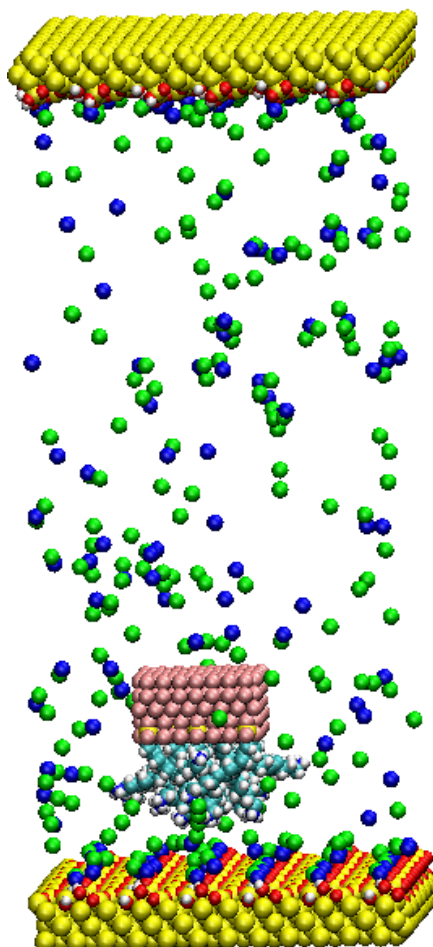


Figure 6.1: Schematic of the starting configuration of the model tip simulation at a certain distance from the surface. The gold atoms of the tip are shown in pink, with attached organics (bright blue C, dark blue N and white H), Cl^- ions are green and Ca^{2+} ions dark blue, silicon atoms are yellow, oxygen atoms are red and hydrogen white.

Model Atomic Force Microscopy (AFM) Tip Preparation

The model of the functionalized atomic force microscopy (AFM) tip was composed of 20 11-amino-1-undecanethiol ($-\text{S}(\text{CH}_2)_{11}\text{NH}_3^+$) molecules attached to a gold substrate taken from a section of an infinite monolayer that had been equilibrated in aqueous 0.3 M CaCl_2 at 300 K. Evidence of the equilibration of the infinite monolayer has been

given in Figure E.1, Appendix E. Evidence that the entire system containing the model tip had equilibrated is shown in Figure E.2(a)-(c), Appendix E. Figure E.2(d)-(f) (Appendix E) relate to how the structure of the 20 molecule finite 'monolayer' compared to that of the infinite monolayer. This analysis was conducted when the model tip S atoms were at a distance of 2.8 nm from the silica surface and therefore none of the atoms in the monolayer were in contact with the surface. The average difference in z -distance (vertical distance) from the surface between the N atom closest to the silica surface and that furthest away was fairly significant at 1.27 ± 0.027 nm, a difference almost as large as the average thickness of the infinitely-sized monolayer at 1.51 nm. This corresponded to a configuration where some of the gold-adsorbed molecules were splayed outwards from the upright and self-aligned orientation observed for the molecules in the infinite monolayer. The tilt angle in the finite monolayer followed the same general trend with time for all of the attached molecules and, on average, was comparable to that of molecules in the infinite monolayer. The mean squared displacement as a function of time was calculated for the N atom of each of the attached molecules in the finite monolayer and was a reflection of their mobilities. Generally those attached to the more central atoms of the gold substrate had a lower mobility than those that were attached to the outermost atoms, as would be expected considering the splayed nature of the configuration. The model tip was based on this 20 molecule subsection of an infinite monolayer of NH_3^+ terminated long-chain hydrocarbons, the properties of which were equilibrated and compared reasonably to the infinite counterpart.

6.2 Tip Force as a Function of Distance from the Surface

The force experienced by the model tip atoms was recorded when the sulfur and gold atoms of the model tip were restrained at different distances from the silica surface, as shown in Figure 6.2(a). No attractive forces were observed. In order to discern the distance from the silica surface at which the observation of an attractive force might be expected, the time-averaged minimum distance of the nitrogen atoms of the tip to the surface were recorded as a function of fixed sulfur and gold atom distance from the surface, as shown in Figure 6.2(b). In the profile of the change in free energy as

a function of distance from the silica surface, Minimum 1 occurred at ~ 0.22 nm and Minimum 2 at 0.37 nm for all adsorption site configurations at the aqueous CaCl_2 /silica interface, as detailed in Chapter 5 and labelled in Figure 6.2(b). Minimum 2 of the free energy distribution corresponded to a fixed gold and sulfur atom distance of ~ 2 nm from the silica surface and Minimum 1 corresponded to a span of distances from ~ 1 to 1.8 nm from the surface.

For the dataset labelled 'initial config' the series of configurations with gold and sulfur atoms fixed at the different distances from the silica surface were generated by shifting the entire tip towards the surface with no restrictions on the movement of the long chain hydrocarbons. The data point labelled 'idealised' represented an attempt to create a configuration for which there would be an attractive force. In this case, the molecules were less splayed out and resembled the aligned character of the infinite monolayer to a greater extent, with the result that more of the nitrogen atoms coincided with the z -distance from the surface at which the free energy profile was negative and an attractive force would be expected. This made little difference to the force experienced by the model tip however and it even became slightly more repulsive. The force curve recorded for the model AFM tip was of a repulsive nature and an attempt to generate a configuration for which the force experienced by the tip would be attractive did not succeed.

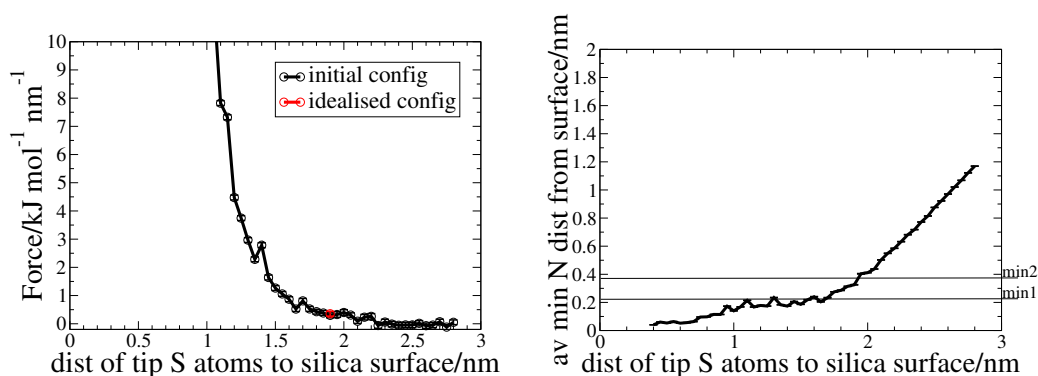


Figure 6.2: (a) Force experienced by the model tip atoms and (b) average minimum N atom distance to the silica surface when the gold and sulfur atoms of the model tip were restrained at different distances from the surface. For (b), 'min 1' and 'min 2' mark the approximate position of minimum 1 and the exact position of minimum 2 for the different adsorption site configurations in at the aqueous CaCl_2 /silica interface.

6.3 Limitations of this Approach

In order to make the calculation computationally feasible, in this system, only 20 11-amino-1-undecanethiol ($-\text{S}(\text{CH}_2)_{11}\text{NH}_3^+$) molecules were considered. One implication of this was that the structure of the infinite SAM was not very well maintained and the molecules of the tip splayed outwards. This might not, therefore, be a very realistic model of the tip and a larger system might be more appropriate. On the otherhand, characterisation of the tip was not possible and it is an assumption that a well-defined SAM of the thiol molecules was formed on the tip. In the real, experimental system, the packing of the molecules may not be so dense or as perfect as that modelled computationally. Furthermore, the lateral positioning of the tip may be important, since very few NH_3^+ -surface O^- interactions were observed. In order to maximise such contacts, a different positioning of the tip may have been needed. Normally, if simulated for long enough, you would expect favourable states - in this case, a configuration in which there were many NH_3^+ -surface O^- contacts - to be found. However, since the Au atoms of the tip were kept rigid in this system, natural rotation and translation was not possible. It would be time-consuming to do this rotation and translation manually and the most favourable arrangement may be difficult to find artificially.

6.4 Conclusion and Future Work

A model AFM tip was created to explore the potential cooperative effects of the adsorption of several NH_3^+ functionalities at the aqueous 0.3 M CaCl_2 /silica interface. This model tip was composed of 20 11-amino-1-undecanethiol ($-\text{S}(\text{CH}_2)_{11}\text{NH}_3^+$) molecules adsorbed to a gold substrate, taken from a subsection of an infinite monolayer of the same type of thiols that had been equilibrated in 0.3 M CaCl_2 solution. The structural differences between the model tip and the infinite monolayer were investigated by comparing quantities such as the tilt angle of the Au-adsorbed organic molecules. The model tip was moved gradually closer to the surface with no restraints on the mobility of the adsorbed organic molecules to generate the initial set of configurations that would be used in the force calculation. The force curve generated using such configurations was entirely repulsive. Even when the tip was far from the silica surface, where the force experienced by the tip atoms was recorded as zero, the adsorbed molecules

were relatively splayed in nature, with the difference between the closest atom to the silica surface and that furthest away at 1.27 nm, almost the same size as the thickness (S-average N z -distance) of the infinite monolayer, 1.5 nm. This suggested that it could be that there were not as many NH_3^+ functionalities at the correct distance from the surface in the model tip as there would be in the real version. An idealised configuration, where the Au-adsorbed molecules were more aligned as in the infinite monolayer was generated and positioned so that more N atoms were at the optimal distance for favourable interaction with the silica surface. This, however, still resulted in a repulsive force for the distance at which it was tested, a distance where attraction would be expected. Further work is required to explore alternative configurations and find cases where there is attraction between the tip and the model surface.

There are various aspects of the system that could be explored in future work. Given that there were 20 NH_3^+ functionalities in the model tip and that the area it covered featured only four O^- adsorption sites, the lateral positioning of the model tip, especially the NH_3^+ functionalities, is particularly important to generate configurations where the model tip experiences an attractive force. In future work, the 'idealised configuration' described above, could be translated and rotated in xy -space to find cases where the number of interactions between the NH_3^+ groups and the deprotonated oxygens of the surface are at a maximum. It might also be that a well-ordered SAM is not a good model for the functionalized AFM tip and that in the real experimental system the molecules are not so densely and perfectly packed, forming more of a 'brush' surface. Furthermore, larger model tips could be investigated. The larger the model tip, the closer in structure it will be to the infinite monolayer and the smaller the difference between the maximum and minimum z -distance from the silica surface of model tip nitrogen atoms to the surface (*i.e* the character of the adsorbed tip molecules will be less splayed and more aligned). If N atoms are similar distances from the surface, the potential for an overall favourable interaction with the silica surface would be increased. The two major directions that have been detailed and directly build on the work carried out thus far concern the lateral positioning of the tip in relation to adsorption sites of the silica surface and the number of organic molecules that make up the tip.

Chapter 7

Conclusion

The main aim of this thesis was to gain insight into the molecular-level interactions at the aqueous electrolyte/amorphous silica interface and their impact on the adsorption of organic matter. The effect of changes to the concentration of the electrolyte solutions on molecular adsorption at the interface was a particular focus and was investigated for various types of electrolyte. While this study was specifically designed to explore why the use of low salinity water leads to increased oil yields in the water flooding of sandstone reservoirs (for which amorphous silica is a model), molecular adsorption at the aqueous electrolyte/amorphous silica interface underlies a wide range of naturally-occurring processes and commercial applications.

Unlike in previous investigations of the 'low salinity' effect at the aqueous electrolyte/amorphous silica interface,⁸ which featured artificial seawater (ASW), a reductionist approach was adopted in the work of this thesis, using pure saline solutions of some of the electrolyte types present in seawater (NaCl, KCl, CaCl₂ and MgCl₂). The two concentrations - 0.1 M ('low salinity') and 0.3 M ('high salinity') - were chosen since they were accessible by both atomistic simulation and chemical force-mapping atomic force microscopy (CFM-AFM) experiment, both of which were employed in this thesis. These were generally much higher than their counterpart concentrations in ASW and diluted ASW²³⁰ and so should be considered as demonstrating the changes that occur when concentration is altered rather than as being representative of the interface at the actual concentrations of ASW and diluted ASW. The adhesion of NH₃⁺ and COOH/COO⁻ moieties, both common functional groups in crude oil, to the aqueous

electrolyte/amorphous silica interface was investigated using CFM-AFM, with adsorption of the former functionality also being studied using an advanced molecular dynamics (MD) simulation technique, metadynamics (metaD) and the potential of mean force (PMF) approach.

The type and concentration of electrolyte influences the character of the interfacial environment, a character crucial to understanding and controlling molecular adsorption at the interface. The impact of electrolyte type and concentration has been the remit of Chapter 4. Analysis of MD simulations predicted that ion structuring differed most significantly between aqueous CaCl_2 and the rest of the electrolyte solutions. Interfacial Ca^{2+} concentration was over double that of any of the other cations and there was a significant presence of interfacial Cl^- ions that was not observed for any of the other aqueous electrolytes. The Ca^{2+} z -density distribution featured two clear peaks at 3 Å and 4.1 Å, with a large peak in Cl^- density in between at 3.3 Å followed by peaks of increasingly decreased magnitude at 4.1 Å, 5.2 Å and 6.5 Å. Lateral density profiles for Ca^{2+} ions within the peaks showed that regions of high density were located in the vicinity of the deprotonated silanols. Indeed, the peaks in the Ca^{2+} z -density were found primarily to represent $\text{Ca}^{2+}_{(\text{O}^-)}$ (Ca^{2+} that was associated with surface O^-). It was then found that Cl^- ions could associate with the $\text{Ca}^{2+}_{(\text{O}^-)}$, with long-lived configurations featuring up to 2 Cl^- ions observed. Such associated Cl^- ions were found to be primarily responsible for the peaks in the Cl^- z -density distributions. As a result, four distinct long-lived (with lifetimes of at least tens of nanoseconds) O^- -based adsorption site types formed: O^- ; $\text{O}^- \text{Ca}^{2+}$; $\text{O}^- \text{Ca}^{2+} \text{Cl}^-$ and $\text{O}^- \text{Ca}^{2+} \text{Cl}^-_2$.

Furthermore, CaCl_2 was the only electrolyte for which the relative proportions of the peaks in the cation z -density distributions showed a dependence on concentration. In 0.1 M solution, the Ca^{2+} peak closest to the surface (at 3 Å) was minimal, while in 0.3 M solution it was of comparable magnitude to the more distant peak (at 4.1 Å). The inner peak was found to be mainly due to Ca^{2+} with 2 associated Cl^- ions and the increase in its magnitude relative to the outer peak related to the greater proportion of $\text{O}^- \text{Ca}^{2+} \text{Cl}^-_2$ sites in 0.3 M (19.9 %) solution compared to 0.1 M (1.3 %). The intensity of the Cl^- z -density distribution also increased with concentration. This change directly related to the increase in the proportion of site types with associated Cl^- (a total of 72.8 % for 0.3 M compared to a total of 25.4 % for 0.1 M). *We hypothesised that the significant changes observed on changing CaCl_2 concentration underly the 'low salinity' effect.*

The dynamics of interfacial ions was also explored in the computational study. The only other cation to exhibit surface residence times of at least the same order of magnitude as Ca^{2+} (57.2 \pm 2.7 ns for 0.1 M and >40 ns for 0.3 M) was Mg^{2+} (>60.0 ns for 0.1 M and >40.0 ns for 0.3 M). Residence times of the monovalent ions were tens to hundreds of picoseconds in size. In addition to ensuring that the surface charge density in the model amorphous silica surface was the same as measured experimentally at pH 5.5, the ζ -potential was considered as another point of connection between experiment and the computational model. In traditional electrical double layer (EDL) models, the ζ -potential is defined as the electrostatic potential at the slipping plane, a region close to the surface where the cation mobility changes sharply. Although a region of reduced mobility was observed, no evidence for a sharp change was found.

Another aspect of traditional EDL models, however, was observed. DLVO theory predicts that the Debye length (width of the EDL) will be smaller the greater the ionic strength of the solution.¹⁶ For CaCl_2 , NaCl and KCl solutions, the width of the EDL was greater in the 0.1 M case (~ 40 Å) compared to the 0.3 M case (~ 25 Å). This is the first time, to the best of our knowledge, that this phenomenon has been observed using atomistic MD simulation. DLVO theory also predicts that the EDL in the case of the CaCl_2 solutions should be smaller than the corresponding monovalent ion solutions. This, however, was not observed. The change in the width of the EDL with concentration has implications for commonly used EOR theories, including fines migration theory and multicomponent ion exchange. In fines migration theory, the increased width of the EDL in low salinity solution, makes interaction between the EDLs of colloidal clay particles more likely, which leads to bulk clay swelling and the release of fine clay particles with associated oil. The multicomponent ion exchange mechanism is not supported, as the width of the EDL was the same for both monovalent electrolytes and the divalent CaCl_2 . The data for MgCl_2 is discarded from this discussion of the EDL, since the EDL width did not change with concentration in this case; this was potentially linked to the strong hydration shell of Mg^{2+} .

Analysis of MD simulations indicated that the electrolyte- and concentration-dependent changes to interfacial water structure were more subtle. All z -density distributions had three main peaks and followed the same approximate shape. For CaCl_2 solution, the third peak was shifted (at 6.2 Å compared to the 5.9 Å of the other distribu-

tions) and was of a sharper, more asymmetric character than that of the other aqueous electrolytes. CaCl_2 was the only case for which the distribution altered - albeit not substantially - on increasing concentration from 0.1 M to 0.3 M, with the latter case featuring two subsidiary peaks at 1.7 Å and 4.9 Å. Furthermore, in the 3.5-6 Å region, the net water orientation vs distance from the surface profiles were concave-down for aqueous CaCl_2 compared to concave-up for the other electrolytes. There was a correlation between the different patterns in the local, lateral water density and orientation and the various long-lived site types (O^- , O^-Ca^{2+} , $\text{O}^-\text{Ca}^{2+}\text{Cl}^-$ and $\text{O}^-\text{Ca}^{2+}\text{Cl}_2^-$). Differences in local water structure associated with O^- and O^-Mg^{2+} site-types in aqueous MgCl_2 were also observed.

The implications of these changes to interfacial water structure with concentration and electrolyte type will now be considered. Interfacial water structure has previously been described as governing molecular adsorption at solid/liquid interfaces and therefore, it is of great importance to oil adsorption at the silica/water interface.²² Since the proportion of the different long-lived sites ($\text{O}^-\text{Ca}^{2+}\text{Cl}^-$ and $\text{O}^-\text{Ca}^{2+}\text{Cl}_2^-$) was dependent on concentration, the interfacial water structure will be dependent on concentration. Furthermore, the proportion of deprotonated silanol groups would be expected to vary with pH and as such pH-dependent differences in interfacial water structure are predicted as a consequence of this. Interfacial water structure has both a pH and concentration dependence and such variations in pH and concentration are likely to have an impact on molecular (*i.e.* oil adsorption) at the silica/water interface.

Molecular adsorption at the aqueous electrolyte/amorphous silica interface was the explicit concern of Chapters 5 and 6. The interoperability of the different parts of the system (organic and amorphous silica) was essential. Force-field interoperability is a topic that has been considered in Chapter 3. The results of CFM-AFM experiments are presented in Chapter 5, and show a substantial dependence on concentration was observed for the adhesion of NH_3^+ in CaCl_2 solution and COOH/COO^- in the divalent ion solutions. Furthermore, adhesion was also much stronger in these cases, ranging from ~50 % to ~1200 % larger compared to in the other electrolyte types. The adsorption of the NH_3^+ functionality was investigated further using computational modelling. In Chapter 5, the free energy of adsorption of the NH_3^+ group of methylammonium to the various aqueous electrolyte/amorphous silica interfaces (NaCl , KCl , CaCl_2 and MgCl_2 at 0.1 M and 0.3 M) was calculated using metadynamics. Since we

hypothesised that the difference in the proportion of the various long-lived site-types (O^- , O^-Ca^{2+} , $\text{O}^-\text{Ca}^{2+}\text{Cl}^-$ and $\text{O}^-\text{Ca}^{2+}\text{Cl}^-_2$) at the aqueous CaCl_2 /amorphous silica interface was the origin of the low salinity effect, adsorption at each of the sites was considered separately.

The free energy profiles for adsorption in all of the electrolyte solutions except CaCl_2 all followed the same general shape and had minima of approximately the same depth, with no significant dependence on concentration. For CaCl_2 , the only site for which the depth of the minima displayed a non-negligible difference (*i.e.* greater than 1.2 kJ mol^{-1}) was O^- , where the adsorption free energy was greater in 0.3 M compared to 0.1 M. This was proposed to relate to the higher interfacial Cl^- concentration in the 0.3 M case.

It is the gradient of the free energy profiles that more properly relates to the experimental adhesion force measurements however and force curves were calculated using the derivative of the free energy profiles. A large change in the force was observed in the force curves for the $\text{Ca}^{2+}\text{Cl}^-_2$ -substituted O^- surface-site configuration that was not seen for any of the other surface-site configuration types or electrolyte types. The magnitude of this change was the same for both 0.1 M and 0.3 M solutions. Since the site-type is more abundant under HS conditions (0.3 M) compared to LS (0.1 M), it follows that a functionalised AFM tip would interact with more of this site-type on average in HS solution compared to LS and thus have a higher adhesion force in the more concentrated solution; We propose this is the basis for the low salinity effect.

The results of Chapter 5 - as well as the hypothesis developed within it that the low salinity effect is due to a large force experienced by NH_3^+ associated with a particular site-type that is more prevalent under high salinity (0.3 M) conditions than low salinity (0.1 M) conditions - can be linked to previously proposed hypotheses (Section 1.1.1). A non-negligible difference (greater than 1.2 kJ mol^{-1}) in the free energy of adsorption of N at the silica/aqueous electrolyte interface was observed for adsorption at the O^- site in CaCl_2 solution. DLVO theory predicts that the attraction of the positively charged adsorbate will be decreased in high salinity solution, as the interfacial concentration of cations is expected to be greater. However, the reverse trend is observed. The greater magnitude of the free energy of adsorption in the high salinity case is correlated with the increased concentration of interfacial chloride ions. The multicomponent ion exchange mechanism predicts that ion bridging should be observed, with Ca^{2+} ions

linking negatively charged polar compounds to the negatively charged surface. While this mechanism was not expected for a positively charged adsorbate, there is a large force associated with the adsorption of N at the $\text{O}^- \text{Ca}^{2+} \text{Cl}^-_2$ site-type, a site-type that is more prevalent under high salinity conditions than low.

The 0.3 M aqueous CaCl_2 /amorphous silica interface was chosen for further investigation in Chapter 6. The Chapter was exploratory and described potential future research directions. In this Chapter, the forces required to constrain the S and Au atoms of a model functionalised AFM tip (a gold substrate with 20 adsorbed 11-amino-1-undecanethiol ($-\text{S}(\text{CH}_2)_{11}\text{NH}_3^+$) molecules) at various z -distances (vertical separations) from the silica surface was recorded. The force curve recorded was repulsive in character however. Suggested future research directions include the use of a larger model tip and the orientation of the tip relative to the surface, both to ensure that the number of surface O^- to tip NH_3^+ interactions are maximised.

The approach adopted in Chapter 5 used just one adsorbate molecule. While this makes analysis of the system straightforward, the potential for cooperative effects between many organic molecules cannot be probed. In a similar study at the aqueous electrolyte/montmorillonite interface, Greenwell *et. al.* used 80 organic molecules in their simulation cell.¹¹ While the work of Chapter 6 attempts to probe the cooperative effects of several organic molecules, there are many limitations. Unlike in the study of Greenwell *et. al.*,¹¹ the molecules are not free to rotate and translate, with fixed anchor points at the S terminus. This potentially prevents the molecules from finding favourable configurations, where there are many interactions between the NH_3^+ groups and O^- atoms of the surface. The tip would need to be translated and rotated manually, a process which would be time-consuming and even then may not find the optimal configurations. Only 20 hydrocarbon molecules were used in the work of Chapter 6. This is not sufficient to maintain an ordered SAM. Patrick *et. al.* modelled the CFM-AFM tip using 278 dodecanethiolate molecules attached to the bottom of a gold sphere with a diameter of 10 nm, with an outer ring of 52 frozen organic molecules to maintain SAM order and the interaction with a planar surface was monitored.⁷ Although the use of more organic molecules may be a more realistic approximation to the tip, the simulations were conducted in vacuum and important interactions with water neglected. The simulation work of this thesis probed only a positively charged adsorbate at the negatively charged silica/aqueous electrolyte interface. A common EOR mechanism -

multicomponent ion exchange - features cation bridging (normally divalent Ca^{2+} ions) between negatively charged adsorbates and negatively charged surfaces. In order to test this proposed mechanism properly, the interaction of negatively charged adsorbates, such as R-COO^- , with the silica surface should be probed by atomistic simulation and not just by CFM-AFM.

Bibliography

- [1] Butenuth, A.; Moras, G.; Schneider, J.; Koleini, M.; Köppen, S.; Meissner, R.; Wright, L. B.; Wright, T. R.; Colombi Ciacchi, L. *Phys. Status Solidi B* **2012**, *249*, 292–305.
- [2] Ostroverkhov, V.; Waychunas, G. A.; Shen, Y. R. *Chem. Phys. Lett.* **2004**, *386*, 144–148.
- [3] Notman, R.; Walsh, T. R. *Langmuir* **2009**, *25*, 1638–1644.
- [4] Musso, F.; Mignon, P.; Ugliengo, P.; Sodupe, M. *Phys. Chem. Chem. Phys.* **2012**, *14*, 10507–10514.
- [5] Wallace, A. F.; Gibbs, G. V.; Dove, P. M. *J. Phys. Chem. A* **2010**, *114*, 2534–2542.
- [6] Saha, J. K.; Ahn, Y.; Kim, H.; Schatz, G. C.; Jang, J. *J. Phys. Chem. C* **2011**, *115*, 13193–13199.
- [7] Patrick, D. L.; Flanagan, IV, J. F.; Kohl, P.; Lynden-Bell, R. M. *J. Am. Chem. Soc.* **2003**, *125*, 6762–6773.
- [8] Hassenkam, T.; Mitchell, A. C.; Pedersen, C. S.; Skovbjerg, L. L.; Bovet, N.; Stipp, S. L. S. *Colloids and Surfaces A: Physicochem. Eng. Aspects* **2012**, *403*, 79–86.
- [9] Noy, A.; Vezenov, D. V.; Lieber, C. M. *Annu. Rev. Mater. Sci.* **1997**, *27*, 381–421.
- [10] Huang, X.; Hagen, M.; Kim, B.; Friesner, R. A.; Zhou, R.; Berne, B. J. *J. Phys. Chem. B* **2007**, *111*, 5405–5410.

- [11] Underwood, T.; Erastova, V.; Cubillas, P.; Greenwell, H. C. *J. Phys. Chem. C* **2015**, *119*, 7282–7294.
- [12] Yamamoto, M.; Taguchi, K.; Sasaki, K. *Chemical Geology* **1991**, *93*, 193–206.
- [13] Zhang, T. M.; Liang, Y. Z.; Li, B. Y.; Cui, H.; Huang, L. F.; Guo, F. Q.; Zhao, C. X. *Ann Chim-Rome* **2004**, *94*, 783–794.
- [14] Tang, G. Q.; Morrow, N. R. *J. Petrol. Sci. Eng.* **1999**, *24*, 99–111.
- [15] Sheng, J. *J. Petrol. Sci. Eng.* **2014**, *120*, 216–224.
- [16] Verwey, E. J. W.; Overbeek, J. T. G. *Theory of the Stability of Lyophobic Colloids*; Courier Dover Publications: New York, 1999.
- [17] Sposito, G.; Oxford University Press: New York, 2008; chapter ?
- [18] Lager, A.; adn C. J. J. Black, K. J. W.; Singleton, M.; Sorbie, K. S. *Petrophysics* **2008**, *49*, 28–35.
- [19] RezaeiDoust, R.; Puntervold, T.; Strand, S.; Austad, T. *Energy Fuels* **2009**, *23*, 4479–4485.
- [20] Rimola, A.; Costa, D.; Sodupe, M.; Lambert, J.-F.; Ugliengo, P. *Chem. Rev.* **2013**, *113*, 4216–4313.
- [21] Gunko, V. M.; Turov, V. V.; Zarko, V. I.; Voronin, E. F.; Tischenko, V. A.; Dudnik, V. V.; Pakhlov, E. M.; Chuiko, A. A. *Langmuir* **1997**, *13*, 1529–1544.
- [22] Schneider, J.; Ciacchi, L. C. *J. Am. Chem. Soc.* **2012**, *134*, 2407–2413.
- [23] Jena, K. C.; Hore, D. K. *Phys. Chem. Chem. Phys.* **2010**, *12*, 14383–14404.
- [24] Hall, S. A.; Jena, K. C.; Covert, P. A.; Roy, S.; Trudeau, T. G.; Hore, D. K. *J. Phys. Chem. B* **2014**, *118*, 5617–5636.
- [25] Hench, L. L.; Splinter, R. J.; Allen, W. C.; Greenlee, T. K. *J. Biomed. Mater. Res. Sympposium* **1971**, *5*, 117–141.

- [26] Letaief, N.; Lucas-Girot, A.; Oudadesse, H.; Meleard, P.; Pott, T.; Jelassi, J.; Dorbez-Sridi, R. *J. Non-Cryst. Solids* **2014**, *402*, 194–199.
- [27] Schröder, H. C.; Wang, X.; Tremel, W.; Ushijima, H.; Müller, W. E. G. *Nat. Prod. Rep.* **2008**, *25*, 455–474.
- [28] Kalmar, L.; Homola, D.; Varga, G.; Tompa, P. *Bone* **2012**, *51*, 528–534.
- [29] Parida, S. K.; Dash, S.; Patel, S.; Mishra, B. K. *Adv. Colloid Interface Sci.* **2006**, *121*, 77–110.
- [30] Morrow, B. A.; Cody, I. A.; Lee, L. S. M. *J. Phys. Chem.* **1976**, *80*, 2761–2767.
- [31] Dove, P. M.; Craven, C. M. *Geochim. Cosmochim. Acta* **2005**, *69*, 4963–4970.
- [32] Ostroverkhov, V.; Waychunas, G. A.; Shen, Y. R. *Phys. Rev. Lett.* **2005**, *94*, No. 046102.
- [33] Salis, A.; Parsons, D. F.; Boström, M.; Medda, L.; Barse, B.; Ninham, B. W.; Monduzzi, M. *Langmuir* **2010**, *26*, 2484–2490.
- [34] Azam, M. S.; Weeraman, C. N.; Gibbs-Davis, J. M. *J. Phys. Chem. Lett.* **2012**, *3*, 1269–1274.
- [35] Azam, M. S.; Weeraman, C. N.; Gibbs-Davis, J. M. *J. Phys. Chem. C.* **2012**, *3*, 1269–1274.
- [36] Fournier, R. O.; Marshall, W. L. *Geochim. Cosmochim. Acta* **1982**, *47*, 587–596.
- [37] Azaroual, M.; Fouillac, C.; Matray, J. M. *Chemical Geology* **1997**, *140*, 155–165.
- [38] Icenhower, J. P.; Dove, P. M. *Geochim. Cosmochim. Acta* **2000**, *64*, 4193–4203.
- [39] Loucaides, S.; Cappellen, P. V.; Behrends, T. *Limnol. Oceanogr.* **2008**, *53*, 1614–1621.
- [40] Bai, S.; Urabe, S.; Okaue, Y.; Yokoyama, T. *J. Colloid Interface Sci.* **2009**, *331*, 551–554.

- [41] Takahashi, Y.; Minai, Y.; Ambe, S.; Makide, Y.; Ambe, F. *Geochim. Cosmochim. Acta* **1999**, *63*, 815–836.
- [42] Sverjensky, D. A. *Geochim. Cosmochim. Acta* **2006**, *70*, 2427–2453.
- [43] Pivovarov, S. *J. Colloid Interface Sci.* **2008**, *319*, 374–376.
- [44] Porus, M.; Labbez, C.; Maroni, P.; Borkovec, M. *J. Chem. Phys.* **2011**, *135*, No. 063701.
- [45] Morag, J.; Dishon, M.; Sivan, U. *Langmuir* **2013**, *29*, 6317–6322.
- [46] Engemann, S.; Reichert, H.; Dosch, H.; Bilgram, J.; Honkimäki, V.; Snigirev, A. *Phys. Rev. Lett.* **2004**, *92*, No. 205701.
- [47] Sermon, P. A. *J. Chem. Soc., Faraday Trans* **1980**, *76*, 885–888.
- [48] Stålgren, J. J. R.; Boschkova, K.; Ericsson, J.-C.; Frank, C. W.; Knoll, W.; Satija, S.; Toney, M. F. *Langmuir* **2007**, *23*, 11943–12460.
- [49] Jena, K. C.; Hore, D. K. *J. Phys. Chem. C* **2009**, *113*, 15364–15372.
- [50] Du, Q.; Freyz, E.; Shen, Y. R. *Phys. Rev. Lett.* **1994**, *72*, 238–241.
- [51] Dewan, S.; Yeganeh, M. S.; Borguet, E. *J. Phys. Chem. Lett.* **2013**, *4*, 1977–1982.
- [52] Jena, K. C.; Covert, P. A.; Hore, D. K. *J. Phys. Chem. Lett.* **2011**, *2*, 1056–1061.
- [53] Covert, P. A.; Jena, K. C.; Hore, D. K. *J. Phys. Chem. Lett.* **2014**, *5*, 143–148.
- [54] Yang, Z.; Li, Q.; Chou, K. C. *J. Phys. Chem. C* **2009**, *13*, 8201–8205.
- [55] Flores, S. C.; Kherb, J.; Konelick, N.; Chen, X.; Cremer, P. S. *J. Phys. Chem. C* **2012**, *116*, 5730–5734.
- [56] Flores, S. C.; Kherb, J.; Cremer, P. S. *J. Phys. Chem. C* **2012**, *116*, 14408–14413.
- [57] Azam, M. S.; Darlington, A.; Gibbs-Davis, J. M. *J. Phys. Condens. Matter* **2014**, *26*, No. 244107.

- [58] Cardenas, J. F. *Colloids and Surfaces A: Physicochem. Eng. Aspects* **2005**, 266, 147–149.
- [59] Brown, M. A.; Arrigoni, M.; Héroguel, F.; Redondo, A. B.; Giordana, L.; van Bokhoven, J. A.; Pacchioni, G. *J. Phys. Chem. C* **2014**, 118, 29007–29016.
- [60] Shchukarev, A. V. *Colloid J.* **2007**, 69, 514–525.
- [61] Siretanu, I.; Ebeling, D.; Andersson, M. P.; Stipp, S. L. S.; Philipse, A.; Stuart, M. C.; van den Ende, D.; Mugele, F. *Sci. Rep.* **2014**, 4, No. 4956.
- [62] Benning, L. G.; Hulshoff, M.-A.; Blanco, J. D. R.; Elliott, T.; Oelkers, E. H.; Stipp, S. L. S. *Geochem. Perspect.* **2013**, 1, 483–742.
- [63] Li, D.; Oxford, 2004; chapter 2.
- [64] Gouy, G. *Ann. Phys. (Paris)* **1910**, 49, 457–468.
- [65] Chapman, D. L. *Philos. Mag.* **1913**, 25, 475–481.
- [66] Stern, O. *Z. Elektrochem.* **1924**, 30, 508–516.
- [67] Dukhin, A.; Dukhin, S.; Goetz, P. *Langmuir* **2005**, 21, 9990–9997.
- [68] Helmholtz, H. *Annalen d. Phys. u. Chem.* **1879**, 7, 337–382.
- [69] Grahame, D. C. *Chem. Rev.* **1947**, 41, 441–501.
- [70] Hatlo, M. M.; van Roij, R.; Lue, L. *EPL* **2012**, 97, No. 28010.
- [71] Henderson, D.; Lamperski, S.; Bhuiyan, L. B.; Wu, J. *J. Chem. Phys.* **2013**, 138, No. 144704.
- [72] Zhang, H.; Hassanali, A. A.; Shin, Y. K.; Knight, C.; Singer, S. J. *J. Chem. Phys.* **2011**, 134, No. 024705.
- [73] Lykema, J. *Colloids and Surfaces A: Physicochem. Eng. Aspects* **1994**, 92, 41–49.
- [74] Zukoski IV, C. F.; Saville, D. A. *J. Colloid Interface Sci.* **1986**, 114, 32–44.

- [75] Zukoski IV, C. F.; Saville, D. A. *J. Colloid Interface Sci.* **1986**, *114*, 45–54.
- [76] Bukšek, H.; Luxbacher, T.; Petrinić, I. *Acta Chim. Slov.* **2010**, *57*, 700–706.
- [77] Dukhin, S. S.; Zimmerman, R.; Werner, C. *Colloids and Surfaces A: Physicochem. Eng. Aspects* **2001**, *195*, 103–112.
- [78] López-García, J. J.; Grosse, C.; Horno, J. *J. Phys. Chem. B.* **2007**, *111*, 8985–8992.
- [79] Lorenz, C. D.; Crozier, P. S.; Anderson, J. A.; Travesset, A. *J. Phys. Chem. C.* **2008**, *112*, 10222–10232.
- [80] Gupta, P. K.; Meuwly, M. *Faraday Discuss.* **2013**, *167*, 329–346.
- [81] Joseph, S.; Aluru, N. R. *Langmuir* **2006**, *22*, 9041–9051.
- [82] Emami, F. S.; Puddu, V.; Berry, R. J.; Varshney, V.; Patwardhan, S. V.; Perry, C. C.; Heinz, H. *Chem. Mater.* **2014**, *26*, 2647–2658.
- [83] Skelton, A. A.; Fenter, P.; Kubicki, J. D.; Wesolowski, D. J.; Cummings, P. T. *J. Phys. Chem. C.* **2011**, *115*, 2076–2088.
- [84] Skelton, A. A.; Wesolowski, D. J.; Cummings, P. T. *Langmuir* **2011**, *27*, 8700–8709.
- [85] Lopes, P. E. M.; Murashov, V.; Tazi, M.; Demchuk, E.; MacKerell, Jr., A. D. *J. Phys. Chem. B.* **2006**, *110*, 2782–2792.
- [86] Ho, T. A.; Argyris, D.; Papavassiliou, D. V.; Striolo, A.; Lee, L. L.; Cole, D. R. *Mol. Simul.* **2011**, *37*, 172–195.
- [87] Sulpizi, M.; Gaigeot, M.-P.; Sprik, M. *J. Chem. Theory Comput.* **2012**, *8*, 1037–1047.
- [88] Gaigeot, M.-P.; Sprik, M.; Sulpizi, M. *J. Phys. Condens. Matter.* **2012**, *24*, No. 124106.
- [89] Cimas, A.; Tielens, F.; Sulpizi, M.; Gaigeot, M.-P.; Costa, D. *J. Phys. Condens. Matter.* **2014**, *26*, No. 244106.

- [90] Fogarty, J. C.; Aktulga, H. M.; Grama, A. Y.; van Duin, A. C. T.; Pandit, S. A. *J. Chem. Phys.* **2010**, *132*, No. 174704.
- [91] DelloStritto, M. J.; Kubicki, J.; Sofo, J. O. *J. Phys. Condens. Matter.* **2014**, *26*, No. 244101.
- [92] Kubicki, J. D.; Sofo, J. O.; Skelton, A. A.; Bandura, A. V. *J. Phys. Chem. C.* **2012**, *116*, 17479–17491.
- [93] Ma, Y.-M.; Zhang, H.; Zhang, B.-J. *Mol. Simul.* **2014**, *40*, 634–639.
- [94] Cygan, R. T.; Liang, J. J.; Kalinichev, A. G. *J. Phys. Chem. B.* **2004**, *108*, 1255–1266.
- [95] Kroutil, O.; Chval, Z.; Skelton, A. A.; Predota, M. *J. Phys. Chem. C.* **2015**, *119*, 9274–9286.
- [96] Ricci, M.; Spijker, P.; Voitchovsky, K. *Nat. Commun.* **2014**, *5*, No. 4400.
- [97] de Lara, L. S.; Rigo, V. A.; Michelon, M. F.; Metin, C. O.; Nguyen, Q. P.; Miranda, C. R. *J. Phys. Condens. Matter.* **2015**, *27*, No. 325101.
- [98] Metin, C. O.; Lake, L. W.; Miranda, C. R.; Nguyen, Q. P. *J. Nanopart. Res.* **2011**, *13*, 839–850.
- [99] Cruz-Chu, E. R.; Aksimentiev, A.; Schulten, K. *J. Phys. Chem. B.* **2006**, *110*, 21497–21508.
- [100] Dewan, S.; Carnevale, V.; Bankura, A.; Eftekhari-Bafrooei, A.; Fiorin, G.; Klein, M. L.; Borguet, E. *Langmuir* **2014**, *30*, 8056–8065.
- [101] Raiteri, P.; Gale, J. D. *J. Am. Chem. Soc.* **2010**, *132*, 17623–17634.
- [102] Jorgensen, W. L.; Chandrasekhar, J.; Madura, J. D.; Impey, R. W.; Klein, M. L. *J. Chem. Phys.* **1983**, *79*, 926–935.
- [103] Dill, K. A. *Biochemistry* **1990**, *29*, 7133–7155.
- [104] Kitao, A.; Hirata, F.; Go, N. *Chem. Phys.* **1991**, *158*, 447–472.

- [105] Fennell, C. J.; Dill, K. A. *J. Stat. Phys.* **2011**, *145*, 209–226.
- [106] Cramer, C. J.; Truhlar, D. G. *Chem. Rev.* **1999**, *99*, 2161–2200.
- [107] Lazaridis, T.; Karplus, M. *Curr. Opin. Struct. Biol.* **2000**, *10*, 139–145.
- [108] Bashford, D.; Case, D. A. *Ann. Rev. Phys. Chem.* **2000**, *51*, 129–152.
- [109] Lopes, P. E. M.; Roux, B.; MacKerell, A. D. *Theor. Chem. Acc.* **2009**, *124*, 11–28.
- [110] Berendsen, H. J. C.; Postma, J. P.; van Gunsteren, W. F.; Hermans, J. *Intermolecular Forces*; Reidel, Dordrecht, 1981.
- [111] MacKerell Jr., A. D.; Bashford, D.; Bellott, M.; Dunbrack, R. L.; Evanseck, J. D.; Field, M. J.; Fischer, S.; Gao, J.; Guo, H.; Ha, S.; Joseph-McCarthy, D.; Kuchnir, L.; Kuczero, K.; Lau, F. T. K.; Mattos, C.; Michnick, S.; Ngo, T.; Nguyen, D. T.; Prodhom, B.; Reiher, W. E.; Roux, B.; Schlenkrich, M.; Smith, J. C.; Stote, R.; Straub, J.; Watanabe, M.; Wiorkiewicz-Kuczero, J.; Yin, D.; Karplus, M. *J. Phys. Chem. B* **1998**, *102*, 3586–3616.
- [112] Brooks, B. R.; Bruccoleri, R. E.; Olfason, B. D.; States, D. J.; Swaminathan, S.; Karplus, M. *J. Comp. Chem.* **1983**, *4*, 187–217.
- [113] Pearlman, D. A.; Case, D. A.; Caldwell, J. W.; Ross, W. S.; Cheatham III, T. E.; DeBolt, S.; Ferguson, D.; Seibel, G.; Kollman, P. *Comp. Phys. Comm.* **1995**, *91*, 1–41.
- [114] Cornell, W. D.; Cieplak, P.; Bayly, C. I.; Gould, I. R.; Merz Jr., K. M.; Ferguson, D. M.; Spellmeyer, D. C.; Fox, T.; Caldwell, J. W.; Kollman, P. A. *J. Am. Chem. Soc.* **1995**, *117*, 5179–5197.
- [115] Jorgensen, W. L.; Tirado-Rives, J. *J. Am. Chem. Soc.* **1988**, *110*, 1657–1666.
- [116] Jorgensen, W. L.; D. S, M.; Tirado-Rives, J. *J. Am. Chem. Soc.* **1996**, *118*, 11225–11236.
- [117] van Gunsteren, W. F.; Berendsen, H. J. C. *Gromos-87 Manual Biomos*; BV Nijenborgh 4, 9747 AG Groningen. The Netherlands, 1987.

- [118] van Gunsteren, W. F.; Billeter, S. R.; Eising, A. A.; Hünenberger, P. H.; Krüger, P.; Mark, A. E.; Scott, W. R. P.; Tironi, I. G. *GROMOS96 Manual and User Guide*; Zürich, Switzerland: Vdf Hochschulverlag AG an der ETH Zürich, 1996.
- [119] Neria, E.; Fisher, S.; Karplus, M. *J. Chem. Phys.* **1996**, *105*, 1902–1921.
- [120] Glass, D. C.; Krishnan, M.; Nutt, D. R.; Smith, J. C. *J. Chem. Theory Comput.* **2010**, *6*, 1390–1400.
- [121] Zhang, C.; Raugei, S.; Eisenberg, B.; Carloni, P. *J. Chem. Theory Comput.* **2010**, *6*, 2167–2175.
- [122] Agarwal, M.; Kushwaha, H. R.; Chakravarty, C. *J. Phys. Chem.* **2010**, *114*, 651–659.
- [123] Paschek, D.; Day, R.; Garcia, A. E. *Phys. Chem. Chem. Phys.* **2011**, *13*, 19840–19847.
- [124] Wu, C.; Chen, M.; Guo, C.; Zhao, X.; Yuan, C. *J. Phys. Chem. B.* **2010**, *14*, 4692–4701.
- [125] Takemura, K.; Kitao, A. *J. Phys. Chem. B.* **2007**, *111*, 11870–11872.
- [126] Wu, Y.; Tepper, H. L.; Voth, G. A. *J. Chem. Phys.* **2006**, *124*, No. 024503.
- [127] Wright, L. B.; Walsh, T. R. *J. Phys. Chem. C.* **2012**, *116*, 2933–2945.
- [128] Meissner, R. H.; Wei, G.; Colombi Ciacchi, L. *Soft Matter* **2015**, *11*, 6254–6265.
- [129] Meissner, R. H.; Schneider, J.; Schiffels, P.; Colombi Ciacchi, L. *Langmuir* **2014**, *30*, 3487–3494.
- [130] Pichot, R.; Spyropoulos, F.; Norton, I. T. *J. Colloid Interface Sci.* **2012**, *377*, 396–405.
- [131] Puddu, V.; Perry, C. C. *ACS Nano* **2012**, *6*, 6356–6363.
- [132] Puddu, V.; Perry, C. C. *Langmuir* **2014**, *30*, 227–233.

- [133] Drechsler, A.; Synytska, A.; Uhlmann, P.; Stamm, M.; Kremer, F. *Langmuir* **2012**, *28*, 15555–15565.
- [134] Drechsler, A.; Synytska, A.; Uhlmann, P.; Elmahdy, M. M.; Stamm, M.; Kremer, F. *Langmuir* **2010**, *26*, 6400–6410.
- [135] Vlasova, N. N.; Golovkova, L. P. *Colloid J.* **2004**, *66*, 657–662.
- [136] Patwardhan, S. V.; Emami, F. S.; Berry, R. J.; Jones, S. E.; Naik, R. R.; Deschaume, O.; Heinz, H.; Perry, C. C. *J. Am. Chem. Soc.* **2012**, *134*, 6244–6256.
- [137] Notman, R.; Oren, E. E.; Tamerler, C.; Sarikaya, M.; Samudrala, R.; Walsh, T. R. *Biomacromolecules* **2010**, *11*, 3266–3274.
- [138] Phillips, D. C.; York, R. L.; Mermut, O.; McCrea, K. R.; Ward, R. S.; Somorjai, G. A. *J. Phys. Chem. C.* **2006**, *111*, 255–261.
- [139] Lopes, I.; Piao, L.; Stievano, L.; Lambert, J. F. *J. Phys. Chem. C.* **2009**, *113*, 18163–18172.
- [140] Mermut, O.; Phillips, D. C.; York, R. L.; McCrea, K. R.; Ward, R. S.; Somorjai, G. A. *J. Am. Chem. Soc.* **2006**, *128*, 3598–3607.
- [141] Stievano, L.; Piao, L.; Lopes, I.; Meng, M.; Costa, D.; Lambert, J. F. *Eur. J. Mineral* **2007**, *19*, 321–331.
- [142] Oren, E. E.; Tamerler, C.; Sahin, D.; Hnilova, M.; Seker, U. O.; Sarikaya, M.; Samudrala, R. *Bioinformatics* **2007**, *23*, 2816–2822.
- [143] Hayashi, T.; Sano, K. I.; Shiba, K.; Iwahori, K.; Yamashita, I.; Hara, M. *Langmuir* **2009**, *25*, 10901–10906.
- [144] Gao, Q.; Xu, W. J.; Xu, Y.; Wu, D.; Sun, Y. H.; Deng, F.; Shen, W. L. *J. Phys. Chem. B.* **2008**, *112*, 2261–2267.
- [145] Kitadai, N.; Yokoyama, T.; Nakashima, S. *J. Colloid Interface Sci.* **2009**, *329*, 31–37.

- [146] O'Brien, C. P.; Stuart, S. J.; Bruce, D. A.; Latour, R. A. *Langmuir* **2008**, *24*, 14115–14124.
- [147] Felice, R. D.; Corni, S. *J. Phys. Chem. Lett.* **2011**, *2*, 1510–1519.
- [148] Dubois, L. H.; Nuzzo, R. G. *Ann. Rev. Phys. Chem.* **1992**, *43*, 437–463.
- [149] Dubois, L. H.; Zegarski, B. R.; Nuzzo, R. G. *J. Chem. Phys.* **1993**, *98*, 678–688.
- [150] Poirier, G. E. *Chem. Rev.* **1997**, *97*, 1117–1128.
- [151] Schreiber, F. *Planet. Space Sci.* **2000**, *65*, 151–257.
- [152] Love, J. C.; Estroff, L. A.; Kriebel, J. K.; Nuzzo, R. G.; Whitesides, G. M. *Chem. Rev.* **2005**, *105*, 1103–1170.
- [153] Fischer, D.; Curioni, A.; Andreoni, W. *Langmuir* **2003**, *19*, 3567–3571.
- [154] Cao, Y.; Ge, Q.; Dyer, D. J.; Wang, L. *J. Phys. Chem. B.* **2003**, *107*, 3803–3807.
- [155] Gottschlalk, J.; Hammer, B. *J. Chem. Phys.* **2002**, *116*, 784–790.
- [156] Yourdshahyan, Y.; Rappe, A. M. *J. Chem. Phys.* **2002**, *117*, 825–833.
- [157] Krüger, D.; Fuchs, H.; Rousseau, R.; Marx, D.; Parrinello, M. *J. Chem. Phys.* **2001**, *115*, 4776–4786.
- [158] Zhang, Y.; Barnes, G. L.; Yan, T.; Hase, W. L. *Phys. Chem. Chem. Phys.* **2010**, *12*, 4435–4445.
- [159] Zhang, L.; Leng, Y.; Jiang, S. *Langmuir* **2003**, *19*, 9742–9747.
- [160] Dirama, T. E.; Johnson, J. A. *Langmuir* **2007**, *23*, 12208–12216.
- [161] Alkis, S.; Krause, J. L.; Fry, J. N.; Cheng, H. P. *Phys. Rev. B* **2009**, *79*(No. 121402).
- [162] Schapotschnikow, P.; Vlugt, T. J. H. *J. Phys. Chem. C.* **2010**, *114*, 2531–2537.
- [163] Hung, S. W.; Hsiao, P. Y.; Chieng, C. C. *IEEE Trans. Nanobiosci.* **2010**, *9*, 297–306.

- [164] Gannon, G.; Greer, J. C.; Larsson, J. A.; Thompson, D. *ACS Nano* **2010**, *4*, 921–932.
- [165] Saha, J. K.; Kim, H.; Jang, J. *J. Phys. Chem. C* **2012**, *116*, 25928–25933.
- [166] Ramin, L.; Jabbarzadeh, A. *Modelling Simul. Mater. Sci. Eng.* **2012**, *20*(No. 085010).
- [167] Ramin, L.; Jabbarzadeh, A. *J. Chem. Phys.* **2012**, *137*, No. 174706.
- [168] Ramin, L.; Jabbarzadeh, A. *Langmuir* **2012**, *28*, 4102–4112.
- [169] Saha, J. K.; Yang, M.; Jang, J. *Bull. Korean Chem. Soc.* **2013**, *34*, 3790–3794.
- [170] Ramin, L.; Jabbarzadeh, A. *Langmuir* **2013**, *29*, 13367–13378.
- [171] Pipolo, S.; Benassi, E.; Corni, S. *Langmuir* **2013**, *29*, 10505–10512.
- [172] Kang, H.; Kim, Y.; Choi, I.; Chang, R.; Yeo, W. S. *Anal. Chim. Acta* **2014**, *843*, 38–45.
- [173] Vasumathi, V.; Natalia, M.; Cordeiro, D. S. *Chem. Phys. Lett.* **2014**, *600*, 79–86.
- [174] Liu, J.; Liao, C.; Zhou, J. *Langmuir* **2013**, *29*, 11366–11374.
- [175] Guardingo, M.; Bellido, E.; Miralles-Lluma, R.; Faraudo, J.; Sedo, J.; Tatay, S.; Verdaguer, A.; Busque, F.; Ruiz-Molina, D. *Phys. Rev. B* **2009**, *79*, No. 121402.
- [176] Heinz, H.; Vaia, R. A.; Farmer, B. L.; Naik, R. R. *J. Phys. Chem. C* **2008**, *112*, 17281–17290.
- [177] Ahn, Y.; Saha, J. K.; Schatz, G. C.; Jang, J. *J. Phys. Chem. C* **2011**, *115*, 10668–10674.
- [178] Kawai, S.; Canova, F. F.; Glatzel, T.; Foster, A. S.; Meyer, E. *Phys. Rev. B* **2011**, *84*, No. 115415.
- [179] Reischl, B.; Watkins, M.; Foster, A. S. *J. Chem. Theory Comput.* **2013**, *9*, 600–608.

- [180] Watkins, M.; Shluger, A. L. *Phys. Rev. Lett.* **2010**, *105*, No. 196101.
- [181] Watkins, M.; Berkowitz, M. L.; Shluger, A. L. *Phys. Chem. Chem. Phys.* **2011**, *13*, 12584–12594.
- [182] Vezenov, D. V.; Noy, A.; Ashby, P. J. *Adhes. Sci. Technol.* **2005**, *19*, 313–364.
- [183] Ewers, B. W.; Batteas, J. D. *J. Phys. Chem. C.* **2012**, *116*, 25165–25177.
- [184] Darden, T. A.; York, D.; Pedersen, L. *J. Chem. Phys.* **1993**, *98*, 10089–10092.
- [185] Ewald, P. P. *Ann. Physik* **1921**, *64*, 253–287.
- [186] Deserno, M.; Holm, C. *J. Chem. Phys.* **1998**, *109*, 7678–7693.
- [187] Zimmerman, K. J. *Comp. Chem.* **1991**, *12*, 310–319.
- [188] Sugita, Y.; Okamoto, Y. *Chem. Phys. Lett.* **1999**, *314*, 141–151.
- [189] Liu, P.; Kim, B.; Friesner, R. A.; Berne, B. J. *Proc. Natl. Acad. Sci. USA* **2005**, *102*, 13749–13754.
- [190] Terakawa, T.; Kameda, T.; Takada, S. *J. Comp. Chem.* **2010**, *32*, 1228–1234.
- [191] Laio, A.; Gervasio, F. L. *Rep. Prog. Phys.* **2008**, *71*, No. 126601.
- [192] Barducci, A.; Bussi, G.; Parrinello, M. *Phys. Rev. Lett.* **2008**, *100*, No. 020603.
- [193] Trzesniak, D.; Kunz, A.-P. E.; vanGunsteren, W. F. *Chem. Phys. Chem.* **2007**, *8*, 162–169.
- [194] Hess, B.; Kutzner, C.; van der Spoel, D.; Lindahl, E. *J. Chem. Theory Comput.* **2008**, *4*, 435–447.
- [195] Bonomi, M.; Branduardi, D.; Bussi, G.; Camilloni, C.; Provasi, D.; Raiteri, P.; Donadio, D.; Marinelli, F.; Pietrucci, F.; Broglia, R. A.; Parrinello, M. *Comp. Phys. Comm.* **2009**, *180*, 1961–1972.
- [196] Mamatkulov, S.; Fyta, M.; Netz, R. R. *J. Chem. Phys.* **2013**, *138*, No. 024505.

- [197] Ponder, J. W.; Ren, P.; Pappu, R. V.; Hart, R. K.; Hodgson, M. E.; Cistola, D. P.; Kundrot, C. E.; Richards, F. M. *Washington University School of Medicine, Saint Louis, MO* **2004**, 3.
- [198] Hanwell, M. D.; Curtis, D. E.; Lonie, D. C.; Vandermeersch, T.; Zurek, E.; Hutchison, G. R. *J. Cheminform* **2012**, 4, No. 17.
- [199] Foloppe, N.; MacKerell Jr, A. D. *J. Comp. Chem.* **2000**, 21, 86–104.
- [200] Allen, M. P.; Tildesley, D. J. *Computer Simulation of Liquids*; Clarendon Press: Oxford, United Kingdom, 1 ed., 1987.
- [201] Nosé, S. *Mol. Phys.* **1984**, 52, 255–268.
- [202] Hoover, W. G. *Phys. Rev. A* **1985**, 31, 1695–1697.
- [203] Nosé, S.; Klein, M. L. *Mol. Phys.* **1983**, 50, 1055–1076.
- [204] Parrinello, M.; Rahman, A. *J. Appl. Phys.* **1981**, 52, 7182–7190.
- [205] Berendsen, H. J. C.; Postma, J. P. M.; van Gunsteren, W. F.; DiNola, A.; Haak, J. R. *J. Chem. Phys.* **1984**, 81, 3684–3690.
- [206] Humphrey, W.; Dalke, A.; Schulten, K. *J. Molec. Graphics* **1996**, 14, 33–38.
- [207] Patriksson, A.; van der Spoel, D. *Phys. Chem. Chem. Phys.* **2008**, 10, 2073–2077.
- [208] Daura, X.; Gademann, K.; Jaun, B.; Seebach, D.; van Gunsteren, W. F.; Mark, A. E. *Angew. Chem. Int. Ed. Engl.* **1999**, 38, 236–240.
- [209] Juhl, K. M. S.; Pedersen, C. S.; Bovet, N.; Dalby, K. N.; Hassenkam, T.; Andersson, M. P.; Okhrimenko, D.; Stipp, S. L. S. *Langmuir* **2014**, 30, 14476–14485.
- [210] Cole, D. J.; Payne, M. C.; Csanyi, G.; Spearing, S. M.; Ciacchi, L. C. *J. Chem. Phys.* **2007**, 127, No. 204704.
- [211] D’Souza, A. S.; Pantano, C. G. *J. Am. Ceram. Soc.* **1999**, 82, 1289–1293.

- [212] Zhuravlev, L. T. *Colloids and Surfaces A: Physicochem. Eng. Aspects* **2000**, *173*, 1–38.
- [213] Tang, W.; Sanville, E.; Henkelman, G. *J. Phys. Condens. Matter* **2009**, *21*, No. 084204.
- [214] Radmacher, M.; Cleveland, J. P.; Fritz, M.; Hansma, H. G.; Hansma, P. K. *Biophys. J.* **1994**, *66*, 2159–2165.
- [215] Baselt, D. R.; J. D, B. *J. Appl. Phys.* **1994**, *76*, 33–38.
- [216] Burnham, N. A.; Colton, R. J.; Pollock, H. M. *J. Vac. Sci. Technol.* **1991**, *A9*, 2548–2556.
- [217] Hassenkam, T.; Skovbjerg, L. L.; Stipp, S. L. S. *Proc. Natl. Acad. Sci. USA* **2009**, *106*, 6071–6076.
- [218] Lower, B. H.; Lins, R. D.; Oestreicher, Z.; Straatsma, T. P.; Hochella, M. F.; Shi, L.; Lower, S. K. *Environ. Sci. Technol.* **2008**, *42*, 3821–3827.
- [219] Huang, Z. H.; Jin, H. Y.; Che, S. N. *Dalton Trans.* **2014**, *43*, 16169–16172.
- [220] Kabsch, W.; Sander, C. *Biopolymers* **1983**, *22*, 2577–2637.
- [221] Schulz, J. C. F.; Schmidt, L.; Best, R. B.; Dzubiella, J.; Netz, R. R. *J. Am. Chem. Soc.* **2012**, *134*, 6273–6279.
- [222] Leung, K.; Rempe, S. B. *J. Am. Chem. Soc.* **2004**, *126*, 344–351.
- [223] Hugosson, H. W.; Laio, A.; Maurer, P.; Rothlisberger, U. *J. Comp. Chem.* **2006**, *27*, 672–684.
- [224] Liang, T.; Walsh, T. R. *Phys. Chem. Chem. Phys.* **2006**, *8*, 4410–4419.
- [225] Liang, T.; Walsh, T. R. *Mol. Simul.* **2007**, *33*, 337–342.
- [226] Israelavhbili, J. N.; Pashley, R. M. *Nature* **1983**, *306*, 249–250.
- [227] Boek, E. S.; Coveney, P. V.; Skipper, N. T. *J. Am. Chem. Soc.* **1995**, *117*, 12608–12617.

- [228] Teich-McGoldrick, S. L.; Greathouse, J. A.; Jove-Colon, C. F.; Cygan, R. T. *J. Phys. Chem.* **2015**, *119*, 20880–20891.
- [229] Bourg, I. C.; Sposito, G. *J. Colloid Interface Sci.* **2011**, *360*, 701–715.
- [230] Kester, D. R.; Duedall, I. W.; Connors, D. N.; Pytkowicz, R. M. *Limnol. Oceanogr.* **1967**, *12*, 176–179.
- [231] Skovbjerg, L. L.; Okhrimenko, D. V.; Khoo, J.; Dalby, K. N.; Hassenkam, T.; Makovicky, E.; Stipp, S. L. S. *Energy Fuels* **2013**, *27*, 3642–3652.
- [232] Matthiesen, J.; Bovet, N.; Hilner, E.; Andersson, M. P.; Schmidt, D. A.; Webb, K. J.; Dalby, K. N.; Hassenkam, T.; Crouch, J.; Collins, I. R.; Stipp, S. L. S. *Energy Fuels* **2014**, *28*, 4849–4858.
- [233] Lee, S. Y.; O’Sullivan, M.; Routh, A. F.; Clarke, S. M. *Langmuir* **2009**, *25*, 3981–3984.
- [234] Mugele, F.; Bera, B.; Cavalli, A.; Siretanu, I.; Maestro, A.; Duits, M.; Cohen-Stuart, M.; van den Ende, D.; Stocker, I.; Collins, I. *Sci. Rep.* **2015**, *5*, No. 10519.

Note that ‘Die Berechnung Optischer and Electrostatischer Gitterpotentiale’ is written in German.¹⁸⁵ ‘How to Mesh Up Ewald Sums. I. A Theoretical and Numerical Comparison of Various Particle Mesh Routines’ provides a summary.¹⁸⁶

Note that ‘Studien Über Electriche Grenzschichten’⁶⁸ and ‘Zur Theory de Electrolytischen Doppelschicht’⁶⁶ are written in German and ‘Sur la Constitution de la Charge Electrique a la Surface d’ un Electrolyte’ is written in French.⁶⁴ An overview of the concepts can be found in ‘The Water-Amorphous Silica Interface: Analysis of the Stern Layer and Surface Conduction’.⁷²

Appendix A

Additional Information: Methods

Table A.1: Non-bonded force-field parameters - RGD - ARG.

Atom Type	Atom ID	Charge/e	Mass/u	Epsilon/kJ mol ⁻¹	Sigma/nm
NH3	N	-0.3	14.007	0.329632525712	0.8368
HC	H1	0.33	1.008	0.0400013524445	0.192464
HC	H2	0.33	1.008	0.0400013524445	0.192464
HC	H3	0.33	1.008	0.0400013524445	0.192464
CT1	CA	0.21	12.011	0.405358916754	0.08368
HB	HA	0.1	1.008	0.235197261589	0.092048
CT2	CB	-0.18	12.011	0.387540942391	0.23012
HA	HB1	0.09	1.008	0.235197261589	0.092048
HA	HB2	0.09	1.008	0.235197261589	0.092048
CT2	CG	-0.18	12.011	0.387540942391	0.23012
HA	HG1	0.09	1.008	0.235197261589	0.092048
HA	HG2	0.09	1.008	0.235197261589	0.092048
CT2	CD	0.2	12.011	0.387540942391	0.23012
HA	HD1	0.09	1.008	0.235197261589	0.092048
HA	HD2	0.09	1.008	0.235197261589	0.092048
NC2	NE	-0.7	14.007	0.329632525712	0.8368
HC	HE	0.44	1.008	0.0400013524445	0.192464
C	CZ	0.64	12.011	0.356359487256	0.46024
NC2	NH1	-0.8	14.007	0.329632525712	0.8368
HC	HH11	0.46	1.008	0.0400013524445	0.192464
HC	HH12	0.46	1.008	0.0400013524445	0.192464
NC2	NH2	-0.8	14.007	0.329632525712	0.8368
HC	HH21	0.46	1.008	0.0400013524445	0.192464
HC	HH22	0.46	1.008	0.0400013524445	0.192464
C	C	0.51	12.011	0.356359487256	0.46024
O	O	-0.51	15.999	0.302905564168	0.50208

Table A.2: Non-bonded force-field parameters - RGD - GLY.

Atom Type	Atom ID	Charge/e	Mass/u	Epsilon/kJ mol ⁻¹	Sigma/nm
NH1	N	-0.47	14.007	0.329632525712	0.8368
H	HN	0.31	1.008	0.0400013524445	0.192464
CT2	CA	-0.02	12.011	0.387540942391	0.23012
HB	HA1	0.09	1.008	0.235197261589	0.092048
HB	HA2	0.09	1.008	0.235197261589	0.092048
C	C	0.51	12.011	0.356359487256	0.46024
O	O	-0.51	15.999	0.302905564168	0.50208

Table A.3: Non-bonded force-field parameters - RGD - ASP.

Atom Type	Atom ID	Charge/e	Mass/u	Epsilon/kJ mol ⁻¹	Sigma/nm
NH1	N	-0.47	14.007	0.329632525712	0.8368
H	HN	0.31	1.008	0.0400013524445	0.192464
CT1	CA	0.07	12.011	0.405358916754	0.08368
HB	HA	0.09	1.008	0.235197261589	0.092048
CT2	CB	-0.28	12.011	0.387540942391	0.23012
HA	HB1	0.09	1.008	0.235197261589	0.092048
HA	HB2	0.09	1.008	0.235197261589	0.092048
CC	CG	0.62	12.011	0.356359487256	0.29288
OC	OD1	-0.76	15.999	0.302905564168	0.50208
OC	OD2	-0.76	15.999	0.302905564168	0.50208
CC	C	0.34	12.011	0.356359487256	0.29288
OC	OT1	-0.67	15.999	0.302905564168	0.50208
OC	OT2	-0.67	15.999	0.302905564168	0.50208

Table A.4: Non-bonded force-field parameters - SPT - SER.

Atom Type	Atom ID	Charge/e	Mass/u	Epsilon/kJ mol ⁻¹	Sigma/nm
NH3	N	-0.3	14.007	0.329632525712	0.8368
HC	H1	0.33	1.008	0.0400013524445	0.192464
HC	H2	0.33	1.008	0.0400013524445	0.192464
HC	H3	0.33	1.008	0.0400013524445	0.192464
CT1	CA	0.07	1.008	0.405358916754	0.08368
HB	HA	0.09	1.008	0.235197261589	0.092048
CT2	CB	0.05	12.011	0.387540942391	0.23012
HA	HB1	0.09	1.008	0.235197261589	0.092048
HA	HB2	0.09	1.008	0.235197261589	0.092048
OH1	OG	-0.66	15.999	0.315378146222	0.6363864
H	HG1	0.43	1.008	0.0400013524445	0.192464
C	C	0.51	1.008	0.356359487256	0.46024
O	O	-0.51	15.999	0.302905564168	0.50208

Table A.5: Non-bonded force-field parameters - SPT - PRO.

Atom Type	Atom ID	Charge/e	Mass/u	Epsilon/kJ mol ⁻¹	Sigma/nm
N	N	-0.29	14.007	0.329632525712	0.8368
CP3	CD	0.00	12.011	0.387540942391	0.23012
HA	HD1	0.09	1.008	0.235197261589	0.092048
HA	HD2	0.09	1.008	0.235197261589	0.092048
CP1	CA	0.02	12.011	0.405358916754	0.08368
HB	HA	0.09	1.008	0.235197261589	0.092048
CP2	CB	-0.18	12.011	0.387540942391	0.23012
HA	HB1	0.09	1.008	0.235197261589	0.092048
HA	HB2	0.09	1.008	0.235197261589	0.092048
CP2	CG	-0.18	12.011	0.387540942391	0.23012
HA	HG1	0.09	1.008	0.235197261589	0.092048
HA	HG2	0.09	1.008	0.235197261589	0.092048
C	C	0.51	1.008	0.356359487256	0.46024
O	O	-0.51	15.999	0.302905564168	0.50208

Table A.6: Non-bonded force-field parameters - SPT - THR.

Atom Type	Atom ID	Charge/e	Mass/u	Epsilon/kJ mol ⁻¹	Sigma/nm
NH1	N	-0.47	14.007	0.329632525712	0.8368
H	HN	0.31	1.008	0.0400013524445	0.192464
CT1	CA	0.07	1.008	0.405358916754	0.08368
HB	HA	0.09	1.008	0.235197261589	0.092048
CT1	CB	0.14	1.008	0.405358916754	0.08368
HA	HB	0.09	1.008	0.235197261589	0.092048
OH1	OG1	-0.66	15.999	0.315378146222	0.6363864
H	HG1	0.43	1.008	0.0400013524445	0.192464
CT3	CG2	-0.27	12.011	0.367050271874	0.33472
HA	HG21	0.09	1.008	0.235197261589	0.092048
HA	HG22	0.09	1.008	0.235197261589	0.092048
HA	HG23	0.09	1.008	0.235197261589	0.092048
CC	C	0.34	12.011	0.356359487256	0.29288
OC	OT1	-0.67	15.999	0.302905564168	0.50208
OC	OT2	-0.67	15.999	0.302905564168	0.50208

Table A.7: Non-bonded force-field parameters - Methylammonium.

Atom Type	Atom ID	Charge/e	Mass/u	Epsilon/kJ mol ⁻¹	Sigma/nm
CT3	CE	0.16	12.011	0.367050271874	0.33472
NH3	NZ	-0.30	14.007	0.329632525712	0.8368
HA	HE1	0.05	1.008	0.235197261589	0.092048
HA	HE2	0.05	1.008	0.235197261589	0.092048
HA	HE3	0.05	1.008	0.235197261589	0.092048
HC	HZ1	0.33	1.008	0.0400013524445	0.192464
HC	HZ2	0.33	1.008	0.0400013524445	0.192464
HC	HZ3	0.33	1.008	0.0400013524445	0.192464

Table A.8: Non-bonded force-field parameters - Gold and 11-amino-1-undecanethiol.

Atom Type	Atom ID	Charge/e	Mass/u	Epsilon/kJ mol ⁻¹	Sigma/nm
AU	AU	0.0	196.967	0.2951	22.133
S	S	0.000	32.060	0.356359487256	1.8828
CT2	C	-0.129	12.011	0.387540942391	0.23012
HA	H	0.09	1.008	0.235197261589	0.092048
HA	H	0.09	1.008	0.235197261589	0.092048
CT2	C	-0.181	12.011	0.387540942391	0.23012
HA	H	0.09	1.008	0.235197261589	0.092048
HA	H	0.09	1.008	0.235197261589	0.092048
CT2	C	-0.180	12.011	0.387540942391	0.23012
HA	H	0.09	1.008	0.235197261589	0.092048
HA	H	0.09	1.008	0.235197261589	0.092048
CT2	C	-0.180	12.011	0.387540942391	0.23012
HA	H	0.09	1.008	0.235197261589	0.092048
HA	H	0.09	1.008	0.235197261589	0.092048
CT2	C	-0.180	12.011	0.387540942391	0.23012
HA	H	0.09	1.008	0.235197261589	0.092048
HA	H	0.09	1.008	0.235197261589	0.092048
CT2	C	-0.180	12.011	0.387540942391	0.23012
HA	H	0.09	1.008	0.235197261589	0.092048
HA	H	0.09	1.008	0.235197261589	0.092048
CT2	C	-0.180	12.011	0.387540942391	0.23012
HA	H	0.09	1.008	0.235197261589	0.092048
HA	H	0.09	1.008	0.235197261589	0.092048
CT2	C	-0.180	12.011	0.387540942391	0.23012
HA	H	0.09	1.008	0.235197261589	0.092048
HA	H	0.09	1.008	0.235197261589	0.092048
CT2	C	-0.180	12.011	0.387540942391	0.23012
HA	H	0.09	1.008	0.235197261589	0.092048
HA	H	0.09	1.008	0.235197261589	0.092048
CT2	C	-0.180	12.011	0.387540942391	0.23012
HA	H	0.09	1.008	0.235197261589	0.092048
HA	H	0.09	1.008	0.235197261589	0.092048
CT2	C	0.16	12.011	0.387540942391	0.23012
HA	H	0.05	1.008	0.235197261589	0.092048
HA	H	0.05	1.008	0.235197261589	0.092048
NH3	N	-0.30	14.007	0.329632525712	0.8368
HC	HH	0.33	1.008	0.0400013524445	0.192464
HC	HH	0.33	1.008	0.0400013524445	0.192464
HC	HH	0.33	1.008	0.0400013524445	0.192464

Table A.9: Non-bonded force-field parameters - Silica.

Atom Type	Atom ID	Charge/e	Mass/u	Epsilon/kJ mol ⁻¹	Sigma/nm
SiB-1	SiB	0.400000	28.085000	2.85088e-01	1.25427952
SiB-2	SiB	0.000000	28.085000	2.85088e-01	1.25427952
SiB-3	SiB	1.200000	28.085000	2.85088e-01	1.25427952
SiB-4	SiB	0.800000	28.085000	2.85088e-01	1.25427952
SiB-5	SiB	1.300000	28.085000	2.85088e-01	1.25427952
SiB-6	SiB	1.600000	28.085000	2.85088e-01	1.25427952
SiB-7	SiB	1.000000	28.085000	2.85088e-01	1.25427952
SiB-8	SiB	0.600000	28.085000	2.85088e-01	1.25427952
OSi-1	OSi	-0.800000	16.000000	3.13953e-01	1.090258352
OSi-2	OSi	-0.900000	16.000000	3.13953e-01	1.090258352
OHs	OHs	-0.600000	16.000000	2.93997e-01	0.627139760
HOs	HOs	0.400000	1.000000	1.78180e-01	0.086834736

Table A.10: Non-bonded force-field parameters - SPC/Fw.

Atom Type	Atom ID	Charge/e	Mass/u	Epsilon/kJ mol ⁻¹	Sigma/nm
OWT3	OW	-0.82	15.99940	3.165492e-01	6.502995e-01
HWT3	HW1	0.41	1.008000	0.0	0.0
HWT3	HW2	0.41	1.008000	0.0	0.0

Table A.11: Non-bonded force-field parameters - TIPS3P.

Atom Type	Atom ID	Charge/e	Mass/u	Epsilon/kJ mol ⁻¹	Sigma/nm
OT	OW	-0.834	15.99940	0.315057422683	0.6363864
HT	HW1	0.417	1.008000	0.0400013524445	0.192464
HT	HW2	0.417	1.008000	0.0400013524445	0.192464

Table A.12: Non-bonded force-field parameters - ions.

Atom Type	Atom ID	Charge/e	Mass/u	Epsilon/kJ mol ⁻¹	Sigma/nm
NA	NA	1.00	22.989770	0.242992625373	0.1962296
K	K	1.00	39.102000	0.314264522824	0.364008
CL	CL	-1.00	35.450000	0.404468018036	0.6276
CAL	CAL	2.00	40.080000	0.24357170954	0.50208
MG	MG	2.00	24.305000	0.211142996199	0.06276

Table A.13: Repulsive potential between different ion pairs in metadynamics aq. CaCl₂/amorphous silica simulations.

atom 1	atom 2	V(c6)/kJ mol ⁻¹	W(c12)/kJ mol ⁻¹
CLA	SCA (surface bound CAL)	0.0000000000000000	3.1182596765347324e-06
CAL	SOH (surface O ⁻)	0.0000000000000000	3.3689455901748717e-07

Appendix B

Additional Information: Testing the Inter-Operability of the CHARMM and SPC/Fw Force-Fields for Conformational Sampling

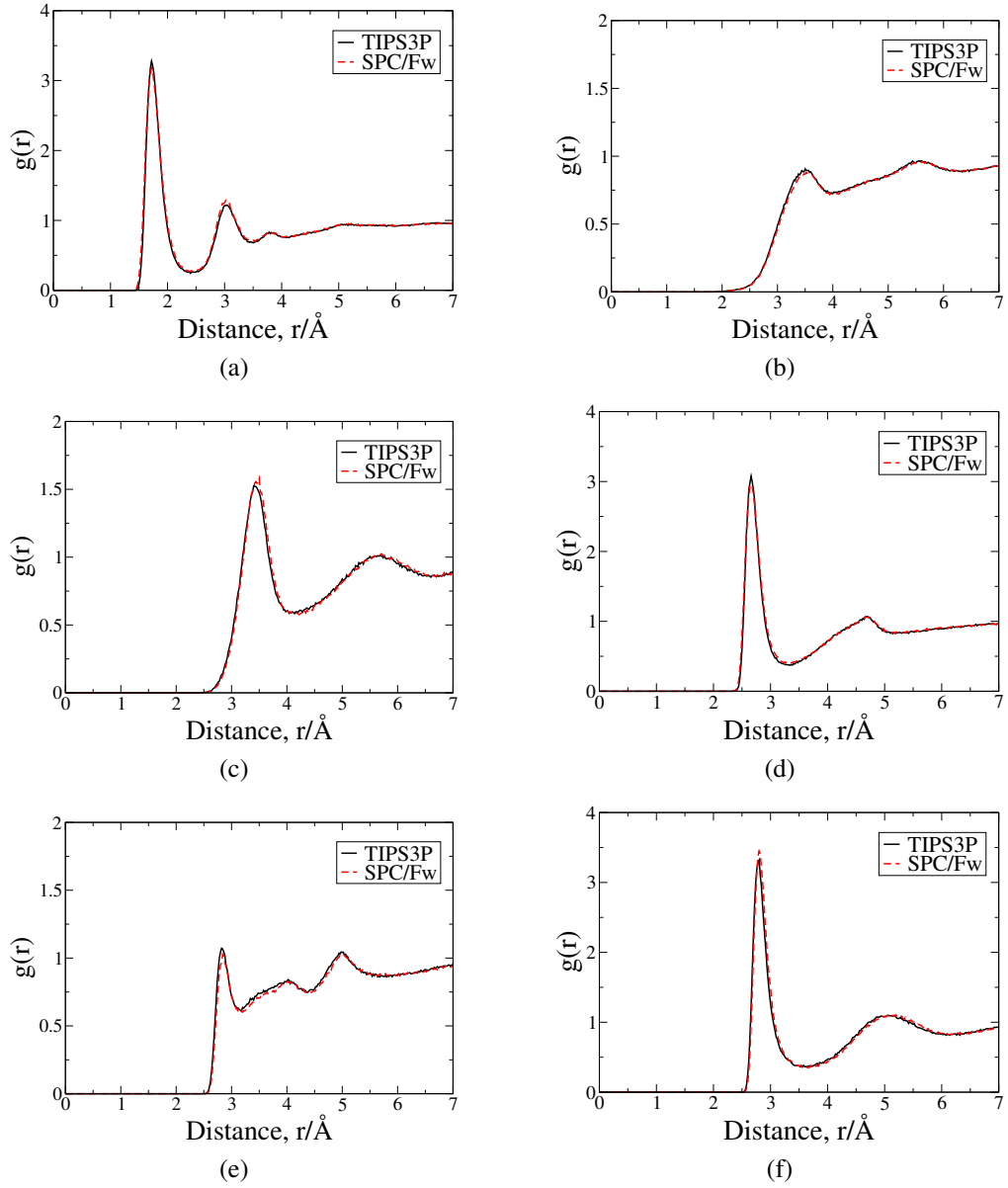


Figure B.1: RDFs $g_{O-H_W}(r)$ between RGD's (a) oxygen atoms of the sidechain carboxylate group (b) nitrogen atoms of the guanidinium group (c) ammonium nitrogen atom and the hydrogen atoms of water. RDFs $g_{O-O_W}(r)$ between RGD's (d) oxygen atoms of the sidechain carboxylate group (e) nitrogen atoms of the guanidinium group (f) ammonium nitrogen atom and the oxygen atoms of water

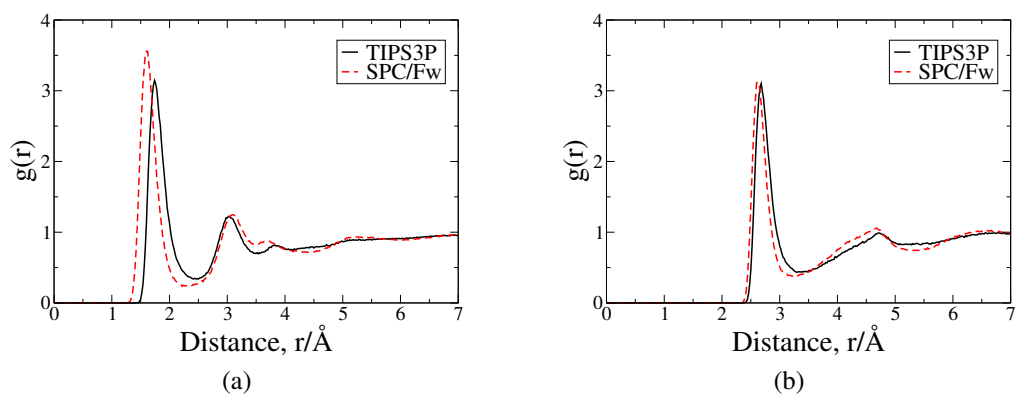


Figure B.2: Exemplar RDFs for RGD: (a) $g_{O-H_W}(r)$ between the oxygen atoms of the terminal carboxylate group and the hydrogen atoms of water and (b) $g_{O-O_W}(r)$ between the oxygen atoms of the terminal carboxylate group and the oxygen atoms of water.

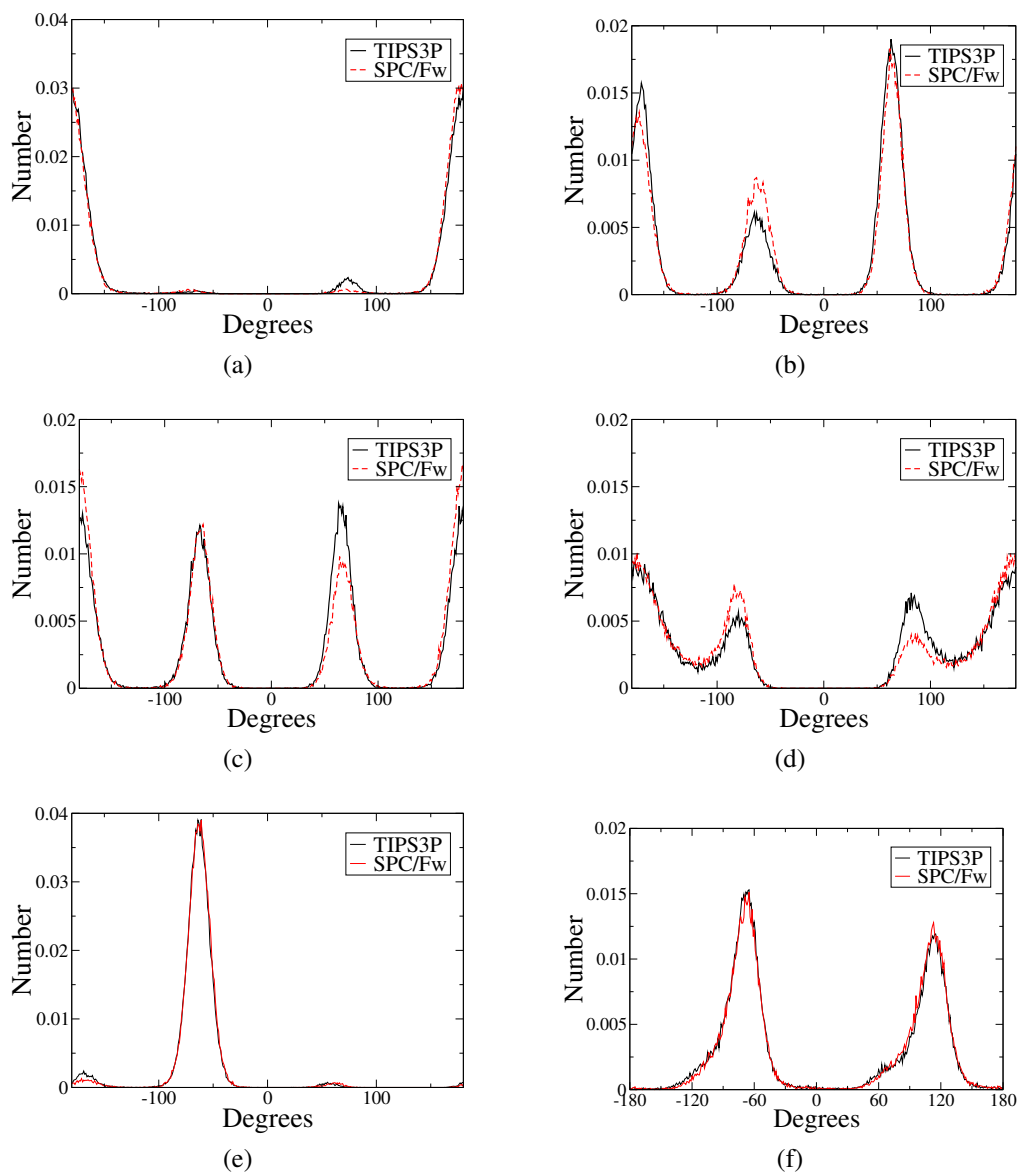


Figure B.3: Dihedral angle distributions for (a) terminal $N-C_{\alpha}-C_{\beta}-C_{\gamma}$, residue R (b) $C_{\alpha}-C_{\beta}-C_{\gamma}-C_{\delta}$, residue R (c) $C_{\beta}-C_{\gamma}-C_{\delta}$ -sidechain N, residue R (d) $C_{\gamma}-C_{\delta}$ -sidechain N- $C_{\delta}-C_{\epsilon}$, residue R (e) $N-C_{\alpha}-C_{\beta}-C_{\gamma}$, residue D (f) $C_{\alpha}-C_{\beta}-C_{\gamma}-O$, residue D

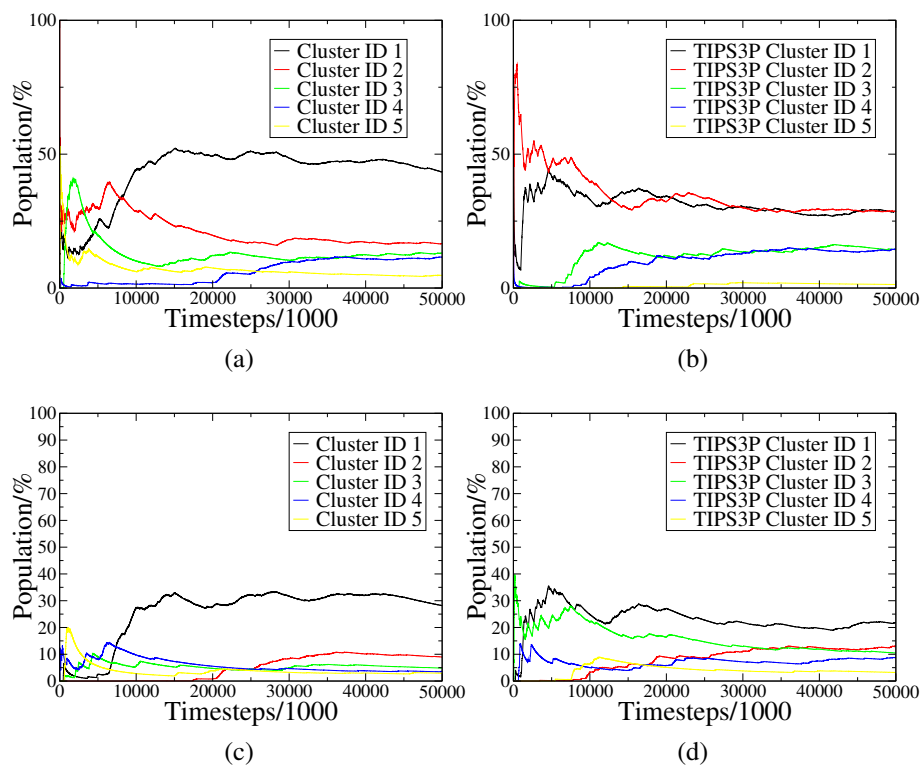


Figure B.4: The percentage growth of clusters for the RGD peptide as a function of simulation timestep for (a) TIPS3P, backbone (b) SPC/Fw, backbone (c) TIPS3P, peptide (d) SPC/Fw, peptide.

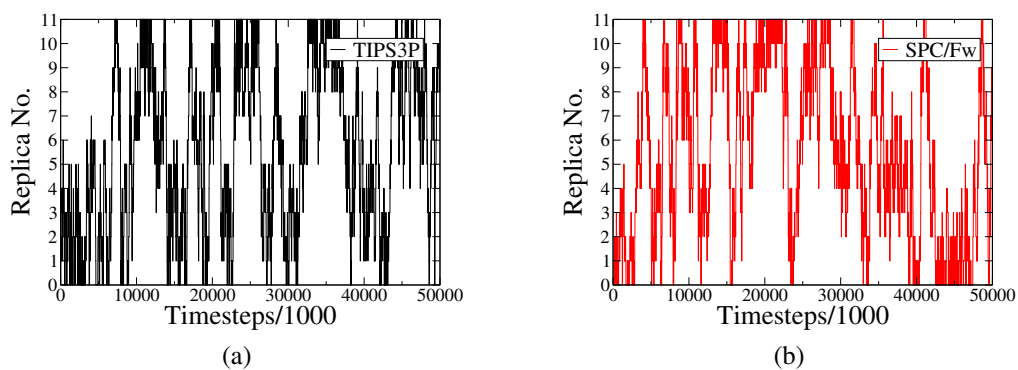


Figure B.5: Replica pathway of the initial 'replica 0' for the SPT system for (a) TIPS3P (b) SPC/Fw.

Appendix C

Additional Information: Water and Ion Structure at the Aqueous Electrolyte/Amorphous Silica Interface

Table C.1: Number of waters required to achieve a bulk water pressure of 1 atm for the different electrolyte solutions.

Electrolyte Solution	Number of waters
LS NaCl	9028
HS NaCl	9009
LS KCl	8997
HS KCl	8959
LS CaCl ₂	9039
HS CaCl ₂	9017
LS MgCl ₂	9044
HS MgCl ₂	9035

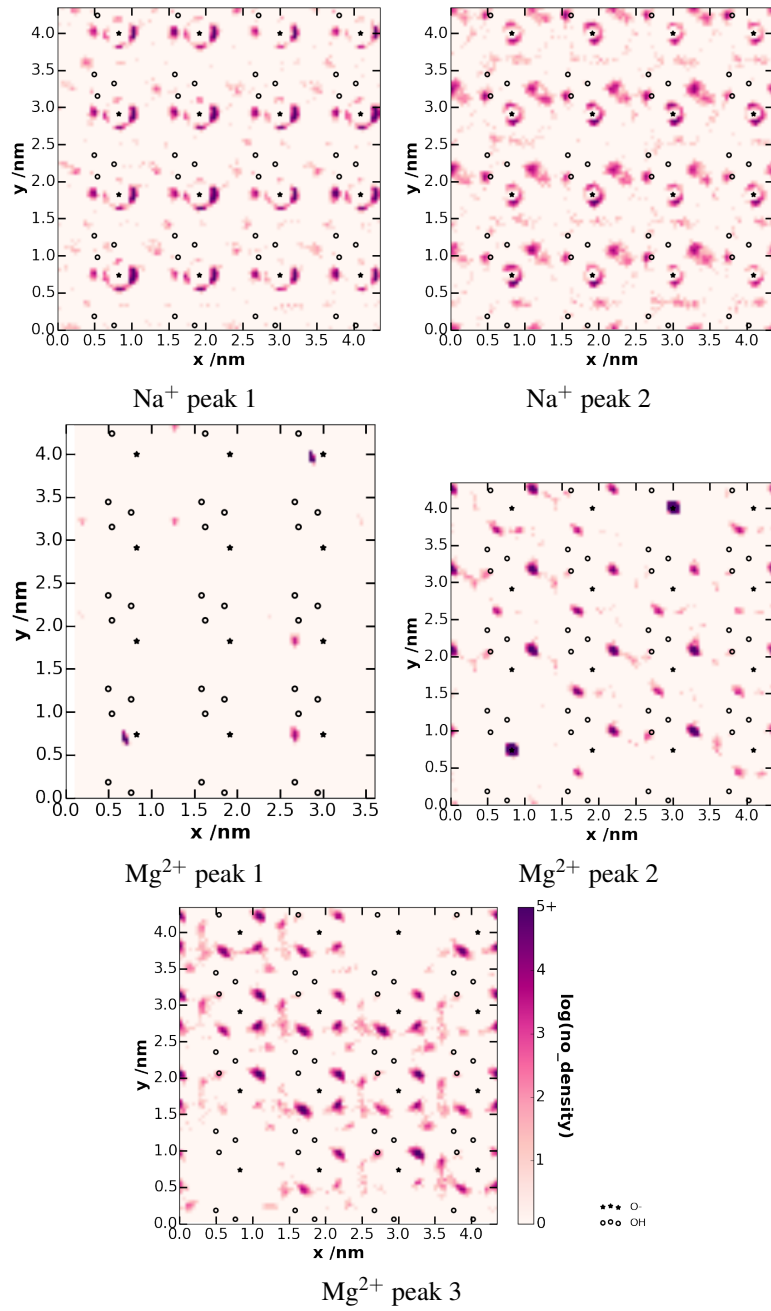


Figure C.1: $\rho_{Z_{max}}(xy)$: lateral cation density profiles at maxima in the ion concentration vs distance from the surface distributions for NaCl and MgCl₂ solutions (LS 0.1 M). The units of the number density are arbitrary and the same in all lateral profiles throughout this section.

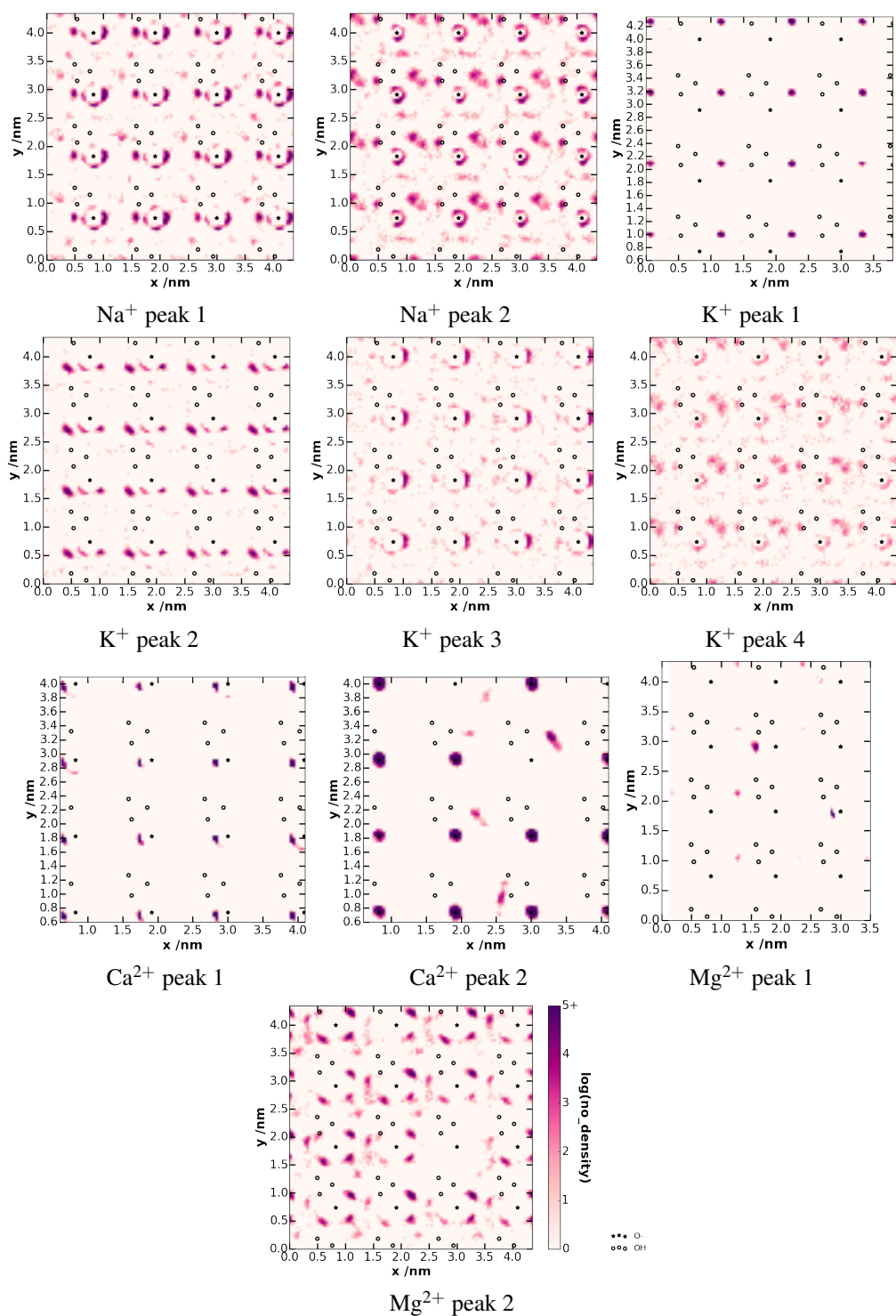


Figure C.2: $\rho_{Zmax}(xy)$: lateral cation density profiles at maxima in the ion concentration vs distance from the surface distributions for NaCl, KCl, CaCl₂ and MgCl₂ solutions (HS 0.3 M). The units of the number density are arbitrary and the same in all lateral profiles throughout this section.

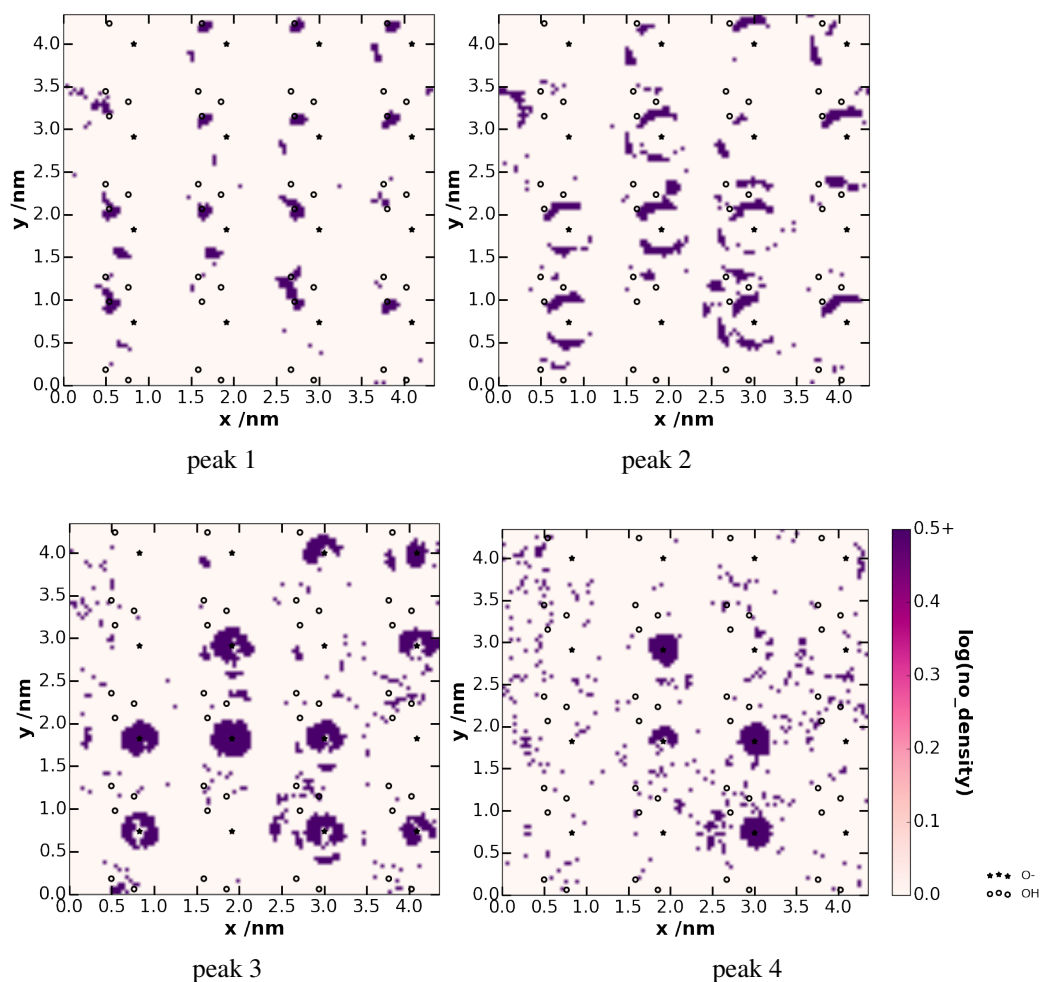


Figure C.3: $\rho_{Z_{\max}}(xy)$: lateral Cl^- density profiles at maxima in the ion concentration vs distance from the surface distributions for CaCl_2 solution (LS 0.3 M). The units of the number density are arbitrary and the same in all lateral profiles throughout this section.

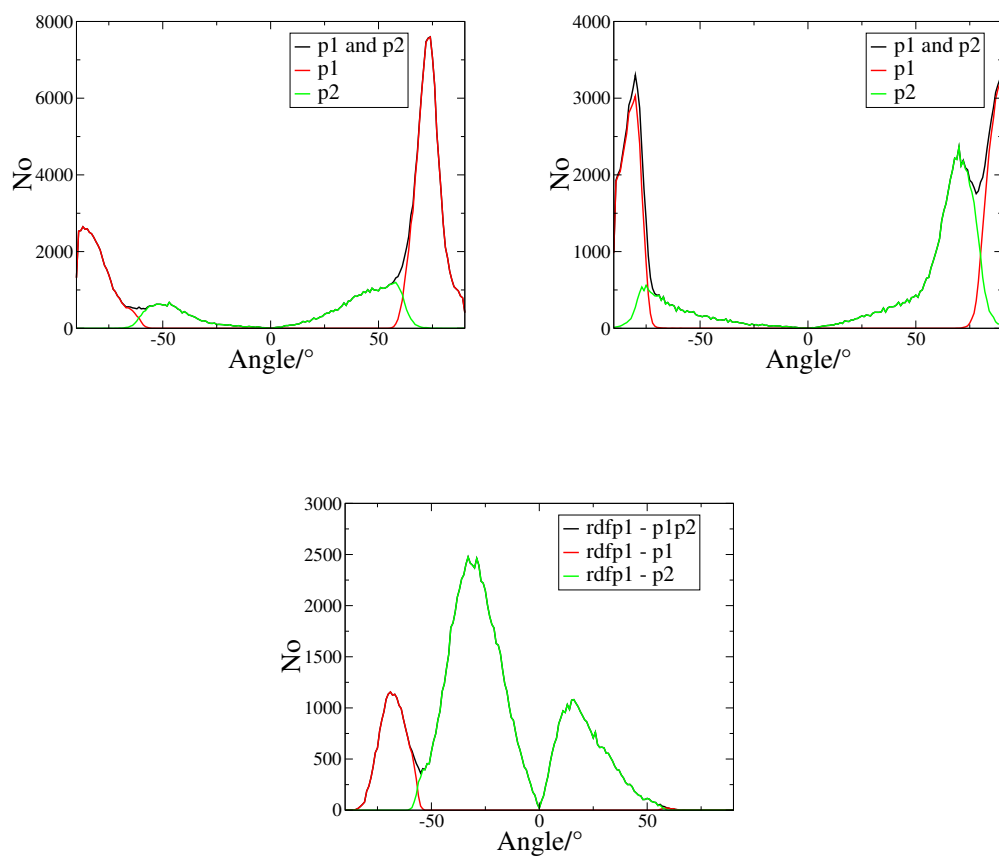


Figure C.4: Distributions of the angle made between the surface normal and r_{M-O} , where $r_{M-O} = r_M - r_O$. p refers to the peak in the CSDP(O^- -Mrdfp1).

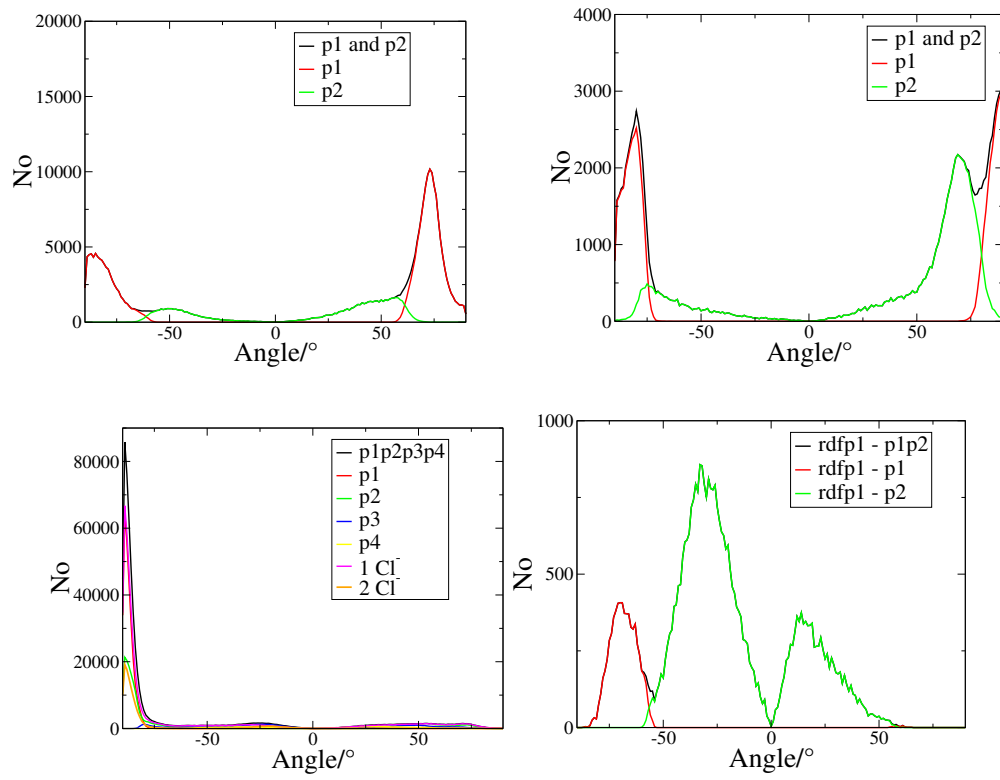


Figure C.5: Distributions of the angle made between the surface normal and r_{M-O} , where $r_{M-O} = r_M - r_O$. p refers to the peak in the CSDP(O^- -Mrdfp1).

Table C.2: Summary of distances from the surface of peaks in the ion density profiles.

Solution	Concentration/M	Ion	Peak ID No	distance from surface/Å
NaCl	0.1 & 0.3	Na ⁺	1	3.2
	0.1 & 0.3	Na ⁺	2	3.9
KCl	0.1 & 0.3	K ⁺	1	1.6
	0.1 & 0.3	K ⁺	2	2.8
	0.1 & 0.3	K ⁺	3	3.6
	0.1 & 0.3	K ⁺	4	4.3
CaCl ₂	0.1 & 0.3	Ca ²⁺	1	3
	0.1 & 0.3	Ca ²⁺	2	4.1
	0.1 & 0.3	Cl ⁻	1	3.3
	0.1 & 0.3	Cl ⁻	2	4.1
	0.1 & 0.3	Cl ⁻	3	5.2
MgCl ₂	0.1 & 0.3	Cl ⁻	4	6.5
	0.1	Mg ²⁺	1	3
	0.1	Mg ²⁺	2	3.8
	0.1	Mg ²⁺	3	4.2
	0.3	Mg ²⁺	1	3
	0.3	Mg ²⁺	2	4.2

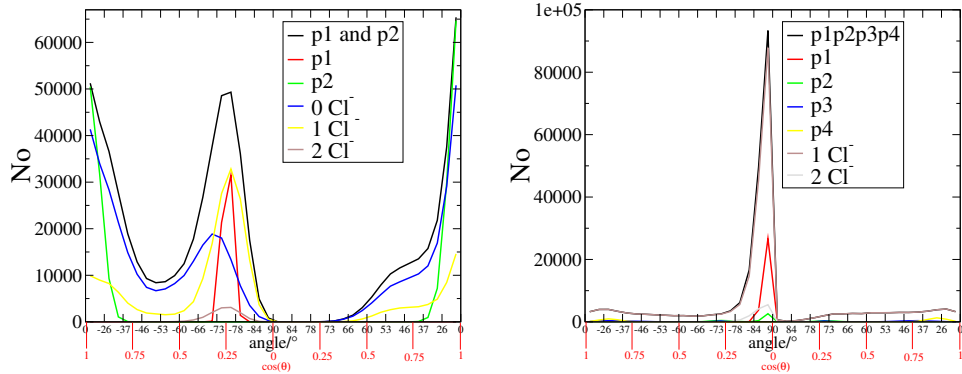


Figure C.6: Distributions of $\cos(\theta)$ where θ is the angle made between the surface normal and: (a) r_{Ca-O} , where $r_{Ca-O} = r_{Ca} - r_O$ (b) r_{Cl-O} , where $r_{Cl-O} = r_{Cl} - r_O$. p refers to the particular peak in the CSDP(rdfp1) and n Cl⁻ indicates the distributions when n Cl⁻ ions were associated

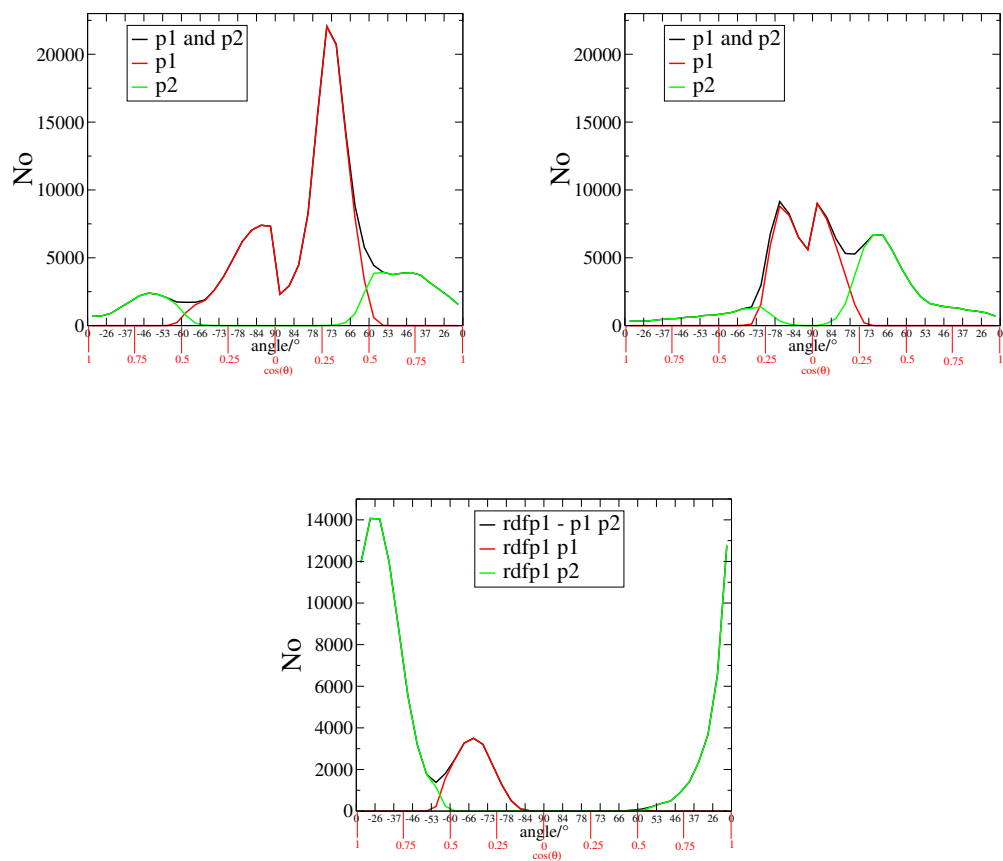


Figure C.7: Distributions of $\cos(\theta)$ where θ is the angle made between the surface normal and r_{M-O} , where $r_{M-O} = r_M - r_O$. p refers to the peak in the CSDP(O^- -Mrdfp1).

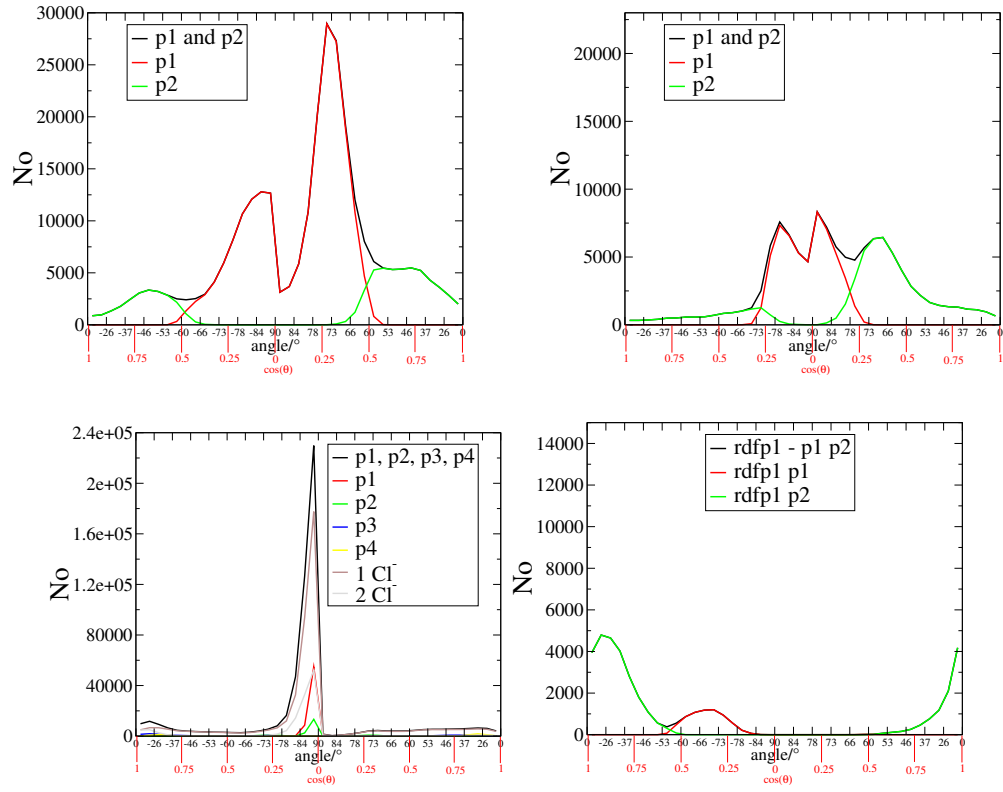


Figure C.8: Distributions of $\cos(\theta)$ where θ is the angle made between the surface normal and r_{M-O} , where $r_{M-O} = r_M - r_O$. p refers to the peak in the CSDP(O^- -Mrdfp1).

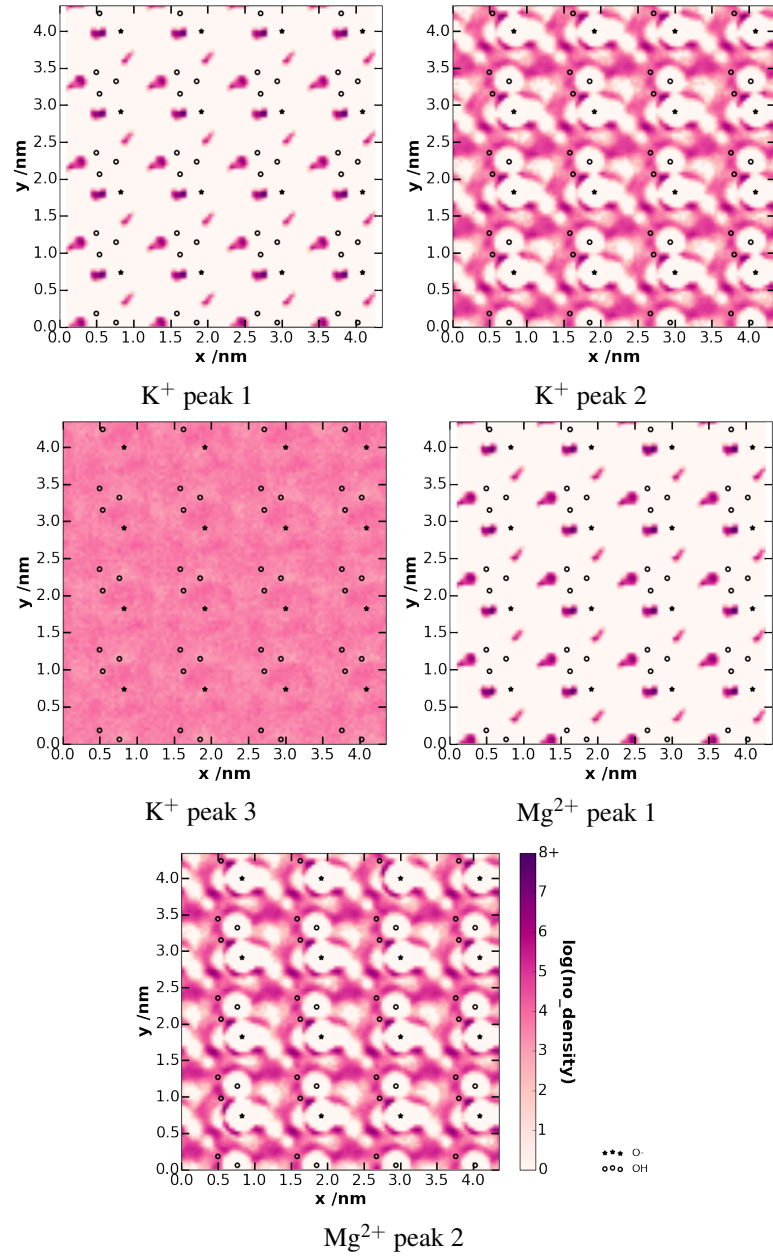


Figure C.9: $\rho_{Z_{max}}(xy)$: additional lateral water density profiles at maxima in the water density *vs* distance from the surface distributions for KCl and MgCl₂ solution (0.1 M). Blue dots represent deprotonated silanols and green dots represent protonated silanols. The units of the number density are arbitrary and the same in all lateral profiles throughout this section.

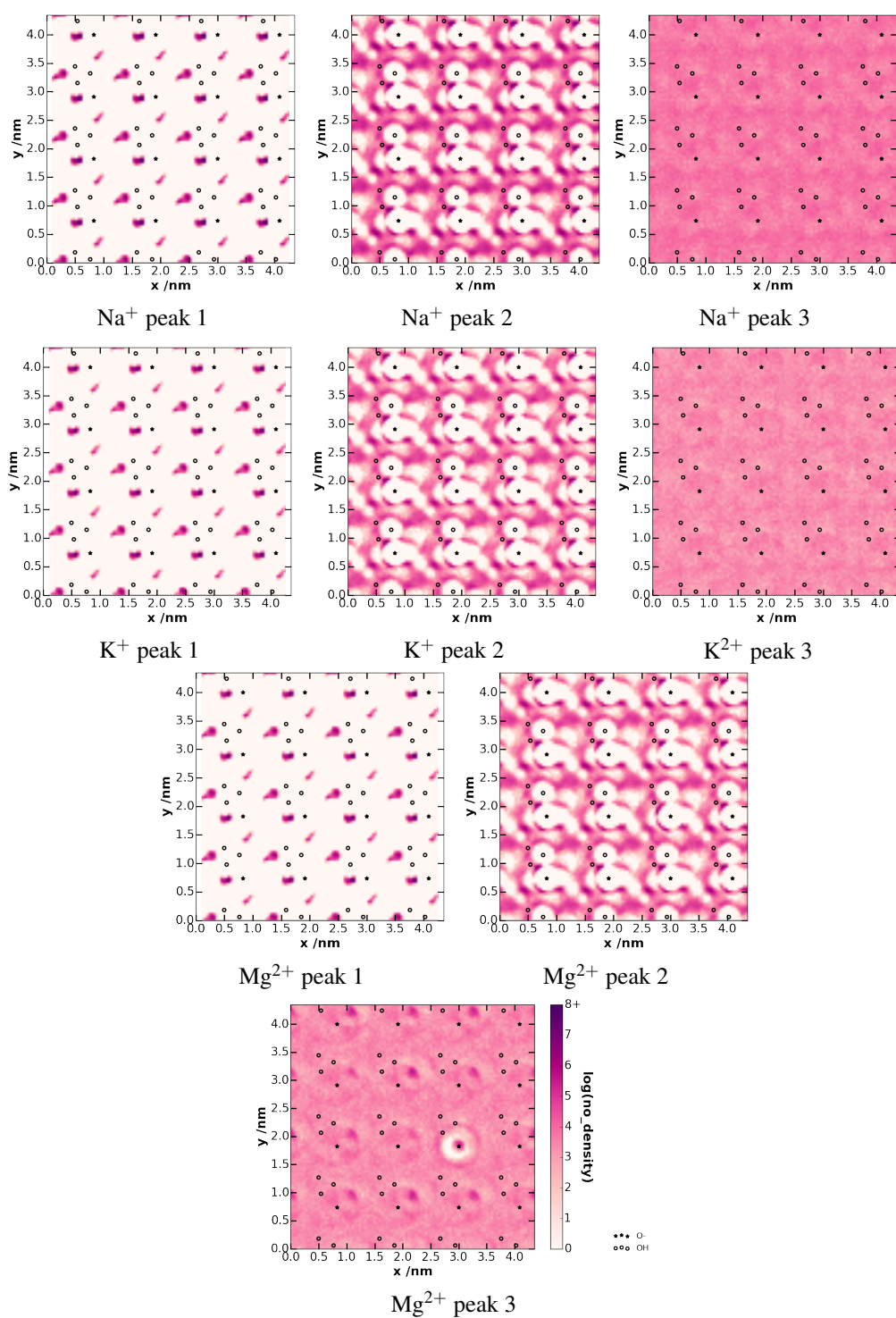


Figure C.10: $\rho_{Zmax}(xy)$: lateral water density profiles at maxima in the water density vs distance from the surface distributions for NaCl, MgCl₂ and CaCl₂ solution (0.3 M). The units of the number density are arbitrary and the same in all lateral profiles throughout this section.

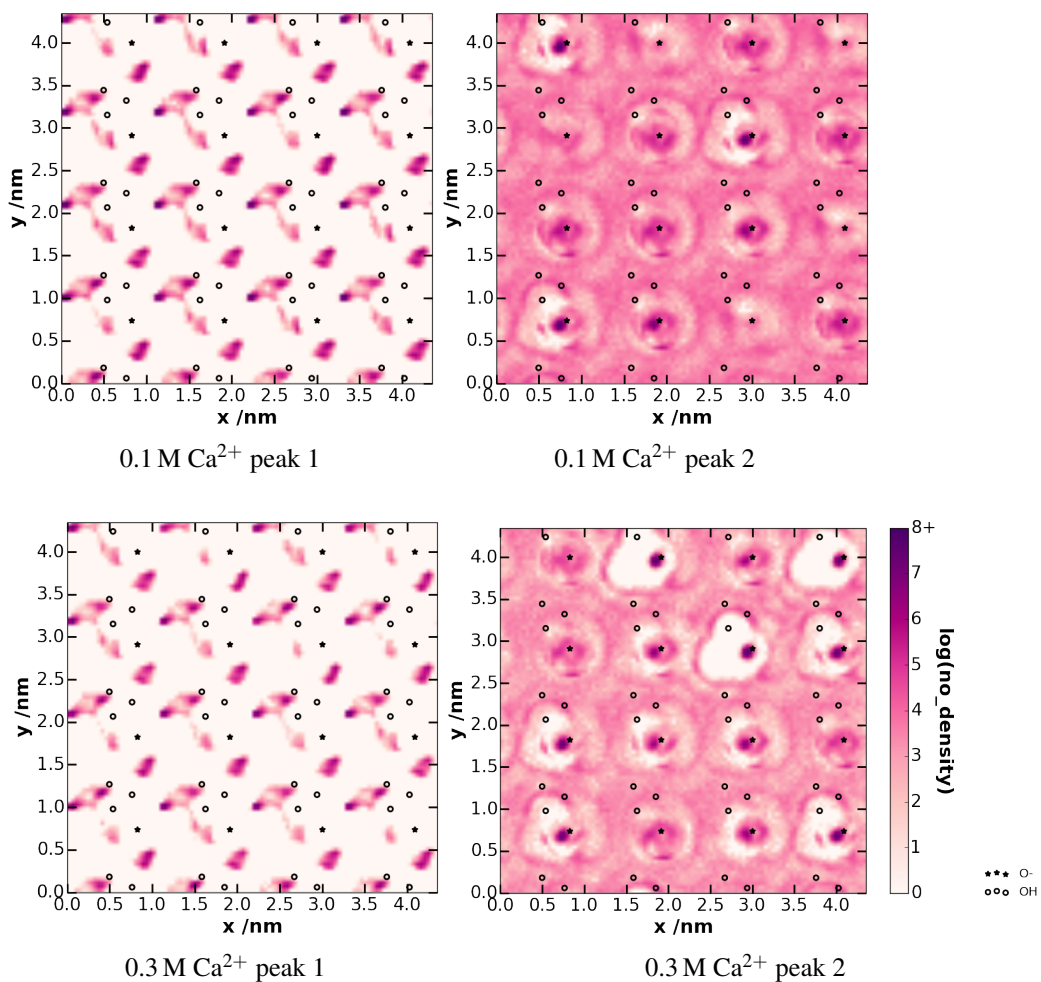


Figure C.11: $\rho_{Z_{\max}}(xy)$: Lateral water density profiles at maxima of the secondary layers in the water density vs distance from the surface distributions for 0.3 M CaCl_2 solution and at the counterpart distances in 0.1 M solution. The units of the number density are arbitrary and the same in all lateral profiles throughout this section.

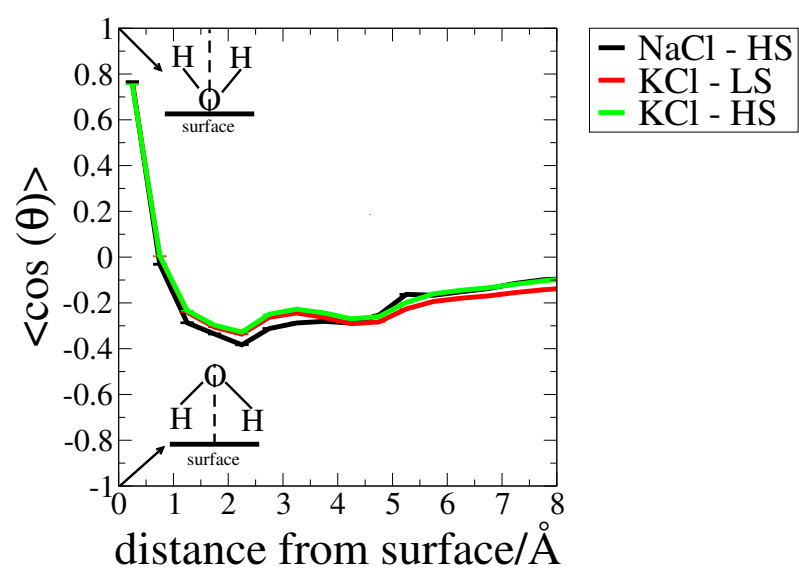


Figure C.12: Net water orientation as a function of distance for a selection of the electrolyte solutions investigated.

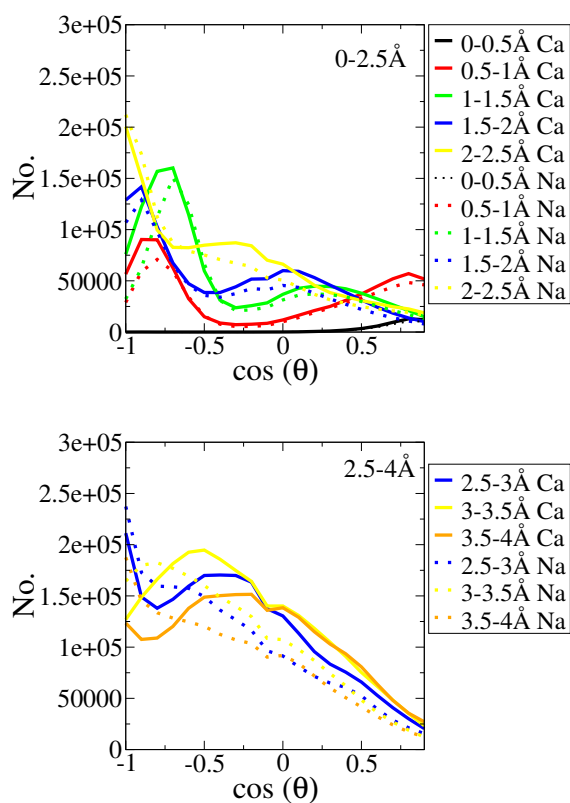


Figure C.13: Full distributions of $\cos(\theta)$ between 0-2.5 Å and between 2.5-4 Å for 0.3 M CaCl_2 denoted Ca and 0.1 M NaCl, denoted Na.

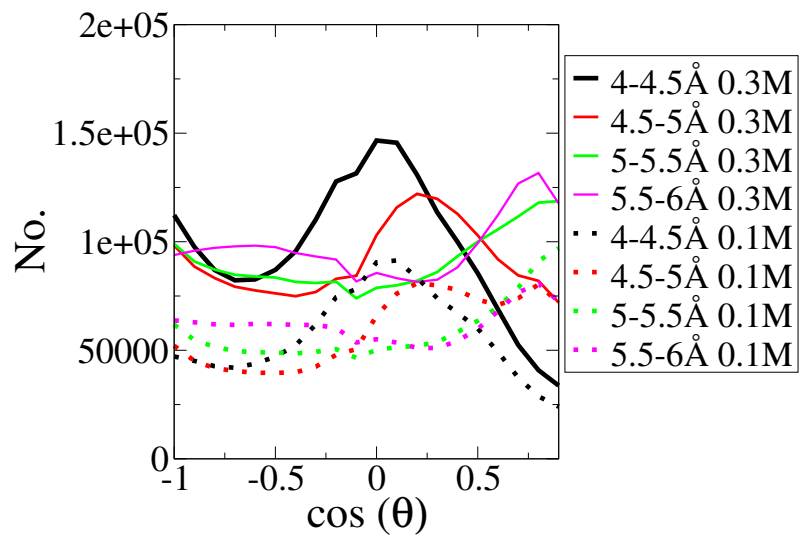
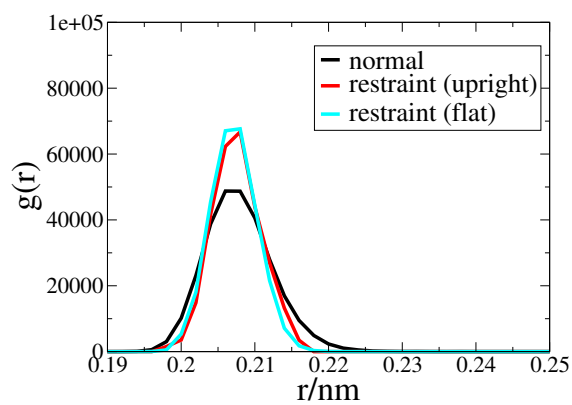


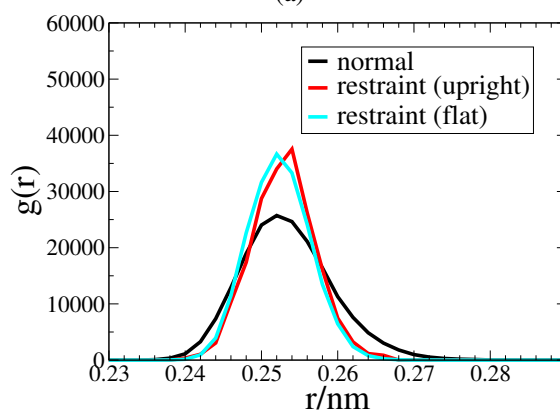
Figure C.14: Full distributions of $\cos(\theta)$ between 4-6 Å for 0.1 M and 0.3 M CaCl_2 .

Appendix D

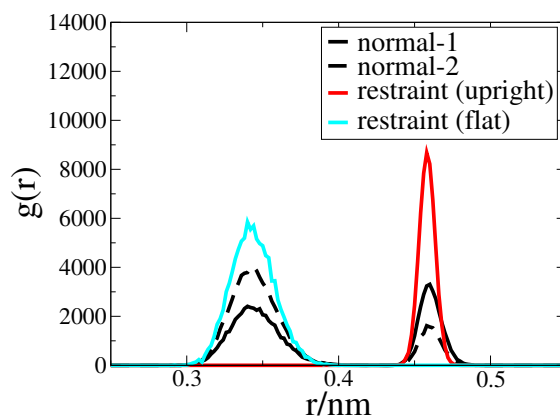
Additional Information: The Role of Ion Type in the Low Salinity Effect: an Experimental and Computational Study



(a)



(b)



(c)

Figure D.1: RDFs between (a) O^- to 'bound' Ca^{2+} (b) Ca^{2+} to 'bound' Cl^- (c) O^- to 'bound' Cl^-

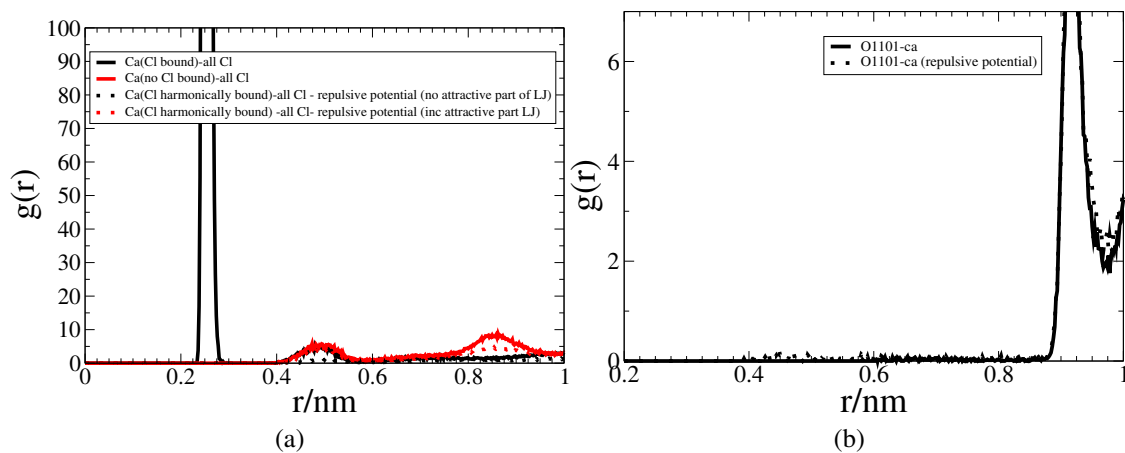


Figure D.2: rdfs between (a) O^- bound Ca^{2+} and all chloride ions apart from any officially associated Cl^- . (b) O^- and all Ca^{2+} ions.

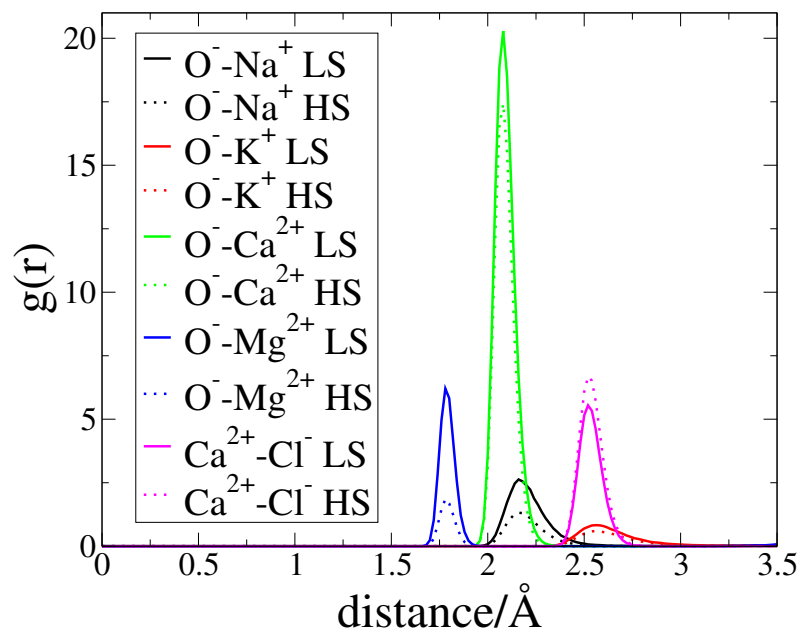


Figure D.3: Cation-deprotonated oxygen and chloride ion-surface bound calcium ion RDFs

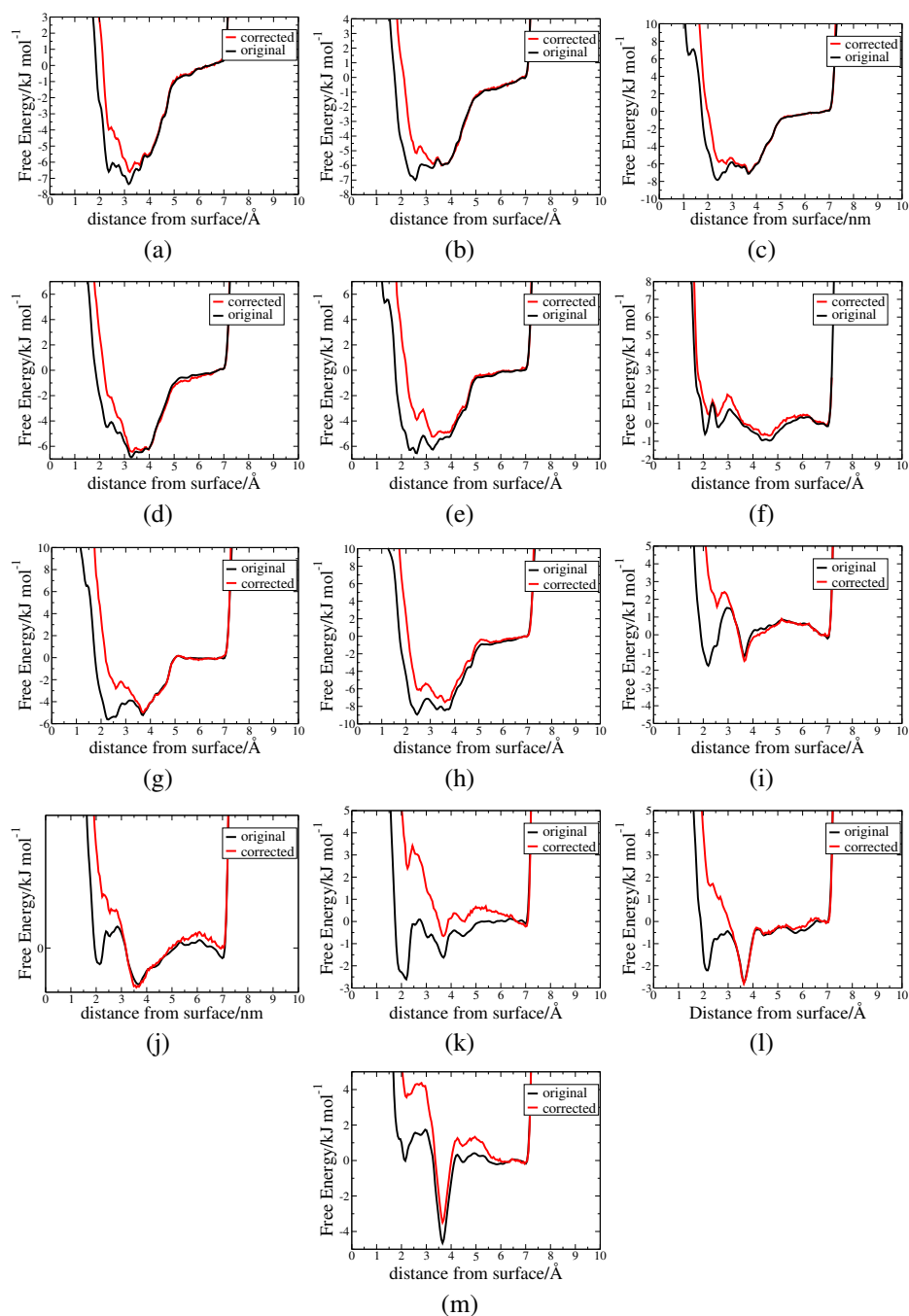


Figure D.4: The remainder of the free energy profiles from the final metadynamics simulations, a comparison between the corrected and uncorrected versions for (a) HS aq. NaCl (b) LS aq. KCl (c) HS aq. KCl (d) unbound state, LS aq. MgCl₂ (e) unbound state, HS aq. MgCl₂ (f) bound state, LS aq. MgCl₂ (g) O⁻, aq. LS CaCl₂ (h) O⁻, aq. HS CaCl₂ (i) O⁻Ca²⁺, aq. LS CaCl₂ (j) O⁻Ca²⁺, aq. HS CaCl₂ (k) O⁻Ca²⁺Cl⁻, aq. LS CaCl₂ (l) O⁻Ca²⁺Cl⁻, aq. HS CaCl₂ (m) O⁻Ca²⁺Cl₂⁻, aq. LS CaCl₂ (n) O⁻Ca²⁺Cl₂⁻, aq. HS CaCl₂

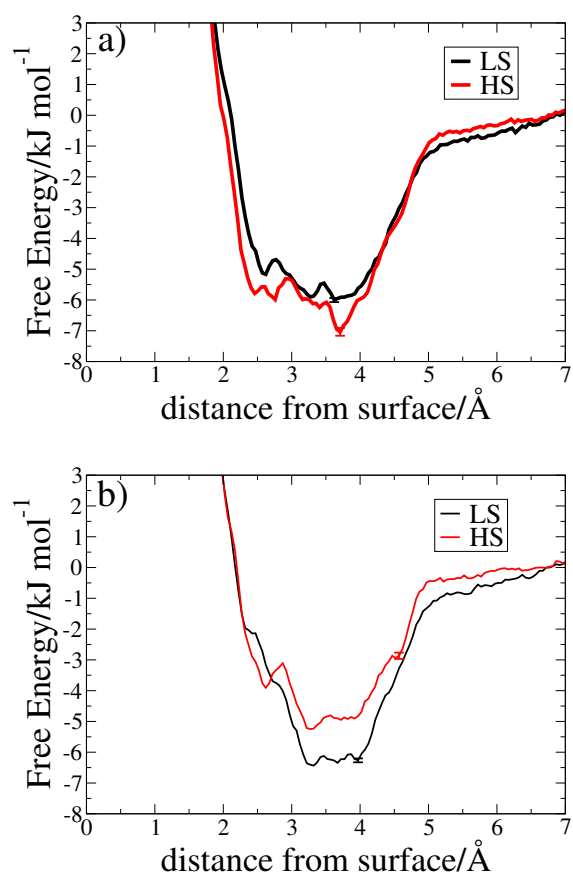


Figure D.5: Free energy profiles for the adsorption of the nitrogen of methylammonium to the silica surface in different salt solutions (a) KCl (b) MgCl₂ solution, unoccupied O⁻

Appendix E

Additional Information: Further and Future Investigation of the Low Salinity Effect: A More Sophisticated Model of the Functionalized Atomic Force Microscopy (AFM) Tip

Simulations were conducted with two different initial configurations. For starting point 1, the Cl^- ions were positioned randomly and for starting point 2, the Cl^- ions were positioned directly above the NH_3^+ groups. Furthermore, in the case of starting point 2, the volume of solution next to the monolayer was in direct contact with the gold substrate, while for starting point 1, there was a vacuum buffer. This accounted for the different characters of the water density and Cl^- concentration profiles at ~ 0 nm from the 'vacuum'. Other than this difference, the distributions displayed the same characteristics. The N atom distributions and average monolayer thicknesses were well-reproduced between the two cases. The tilt and azimuthal angles, however, had a dependence on the initial positioning of the Cl^- ions, though the averages did not differ greatly between the two cases.

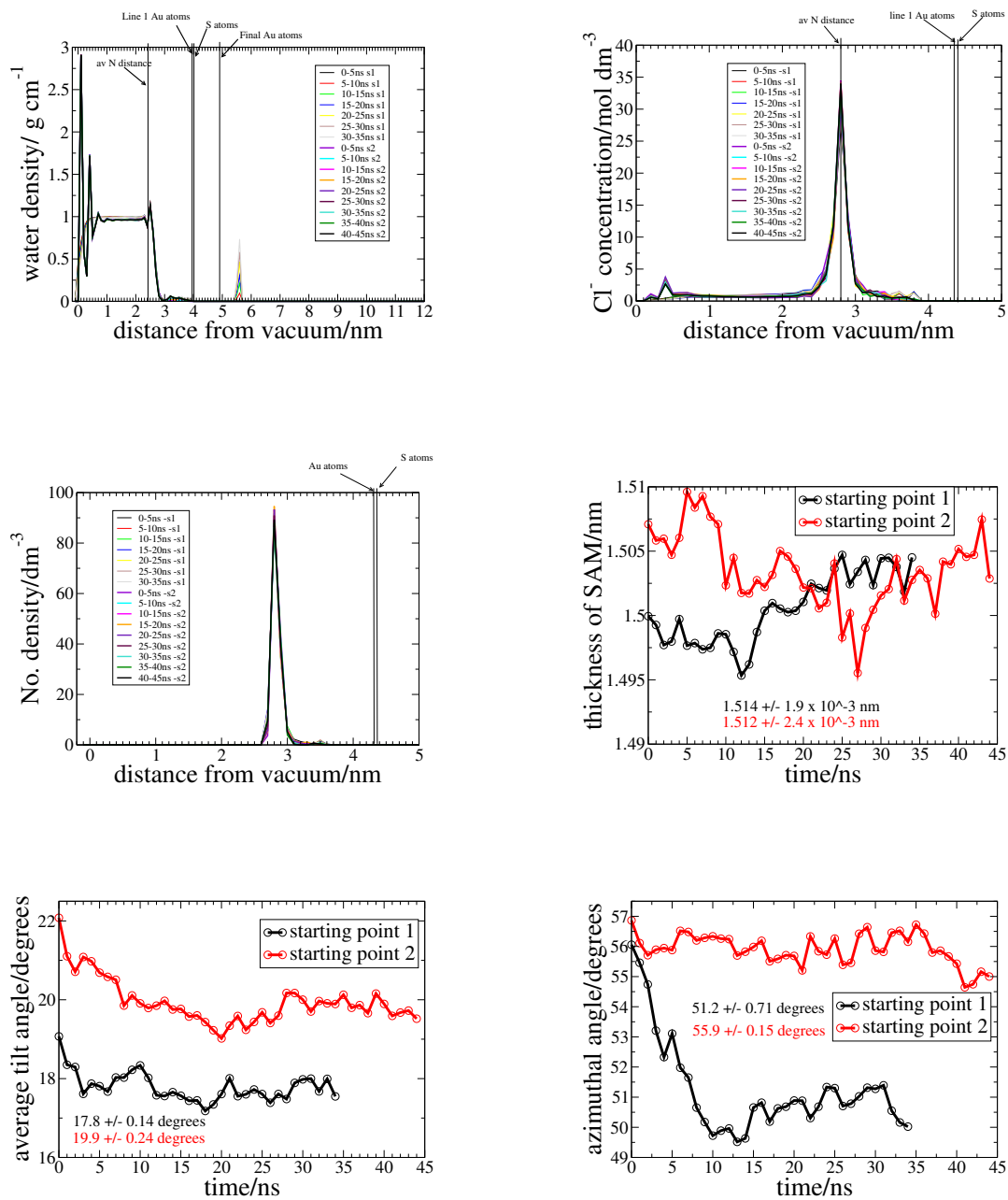


Figure E.1: Evidence for the equilibration of the infinitely-sized monolayer. SP refers to starting point. (a) water density as a function of distance from the vacuum/gold surface (b) Cl^- density as a function of distance from the vacuum/gold surface (c) N density profiles as a function of distance from the vacuum/gold surface (d) monolayer thickness with time (e) tilt angle with time (f) azimuthal tilt angle with time.

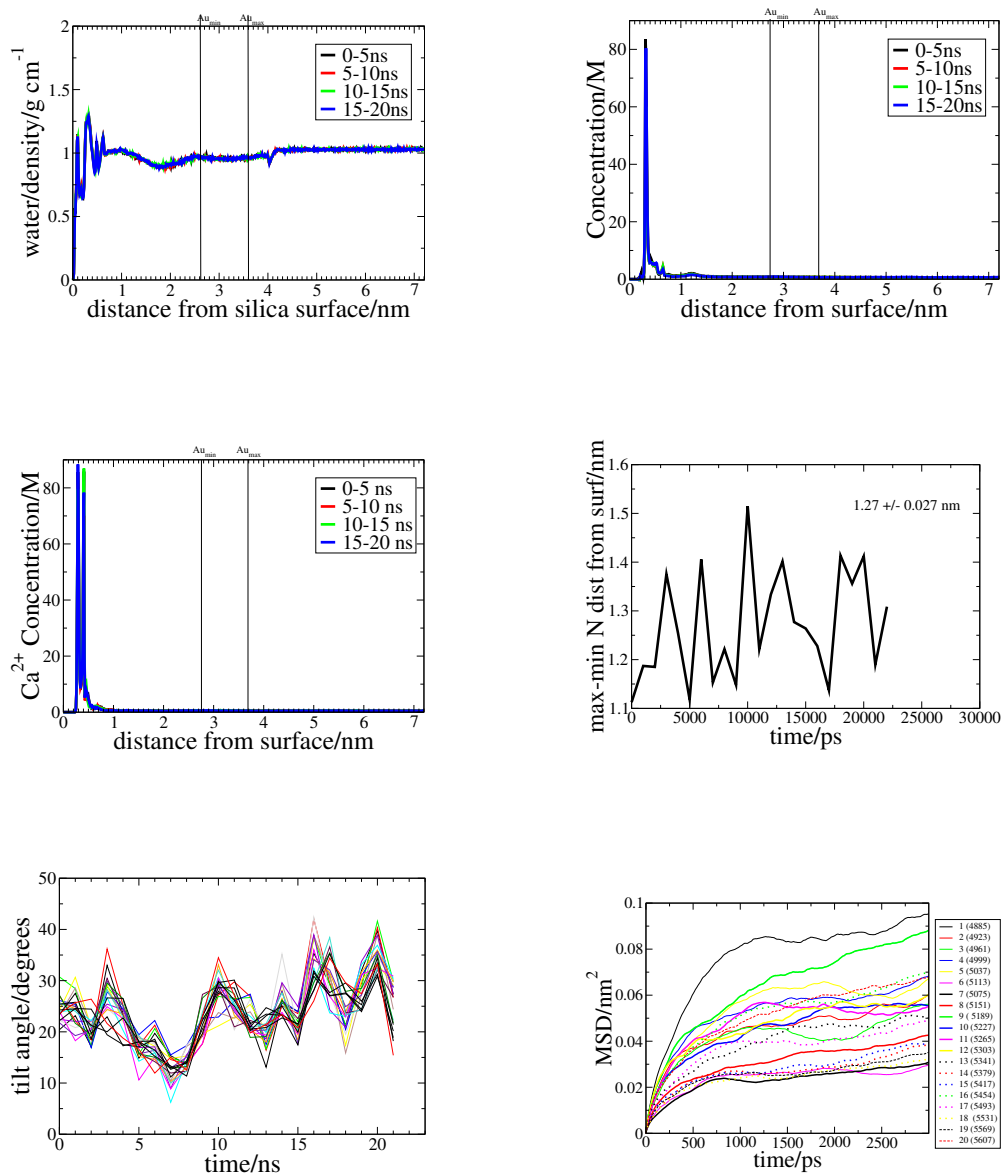


Figure E.2: Evidence for the equilibration of the system that featured the model AFM tip and the model tip as a reasonable representation of the infinite monolayer (a) water density as a function of distance from the silica surface (b) Cl^- density as a function of distance from the silica surface (c) Ca^{2+} density as a function of distance from the silica surface (d) maximum N atom distance from the surface - minimum N atom distance from the surface (e) tilt angle of each of the Au-adsorbed molecules with time (f) mean square displacement of the N atom of the head group of each of the adsorbed molecules with time.